Corona Discharge and Arcing around Wires under the Influence of High Electric Fields.

John Lee Evans

Department of Electrical Engineering

University of Nottingham

This dissertation is submitted for the degree of

Doctor of Philosophy

I would like to dedicate this to my late mother Joyce.

Declaration

I hereby declare that except where specific reference is made to the work of others, the contents of this dissertation are original and have not been submitted in whole or in part for consideration for any other degree or qualification in this, or any other University. This dissertation is the result of my own work and includes nothing that is the outcome of work done in collaboration, except where specifically indicated in the text. This dissertation contains less than 65,000 words including appendices, bibliography, footnotes, tables and equations and has less than 150 figures.

John Lee Evans

Acknowledgements

I would like to take this opportunity to acknowledge my supervisors; Professor David Thomas and Dr Steve Greedy for their support and patience throughout the development of this thesis. I would also like to thank the Atomic Weapons Establishment for their financial support during the initial three years. Appreciation must go to both parties for giving me the opportunity in the first place. Finally, I would also like to thank Dr Christopher Smartt for his incite in regards to the Transmission-Line Modelling Method that proved highly beneficial during difficult times in the initial stages.

Abstract

An Electromagnetic Pulse (EMP) resulting from, for example, the detonation of a nuclear weapon is characterised by a wave of electromagnetic activity able to couple with power lines and electro-sensitive equipment with the potential of rendering an establishment or on a greater scale, a whole city impotent. Protection against such occurrences is of paramount importance. It is now accepted that an important consideration when devising protective schemes against such phenomena is an accurate understanding of the effects on propagating waveforms such as those coupled to wires, when electrical breakdown of the dielectric material surrounding such wires occurs, otherwise known as electrical discharge. Such issues can occur around the affected wires if the electric fields generated exceed the dielectric strength of the surrounding medium, typically air or soil. Under these circumstances, the signature of the coupled waveform is known to change in characteristic ways. The form and degree of distortion needs to be understood if the harmful effects are to be prevented by protection systems put in place.

The purpose of this thesis is to first describe the mechanisms that lead to the development of the Nuclear–Electromagnetic Pulse (NEMP) and the mechanisms of the discharge that can result once such pulses have coupled to a wire. Next, some of the previous corona-modelling approaches are discussed. Many of the modelling approaches have been applied to 1-D transmission-line simulations. When 3-D simulations have been performed, the Finite-Difference (Time Domain) or FD-TD approach seems to be the preferred method. At the time of writing, no 3-D Transmission Line simulations of discharge phenomena around wires were available. Hence, here, the 3-D Transmission Line Modelling Method (TLM) is described with a view to modelling such behaviour. In particular, the Embedded-Wire-Node (EWN) is used to model the discharge development around the wire. This is a fine-wire technique used to reduce computational fatigue. The node can be adapted to accept changes related to electrical discharge allowing for a real-time, self-consistent recreation of such effects.

The 3-D TLM approach proves to be a decent candidate to the modelling of such behaviour. Both advantages and disadvantages of this method are discussed.

Contents

Contents ix
List of Figures xiii
List of Tables xix
Nomenclature xxi
Chapter 0 Introduction and Thesis Outline xxxii
Chapter 1 The Electromagnetic Pulse (EMP) 34
1.1 Historical Perspective 34
1.2 EMP Generation 36
1.2.1 Primary Electron Production -The Compton Current Density 40
1.2.2 Air Conductivity. 42
1.3 The Source Region and Altitude Dependence. 45
1.3.2 HEMP line Coupling: 53
1.4 Chapter summary. 54
Chapter 2 Electrical Discharge 56
2.1 Basic Definitions 57
2.1.1 Drift velocity and mobility 57
2.1.2 Mean free path and cross section. 58
2.2 Ionisation Processes. 59
2.3 De-ionisation Processes 62
2.3.1 Electron-ion recombination 62
2.3.2 Dissociative recombination. 62
2.3.3 Electron attachment/detachment: 63
2.3.4 Diffusion. 63
2.3.5 Energy lost to increased molecular vibrations. 64
2.4 Sources of Free Electrons. 64
2.4.1 Natural Process: 64
2.4.2 Cathode Processes: 64
2.5 Electrical Breakdown. 65
2.5.1 Critical Electric Field 65

2.5.2 Physical processes describing electric discharge 66
2.6 Corona Discharges 76
2.6.1 Negative Corona Modes. 77
2.6.2 Positive Corona Modes. 79
2.6.3 Dependence of electrical breakdown on atmospheric conditions. 81
2.7 Lightning 82
2.8 Summary. 83
Chapter 3 The Transmission-Line Modelling Technique 84
3.1 Basic principles (1-D TLM) 85
3.1.1 Introduction of stubs 89
3.1.2 Scattering 91
3.1.3 The Connection Process: 93
3.2 Three-Dimensional TLM: 94
3.2.1 Introducing relative permittivity, permeability to the 3-D SCN mesh. 98
3.2.2 Propagation through a 3-D mesh. 99
3.3 Introducing wires to the mesh. 101
3.3.1 The Embedded Wire Node (EWN) 102
3.4 Using the node output values to find other useful information. 108
3.4.1 Electric Current 108
3.4.2 Electric charge 110
3.5 Summary 115
Chapter 4 Modelling the Effects of Corona on Coupled Transients. 117
4.1 Distortions on propagating waveforms due to electrical breakdown 118
4.2 The Choice and Magnitude of Corona Parameter to Recreate Corona Effects. 122
4.3 Transmission Line Equations adapted for Corona 135
4.4 Soil Ionisation 140
4.4.1 Introduction. 140
4.4.2 Grounding Systems - basic calculations and high frequency considerations. 141
4.4.3 Soil Ionisation Models 146
4.5 Summary 153
Chapter 5 Results and Discussion 154
5.1 Tests 155
5.1.1 Simple square coax (EWN): 155
5.1.2 Square coaxial transmission line (using SCN only): 156
5.1.3 Wire below ground – static resistance: 158
5.2 Corona Models 160
5.2.1 Corona as an apparent increase in Conductor Radius 161

5.2.2 Corona as a region of nominal conductivity (Thang et al.). 168
5.2.3 Simulating corona development based on parameters found using the Cooray Equations. 178
5.2.4 Soil breakdown. 188
Chapter 6 Conclusions. 197
Chapter 7 Future Work 203
References 205
Appendix A A-1
A.1 The Source Region. A-1
A.1.1 The Symmetrical Source Region. A-6
A.1.2 Source Region related to a Surface Burst A-9
A.1.3 The High-Altitude EMP (HEMP). A-13
Appendix B B-1
B.1 The Transmission Line Equations (Telegraphers equations) B-1
B.1.1 Related to Two Conductor Transmission Line B-1
B.2 Relating theTL equations to the Embedded Wire Node (EWN). B-6
B.3 TL Equations in the presence of Corona B-7

List of Figures

Figure 1-1 Flow diagram describing the basic mechanisms resulting in EMP generation [3]. 39

Figure 1-2 Qualitative representation of the source magnitudes of gamma radiation from different mechanisms following a surface burst nuclear explosion. [13] 40

Figure 1-3 Compton scattering- a photon (x-ray or γ-ray of a given wavelength) collides with an atom or molecule imparting some of its energy resulting in a reduction in its wavelength proportional to the angle of collision. 41

Figure 1-4 The'charge-separation model' describing the fields that form in the source region following an explosion. (based on [15]) 43

Figure 1-5 Graph by Longmire depicting the transient behaviour of the vertical electric field at various distances from the burst epicentre of a nominal 1MT surface burst. (Taken from [15]) 44

Figure 1-6 Graph by Longmire depicting the transient behaviour of the radial electric field within the source region of a 1MT surface burst (taken from [15]) 45

Figure 1-7 Geometry of a surface burst. The ground enforces asymmetry such that the source region can be considered hemispherical. Hence, a net current can be defined vertically [3] .. 48

Figure 1-8 The generation of an azimuthal magnetic field. Loop currents in the vicinity of the ground emerge due to the ground conductance shorting the radial fields created by the primary Compton current. Concentric magnetic field lines centred around the polar axis form (B_{in} is the magnetic field into page, B_{out} is the field out of the page [3]. 48

Figure 1-9 Diagram depicting the potential areas affected by HEMP in relation to the height of burst [17] 49

Figure 1-10 The source region resulting from a high-altitude (100 km) nuclear explosion [3]. 50

Figure 1-11 Deflection of the Compton current by the Earth's geomagnetic field (e^- = Compton electrons, S=Poynting vector) [18] 51

Figure 1-12 A generic HEMP waveform. Note the absence of the ground component [18]. . 52

Figure 2-1 The free-path of a gas molecule, where 2*d* represents the cross-section of the particle (recreated from [22] 59

Figure 2-2 Qualitative depiction of variation of ionisation and attachment frequencies with electric field [22] 66

Figure 2-3 Left: photograph of an electron avalanche[28]. Right: depiction of space charge throughout the avalanche. 68

Figure 2-4 Stages of positive streamer formation (adapted from[23]) 72

Figure 2-5 The active region of a positive (cathode directed) streamer [23]..... 73

Figure 2-6 Basic depiction of the progression of a positive streamer. Electrons produced via secondary avalanches move to neutralize the positive charge at the streamer head. Positive charge from the secondary avalanches is left behind forming the extension to the streamer. (adapted from [23]) 73

Figure 2-7 Formation of a negative streamer. Secondary avalanches propagate away from the wire leaving behind positive ions. These are neutralized from electrons that are taken from the wire, conducted via the streamer channel[23]. 75

Figure 2-8: The space charges formed through negative corona development. As the charges develop the radial field is modified in such a way that S_0 edges closer and closer to the wire surface [22] 78

Figure 2-9: Distortion of the radial electric field due to space charge formed during positive corona development [22] 82

Figure 3-1A basic x-directed transmission line segment 85

Figure 3-2 A propagating electromagnetic wave in the *x*-direction with electric and magnetic field components polarized as shown. In the diagram, each field value (represented by an arrow) should have its respective node to meet the $\lambda/10$ criterion (see later). 87

Figure 3-3 A 1-D line segment of length Δx. The link lines represent free space while the stub in the centre represents any necessary relative permittivity. 90

Figure 3-4 Thévenin equivalent circuit with the impedance of an open circuit stub at the centre of the node representing relative permittivity 92

Figure 3-5 The Symmetrical Condensed Node (SCN). Two notations are demonstrated [38]. 94

Figure 3-6 The three cluster arrangements that constitute the SCN [40]. 95

Figure 3-7 Propagation of a wave in a 3-D SCN mesh. The propagation takes place in two stages hence the speed of propagation on each TL segment must be twice the speed of light. 100

Figure 3-8 The short-circuit SCN: all pulses incident on the node are reflected away from the cell [27]. 101

Figure 3-9 The position of the embedded-wire within the SCN..... 102

Figure 3-10 (a) The sub-circuit of the SCN coupled to the embedded wire (b) The Thévenin equivalent of the sub-circuit..... 103

Figure 3-11 The cell can be approximated as a cylinder to which a fictitious radius can be assigned. This allows a capacitance or inductance value to be determined..... 104

Figure 3-12 TL representation of the EWN. The upper circuit represents the wire while the lower circuit represents the relevant SCN sub-circuit. 107

Figure 3-13 The Thévenin equivalent of the EWN. 108

Figure 3-14 Thévenin equivalent circuit representing the *y*-directed current flowing through a short-circuited 3-D SCN node. 109

Figure 3-15. Using the closed path of magnetic field about a wire to calculate current (EWN)[40]. 110

Figure 3-16 Using the relevant field values (node voltages) about a conductor to obtain charge (Gauss' Law) 111

Figure 3-17. Using the radial displacement field from the conductor to obtain its charge.... 112
Figure 3-18. Using capacitance to find the charge (per unit length) of a wire. 113
Figure 3-19. (a) EWN wire node adapted for conductive environment, (b) Thévenin equivalent of the EWN..... 114
Figure 4-1 A typical q-V characteristic describing the relation between total charge (q) and applied voltage (V) on a wire. A deviation from the characteristic capacitance of the line is evident once the breakdown voltage (Vb) is exceeded..... 119
Figure 4-2 Distortions found experimentally on a propagating waveform. Readings taken at various points along the power line (sequentially from A to D) [50]..... 121
Figure 4-3 Simple diagram showing the typical distortions expected during corona. A retardation (delay per distance travelled) can be assigned to voltage components above the breakdown voltage threshold [51]. 122
Figure 4-4 (a) corona development around a wire modelled as a radial extension of the conductor (b) relation to critical breakdown field, E_b..... 123
Figure 4-5 Transmission line graphic with the additional capacitance added when line voltage exceeds a given threshold 124
Figure 4-6 A linear capacitance is added when the line is represented as in figure 4.5. 124
Figure 4-7 introduction of a second addition conductance at a higher threshold 125
Figure 4-8 Top: 1D transmission line used to recreate corona effects. Below: Thévenin equivalent circuit used in a 1-D TLM node in the Christopoulos simulation ($Z=695\Omega$, V_b = 386 kV) [53]..... 126
Figure 4-9 Corona related distortions imparted on a bi-exponential waveform propagating on a wire undergoing corona using the 1-D TLM node suggested by Christopoulos [53].Dotted line represents experimental results obtained by Wagner et al [50] 127
Figure 4-10 The retardation of voltage components above the breakdown voltage threshold using a single capacitance value to depict corona development..... 127
Figure 4-11 Diagram to describe the basic premise behind the FD-TD model presented by Thang et al [55] 129
Figure 4-12 The stages chosen by Cooray to describe corona development about a wire assuming a cylindrical breakdown region [61] 134
Figure 4-13 Interaction of an external electric field component with a line element inducing identical infinitesimal current pulses in the directions of P1 and P2[57]. 138
Figure 4-14 The three current components that constitute the total current at a particular point on a corona-affected wire [57] 140
Figure 4-15 Major elements of a grounding system (adapted from [64] 142
Figure 4-16 (a) Circuit description of an underground transmission line segment. (b) The complex nature of the currents entering and leaving a rod segment.[64] 143
Figure 4-17 Injected current and leakage current density at various points on a grounded rod [58] 148
Figure 4-18 Various means of electrocution near a grounding rod subjected to a lightning strike: (a) touch potential , (b) step potential , (c) transferred potential [78]..... 152

Figure 5-1: Square coaxial TL with central conductor of radius 0.0065m modelled using EWN. Outer conductor side length , b = 0.14m. Total length of coax = 12m. 155

Figure 5-2 The impedance of a coaxial wire , measured at the midpoint modelled using the Embedded wire node within a GSCN mesh. 156

Figure 5-3 Capacitance per-unit length of square coaxial TL. 157

Figure 5-4. horizontal electrode , l =12, a (electrode radius) = 0.0065m, h (depth below ground level) = 0.5 m, buried in ground with soil resistivity, ρs= 500 Ω m. 159

Figure 5-5: horizontal electrode, 0.005m radius , 90m length , buried at 0.6m in soil of resistivity = 5000 Ωm. Mesh size 270 cells x 45 cells x 45 cells (90m x 15m x 15m) , dl = 0.3333 m 159

Figure 5-6: Horizontal electrode, 0.005m radius , 90m length , buried at 0.6m in soil of resistivity = 2000 Ωm. Mesh size 270 cells x 45 cells x 45 cells (90m x 15m x 15m) , dl = 0.3333 m 160

Figure 5-7 Schematic to demonstrate the principle behind the increasing radius approach to corona modelling. 163

Figure 5-8 The basic EWN with link-line and stub TL to account for capacitance and inductance. 164

Figure 5-9 Distortions on a propagating waveform at various points along the line when corona is modelled as an increase in wire radius. The blue lines represent the experimental results [50]. Other colours are based on simulation. 164

Figure 5-10 'Fictitious radius' development at a node close to the wire excitation node. 165

Figure 5-11: Change in node capacitance with radius increase. 165

Figure 5-12: Using an increasing conductor radius to represent corona. The radial extent of the corona is governed by the streamer criterion (Ec = 0.5 MV/m) and a decay constant (= 0.5 μs). 166

Figure 5-13: Both changes to inductance and capacitance are introduced to the EWN in accordance with the new conductor radius. The effects are dramatically reduced although some residual capacitance still appears to be unaccounted for. 167

Figure 5-14: Development of conductance within the EWN as corona is deemed to develop. 169

Figure 5-15 Comparison of the shunt corona current found analytically (red) and found solving the Thévenin equivalent circuit (blue). 169

Figure 5-16 Radial corona current measured analytically and by solving the Thévenin circuit when the corona radius is fixed at cell boundary. 171

Figure 5-17 :The voltage distribution within the EWN during corona development. 172

Figure 5-18: Thévenin equivalent node circuits representing the corona development : a) using conductance with an (unknown) voltage source representing unaffected voltage . This will ensure the correct corona conduction current, I_c, (b) Applying a current source, I_c, to ensure correct representation of radial corona current. 173

Figure 5-19 Distortions on a propagating waveform applying conductance across the entire EWN node calculated using the method proposed by Thang et al [55]. 174

Figure 5-20 Corona distortions created by incorporating the shunt current to the EWN, as predicted by the method proposed by Thang et al [55] 175

Figure 5-21 Using a corona conductivity of 40 μS/m to represent the corona sheath. The associated conduction current is added as a current source to the EWN. 176

Figure 5-22 The q-V characteristic (red) for the method described by Thang et al. Also plotted are the individual charge quantities ; blue - charge contained within corona sheath, green- line charge. 177

Figure 5-23 The q-V characteristic found by integrating the conduction and displacemnt currents within the EWN (red) and integrating the displacement current outside the EWN (green). 177

Figure 5-24: Q-V graph (red) created when applying the Cooray equations to an EWN with side length = 0.8m. R_a = 0.0035m, and outer conductor radius, R_b = 0.4m. Breakdown voltage V_b = 102kV. The other curves show the predicted increase in corona charge post breakdown (blue) and the simultaneous fall in line charge (green) 180

Figure 5-25 Radial development of corona 180

Figure 5-26 Radial corona current [A/m] variation with time. 181

Figure 5-27 Capacitance increase during the corona development found using the corona charge given by the Cooray equations. 181

Figure 5-28 Conductance variation associated with corona development found using the time derivative of capacitance 182

Figure 5-29 Comparison of corona radii that develop for a range of surge waveforms with differing peak voltages 183

Figure 5-30 Thévenin equivalent circuit used to describe the introduction of extra capacitance suggested by the Cooray equations, to the EWN. 184

Figure 5-31 Using additional capacitance associated with the corona charge as predicted by the Cooray equations 184

Figure 5-32: The distortions on a propagating waveform when the addition capacitance suggested by the Cooray equations in increased by a factor of 1.3. A closer match to the experimental data is achieved. 185

Figure 5-33: Typical corona conductance profile found by taking the time derivative of corona associated capacitance 186

Figure 5-34 Using the corona radius as predicted by the Cooray equations to obtain an associated corona conductance with a chosen conductivity of 20 μS/m 186

Figure 5-35 Using a corona current source as predicted by the Cooray equations to recreate distortions on a propagating waveform 187

Figure 5-36 comparing the effect of the ionisation factor when applied to varying regions of soil. 190

Figure 5-37 Varying regions of soil affected by the ionisation factor related to line current and critical electric field 190

Figure 5-38 Comparing pulse waveform at equidistant points along a 12m grounded horizontal rod with and without the effects of soil ionisation ($\rho s = 500\Omega\text{m}, \varepsilon r = 10$). 191

Figure 5-39 Comparing the inclusion of soil ionisation effects on the potential of a horizontal electrode buried in soil ($\rho s = 270\Omega\text{m}, \varepsilon r = 12$). 191

Figure 5-40 Comparing the inclusion of soil ionisation effects on the potential of an horizontal electrode buried in soil ($\rho s = 270\Omega\text{m}, \varepsilon r = 12$). 192

Figure 5-41 Touch potential: The difference between the contact potential and the ground potential is the touch potential ($\rho s = 1000\Omega\text{m}, \varepsilon r = 6$). 193

Figure 5-42. Touch potential ($\rho s = 500\Omega\text{m}, \varepsilon r = 10$). 193

Figure 5-43 The potential on the electrode at its midpoint and ground potential 0.5m either side of the midpoint. ($\rho s = 270\Omega\text{m}\,, \varepsilon r = 12$). 194

Figure 5-44: The step potential experienced above the midpoint of grounding electrode. ($\rho s = 270\Omega\text{m}\,, \varepsilon r = 12$) 195

Figure 5-45: The cross-section of the wire under ground, showing the electric field finding its correct configuration early within the process (100 time steps). 196

Figure 5-46 Further into the simulation the electric field behaviour is established (4000 time steps). 196

List of Tables

Table 1-1 Approximate average energies and effective absorption lengths in air of gamma source components from hypothetical one megaton surface-burst [13]. 38

Nomenclature

Symbol	Description [S.I. unit]	Equation reference
μ	Mobility [ms^{-1}/ Vm^{-1}]	(2.1)
$\boldsymbol{v_d}$	Drift velocity [ms^{-1}]	(2.1)
$\boldsymbol{E}$	Electric field strength [Vm^{-1}]	(2.1)
λ_{MFP}	Mean free path [m]	(2.2)
σ_{cs}	Microscopic cross-section [m^2]	(2.2)
λ_{ion}	Mean free path for ionising collisions [m]	(2.3)
σ_{ion}	Microscopic cross-section for ionisation [m^2]	(2.3)
α	Number of ionising collisions/unit length [m^{-1}] (Townsend's primary ionisation coefficient)	(2.4)
P_{ion}	Probability of ionisation	(2.5)
h	Planck's constant [J s]	(2.6)

ν	Frequency (Hz)	(2.6)
ν_i	Frequency of ionisation [cm^3s^{-1}]	(2.9)
ν_a	Frequency of attachment [cm^3s^{-1}]	(2.10)
η	Number of collisions resulting in attachment	(2.12)
E_r	Radial electric field [Vm^{-1}]	(2.13)
q_e	Electron charge [C]	(2.13)
ε_0	Permittivity of free space [F/m]	(2.13)
D	Coefficient of diffusion [$m^2 s$]	(2.14)
Q_s	Total charge in streamer head [C]	(2.16)
R_s	Radius of streamer head [m]	(2.16)
E_B	Critical field for electrical Breakdown [V/m]	(2.18)
δ	Relative air density correction factor	(2.18)
p_0	Standard atmospheric pressure [Pa]	(2.19)
T_0	Standard atmospheric temperature [K]	(2.19)
C_d	Line capacitance per-unit length [F/m]	(3.1)
I	Line current [A]	(3.1)
V	Line voltage [V]	(3.1)

L_d	Line inductance per-unit length [H/m]	(3.2)
v_p	Propagation speed (along TL) [m/s]	(3.5)
Z	Characteristic Impedance [Ω]	(3.6)
ε_r	Relative permittivity	(3.7)
μ_r	Relative permeability	(3.8)
c	Speed of EM wave [ms^{-1}]	(3.9)
c_0	Speed of EM wave (free space) [ms^{-1}]	(3.10)
Z_0	Impedance of free space [Ω]	(3.11)
Z_{LINK}	Impedance of link-line [Ω]	(3.20)
τ	Transit time [s]	(3.20)
Z_{STUB}	Impedance of stub [Ω]	(3.23)
Γ	Reflection coefficient	(3.26)
k	Simulation time-step	(3.27)
$VL^i(n,k)$	Voltage pulse incident on node *n* from its Left hand side at time-step *k* [V]	(3.7)
$VR^i(n,k)$	Voltage pulse incident on node *n* from its Right hand side at time-step *k* [V]	(3.27)
$VC^i(n,k)$	Voltage pulse incident on node *n* at stub (capacitive) time-step *k* [V]	(3.27)
Z_c	Impedance of stub representing	(3.27)

	capacitance [Ω]	
$VL^r(n,k)$	Voltage pulse reflected (scattered) from the Left hand side of node *n* at time-step *k* [V]	(3.28)
$VR^r(n,k)$	Voltage pulse reflected (scattered) from the Right hand side of node *n* at time-step *k* [V]	(3.29)
$VC^r(n,k)$	Voltage pulse reflected (scattered) from the Capacitive stub at node *n* at time-step *k* [V]	(3.30)
$\boldsymbol{S}$	Scatter matrix (TLM)	(3.34)
Y	Admittance (TL) [S]	(3.38)
G_{ei}	Conductance related to electric losses in the 'i'th direction [S]	(3.38)
R_{mi}	Resistance related to magnetic losses in the 'i'th direction [Ω]	(3.39)
χ_e	Electric susceptibility	(3.46)
v_{TLM}	Pulse propagation speed along the TL segments of the 3-D SCN.[ms^{-1}]	(3.53)
r_w	Embedded wire radius[m]	(3.55)
r_{cf}	Fictitious radius linked to SCN cell boundary to calculate wire capacitance [m]	(3.55)

r_{lf}	Fictitious radius linked to SCN cell boundary to calculate wire inductance [m]	(3.55)
k_{wi}	Dimensionless geometrical factor related to wire radius and SCN cell wall	(3.57)
η_0	Intrinsic impedance of free space [Ω]	(3.59)
Q_{wire}	Wire charge per-unit length [C/m]	(3.67)
$\boldsymbol{J}_{r-disp}$	Radial displacement current density [A/m^2]	(3.68)
I_r	Radial current [A]	(3.68)
V_{EWN}	Voltage between embedded wire SCN cell boundary [V]	(3.70)
E_{r-surf}	Radial electric field strength at surface of wire[V/m]	(3.71)
I_G	Shunt current within EWN (in presence of conductance [A]	(3.72)
ΔC_d	Extra line capacitance due to corona development [F/m]	(4.2)
v_L	Speed of light in the absence of corona [m/s]	(4.2)
ΔT	Delay of a voltage component associated with corona at given propagation distance, d. [s]	(4.3)

E_{ij}^{k}	Radial electric field in the 'i' th direction, 'j' = 'a', 'b', 'l', 'r' (above, below, left, right respectively)[V/m]	(4.7)
E_c	Critical electric field for streamer propagation [V/m]	(4.9)
R_c	Corona radius (for an assumed cylindrical region)[m]	(4.9)
V_B	Breakdown voltage for corona inception[V]	(4.10)
τ	Decay constant related to radial electric field on wire surface during corona development [s^{-1}]	(4.11)
q_a	Charge per-unit length on central conductor (coax) [C/m]	(4.12)
R_a	Radius of central conductor (coax. cylinder) [m]	(4.12)
$V(t)$	Instantaneous voltage across coax conductors [V]	(4.13)
R_b	Radius of outer conductor (coax. cyl)[m]	(4.13)
ρ_c	Volume charge density at unit radial length within coronal sheath [C/m^2]	(4.13)
q_c	Total charge per-unit length in the corona sheath [C/m]	(4.14)

Q_{coax}	Total charge contained within coax[C/m]	(4.15)
ρ_{cm}	Maximum volume charge density [C/m^2]	(4.16)
R_{cm}	Maximum radius of corona sheath [m]	(4.16)
ρ_{cb}	Volume charge density of back corona sheath [C/m^2]	(4.18)
R_{cb}	Radius of back corona sheath [m]	(4.18)
q_{cb}	Charge per-unit length within the back corona sheath [C/m]	(4.19)
$E_x^i(t,x,h)$	Electric field component capable of coupling with an *x*-directed wire at a height, *h*, above ground [V/m]	(4.22)
C_d^{tot}	Total capacitance per-unit length under corona conditions [F/m]	(4.30)
C_d^c	Capacitance per-unit length due to corona [F/m]	(4.32)
G_d^c	Conductance per-unit length related to corona [S/m]	(4.35)
$dI_{P1}(t,x_1)$	Infinitesimal current induced at a point x_1 by external electric field [A]	(4.37)
$dI_{P2}(t,x_2)$	Infinitesimal current induced at a point x_2 by external electric field [A]	(4.38)

$dI_{c\_P1}(t, x_1)$	Infinitesimal current entering wire at a point, x_1, due to corona development [A]	(4.39)
$dI_{c\_P1}(t, x_1)$	Infinitesimal current entering wire at a point, x_2, due to corona development [A]	(4.40)
I_G	Shunt current per unit length related to conductivity [A/m]	(4.41)
ρ_s	Soil resistivity [Ωm]	(4.41)
I_{disp}	Displacement current per unit length [A/m]	(4.42)
ε_s	Permittivity of soil [F/m]	(4.42)
R_T	Grounding resistance [Ω]	(4.43)
L	Electrode length [m]	(4.44)
a	Electrode radius [m]	(4.44)
d	Electrode depth below ground surface [m]	(4.44)
Z_p	Peak grounding impedance [Ω]	(4.46)
V_p	Peak potential [V]	(4.46)
I_p	Peak current [A]	(4.46)
$R_{hemi}(t)$	Time varying grounding resistance if a hemispherical grounding rod under	(4.47)

	ionising conditions [Ω]	
$r_{ion}(t)$	Assumed conductor radius under ionisation [m]	(4.47)
R_d	Electrode resistance per-unit length [Ω/m]	(4.48)
ρ_{cond}	Electrode resistivity [Ωm]	(4.48)
$J_T(n)$	Leakage current density at node *n* [A/m^2]	(4.52)
A_s	Surface area of segment [m^2]	(4.52)
I_B	Current threshold associated with ionisation [A/m]	(4.55)
K_B	Ionisation factor	(4.56)
δ	Skin depth [m]	(4.59)
$\dot{\Phi}_\gamma$	Gamma Flux [MeV/m^{2}s]	**(A.**1)
$\dot{D}$	Dose rate [Rad $\equiv 10^{-2}$J/kg]	**(A.**1)
$\dot{\Phi}_\gamma$	Electron flux [MeV/m^{2}s]	(A.3)
R_{mf}	Mean forward range [m]	(A.3)
γ_s	Scattering mean path [m]	(A.3)
J_r^c	Radial Compton current density [A/m^2]	(A.4)

q_e	Electron charge [C]	(A.4)
J_t^c	Transverse Compton Current Density [A/m^2]	(A.5)
R_L	Larmor Radius [m]	(A.5)
S_e	Production rate of free electrons [s^{-1}]	(A.11)
k_a	Avalanche rate constant [s^{-1}]	(A.11)
N_e	Number density of electrons [m^{-3}]	(A.11)
N_+	Number density of positive ions [m^{-3}]	(A.11)
k_1	Rate constant (electron attachment)[s^{-1}]	(A.11)
k_2	Rate constant (dissociative recombination)[cm^3s^{-1}]	(A.12)
N_-	Number density of negative ions [m^{-3}]	(A.12)
k_3	Rate constant (mutual recombination)[$cm^3\ s^{-1}$]	(A.12)
$\boldsymbol{v_e}$	Average velocity of electron [ms^{-2}]	(A.16)
μ_e	Electron mobility [$ms^{-1}/\ Vm^{-1}$]	(A.16)
N_I	Number density of ions. [m^{-3}]	(A.18)
μ_I	Ion mobility [$ms^{-1}/\ Vm^{-1}$]	(A.18)

$\boldsymbol{E_s}$	Saturation electric field strength [V/m]	(A.23)
$H_{\boldsymbol{\phi}}$	Azimuthal component of magnetic field intensity	(A.24)
$E_{\boldsymbol{\theta}}$	Polar component of electric field [V/m]	(A.24)
J_{θ}^{c}	Polar component of Compton current density [A/m^2]	(A.25)
$F_{\boldsymbol{r}}$	Outgoing field [V/m]	(A.27)
G_r	Incoming field [V/m]	(A.28)
τ	Retarded time [m]	(A.29)
$J_{\boldsymbol{n}}$	Normal component of current density [A/m^2]	(A.36)

Chapter 0 Introduction and Thesis Outline.

It is now widely accepted that if protection strategies are to be suitably employed against an Electromagnetic Pulse (EMP) resulting from nuclear detonations then the distorting effects of corona development around conductors must be accounted for. Many solvers used to simulate the behaviour and impact of an EMP based on the Transmission- Line Modelling approach were bereft of this phenomenon and hence a project has been proposed to consolidate the present theory in regards to the description of corona with a view to incorporating a real-time simulation of such effects within the software and improving the theory where possible.

One-dimensional simulations using TLM are readily available, but at the time of writing, 3-D approaches were not known to the author. Ideally, such simulations will depict effects due to localised areas of corona discharge whilst presenting the correct final waveform at the protected end of the line. Hence, the effects rely on a self-consistent relationship between the EM fields and the particular sections of wire undergoing the non-linear phenomenon of corona discharge. Such effects should be demonstrable in all media provided the suitable conditions are met.

The 3-D TLM method employed within this thesis uses the Embedded-Wire Node. This node reduces the need for high resolution meshes whilst simultaneous accommodating the self-consistency that is required. The node in its most basic representation must account for the extra capacitance and inductance it introduces to the domain. Once this is achieved, the local voltage and current solutions within the node summarise all activity there. This, essentially, is the region where all non-linear corona related changes are felt. The node must be adapted to include time-varying parameters that are associated with corona development and the voltages and currents made available must account for these changes.

The corona changes can be described using different parameters. The choice of parameter will depend on simplicity, accuracy and limitations due to how it is calculated in real time.

This thesis presents the adaptation of the EWN within a 3-D environment, contrasting different approaches and comparing with experimental data. A discussion on the successes, limitations and difficulties encountered within the process is also summarised. The adapted EWN is shown to replicate empirical data produced under corona inducing surges to a decent standard.

To begin, an historical context to the EMP is provided.

Chapter 1 The Electromagnetic Pulse (EMP)

The Electro-Magnetic Pulse (EMP) is essentially a short burst of electromagnetic radiation originating from an event that can be natural, for example, a result of lightning or a man-made event such as that formed following a nuclear detonation. Here, the latter is described. The pulse has the capability to couple to wires resulting in varying degrees of destruction depending on its magnitude.

1.1 Historical Perspective

Enrico Fermi, a physicist working at the Manhattan project based in Los Alamos, USA, is generally credited with the idea that an Electromagnetic Pulse can be emitted from a Nuclear explosion (NEMP) as he had suggested shielding techniques should be applied to testing equipment during the first detonation of a nuclear bomb (also known as the TRINITY event in 1945, towards the end of World War II) [1], [2].

Direct evidence of such effects started to emerge in the 1950's as British atomic tests detected failure of equipment due to something they termed 'radioflash' at the time; the electromagnetic pulse as we know it as today, although there may have been some deliberate investigations beforehand in the US [3]. In 1954, Garwin proposed the relevance of the Compton current as a current source originating from the prompt gamma radiation emerging from the burst epicentre [3]. As this greater understanding of the physics associated with the EMP grew, so did the appreciation of the magnitude, not only of the pulse itself but also of the problem it posed to infrastructure. This led to meetings between the US and the UK to discuss the various vulnerabilities of military systems [4]. Attention had been mainly focused towards surface-bursts; explosions in the vicinity of the ground and their potential effects on

sensitive equipment but towards the end of the 1950's an awareness of the unique nature of High-Altitude EMP (HEMP) i.e. detonations above the Earth's atmosphere became apparent due to results obtained from a series of experiments titled 'Operation Hardback' which concluded in 1958 [5] . The magnitude of the pulse grossly exceeded estimates and further the pulse was polarised horizontally as opposed to the vertically polarised pulses of low-altitude bursts. Subsequently, attentions gradually became centred on this form of EMP.

In 1962, the FISHBOWL high-altitude tests (part of the OPERATION DOMINIC tests) confirmed these findings, in particular, the STARFISH PRIME test executed above Johnson Island , USA [6]. This represented the detonation of a 1.4-1.5 MT nuclear bomb at a height of 400 km above ground. Effects of the detonation were felt in Hawaii which is approximately 1500 km in the form of damage to streetlights, effects on the telecommunication network and the setting off of burglar alarms [7].

A lack of understanding of the mechanisms associated with an EMP generated at such heights and lack of sensitivity in the equipment used to measure the high frequency content meant that initially the impact of such pulses had been under appreciated. In the early 1960's, sizable advances in the understanding of such phenomena were made despite ground testing ceasing in 1962 (underground testing remained). Notable interventions from now accepted, eminent authorities on the subject matter were released. In 1964, Conrad Longmire gave a series of lectures at the Air Force Weapons Laboratory (AFWL) describing the theory of the physical mechanisms responsible for the EMP, not only from surface bursts (SB-EMP) but also proposing a mechanism for the high-frequency signal related to HEMP based on the geomagnetic field turning of the Compton current [3]. Later, this 'high-frequency approximation' was introduced literally, by Karzas and Latter [8].

The aboveground nuclear treaty entered into force in October 1963, prohibiting nuclear explosions "in the atmosphere, in outer space and under water". Hence, the development of EMP Simulators able to investigate the effects of EMP both within its source region- the region comprised of the Compton currents responsible for the EMP and the region outside became prevalent and combined with detailed theoretical work, led to a much greater

understanding of the NEMP with a greater appreciation of the vulnerabilities of missiles, aircraft, satellites and communication systems and the need for protective measures [10].

Another approach to understanding the effects of EMP on various electrical infrastructure was to formulate computer simulations based on various numerical models. However, up until 1986, it appears that the effects of corona / ionisation of the media surrounding wires was overlooked. Hence, distortions known to occur on propagating waveforms such as those that would be experienced after a coupled EMP were omitted.

In 1986, Blanchard et al prepared a manuscript summarising existing corona models that were available at that time with a view to applying them to coupled EMP. Originally, the models were used to predict similar effects resulting from lightning strikes. There is an abundance of empirical data based on lightning pulses and corona effects. However, lightning strikes have a much slower rise-time than NEMP (microseconds as opposed to nanoseconds). Hence, a corona experiment was conducted at a facility in New Mexico in 1986 [11]. Only positive corona were investigated. Despite certain limitations corona effects were demonstrated. Further, the models available had varying success in recreating the results. Each had success in specific data ranges. In particular, some were able to contend with the fast rise-time. Experimental limitations further complicated the results and the conclusion was more work was necessary.

1.2 EMP Generation.

The signal amplitudes emanating from a nuclear blast vary considerably as there are many factors that contribute to the final transient profile. For continuity, papers generally refer to a one Megaton explosion but external factors such as location of the burst and the location of the observer will also have a large influence on the resulting signal that is experienced. The physical characteristics of the weapon will also impact the final result; yield, shape, component materials etc., all of which make prediction of the signal very difficult [12]. However, the physics that underlie the formation of the EMP are well understood. The

physics applies to the 'Source Region', named in such a way as this is the region responsible for all the source terms that generate the EMP.

An outline of the basic mechanisms that result in NEMP is presented in Figure 1-1 by means of a flow diagram suggested by Lee [3]. The following will explain the development in more detail. The majority of the theory related to NEMP is based on works proposed by Longmire in his seminal paper on the subject [13]. A more detailed description of the physics associated with the origin of an EMP can be found in Appendix A. The emphasis here is to describe the origin of the EMP in respect to the different altitudes at which the explosion takes place. This description can be reduced to an explosion on or near the ground or one above the Earth's atmosphere.

Following a nuclear explosion an expulsion of gamma ray and x-ray photons is emitted radially from the epicentre. This represents a small fraction (of the order 0.003) of the bomb's energy [14]. These 'prompt' gamma photons each have an energy of approximately 1-2 MeV whereas X-ray photon energies are in the realms of KeV and are therefore generally neglected when considering EMP phenomena due to the markedly lower absorption length [3]. The gamma energy made available following a nuclear explosion result from various aspects of the explosion and therefore the energy distribution with time can vary accordingly.

Table 1-1 lists the energy of various sources of gamma influencing the final EMP profile, for a standardised 1-megaton burst just above the ground surface with their average energies and absorption lengths. The prompt gamma pulse that emerges from the burst directly typically, has a rise time of a few nanoseconds and a decay time of a few tens of nanoseconds [13]. Any subsequent gamma photons are generated by the interaction of neutrons, also ejected from the explosion, by interacting with the surroundings. A burst near the ground will provide gamma by inelastic scattering (in the same timeframe as the prompt gamma release) while 'ground-capture' gamma result as neutrons lose energy and remain in the ground. Neutrons may also undergo inelastic scattering with the surrounding air. The gammas that result will have a longer decay time due to the relatively low air density. Finally, 'fission fragment' gammas result from the beta-decay that result from fission of larger atom nuclei. The fission fragment gamma will have longest duration.

Gamma Component	Energy (MeV)	Absorption Length (gm/cm^2)
Prompt	1.5	40
Air Inelastic	4	52
Ground Capture	3	38
Air Capture	6	58
Fission Fragment	1	37

Table 1-1 Approximate average energies and effective absorption lengths in air of gamma source components from hypothetical one megaton surface-burst [13].

Figure 1-2 gives a qualitative impression of the relative source strengths and time frame (retarded time) for all the different gamma sources during a surface burst. As previously stated, the location of the burst will change the profile. For example, a high-altitudinal burst will be devoid of the ground capture gamma.

The origin of the EMP, following an explosion emitting a gamma source, can be traced back to three main factors:

i) Primary Ionization of the medium (The Compton Current Density).
ii) Secondary ionization, reattachment, recombination processes (air conductivity).
iii) Asymmetry of the source region-the region responsible for the EMP dictated by the space where (i) and (ii) are taking place.

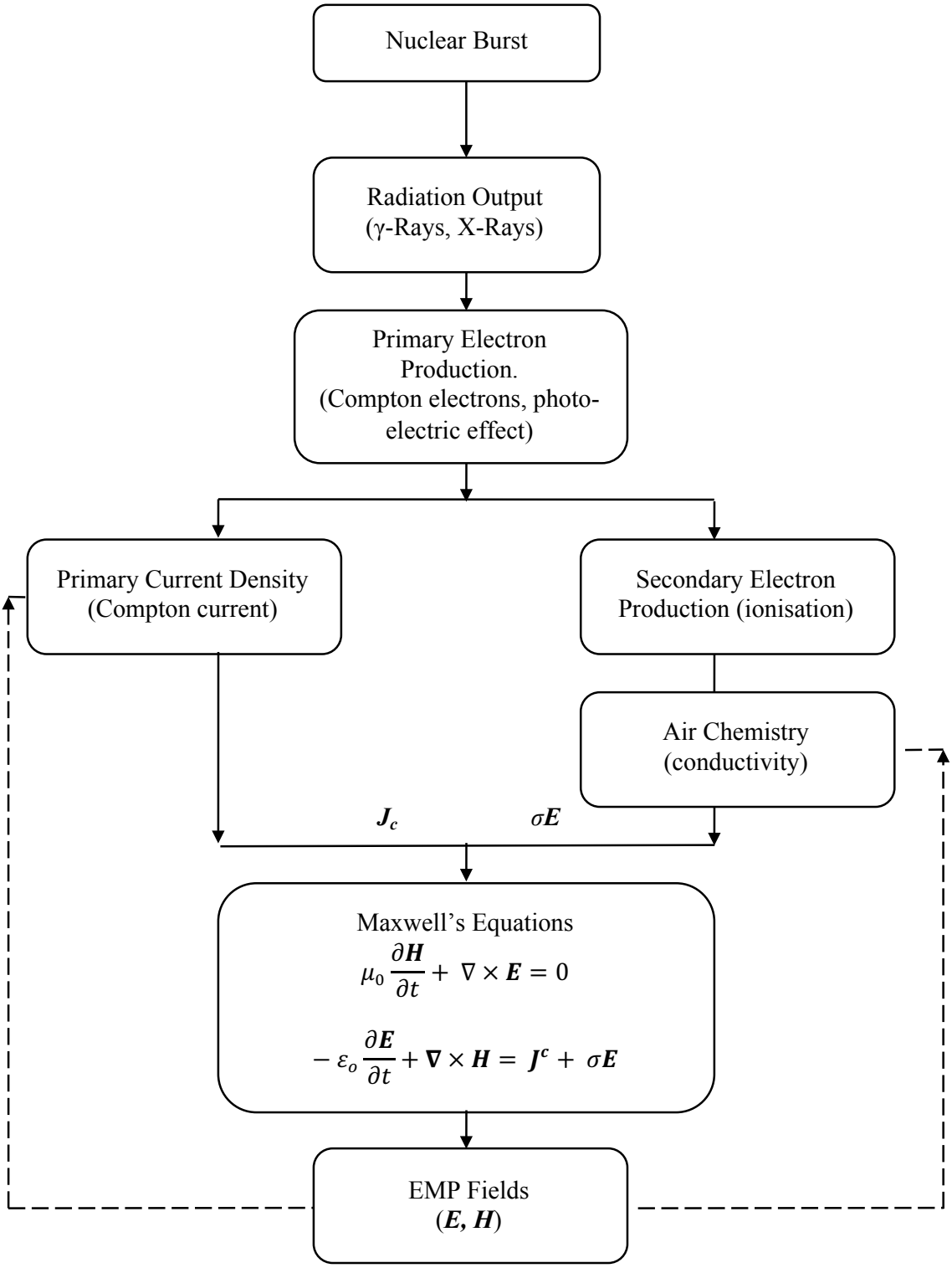

Figure 1-1 Flow diagram describing the basic mechanisms resulting in EMP generation [3].

All these processes are altitude dependent for reasons described in the next section (see also Appendix A). There is also a dependence on the local fields generated by the processes present within the source region meaning they are time-varying quantities and non-linear.

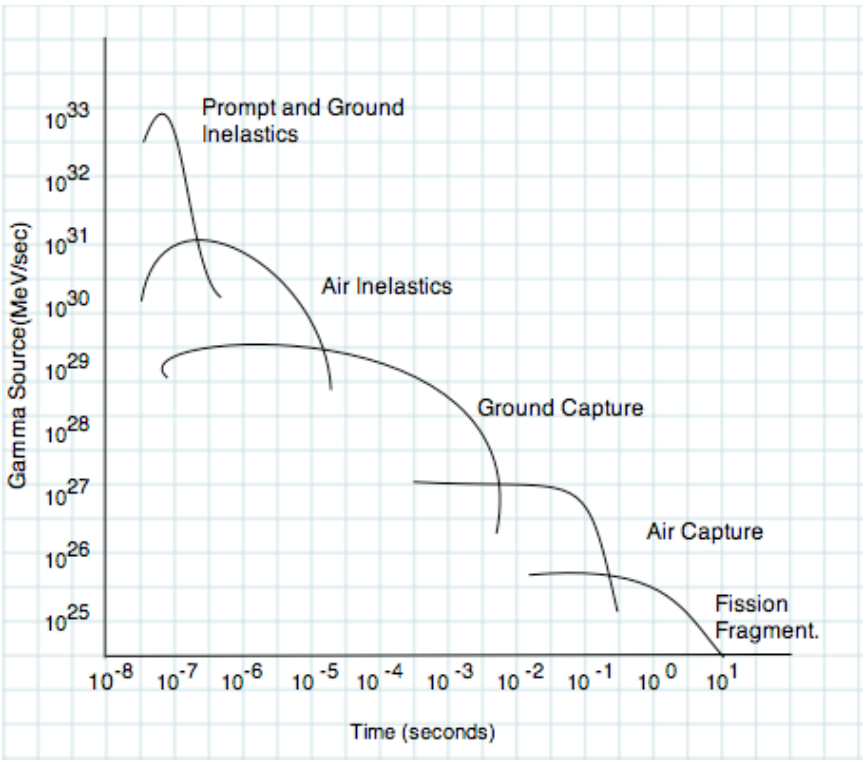

Figure 1-2 Qualitative representation of the source magnitudes of gamma radiation from different mechanisms following a surface burst nuclear explosion. [13]

1.2.1 Primary Electron Production -The Compton Current Density

The gamma radiation produced by a nuclear explosion is assumed to be ejected radially from the burst epicentre and will be travelling at the speed of light. These will interact with the surrounding media freeing electrons from their parent atoms / molecules via the Compton Process as they propagate. These Compton recoil electrons are also assumed to move in the

same radial direction as the original gamma photon responsible for the ionisation although there will be a slight deviation in reality (Figure 1-3). The Compton current will travel at relativistic speeds (ninety percent speed of light) [14].

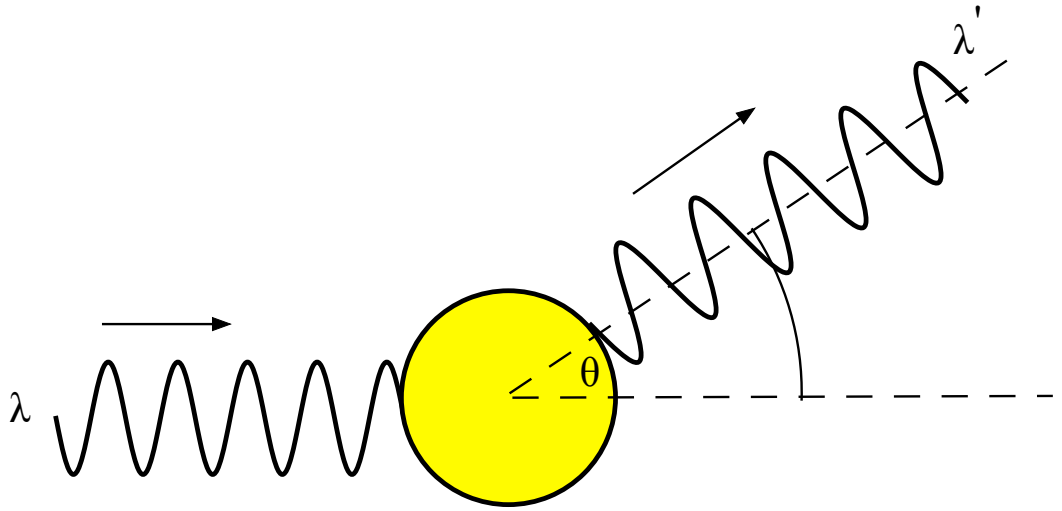

Figure 1-3 Compton scattering- a photon (x-ray or γ-ray of a given wavelength) collides with an atom or molecule imparting some of its energy resulting in a reduction in its wavelength proportional to the angle of collision.

Each 1 MeV gamma ray eventually produces around 30000 electron-ion pairs. The time to meet this quota will be much greater at higher altitudes (30 km) i.e. 50 ns compared to the few nanoseconds near ground level due to the longer mean free path in the less dense atmosphere [12]. A primary radial Compton current results accompanied by an associated radial electric field. Note, this field will in turn affect the Compton current. Hence, a model to include this effect must be self-consistent.

At higher altitudes (≥ 100 km), the primary Compton current will be deflected appreciably by the Earth's geomagnetic field. Therefore, to understand the EMP created at high-altitudes, two Compton current density components must be considered; the original radial component, J_c^r, and a transverse component J_c^t. This latter component will be present at lower altitudes also but at altitudes of 50 km to 30 km, where the source region of HEMP is considered to exist the mean forward range of the electrons is comparable to that of the the *Larmor radius* – the radius associated with the curved path the electron follows in the Earth's magnetic field.

This is approximately 100 m at mid-altitudes (30 km). Hence, the turning effect is established. At lower altitudes the deflection can be ignored, as the mean forward range of the electrons at this height is only a few metres. Hence, any resultant field derived from the deflected current at this height is negligible [13].

As they propagate, the primary electrons generated via the Compton process will lose energy via secondary collisions. These collisions can result in further ionisation. Eventually, the primary recoil electrons are brought to rest, placing a finite size on the *source region* (sometimes called the 'deposition region'). The source region can be defined as simply as the region responsible for producing an EMP. Depending on how it is characterised, i.e. based on the radial distance at which the peak Compton current density has a maximum lower limit or the distance at say, the increase in air conductivity doesn't increase beyond a certain amplitude the spatial extent of the source region is open to conjecture. However, estimates have been provided. The nominal source region created from weapon of yield 10000 kilotons can extend up to 10 km [15].

1.2.2 Air Conductivity.

Air conductivity is influenced by a number of processes. Free electrons and to a lesser extent, the residual positive ions, all produced by secondary processes, as the Primary electrons collide with molecules in their path will contribute to conductivity. These charged particles are defined by their relatively low energy. These will move under the influence of the electric field based on the charge separation that results as the primary Compton Current, J_c, propagates away from the burst epicentre. Hence, this conduction current, J_σ, will act to compromise size of the Primary Compton Current as it flows in the opposite direction to the Primary current and therefore influences the size of the signal. (Figure 1-4).

Some of the secondary electrons may have enough energy post-scattering (or acquire energy from the electric field) to produce tertiary electrons following further collisions. This process describes an *electron avalanche* (see Chapter 2 for a detailed discussion). Each Compton recoil electron produces around 3×10^4 electron-ion pairs before its energy is expended [16].

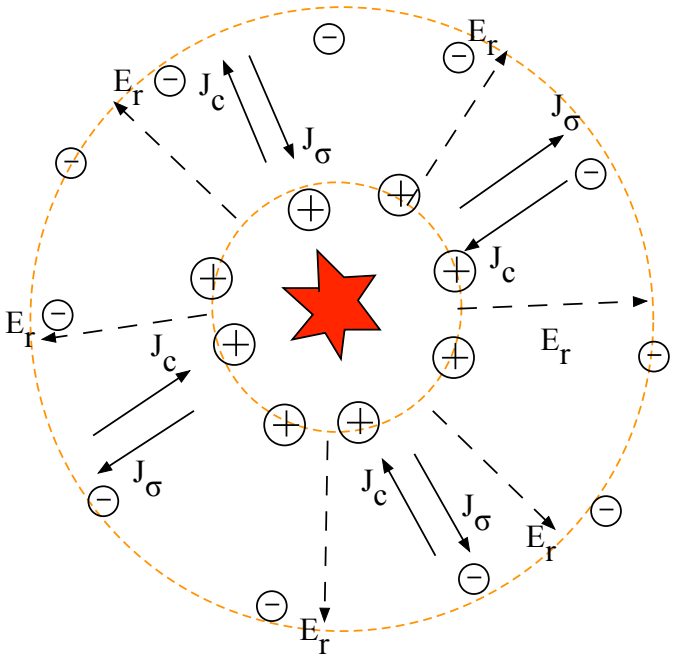

Figure 1-4 The 'charge-separation model' describing the fields that form in the source region following an explosion. (based on [15])

Other processes are present that can limit the magnitude of these currents. Free electrons can be removed from the source region via attachment to oxygen molecules forming electronegative ions or simply recombining with a positive ion. Hence, over time, free electrons will reduce in number. Eventually, they reduce to such an extent that the positive charge concentration becomes significant. Therefore, the time development of the conductivity is also governed by ionisation and reattachment / recombination processes adding further complexity to the description of the source region [13]. A quantitative description of the source currents (Compton currents) and the conductivity of air within the source region can be approximated as shown in Appendix A. Such expressions can be used in simulation software, but also allow one to appreciate the environment contributing to the development of the EMP.

The development of the Primary Compton current density and the corresponding conduction current density result in a complex time-varying electromagnetic environment within the source region. The next section describes how the altitude at which the source region forms

characterises the radiated EMP. However, it is worth noting that the electric field created within the source region; the strong, radial, non-radiated electric field and spatially local EMP signals have the potential to damage electrical and electronic infrastructure located in its vicinity. Longmire presents computation results of conductivity development, and radial and vertical electric fields for nominal 10 kT and 1 MT weapons as a way of illustrating the transient development of such parameters as opposed to a precise depiction of events. Figure 1-5 Figure 1-6 show his results for the vertical and radial electric fields at various distances from a hypothetical surface detonation of a 1 MT bomb, respectively. His calculations predict a peak radial electric field of the order of 10^5 V/m at a distance of 1km from the burst epicentre and a peak of around 10^3 V/m at 40 km (radiated). The radial field component has a similar magnitude at 1km, falling to a peak magnitude of 10^3 V/m at 3 km.

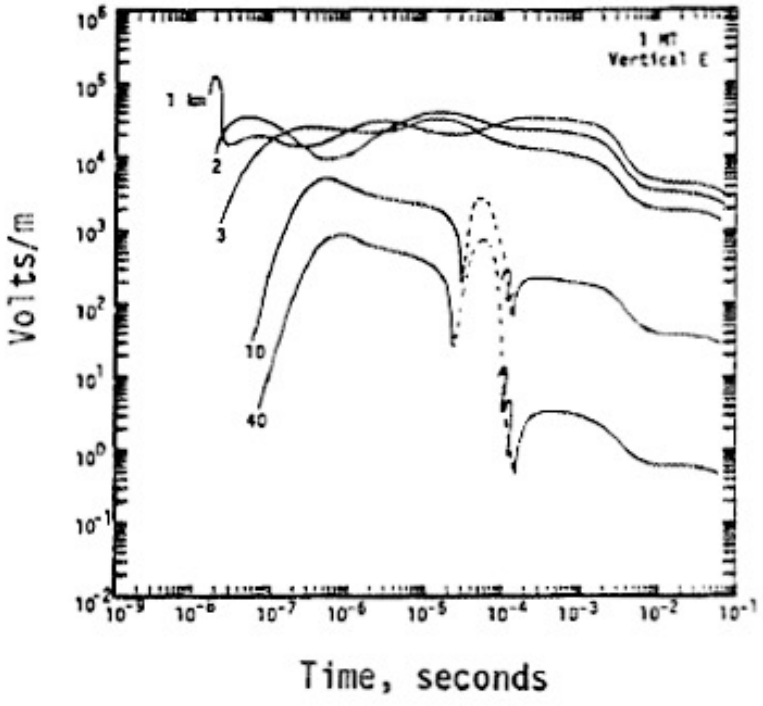

Figure 1-5 Graph by Longmire depicting the transient behaviour of the vertical electric field at various distances from the burst epicentre of a nominal 1 MT surface burst. (Taken from [15]).

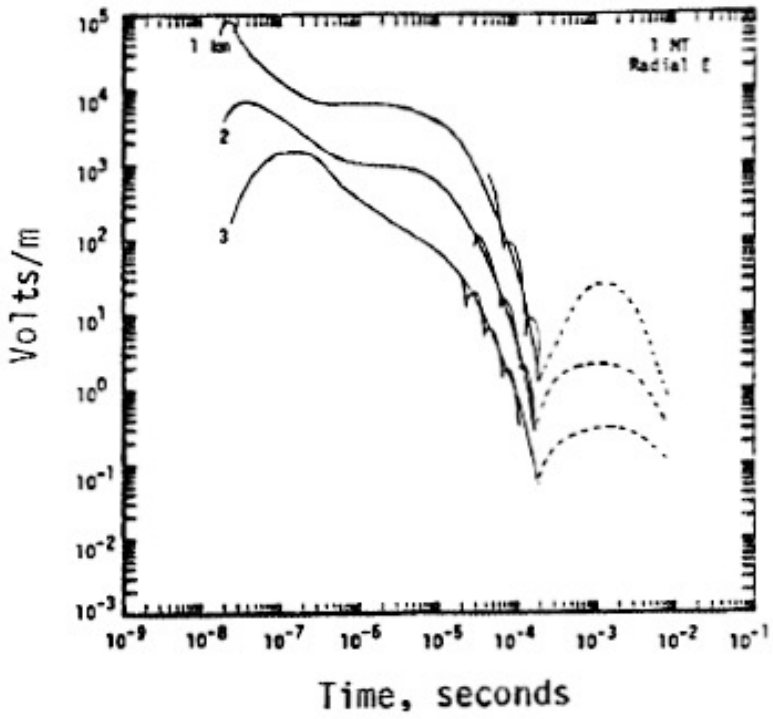

Figure 1-6 Graph by Longmire depicting the transient behaviour of the radial electric field within the source region of a 1 MT surface burst (taken from [15])

1.3 The Source Region and Altitude Dependence.

The altitude at which the explosion takes place, sometimes referred to as the Height of Burst (HOB) will have a major impact on the shape of the source region. The shape, or more precisely, the asymmetry of the source region is the primary source of the radiated EMP [13].

First consider a hypothetical perfectly spherical symmetric source region that is independent of altitude (Figure 1-4). The various currents will form as described in the previous section. Hence, the Compton current and conduction current densities will be concentric about the burst point and of equal magnitude for a given radial distance. The resulting electric field will be purely of the radial form based on the resulting charge separation that forms. Hence, no net

current can be described and subsequently, no radiated pulse is emitted from the region. To give a more of an analytical basis to the basic description above, a common approach is to describe the EMP generation in three phases; the wave phase, the diffusion phase and the quasi-static phase [13][16]. These describe the transient nature of the fields within the source region. These are described in detail in Appendix A however, it is worth a simple description here also. In the spherical coordinate system, the relevant field components are E_r , H_φ. However, there is no magnetic field ($\nabla \times E_r = 0$). Hence, considering the radial electric field, the Maxwell – Ampère equation simplifies to

$$\varepsilon_0 \frac{\partial E_r}{\partial t} + \sigma E_r = -j_r^c \tag{1.1}$$

where j_r^c represents the Compton current density source term (equal to zero outside of the source region) and σE_r is the conductivity current density.

The 'wave-phase' is defined by the period in which the conductivity is small and hence σE_r can be ignored. Hence, the radial field is proportional to the primary Compton current. As this is assumed to increase exponentially (relates to electron avalanches – see Chapter 2) then so does the radial electric field.

The 'diffusion phase' begins when the conduction current becomes comparable to the displacement current and eventually, the displacement current falls to insignificant values. Applying these changes to (1.1) and solving for E_r gives

$$E_r = \frac{-j_r^c}{\sigma} = E_s \tag{1.2}$$

Where E_s is the saturation value of the radial electric field.

The 'quasi-static phase' is characterised by the dominance of ions causing the saturation field to decrease [15].

The symmetrical source region provides a simplified domain in which to apply Maxwell's equations as many of the terms vanish. However, in reality the source region will not be

symmetric regardless of the height of burst. The ground immediately imposes asymmetry to surface or low-altitude bursts source-regions by its mere presence while on the other hand, a high-altitudinal burst, will have its source region shaped by the atmospheric gradient as the gamma eventually pervade through the increasingly dense air. The three phases described for the symmetric case still exist but with more complexity and need to be amended accordingly. Appendix A describes these in more detail. Solution of these equations allows the fields represented in Figure 1-5 and Figure 1-6 to be determined. The next section introduces the impact of altitude on the source region and its connection to the radiated EMP.

1.3.1.1 EMP from Surface Bursts

Following an explosion on or near to the ground, the situation above the ground can be considered similar to that described in the symmetric case. However, the ground, with its relatively high conductivity (e.g. soil $\approx 10^{-2}$ S/m, ocean ≈ 4 S/m) will short out the field near it [13]. Also, radiation will penetrate the denser ground to a much lesser extent. Hence, the radially directed Compton current and the associated radial electric field will emanate from the burst point above the ground creating a hemispherical source region as shown in Figure 1-7.

Above the ground surface, radial currents emerge, again, with their focal point being the burst location. However, the negation of these currents below the ground results in a net vertical component that can be considered perpendicular to the ground. No such net current could be described in the symmetrical case; this is purely a result of the asymmetry. Therefore, a dipole moment perpendicular to the ground at the burst point can be considered. In a similar way to the approach used in antenna theory, the net current, $\boldsymbol{J}_{\boldsymbol{net}}^{\boldsymbol{c}}$, is proportional to the time derivative of the dipole moment and a radiated EMP proportional to the time derivative of this net current propagates like that of a vertical electric dipole. The pulse can travel up to distances of around 100 km from the burst point [12].

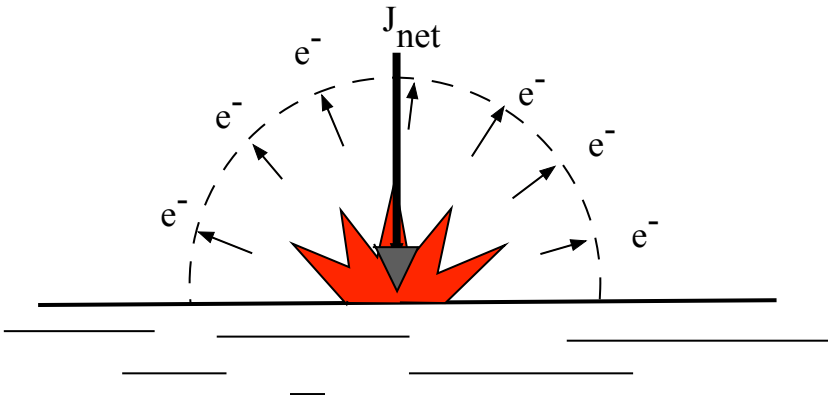

Figure 1-7 Geometry of a surface burst. The ground enforces asymmetry such that the source region can be considered hemispherical. Hence, a net current can be defined vertically [3]

Another field that will result from this geometry is an azimuthal magnetic field (Figure 1-8). Consider the radial Compton currents near to the ground. The relatively high conductivity of the ground will lead to a conductivity current going some way to cancelling the Compton current creating an equilibrium between the two. This results a toroidal current loop comprised of these two currents and a transverse, azimuthal magnetic field results very close to the ground surface [3].

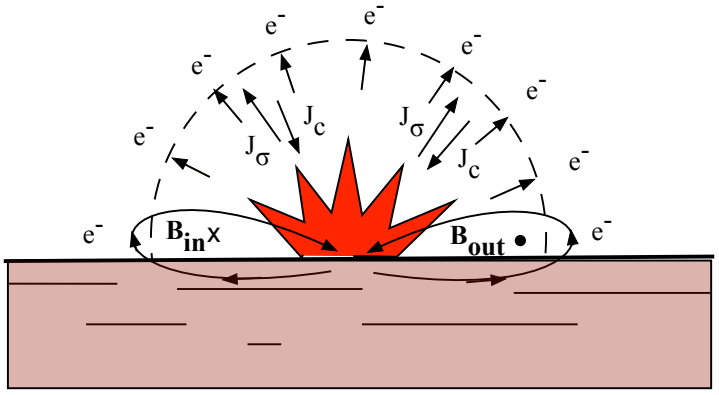

Figure 1-8 The generation of an azimuthal magnetic field. Loop currents in the vicinity of the ground emerge due to the ground conductance shorting the radial fields created by the primary Compton current. Concentric magnetic field lines centred around the polar axis form (B_{in} is the magnetic field into page, B_{out} is the field out of the page [3].

1.3.1.2 High-altitude Electromagnetic Pulse (HEMP)

As discussed in the historical introduction, HEMP was initially underestimated until magnitudes found experimentally greatly exceeded expectations and theoretical explanations became available. This and the potential to effect large areas geographically meant HEMP demanded the utmost attention. Figure 1-9 demonstrates how the areas vulnerable to HEMP increase with height of burst starting at the height that EMP is defined as 'high-altitude' (30 km) [17].

Figure 1-9 Diagram depicting the potential areas affected by HEMP in relation to the height of burst [17].

To understand the origin of the HEMP signal, in particular, early-time HEMP, a net Compton current still provides the basis for a radiated field, whilst secondary processes compete to create a time-varying air conductivity just as for the surface burst. However, it is the transverse component of the Primary Compton Current density resulting from the turning effect of the Earth's geomagnetic field that must be considered.

An explosion above the atmosphere, for example, a height of 100 km above ground, will lead to an emission of the prompt gamma as described in the previous section. Gamma will also be provided by the other mechanisms described (with the omission of ground capture for obvious reasons).

The prompt gamma will emanate from the burst epicentre and can be described by a spherical wave-front as described in the symmetrical example. Interaction with the increasingly dense air (appreciable between 40 -20 km) generates a Compton current assumed to be in the same direction as the gamma stream but now the air density gradient imposes asymmetry on the source region. Hence, a source region results as in Figure 1-10, a somewhat flattened region covering a large area [3].

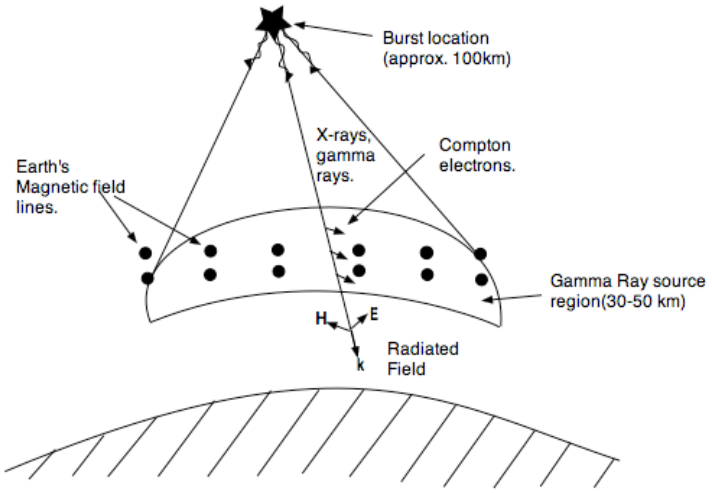

Figure 1-10 The source region resulting from a high-altitude (100 km) nuclear explosion [3].

An electric field will develop within the source region of the charge-separation type described previously. The induced asymmetry now introduces a net current (approximately vertical) that will result in a radiated EM field directed near parallel to the Earth's surface and can therefore be ignored due to altitude.

To understand the origin of the HEMP signal, the Earth's magnetic field must be taken into consideration. The currents generated in the source region will be deflected by the Earth's magnetic field such that they move transversely to the original direction [Figure 1-11]. As they turn a signal; sometimes called synchrotron radiation or *Bremsstrahlung*, is generated both towards and away from the original source. The electrons are travelling at relativistic speeds hence the final signal is a result of all these radial elements adding coherently in a similar manner that a phased array antenna works [3]. A brief, high intensity pulse results. Maximum amplitudes are typically quoted as 50 kV/m [12],[18].

The path that the electrons follow can be described by the gyro or Larmor radius. The primary Compton electrons have a Larmor radius of around 85m taking into account their kinetic energy and the Earth's magnetic field strength. At 30 km the mean stopping range is near twice the Larmor radius. This allows the turning effect to become established. At lower altitudes, the lifetime of the electron is much reduced hence, the transverse current is negligible [14].

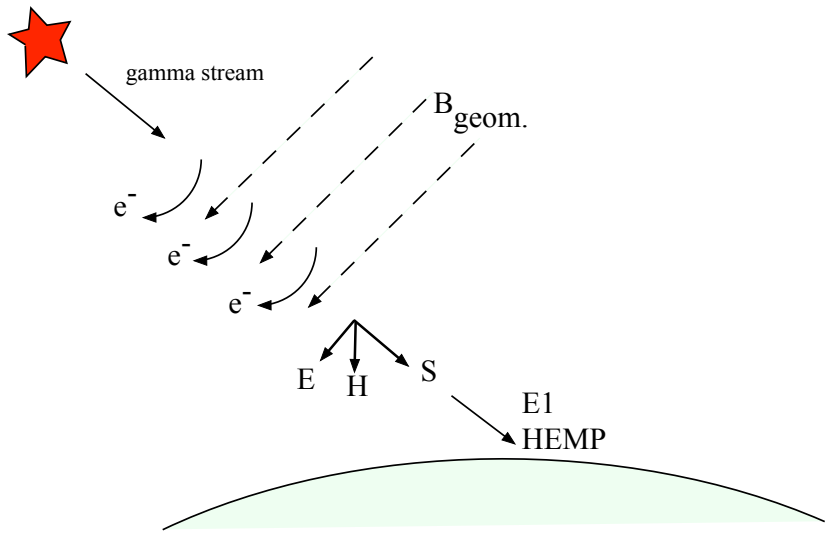

Figure 1-11 Deflection of the Compton current by the Earth's geomagnetic field (e^- = Compton electrons, S=Poynting vector) [18]

When describing HEMP, the waveform is often divided into three phases labelled E1, E2 and E3 as defined by the International Electro-technical Commission (IEC)[19]. The signal originating from the prompt gamma release is known as the E1-HEMP signal as this has the highest amplitude and therefore the potential to induce high voltages when coupled with lines. Figure 1-12 describes a generic HEMP waveform divided into the three phases [18]. It has a very fast rise-time (nanoseconds) meaning that ordinary surge protectors are inadequate. E2 is the intermediate time EMP and relates to the scattered gamma and the gamma produced by neutron interaction. E3 refers to the late-time EMP. The various gammas will interact with the air in ways described previously. Clearly, the signature of the HEMP will be affected by the rates of the relevant processes all of which depend on local electric field, the Earth's magnetic field and air density. Solving the electromagnetic aspect of the source region and the fields radiated from it, involves solving Maxwell's equations as demonstrated for the other altitudes. Again this is described in more detail in Appendix A.

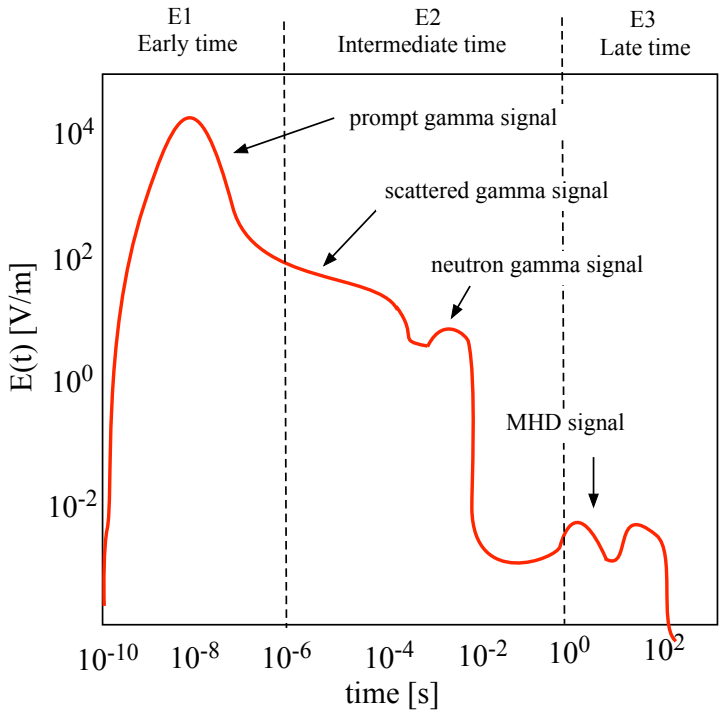

Figure 1-12 A generic HEMP waveform. Note the absence of the ground component [18].

1.3.2 HEMP line Coupling:

The respective EMP fields are formed from the source regions that are shaped according to where the burst takes place. The main concern regarding HEMP is the effects when coupled to lines connecting sensitive equipment. When coupled to conductors, voltage and current surges may be directed towards sensitive circuitry unless mitigation steps are implemented. The signal received at the wire termination will depend on many factors [18]:

1) The waveform amplitude and shape can be affected by the source region from which it arises, which is highly dependent on the height of burst.

2) Line geometry (relative to HEMP electric field component and / or Poynting vector): Only the electric field component parallel to the line will couple with the line.

3) Line altitude (above or below ground): Below ground coupling of wires will depend on the ground's parameters. Usually, burying cables 1-2m is sufficient to protect from the effects of a HEMP.

4) Line length: e.g. considering the 50 kV/m HEMP peak signal, even a 10cm wire could develop a potential of 5kV. Hence, power lines, telephone lines can be subjected to high voltages.

5) Line terminations: circuits and other load impedances will influence the signal. Unless matched, signals arriving at the end of the line will be reflected back and depending on the length of the line can cause damage nearer to the source end.

Often omitted from literature are the effects of corona discharge. Characteristic distortions related to the onset of corona discharge are known to occur on propagating surges provided the breakdown threshold of the surrounding medium is reached. This thesis investigates the associated phenomena on wires above air and underground when subjected to transients akin to those possibly encountered following a hypothetical blast.

The problem of investigating the effects of coupled HEMP on wires is clearly multifaceted due to multitude of variables that can influence the signal both before coupling and after. However, once coupled, the pulse behaves as a TEM signal (ignoring ground effects) on a

transmission line, whereby the electromagnetic fields lie in the plane perpendicular to the line direction.

Before simulating the effects of corona discharge, the next chapter provides a detailed look at the mechanisms associated with its development.

1.4 Chapter summary.

The Electromagnetic Pulse produced by nuclear detonations has the ability to impact civilisation due to the magnitude of voltages and currents it can induce in power-lines and other long-line networks as well as sensitive electronic equipment. Therefore, protection strategies are necessary.

Following a detonation, gamma radiation is expelled from the epicentre. These will interact with media in the proximity. In air, primary Compton currents are generated. As electrons lose energy from scattering conduction currents develop influenced by the radial electric fields that develop. This activity defines a source region.

Generally, an EMP is described by the altitude at which the detonation takes place. A Surface-Burst EMP (SB-EMP) refers to detonations near or on the ground surface. High-Altitude EMP refers to detonations above the Earth's atmosphere (≥ 30 km). A mid-altitude EMP is also referred to occasionally, but their effects are relatively weak and therefore receive less attention.

The signatures of the EMP vary depending on the altitude of the explosion as the altitude impacts the shape of the source region. A surface-burst generates a near hemispherical source region that can extend up to around 10 km. This region will contain large electric fields of the charge-separation type able to effect infrastructure contained therein. The asymmetry of the source region also allows a net current to develop in the vertical meridian that can radiate an EMP transversely. This transient signal is able to disrupt equipment many kilometres beyond the source region boundary.

The generation of HEMP is closely related to that for the surface-burst EMP in so far as the Compton currents and later conduction currents generated from the gamma are responsible for the activity within the source region. However, the major difference is the need to describe a transverse component of the Compton current that relates to a deviation from the radial path caused by a turning effect of the Earth's magnetic field. It is this component that radiates a pulse towards ground. This pulse is characterised by a fast rise-time in the nanosecond timescale with a peak of around 50 kV/m. The height at which such events take place means the EMP can affect large geographical areas (radially thousands of kilometres).

The voltages induced from such phenomena can reach values that exceed the breakdown strength of air and therefore induce corona discharge. Such changes in the medium create distortions in the coupled signal making defence strategies more complicated. An understanding as to the degree of these distortions is required. Based on the nature of the EMP being considered, empirical data is at a minimum and therefore computational simulations are necessary.

Chapter 2 Electrical Discharge

Corona discharge and electric arcing are just two forms of general electrical discharge phenomena. Electrical discharge can be defined simply as the flow of current between two points of differing potential, usually across a dielectric; typically, a gas. Corona discharge is, essentially, a *partial* electrical discharge for reasons that will become clearer later. The term 'arcing' on the other hand is used to describe the complete breakdown between the two oppositely charged electrodes; lightning being a familiar example. Other descriptions describing the discharge in more detail are available depending on how one decides to characterise the discharge. For example, the voltage magnitude required for breakdown in a particular material may be chosen specifically to create a particular effect. The shape and structure of the electrodes can be used to exploit the development of discharge. A simple example of a form of electric discharge that is encountered on a daily basis is the glow discharge; the discharge that occurs in a fluorescent tube. On the other hand, the discharge around power lines is undesirable due to the associated energy losses. This thesis concentrates on another undesirable consequence of electrical discharge, namely, the known distortion of waveforms responsible for the discharge around wires in the first place. Despite this sub-categorisation of the various discharges, a general mechanism can be described for all electrical discharges and this will the be the aim of this chapter. Once this is established all descriptions of particular forms of discharge can be easily deduced.

For the purposes of this thesis, the research is centred on corona discharge in air although related phenomena such as soil ionisation due to the high electric field existing around grounding rods will also be examined. Air generally acts as an efficient insulator around overhead wires allowing extra high voltages to be transmitted long distances without appreciable loss of energy. However, when the air becomes conductive these properties

deteriorate and energy losses ensue. These energy losses lead to deterioration of signals. Further, the signature of a transient propagating on a wire under the influence of corona is known to distort and attenuate in characteristic ways. These aspects become an important consideration when trying to defend against the likes of high-energy emissions from a lightning strike or that resulting from a nuclear burst. When considering grounded electrodes, the surrounding soil, despite already being conductive (a desirable feature when protecting against lightning strikes) will have its qualities affected by ionisation in the vicinity of the wire. This may have an impact on the ground potential rise around grounded installations when subjected to high voltages Only recently has this aspect of the soil qualities been considered when modelling surge behaviour such as lightning strikes on grounding systems e.g. see [20].

A great deal of the theory related to electrical discharges is based around understanding the lightning process. However, to understand such phenomena, the problem needs to be scaled down considerably so that the effect can be investigated under controlled laboratory conditions. Hence, the theory becomes centred around an understanding of the electrical spark at least when considering total breakdown between two conductors of suitably different potential. To describe the mechanisms underlying electrical breakdown in air a basic grasp of air chemistry is necessary. In particular, an understanding of the behaviour of the constituent molecules and electrons under the influence of electromagnetic fields is necessary. The following provides a basic summary of the pertinent details of such behaviour and the terms used.

2.1 Basic Definitions

2.1.1 Drift velocity and mobility.

A charged particle in a gas is subject to many external energy sources. The particle may gain energy and accelerate, unhindered, in the direction of a local electric field. However, energy losses will result from collisions with particles in its path hampering the acceleration. The

mass of the particle will influence both these energy gains/losses. However, after a given time (the *relaxation time*), a constant speed will result termed the *drift velocity - the component in the direction of the field,* v_d.

The ratio of the drift velocity to the electric field is called the *mobility*, μ.

$$\mu = \frac{v_d}{E} \tag{2.1}$$

It can be defined as the drift velocity component in the electric field direction of unit strength. In other words, this suggests the ease at which a particle can move through a given medium when subjected to an electric field [21]

2.1.2 Mean free path and cross section.

When considering electron interaction with other neighbouring atoms and molecules the interaction can be described as *elastic*, whereby all the kinetic energy is conserved (or, equivalently, momentum) or *inelastic* whereby some of the energy is absorbed by the colliding bodies and converted into potential energy. In these circumstances, the electron may attach to the obstructive molecule forming a negatively charged ion or the energy may lead to an atom being left in an excited state. If the energy transferred is greater than the ionisation energy of the atom, then ionisation may occur. The distance between these particular events happening is called the free path, λ_{FP}. For a collection of particles, an average of such paths is called the *mean free path,* λ_{MFP}. Considering such an arrangement, a collision will occur when the centre of two particles come within a distance *r = d/2* (Figure 2-1). Hence, the area of the cross-section (for interception) of a particle, of diameter, *d*, is simply $\sigma_{cs} = \pi d^2$.

λ_{MFP} , can then be defined as

$$\lambda_{MFP} = \frac{1}{n\sigma_{cs}} \tag{2.2}$$

where n, is the atomic or molecular number density of the gas [cm^{-3} or m^{-3}] and σ_{cs} is the microscopic cross-section [m^2] (Not to be confused with conductivity–note the subscript). Hence, the macroscopic cross-section is the product of these two quantities, for that particular process [22].

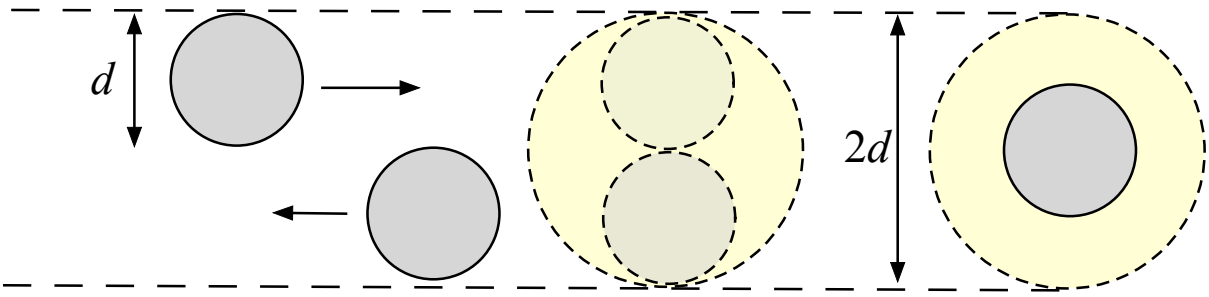

Figure 2-1 The free-path of a gas molecule, where 2*d* represents the cross-section of the particle (recreated from [22]

2.2 Ionisation Processes.

A major consideration when considering electrical discharge is air conductivity. In the realms of Standard Temperature and Pressure (STP), air behaves as an excellent insulator, despite an inherent low level of conductivity existing resulting due to charged particles produced by cosmic radiations and radioactivity present in the atmosphere.

Clearly, air conductivity will depend on the number of free charge carriers present. Processes producing and removing free electrons will take place simultaneously; the rates of both will ultimately dictate the conductivity of the medium.

The source of electrons results from the ionisation of the air molecules. There are many ways this ionisation can occur; collectively termed ionisation processes. Free electrons within the medium will gain kinetic energy in the presence of an electric field and inelastic collisions, will result in the transfer of some of this energy to the interfering atom / molecule in the form

of quanta leaving the particle in an excited state. Any remaining energy may lead to complete ionisation.

An ionisation process can be defined in terms of [23]

i) **Ionisation cross-section:** This cross section will be dependent on the electron energy (only electrons with energy greater than the ionisation energy will result in ionisation directly). However, the combined effort of electrons with lesser energies can also lead to ionisation.

ii) **Coefficient of ionisation, α:** By definition: *the number of ionisation collisions made by an electron moving a unit distance [typically in cm] in the direction of the applied field*. This is sometimes termed the Townsend primary ionisation coefficient.

iii) **Probability of ionisation:** the ratio of the number of ionisation collisions to the number of collisions.

Applying the mean free path definition specifically to direct ionisation collisions, λ_{ion} gives the expression

$$\lambda_{ion} = \frac{1}{n\sigma_{ion}} \tag{2.3}$$

where σ_{ion} is the microscopic cross section for ionisation.

Thus, the number of ionisation collisions made by an electron moving unit length is

$$\alpha = n\sigma_{ion} \tag{2.4}$$

The probability of ionisation is given by

$$P_{ion} = \frac{\sigma_{ion}}{n\sigma_{cs}} \tag{2.5}$$

The number of ionisation collisions an electron makes while travelling unit distance will depend on the electric field, E, and the atmospheric pressure, p.

Ionisation processes include

i) Direct impact: as free electrons gain energy in the electric field, those that acquire energy greater than the discrete amount necessary for excitation may transfer the energy to the incident atom or molecule. If the energy the electron possesses is higher than the ionisation energy, then ionisation can result. Positive ions are also capable of ionising atoms/molecules in their path. However, due to their size and mass, they typically require twice the energy of an electron for ionisation to take place [24][25].

ii) Photo-ionisation: photons of enough energy are also capable of ionisation provided their energy is greater than the ionisation energy of the atom. The process can be described by:

$$A + h\nu = A^+ + e^- \tag{2.6}$$

Here A is the target atom, h is Planck's constant and ν is the frequency of the photon (hence $h\nu$ is the energy of the photon).

iii) Thermal ionisation: the necessary energy to facilitate ionisation is supplied via heat.

iv) Ionisation caused by meta-stable excited atoms: certain atoms that are only excited by the direct contact of an electron will remain excited until deposition of

its energy to a third body. However, whilst in this excited state they are able to contribute to the ionisation of other molecules.

2.3 De-ionisation Processes

The ionisation processes leading to the increase of free electrons are mediated by processes simultaneously removing electrons from the region. The major mechanisms responsible for a reduction in free electrons include [23]:

2.3.1 Electron-ion recombination

As an electrical discharge takes place, neighbouring regions of positive ions and electrons will a tendency for electron-ion recombination. An electron may combine to a nearby ion whilst releasing a photon ($h\nu$), sometimes termed radiative recombination:

$$X^+ + e = X^* + h\nu \tag{2.7}$$

The atom X, in the equation above remains in an excited state, denoted by the asterisk. Thus, further photons may be releases until a ground state is reached.

2.3.2 Dissociative recombination.

This form of recombination initially requires electron energy to dissociate a molecular ion, XY^+, first by attaching itself to the ion leaving it in an excited, unstable state then subsequently dissociating into the constituent atoms to retain stability.

$$XY^+ + e \Leftrightarrow (XY)^* \Leftrightarrow X^* + Y + (\text{kinetic energy}) \tag{2.8}$$

2.3.3 Electron attachment/detachment:

Some molecules have the somewhat peculiar quality of having a ground state in neutrality being higher than its respective negative ionic form thus developing a tendency for the latter. This tendency is usually described as an *electron affinity*. Quantitatively, the magnitude of this electron affinity for a particular molecule is the difference between the ground state energies in neutral and ionic forms. Hence, the greater the electron affinity the more stable the resultant negative ion is. Oxygen, that constitutes approximately 20 % of air volume has a high affinity for free electrons and therefore plays an important part in mediating the ionisation processes.

Generally, the affinity for such behaviour can be related to an **attachment coefficient, η,** defined as *the probability that a free electron be attached to a gas molecule in advancing a distance of 1 cm in the direction of the applied field* [22] (Compare with the ionisation coefficient defined in the previous section).

2.3.4 Diffusion.

Diffusion in a gas acts in such a way for the particles rest in a homogenous state i.e. to maintain a constant density. This will apply to all entities within the gas including charged particles; charge in high concentration will move to areas of lower concentration, thus reducing the charge density in the source region and therefore impedes the ionisation and therefore discharge development. Diffusion of electrons will occur faster due to their size (mobility). This will introduce greater charge separation and therefore introduce an electric field. This induced field will cause the drift positive ions to accelerate whilst retarding the drift of electrons. Eventually, an equilibrium is met where the field is such that both drift at the same rate (ambipolar diffusion).

2.3.5 Energy lost to increased molecular vibrations.

Electron energy that could be used in the process of ionisation can be expended when instigating increases in molecular vibrational and rotational energy levels.

2.4 Sources of Free Electrons.

Free electrons are necessary for discharge processes to initiate. Mechanisms contributing to the free electron density include [23]:

2.4.1 Natural Process:

An immediate source of free electrons results from the ionisation resulting from the absorption of naturally occurring radiations (photons) provided by the surrounding medium.

2.4.2 Cathode Processes:

The band theory of metals predicts that the electrons in a metal are held within a potential well provided by the electrostatic forces within its ionic structure. The energy required to remove an electron from the outer Fermi levels is known as the work function, ϕ of the metal. This can be achieved via the absorption of photons (photoelectric effect), heat (thermionic emission) or following the interaction of other massive particles including positive ions. Typically, during discharge, positive ions will be abundant near the cathode. Alternatively, the potential barrier can be compromised via the application of an electric field. The field can be pictured as reducing the 'height' and 'thickness' of the potential barrier, thus facilitating the release of electrons from the cathode via exceeding the barrier with a lesser energy or tunnelling through the barrier, respectively (the Schottky effect) [26].

2.5 Electrical Breakdown.

2.5.1 Critical Electric Field

For a given electric field, the ionisation and de-ionisation processes compete to either increase or decrease the number of electrons in a given region. Ionisation frequency, ν_i and frequency of attachment, ν_a will vary according to the background electric field. Relating the frequencies to the electron drift velocity, v_d, the coefficients of ionisation and attachment, α and η respectively, can be defined as [27]:

$$\alpha = \frac{\nu_i}{v_d} \tag{2.9}$$

$$\eta = \frac{\nu_a}{v_d} \tag{2.10}$$

Figure 2-2 demonstrates how the frequencies (per unit air density, *N*) vary with electric field. The intersection of the curves describes the equilibrium between both processes. For air at STP, the electric field value at which equilibrium occurs is approximately 2.6×10^4 V/cm [27]. Cumulative ionization will only occur above this value. Hence, the given electric field value is a *critical electric field value for electrical breakdown to take place, E_c.*

Another consideration when determining the feasibility of breakdown is the size of the gap in which this takes place. This is not important for the purpose of this particular work but is worth mentioning nonetheless. The critical field deviates from the value above as the gap shortens. This pertains to the number of electrons freed by ionisation processes required to reach a specified value.

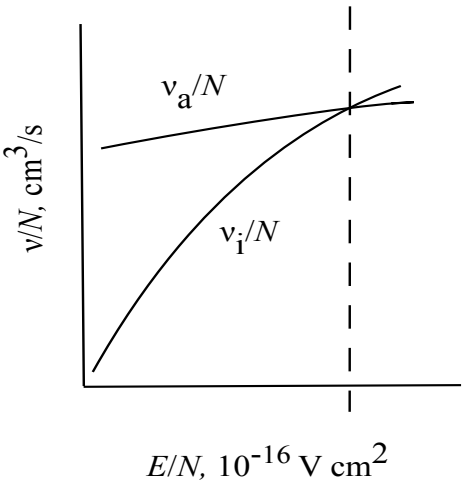

Figure 2-2 Qualitative depiction of variation of ionisation and attachment frequencies with electric field [22]

2.5.2 Physical processes describing electric discharge

The following now aims to describe the mechanisms that contribute to electrical breakdown using the aforementioned theory. The application of an electric field will introduce many of the ionisation and de-ionisation processes both of which will compete with each other in a given environment. A particle of charge, e, subjected to an electric field, $\boldsymbol{E}$, will experience a force, $\boldsymbol{F} = e\boldsymbol{E}$. Both ions and electrons will gain energy in this field but ions, with their larger mass and size, lose energy within a much shorter distance than an electron. Hence, their ability to contribute to electron production via ionisation is negligible while the lighter, more mobile electrons can maintain kinetic energy as many of their collisions can be assumed elastic. Subsequently, their kinetic energy can increase over several free paths even in relatively low electric fields. It is this feature of the electron that enables the *electron avalanche* to flourish.

2.5.2.1 The Electron Avalanche.

A single free electron resulting from a natural event or cathode process can initiate an electron avalanche provided the environment is adequate. Consider a background electric field higher than the critical value for cumulative ionisation i.e. $\alpha > \eta$. Then for a distance *dx*, along an *x* directed electrical field, n_x electrons will give rise to *dn* additional electrons or mathematically [23]

$$dn = n_x(\alpha - \eta)\, dx \tag{2.11}$$

the solution of which is

$$n_x = \exp\left((\alpha - \eta)\, x\right) \tag{2.12}$$

Hence, provided the difference between ionisation and reattachment is positive ($\alpha - \eta > 0$) the number of electrons will increase exponentially with increasing distance. This exponential increase defines the electron avalanche. Note, this simple derivation neglects the local electric field related to the space charge. To estimate the field from the related space charge we can assume the electrons at the head of the avalanche are confined to a spherical region. Then the radial electric field can be represented by [23]

$$E_r = \frac{\exp((\alpha - \eta)\, x) q_e}{4\pi\varepsilon_0 r^2} \tag{2.13}$$

Here, *r* refers to the radius of the approximate spherical region of space charge.

Accounting for diffusion at the avalanche head, the field can be more accurately calculated using [23]

$$E_r = \frac{\exp(\,(\alpha - \eta)\, x) e}{4\pi\varepsilon_0} \left(\frac{v_d}{4Dx}\right) \tag{2.14}$$

where v_d is the drift velocity of the electrons in the *x*-direction and *D* is the coefficient of diffusion.

(The average radial distance of diffusion can be calculated from the equation $r = \sqrt{4dt}$ where $t = x/v_d$)

It follows that there will be a critical length of the avalanche where the field that is attributable to the space charge is comparable to the critical background field. At this stage an electron avalanche will convert itself to a *streamer discharge*. This explains why narrower gaps have a related higher critical value.

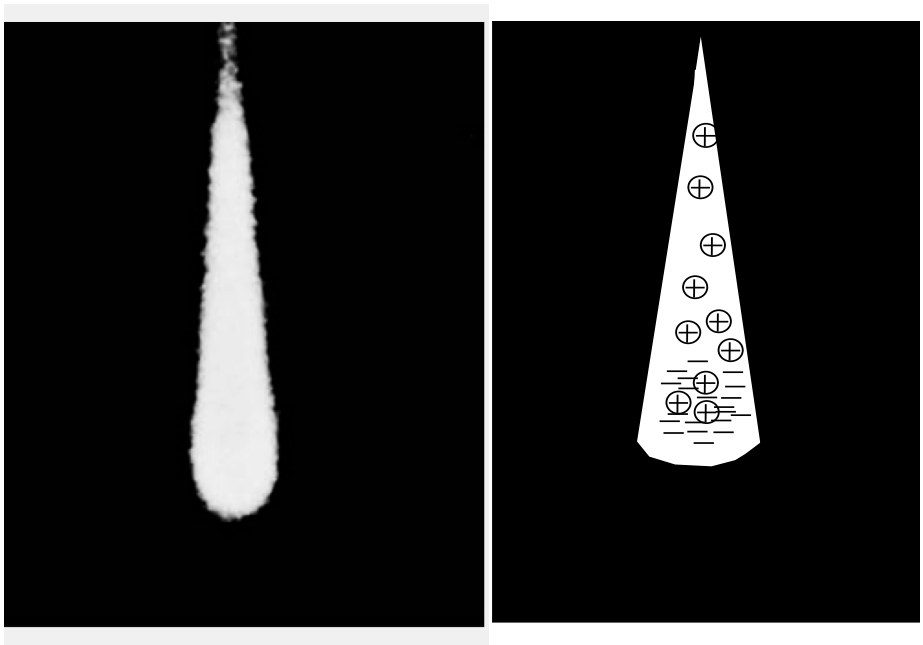

Figure 2-3 Left: photograph of an electron avalanche[28]. Right: depiction of space charge throughout the avalanche.

2.5.2.2 Streamer Formation

The space charge formed at the head of the avalanche will modify the background field. Eventually the field at the head of the avalanche may reach a magnitude necessary to support

the initiation of streamers; the discharge channels that extend into the space between electrodes. As they develop, their channels become increasingly conductive especially with the heat that is also generated contributing to thermal ionisation. The streamers become *leaders*; conductive channels of plasma. The increased conductivity allows the head of the streamer to assume the same potential as that of the wire from which it emanates. Hence, the process can repeat. If the streamers/leaders reach a ground, then complete breakdown results [23]

The avalanche to streamer transition has related critical criteria that are necessary for it to occur. Raether [29] and Meek [30] independently relate this to the number of positive ions present in the avalanche head. In particular, they suggest a critical value, N_c of around 10^8. Assuming the exponential increase of electrons with distance (2.11), a critical length for the transition can be approximated:

$$e^{(\alpha-\eta)x} = 10^8 \tag{2.15}$$

$$\Rightarrow (\alpha - \eta)x = 18$$

This value will, of course, vary with background field for reasons previously described.

As the local field at the streamer head distorts the background electric field, together with the increased photon production present there, secondary free electrons lead to the formation of secondary avalanches moving in a direction determined by the wire polarity. Subsequent avalanches will only occur if the field exceeds 2.6×10^4 V/cm i.e. the minimum field necessary for *cumulative* ionisation in air at atmospheric pressure (see Figure 2-2). The avalanches are confined to a region about the streamer head called the active region (Figure 2-5).

Assuming the head of the streamer to be spherical with radius R_s, containing $Q_s(= 10^8 q_e)$ positive charge then, assuming a typical radial field pattern, the electric field can be described using [23]

$$E(r) = \frac{Q_s}{4\pi\varepsilon_0 r^2} \;\; ; \;\; r > R_s \tag{2.16}$$

This predicts the critical field to be achieved within a radius of 0.23 mm and becomes the necessary radius of the active region. This actually corresponds to an average electric field of around 1-1.5 $\times 10^5$ V/cm [31]. The local charge formed by the secondary avalanches increases the local field suitably to allow propagation in a background field less than the critical breakdown field. This is an important consideration within the models described later (Cooray equations: chapter 4).

2.5.2.3 Streamer propagation:

Concentrating on the propagation of a positive streamer, the elevated field relating to the higher density of positive ions at the streamer head will attract secondary avalanches towards it. These will neutralise the positive space charge at the head while leaving positive space charge in their wake; closer to the cathode (hence the name cathode directed streamer) and as just described in the previous paragraph will be able to propagate in background electric fields less than the critical electric field, E_c.

Negative streamer propagation is different in so far as the electrons that neutralise the positive space charge are provided by the electrode itself, not electrons generated by the secondary avalanches. Another major difference when considering the propagation of a negative streamer is that it propagates into a region of falling electric field. This facilitates the capture of electron via electronegative oxygen molecules and subsequently raises the critical background field for negative streamer propagation in air, hence the following typical critical background fields [32]:

Critical background field for positive streamer propagation = 4-6$\times 10^3$ V/cm

Critical background field for negative streamer propagation = 1-2$\times 10^4$ V/cm

[Note, these will vary depending on air humidity, temperature, gas composition, density]

The simulations by Cooray [61]and Thang et al [55] use critical background fields of 0.5 $\times 10^6$ V/m for positive streamers and 1.5 $\times 10^6$ V/m for negaive streamers.

As has been already alluded to, the formation of the streamers varies somewhat depending on the polarity of the wire.

2.5.2.3.1 Positive Streamers

Figure 2-4 depicts the formation of a positive streamer. Electrons accelerate in the field towards the anode, colliding with molecules and generating an electron avalanche. Eventually, the tip of the avalanche reaches the anode. Electrons within the head are absorbed by the anode leaving the positive ions behind and therefore increasing the local positive charge. The recombination of electrons and positive ions releases many photons (2.7), some with energy to initiate separate electron avalanches at the head of the original. Provided enough positive ions result from these avalanches as the electrons are absorbed by the wire, the space charge electric field will eventually reach the critical field necessary for streamers to occur. Electrons that result from the secondary avalanches will be neutralised by the positive ions that resulted from the original avalanche. A residual positive charge from the latter avalanches, is now the only space charge present located further away from the original positively charged wire surface. This process will repeat provided the critical conditions are met resulting in a positive charge that edges further and further away from the wire and describes the formation of a positive streamer or what is sometimes referred to as a *cathode directed streamer*.

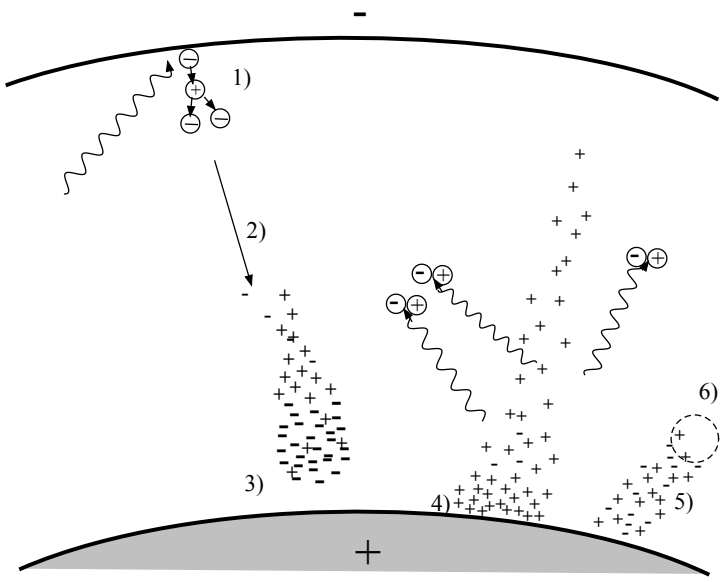

Figure 2-4 Stages of positive streamer formation (adapted from[23])

To summarise:

1) Photon energy liberates an electron
2) Electron accelerates in the electric field towards the positively charged wire. Provided cumulative ionisation is permitted, a *primary* electron avalanche propagates towards the wire (in the direction of increasing field) leaving behind the lesser mobile positive ions.
3) The avalanche reaches the wire (anode). Primary avalanche electrons are absorbed (these may have to lose energy via secondary collisions). This process leads to the further release of photons capable of initiating *secondary* electron avalanches.
4) The residual positive ions are in greatest concentration in the vicinity of the wire. Provided these are in high enough concentration, the space charge related to them will attract electrons generated by the secondary avalanches and a streamer is initiated.
5) The secondary electrons will neutralise the positive charge nearest to the anode. A plasma is formed. This constitutes the streamer channel, while a positive space charge remains at the tip of the channel albeit closer to the ‘cathode’.

6) If the charge at the head (sometimes referred to as the active region) is large enough to recreate the field necessary for the streamer to propagate then the steps above are repeated (Figure 2-5)

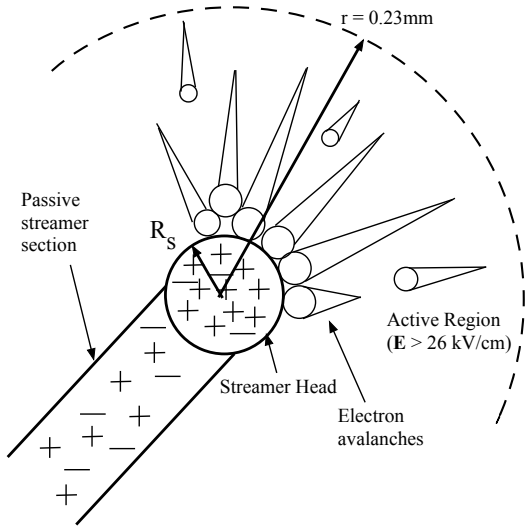

Figure 2-5 The active region of a positive (cathode directed) streamer [23]

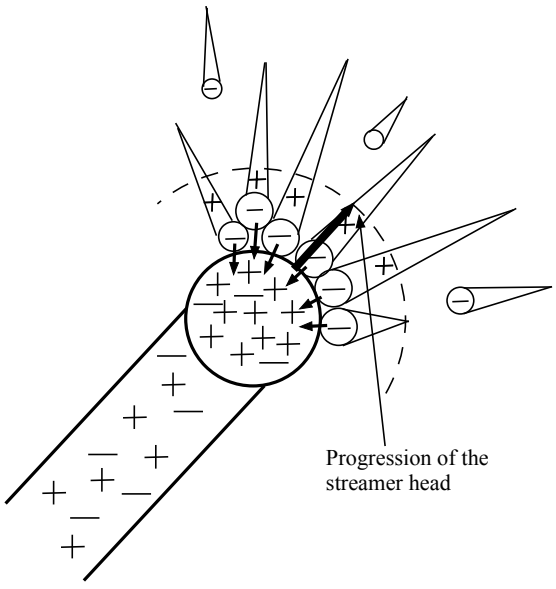

Figure 2-6 Basic depiction of the progression of a positive streamer. Electrons produced via secondary avalanches move to neutralize the positive charge at the streamer head. Positive charge from the secondary avalanches is left behind forming the extension to the streamer. (adapted from [23])

2.5.2.3.2 Negative Streamers.

The process is different when describing negative (anode directed) streamers. If the wire has a negative polarity (cathode), then an electrical field greater than the critical threshold will result in free electrons accelerating away from the wire giving rise to avalanches in the same direction. The major difference here is that the avalanche is propagating into a decreasing electric field. Positive charge will congregate near to the cathode. If the avalanche is able to reach the critical size for the local critical field to be met (2.12), then secondary avalanches result in an extension of positive charge to the wire.

The extension will gradually reach the negatively charged conductor. This positive channel that results will give rise to electrons attracted from the wire surface (via the local field strength and the collisions of the positively charged ions on the wire surface). These electrons will neutralise the positive charge whilst creating a conductive channel connecting the former positive end at the wire surface to the negatively charged head of the original avalanche.

The space charge 'dipole' at the head of the avalanche comprised of a high concentration of electrons at the outermost tip whilst the positive ions remain closer to the wire, result in an electric field that further displaces electrons away from the wire, while the relatively dormant positive charge is neutralised by electrons provided by the wire transported via the conductive channel (Figure 2-7).

To summarise:

1) Photon triggers an electron avalanche. The avalanche propagates away from the cathode into a region of reducing electric field.
2) Positive ions are left behind. Provided the avalanche has reached the critical size secondary avalanches will form directed towards the positive space charge generated from the primary avalanche. These will provide electrons able to neutralise the positive space charge while the positive space charge left behind from the secondary avalanches will remain resulting in a positive space charge nearer to the cathode.

3) Eventually, the positive space charge may reach the cathode freeing more electrons from the cathode (due to direct collision and the increased local field now present there).
4) These electrons neutralise the positive space charge while forming a conductive channel between the wire (cathode) and the head of the streamer (that resulted from the original avalanche).
5) The negative space charge present at the tip of the streamer is further ousted towards the anode while positive space charge that results is neutralised from electrons provided by the cathode via the streamer channel.

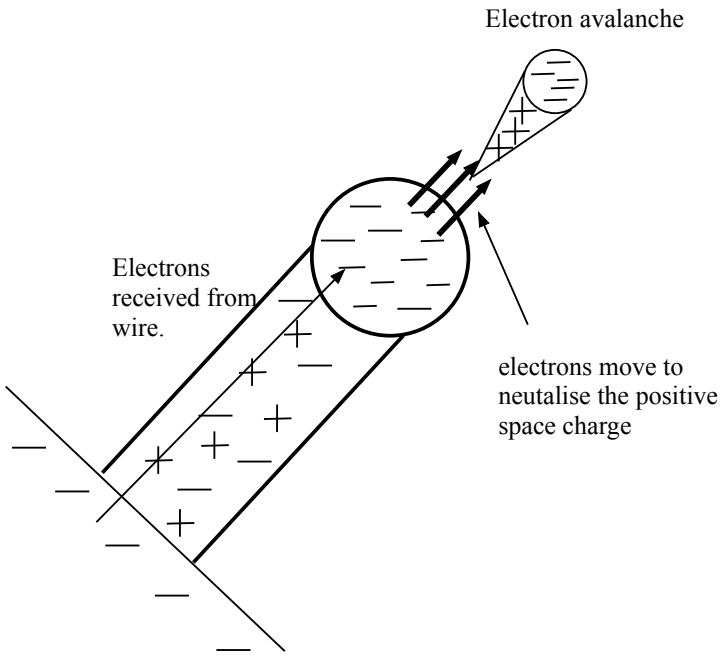

Figure 2-7 Formation of a negative streamer. Secondary avalanches propagate away from the wire leaving behind positive ions. These are neutralized from electrons that are taken from the wire, conducted via the streamer channel[23].

Occasionally, the positive space charge resulting from the primary avalanche reaches the critical value for streamer development before reaching the assistance of the cathode. This can lead to what is known as a mid-gap streamer. This is beyond the scope of this thesis.

2.6 Corona Discharges

A uniform electric field facilitates complete breakdown across gaps in ways previously described. However, non-uniform fields resulting from high applied voltages and suitable metallic structures, provide conditions for partial breakdown that manifest themselves as transient or steady state discharges. Such discharges are termed corona and are the major consideration of this work. Their presence is usually made aware via visible and audible cues. Energy losses result as well as radio interference, insulation deterioration although it can be sometimes used as advantageous phenomenon (Geiger counters, high-speed printers to name a couple of uses). The polarity of the wire will introduce different mechanisms to the corona formation in ways analogous to those in near uniform electric fields.

Now the critical fields described previously are met within a small radial extension from the wire due to the highly non-linear nature of the radial electric field that arises in such circumstances. This will place a limit on the radial extension of the breakdown such that only partial breakdown is reached. The mechanisms describing the progression of corona from the highly energised wire are not too dissimilar to those describing positive and negative streamer propagation in uniform fields. The criteria calculation just need to be amended to account for the non-uniformity of the field. Therefore, the streamer criterion (2.14) now becomes

$$\int_0^{x_c} (\alpha - \eta) dx \approx 18 \tag{2.17}$$

where x_c is the distance within the coronal region.

As air breakdown is of interest, the gas constituents; nitrogen (79%) and oxygen (20%) become important. The electronegative nature of oxygen is an important feature of corona discharge models as it will hamper the formation of electron avalanches that originate in the field. Other factors such as air density, humidity, and the integrity of the wire itself will also influence the discharge process. Hence, a streamer criterion similar to that defined previously can be proposed: *there exists a critical length for the initial electron avalanche equal to* $1/\gamma_i$*, such that the action of secondary processes become sufficient to maintain the discharge in a*

gap in a self-sustained regime of discharge. This critical length corresponding to 10^8 electrons as previously alluded to and an onset voltage can be calculated for such discharge – the streamer criterion [22].

Just as with the descriptions relating to total breakdown, the partial discharge will be dominated by free electrons generated by scattering, the emission of photons by excited molecules that are able to ionize and electron attachment. Electron detachment from negative ions and electron emission from the cathode resulting from ionic bombardment will also provide some free electrons. Free electrons will be removed via electron attachment that will help to dictate the modes of the partial discharge.

2.6.1 Negative Corona Modes.

A sufficiently negatively charged wire (cathode), able to generate electric fields capable of exceeding the breakdown threshold of the surrounding air will lead to the generation of electron avalanches and streamers propagating away from the wire. The electrons are directed towards a falling electric field making them susceptible to electron capture by the Oxygen atoms. These form the negative space charge, away from the wire. Figure 2-8 demonstrates how the radial electric field is modified in the presence of the space charges that form during the process.

Let S_0, represent the boundary where $\alpha = \eta$, that is, where the net ionization is zero and let r_0 corresponds to the radial distance of this boundary in respect to the wire axis. Initially, at a radial distance less than r_0, the ionization coefficient dominates. The positive ions that are left behind exceed the electronegative ions produced by attachment of free electrons to oxygen molecules. Conversely, beyond the boundary, the attachment coefficient dominates and hence the negative ions dominate.

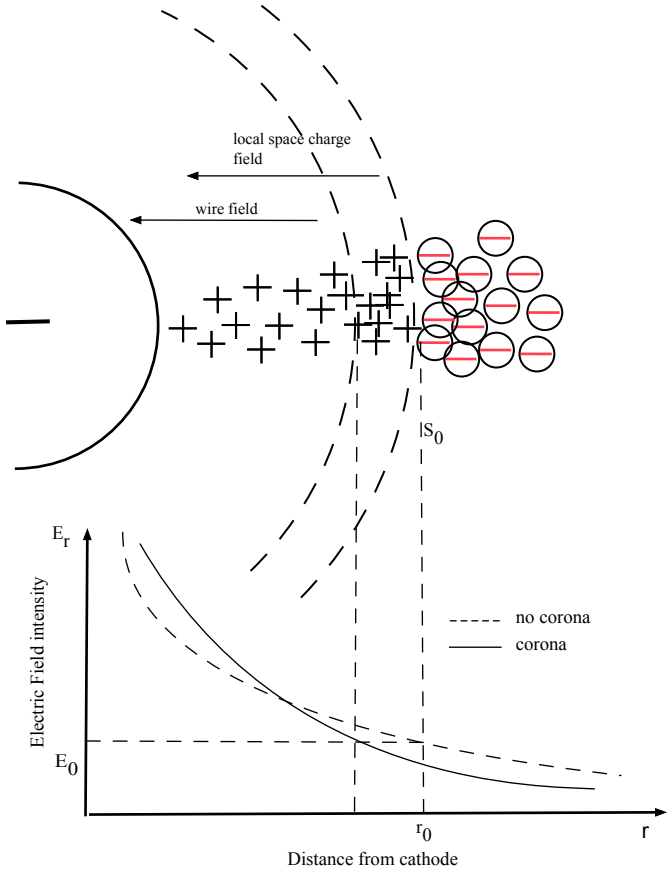

Figure 2-8: The space charges formed through negative corona development. As the charges develop the radial field is modified in such a way that S_0 edges closer and closer to the wire surface [22]

As the diagram demonstrates, the critical edges closer to the wire under the influence of the space charges formed. This variation allows three corona modes to be described here described in order of increasing applied voltage:

1) **Trichel streamers**: This appears as a regular pulse-like activity. The streamer initiates via an initial free electron and is maintained for a short time as primary and secondary avalanches meet the streamer criterion. However, it is quickly suppressed as the ionization-attachment boundary gradually encroaches towards the wire limiting the positive charge to progressively smaller area around the wire, and is subsequently

neutralized by the cathode and the negative ions on the other side of the boundary. Eventually, the negative charge dominates to such an extent that the field falls below the onset field and prevents further discharge. Only when the negative charge has dispersed sufficiently, will the onset field be reached again allowing the discharge process to repeat.

2) **Negative glow:** Characterized by a stable discharge that is sustained by a high electric field. The electron source results from ionic bombardment of the cathode. Electrons gain energy from the field to an extent that secondary ionization is possible. The field is able to remove the ionic space charges responsible for the choking of the discharge that is characteristic of the pulseless glow.

3) **Negative streamers:** If the applied voltage is increased further then negative streamers will form. The ionic bombardment supplies electrons from the cathode, whilst the removal of space charge allows avalanches to develop into streamers that can extend outwards further from the wire and are potentially able to reach an anode to allow total breakdown.

2.6.2 Positive Corona Modes.

If the wire assumes the behaviour of a highly charged anode, then electron avalanches will be possible within the surface S_0. The electrons that result are accelerated towards the positively charged wire in a field that is increasing. Hence, the highest ionization energy is felt at the anode surface. The low mobility of the residual positive ions results in a relatively dormant positive space charge lying away from the anode. The electrons received at the anode are of too great an energy to form negative ions and are instead absorbed by the anode once they have lost sufficient energy by spreading themselves over the anode surface and undergoing

further ionization. It is this behaviour that is responsible for the visible effects over the surface.

The positive charge that rests close to the anode may be of sufficient magnitude to initiate secondary avalanches (streamer criterion). Streamer channels that form will propagate away from the anode enabled by the secondary avalanches. The space charge distribution modifies the radial electric field as demonstrated in Figure 2-9. Notably, the predominance of the positive space charge near to the anode surface creates a depression in the field. Streamers will form in the usual way provided the positive charge meets the streamer criterion.

Again various modes are dictated by the formation of the space charge depending on the applied voltage. In order of increasing voltage these are:

1) **Burst Corona**: The incoming electrons have their highest energy at the anode surface. Before they are absorbed into the anode, they spread across the surface of the wire and contribute to secondary ionization; processes that expend the energy of the electrons allowing them to be neutralized by the wire. A number of positive ions congregate over the anode and the resultant positive space charge decreases the field thus inhibiting the discharge. The process appears as a thin luminous sheath around the surface of the wire.

2) **Onset streamers**: If the positive space charge of the avalanches meets the streamer criterion then streamers will extend outward from the wire. However, they are limited in size as the positive charge produced that resides near the anode reduces the field there below the onset voltage thus choking off the streamer. Only when this space charge is removed can another streamer initiate leading to a ‘dead time’. Hence, the mode has a pulsating aspect to it. Ultimately, with increasing voltage, positive charge is more readily removed as it is pushed further and further away from the wire. Instead the positive glow mode will begin.

3) **Positive Glow**: The discharge activity at the surface of the anode is analogous to the burst corona as it spreads across the anode surface.

4) **Breakdown Streamer**: A further increase in applied voltage will remove the positive charge that has stemmed the formation of streamers. Hence, streamers form in the ways described previously, but to a greater extent and are potentially able to extent to the anode to allow total breakdown.

2.6.3 Dependence of electrical breakdown on atmospheric conditions.

Just as the ionisation (α) and attachment (η) coefficients are dependent on pressure and temperature (or equivalently gas density) it follows that this will lead to a critical electric field for breakdown as this relies on the cumulative ionisation requirement ($\alpha > \eta$). Also dependent on such factors, is the critical electrical field for corona inception. This is encapsulated in Peek's law [33]

$$E_c = 3.15 \times 10^4 \delta \left(1 + \frac{0.305}{\sqrt{\delta r}}\right) \tag{2.18}$$

where r is the radius of the conductor (cm) and δ is the relative density correction factor given by

$$\delta = \left(\frac{T_0 p}{p_0 T}\right) \tag{2.19}$$

Here, p is pressure of the gas (p_0 is standard atmospheric pressure = 1.013 bar) and T is gas temperature (T_0 is standard atmospheric temperature = 293K). Sometimes, a wire surface factor maybe included (denoted by m ranging from 0 to 1 where 1 represents a perfect wire surface. Other equations that aim to refine this relation have been formed since Peek, for example Hartmann [31].

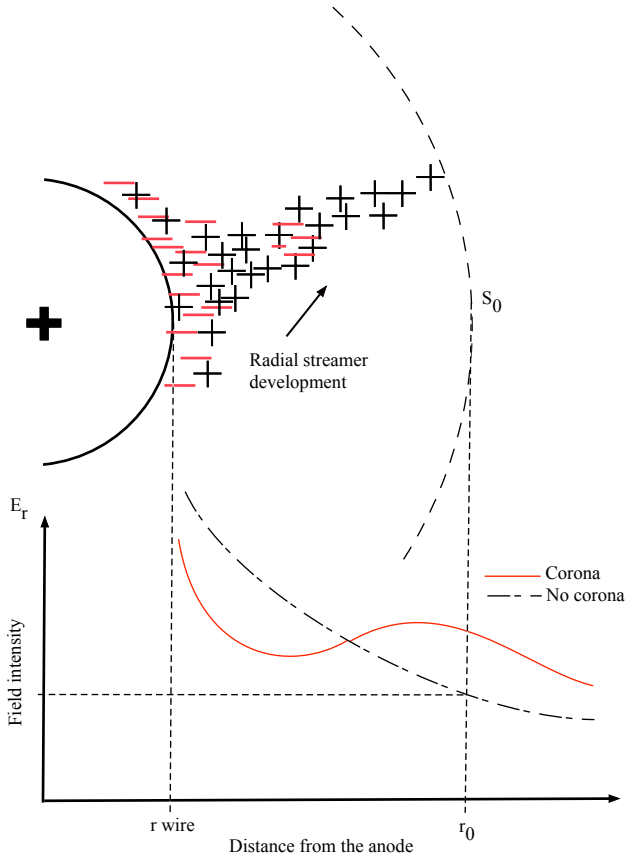

Figure 2-9: Distortion of the radial electric field due to space charge formed during positive corona development [22]

2.7 Lightning

Lightning discharges are essentially a spark on a large scale. The basic mechanisms describing lightning strikes are straightforward. Once the charge magnitude in clouds reaches a suitable threshold, a preliminary breakdown within the cloud results from which, in the case of a downward travelling strike, a *stepped leader* emerges. The stepped leader is a column of charge as described in the previous section. The familiar branching of the leader may occur as it progresses towards the ground. As the stepped leader progresses downwards, towards the Earth's surface, the ground-level electric field increases to such an extent that the field there

may reach the critical field strength for dielectric breakdown. Subsequently, the formation of *connected leaders* can originate from the Earth's surface (or more likely, a tall object on the Earth's surface), able to connect to the stepped leader. The distance between the original stepped leader head and the connected leader is sometimes called the *striking distance* as when the two connect a strike is said to occur; the familiar luminous arc results as a current wave called the *return stroke* results.

The peak current of the return stroke in models is usually taken as 30kA. The wave shape is highly variable but is usually represented as a bi-exponential equation of the form

$$I(t) = A(e^{-\alpha t} - e^{-\beta t})$$

The rise-time of the transient is in the microsecond regime [34] .

2.8 Summary.

The development of electrical discharge is a complex process related to many factors. Air chemistry plays an important part especially in environments with a high background electric field. Under such conditions, a competition between ionisation and de-ionisation processes will ultimately decide on the critical field responsible for cumulative space charge development, E_c. These are dependent on the physical parameters of the gas (air) such as its temperature and pressure both of which will influence air density. The critical breakdown field for corona inception is also dependent on atmospheric conditions as well as the physical attributes of the conductor as this will influence the electric field. Peek, Hartmann have proposed formulae that seek to predict the inception field strength, E_b. For all its complexity, these two field strengths suffice to describe discharge about wires from a macroscopic perspective. The changes in the dielectric result in a space charge about the conductor. This space charge increases the conductivity of the medium in the vicinity of the conductor. The radial extent of the space charge is dictated by the critical field for streamer propagation, E_c.

Chapter 3 The Transmission-Line Modelling Technique

The theory behind the Transmission-Line Modelling Method (TLM) rests on the idea that a given domain can be discretized into many miniature cells or nodes comprised of transmission lines. An analogy can be drawn between the voltage and current waveforms that propagate on the transmission lines and the electric and magnetic field propagation the lines describe. The transmission line impedances correlate with the media in which the simulation takes place. Typically, this will represent impedance of free space with subsequent adjustments made to represent other media if necessary. Thus, a given domain, once transposed into an array of transmission lines, will become a meshwork allowing the electromagnetic field values to be found at precise points. The investigation of fields using circuit analogues was originally suggested by Kron [35] but it was Johns and Beurle [36] in the 1970's that advanced the principle to scattering problems. Since these original concepts, the technique has become further advanced to allow for all manner of electromagnetic investigations. The method can be considered as a differential circuit based approach to solving a region in the time domain.

One-dimensional TLM provides the simplest approach to modelling as only certain field components are represented. Despite its simplicity, it can be useful for certain problems especially if a quick solution is required. Two-dimensional TLM is also used occasionally, adding some complexity to the modelling but this will not be described here. The majority of the modelling within this thesis is performed in three dimensions, using a three-dimensional TLM node. The 3-D TLM node contains all the transmission lines necessary to represent all the electric field and magnetic field components. In particular, the 3-D TLM node employed

throughout this thesis is otherwise known as the Symmetrical Condensed Node (SCN). However, to present the underlying principles of TLM from a modelling perspective, an understanding of a simple one-dimensional approach is valuable.

3.1 Basic principles (1-D TLM).

Consider a 1-D lossless transmission line with intrinsic capacitance per unit length, C_d and inductance per unit length, L_d (Figure 3-1). The line can be divided into sections of length Δx, with each section considered to be situated in a cubic block of space with dimensions $\Delta x \times \Delta y \times \Delta z = \Delta l^3$

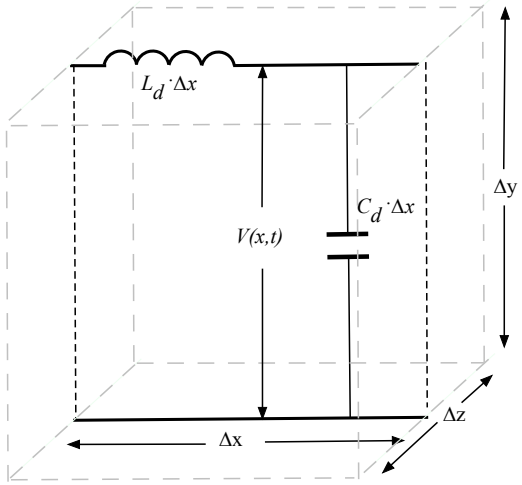

Figure 3-1A basic x-directed transmission line segment

The Transmission Line equations, otherwise known as the Telegrapher's equations, describing voltage and current propagation along such a line are [37]

$$-\frac{\partial I(x,t)}{\partial x} = C_d \frac{\partial V(x,t)}{\partial t} \tag{3.1}$$

$$-\frac{\partial V(x,t)}{\partial x} = L_d \frac{\partial I(x,t)}{\partial t} \tag{3.2}$$

These can be used to derive wave equations for both the voltage and current:

$$\frac{\partial^2 V(x,t)}{\partial x^2} = L_d C_d \frac{\partial V^2(x,t)}{\partial t^2} \tag{3.3}$$

$$\frac{\partial^2 I(x,t)}{\partial x^2} = L_d C_d \frac{\partial I^2(x,t)}{\partial t^2} \tag{3.4}$$

Hence, the speed of propagation, v_p, is given by

$$v_p = \frac{1}{\sqrt{L_d C_d}} \tag{3.5}$$

The surge (characteristic) impedance, Z, can be shown to be

$$Z = \sqrt{\frac{L_d}{C_d}} = \sqrt{\frac{L}{C}} \tag{3.6}$$

Referring to Maxwell's equations, in particular Faraday's equation, if an *x*-directed electromagnetic plane wave with the electric field component polarised in the y-direction and the magnetic field component polarised in the z-direction is considered (Figure 3-2) then in component form the only relevant versions are

$$-\frac{\partial H_z(x,t)}{\partial x} = \varepsilon_0 \varepsilon_r \frac{\partial E_y(x,t)}{\partial t} \tag{3.7}$$

$$-\frac{\partial E_y(x,t)}{\partial x} = \mu_0 \mu_r \frac{\partial H_Z(x,t)}{\partial t} \tag{3.8}$$

The speed of propagation, c, in any given medium is given by

$$c = \frac{1}{\sqrt{\varepsilon_0 \varepsilon_r \mu_0 \mu_r}} \tag{3.9}$$

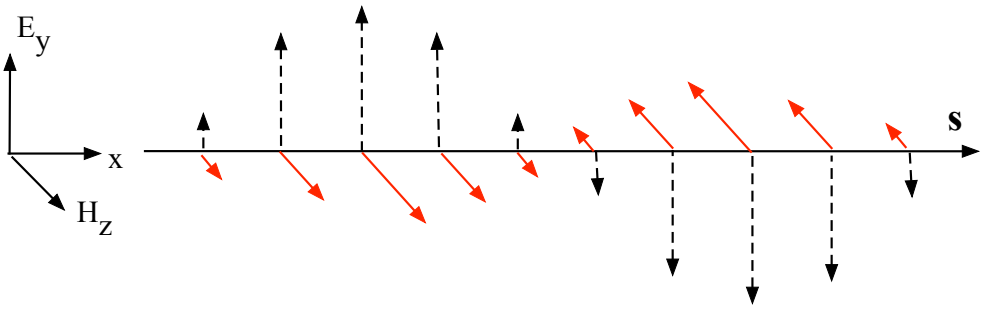

Figure 3-2 A propagating electromagnetic wave in the *x*-direction with electric and magnetic field components polarized as shown. In the diagram, each field value (represented by an arrow) should have its respective node to meet the $\lambda/10$ criterion (see later).

Note, the velocity in free space is

$$c_0 = \frac{1}{\sqrt{\varepsilon_0 \mu_0}} \tag{3.10}$$

and the characteristic impedance of free space , Z_0:

$$Z_0 = \sqrt{\frac{\mu_0}{\varepsilon_0}} \tag{3.11}$$

Comparing equations (3.1) and (3.7), the following equivalences can be isolated:

$$C_d \Leftrightarrow \varepsilon_0 \varepsilon_r \frac{\Delta x \Delta z}{\Delta y} = \varepsilon_0 \varepsilon_r \Delta l \tag{3.12}$$

$$E_y \cdot \Delta y \Leftrightarrow V_y \tag{3.13}$$

While comparing equations (3.2) and (3.8) reveals the equivalences:

$$H_z \cdot \Delta z \Leftrightarrow I_x \tag{3.14}$$

$$L_d \Leftrightarrow \mu_0 \mu_r \frac{\Delta x \Delta y}{\Delta z} = \mu_0 \mu_r \Delta l \tag{3.15}$$

Therefore, it should be possible to model EM wave propagation along a line provided we use a series of cells or nodes constituting a mesh each with a transmission line with impedance Z.

The introduction of discretization can be thought of as sampling the propagating waveform in space and time throughout the mesh. With this in mind, the highest frequency or shortest wavelength of the transients propagating within the mesh will also dictate the adequate cell size or time step to represent the waves sufficiently; an inadequate cell size i.e. a 'large' segment size will not sample the wave to an adequate degree thus giving an inadequate representation of the waveform. It is found that a cell length of at least one tenth of the shortest wavelength considered should be chosen to obtain accurate results [38]. This criterion will therefore determine the resolution of the space being modelled. Other considerations will further dictate the resolution of the mesh. The simulation of thin wires is a frequent problem encountered in many modelling approaches, when dealing with relatively large domains. Thankfully, there are now ways of augmenting the TLM node such that the general resolution is not affected appreciably (the Embedded Wire Node –see later)

The progression of the simulation in real-time demands an update process at discrete time intervals or time-steps. This is the time discretization mentioned previously. Consider a pulse travelling at velocity c. It will traverse a cell in a time, Δt given by

$$\Delta t = \frac{\Delta l}{c} \tag{3.16}$$

Hence, the cell size chosen inadvertently dictates the time step used within the simulation.

The time taken for the pulse to travel from one end of a transmission line segment to the end (or segment within the node). is sometimes called the transit time, τ.

3.1.1 Introduction of stubs

One approach to creating the desired model is to first let the basic line represent free space and then introduce a transmission line stub to model any relative permittivity / permeability that is unaccounted for [38]. Figure 3.3 shows such an arrangement to introduce relative permittivity. Each segment still has a length Δx but now each segment contains two transmission lines of length $\Delta x/2$ representing the impedance of free space, while a TL stub is introduced to represent the extra capacitance needed to describe the wire.

A junction is created within each cell. For the simulation to run correctly, all pulses must reach cell boundaries and junctions at the same time. When this is achieved, the mesh is said to be *synchronised*. Referring to Figure 3-3 we see that a pulse on the link lines will travel a distance $\Delta l/2$ in a time $\Delta t/2$. Let $\Delta t/2$ be the transit time for the link line.

First consider a TL link line with a required per-length capacitance C_d. Then:

$$v_p = \frac{\Delta l}{\Delta t} = \frac{1}{\sqrt{C_d L_d}} \tag{3.17}$$

and therefore (rearranging)

$$L_d = \left(\frac{\Delta t}{\Delta l}\right)^2 \frac{1}{C_d} \tag{3.18}$$

Also the impedance of a link-line with per-length capacitance C_d and per-length inductance L_d is given by

$$Z = \sqrt{\frac{L_d}{C_d}} \tag{3.19}$$

and after substituting (3.18) becomes [38]

$$Z_{LINK} = \frac{\Delta t}{C} = \frac{\tau}{C} \tag{3.20}$$

where $C = C_d \cdot \Delta l$ and is the capacitance of the link line.

Hence, for a given capacitance and time-step the necessary impedance is found using (3.20)

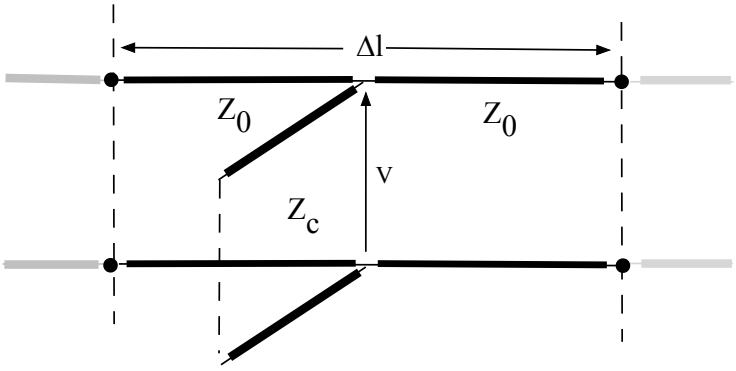

Figure 3-3 A 1-D line segment of length Δx. The link lines represent free space while the stub in the centre represents any necessary relative permittivity.

Now considering the stub to represent the extra capacitance (per unit length), for the line segment with length, Δl, a pulse will have to propagate to the open circuit and back in the same time to maintain synchronism between nodes. Therefore, for a stub to represent the same per-length capacitance, C_d, a round-trip time must be taken into account to maintain synchronisation [38]

Hence, the transit time is now $\Delta t/2$

$$u = \frac{\Delta l}{\Delta t/2} = \frac{1}{\sqrt{C_d L_d}} \tag{3.21}$$

Therefore

$$L_d = \frac{(\Delta t)^2}{4C\Delta l} \tag{3.22}$$

and the characteristic impedance of the stub need to be equal to

$$Z_{STUB} = \frac{\tau}{C} = \frac{\Delta t}{2C} \tag{3.23}$$

A similar rationale can be used to describe inductance link-lines and stubs. The related impedances are given by:

$$Z_L = \frac{L}{\Delta t} \quad [\text{link line}] \tag{3.24}$$

$$Z_{STUB} = \frac{2L}{\Delta t} \quad [\text{stub}] \tag{3.25}$$

3.1.2 Scattering

Once the correct impedances have been introduced to describe problem in hand such that the synchronisation is maintained for a chosen time-step, and the correct medium represented throughout, the voltages and currents are solved within the mesh following an initial excitation.

The activity at a node is best represented by a Thévenin Equivalent Circuit. Figure 3.4 demonstrates the equivalent circuit for one of the nodes in Figure 3-3. Voltage sources represent the voltage presented to the node from each direction. Note the doubling of the incident voltage pulse to provide the Thévenin equivalent voltage sources.

When a voltage pulse arrives at the end or termination of its respective transmission line its behaviour will depend on the boundary conditions at the node:

The reflection coefficient, Γ, is given by

$$\Gamma = \frac{R - Z_0}{R + Z_0} \tag{3.26}$$

Where R is the resistance the pulse is presented with at the termination. (open circuit: $R \to \infty \Rightarrow \Gamma = 1$, closed circuit: $R \to 0 \Rightarrow \Gamma = -1$, matched termination: $R = Z_0 \Rightarrow \Gamma = 0$).

In practice, there will be many, many of these scatterings taking place, in all directions (especially within a 3-D model). With simulations of increasing complexity, lines with different impedances will be necessary and the need for TL stubs will be often encountered. The simple equation above gives a basic impression of scattering at a simple termination of a differing impedance. However, with the added complexity a precise knowledge of the currents and voltages at each node is required.

Figure 3-4 shows the Thévenin equivalent circuit of a node containing a capacitive stub.

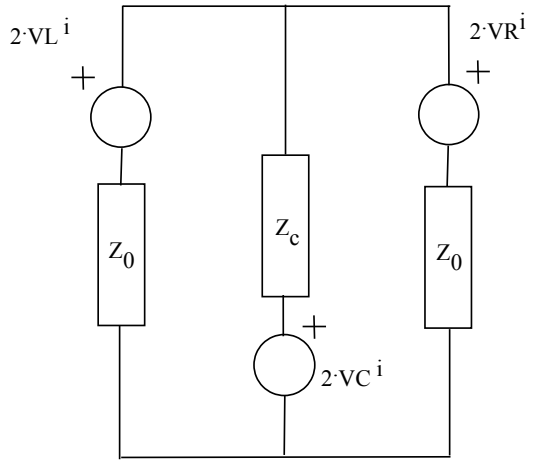

Figure 3-4 Thévenin equivalent circuit with the impedance of an open circuit stub at the centre of the node representing relative permittivity

The Thévenin circuit describes the pulses arriving at the node from neighbouring nodes and from the capacitive stub situated at its centre. At a particular time-step, k, the voltage across this particular node, $V(n, k)$, can be found using Millman's theorem [38]

$$V(n,k) = \frac{\frac{2 \cdot VL^i(n,k)}{Z_0} + \frac{2 \cdot VC^i(n,k)}{Z_c} + \frac{2 \cdot VR^i(n,k)}{Z_0}}{\frac{1}{Z_0} + \frac{1}{Z_c} + \frac{1}{Z_0}} \tag{3.27}$$

where $VL^i(n,k)$ refers to an incoming voltage pulse from the left hand side, $VR^i(n,k)$ from the right hand side and $VC^i(n,k)$, a pulse arriving from the capacitive stub.

When the voltage at the node centre is obtained the reflected (scattered) pulses (superscript 'r') are easily found:

$$VL^r(n,k) = V_n(n,k) - VL^i(n,k) \tag{3.28}$$

$$VR^r(n,k) = V_n(n,k) - VR^i(n,k) \tag{3.29}$$

$$VC^r(n,k) = V_n(n,k) - VC^i(n,k) \tag{3.30}$$

3.1.3 The Connection Process:

For the pulse to propagate throughout the series of cells the pulse emanating from a cell must connect to its neighbour. This linkage of activity is termed the *connection* process. A reflected pulse, scattered in a particular direction will become the incident pulse at the next time-step. Hence, using the example above the connection process is achieved using

$$VL^i(n,k+1) = VR^r(n-1,k) \tag{3.31}$$

$$VL^i(n,k+1) = VR^r(n+1,k) \tag{3.32}$$

$$VC^i(n,k+1) = VC^r(n,k) \tag{3.33}$$

3.2 Three-Dimensional TLM:

A simple description of 1-D propagation along a line using 1-D TLM has been presented. The limitations are immediately evident; only a limited number of electromagnetic field components are represented. Also, the wire is separated from the environment preventing a real-time coupling between objects and surrounding fields. When a 3-D model is necessary, a General Symmetrical Condensed Node (GSCN) is used [41]. Such a node is able to model all electromagnetic components at a particular space-time coordinate while the extra addition of stubs allows for regions with increased permittivity, permeability and conductivity. First, consider the 3-D node representing free space. Figure 3-5 depicts the Symmetrical Condensed Node (SCN)[38]. Each of the six sides of the node accommodates two ports in which the respective pulses can enter and leave the node. The arrows at each port represent the polarisation of the pulse. The notation used to identify the ports can be a simple numbering as on the right hand side of Figure 3-5**.**

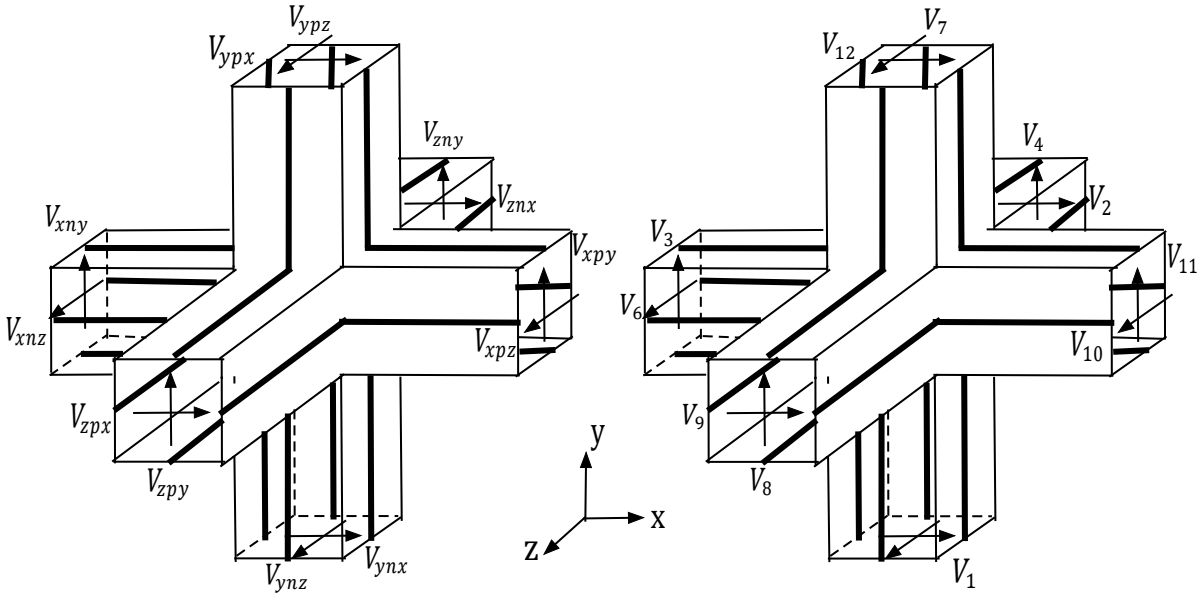

Figure 3-5 The Symmetrical Condensed Node (SCN). Two notations are demonstrated [38].

The node can be considered as the combination of the transmission line clusters shown in Figure 3-6 [40]

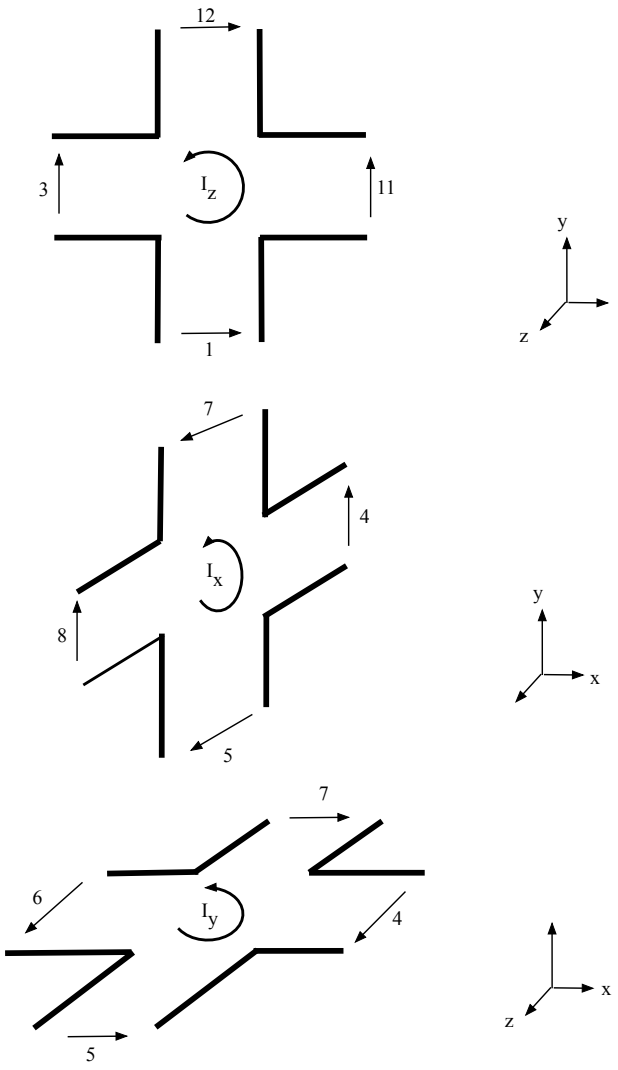

Figure 3-6 The three cluster arrangements that constitute the SCN [40].

The three dimensional nature of the node results in the need for a matrix description. In matrix form, the scattering can be summarised using

$$\boldsymbol{V^r}(k) = \boldsymbol{S}\boldsymbol{V^i}(k) \tag{3.34}$$

where the scattering matrix for the basic SCN is:

$$\mathbf{S} = 0.5\begin{bmatrix} 0 & 1 & 1 & 0 & 0 & 0 & 0 & 0 & 1 & 0 & -1 & 0 \\ 1 & 0 & 0 & 0 & 0 & 1 & 0 & 0 & 0 & -1 & 0 & 1 \\ 1 & 0 & 0 & 1 & 0 & 0 & 0 & 1 & 0 & 0 & 0 & -1 \\ 0 & 0 & 1 & 0 & 1 & 0 & -1 & 0 & 0 & 0 & 1 & 0 \\ 0 & 0 & 0 & 1 & 0 & 1 & 0 & -1 & 0 & 1 & 0 & 0 \\ 0 & 1 & 0 & 0 & 1 & 0 & 1 & 0 & -1 & 0 & 0 & 0 \\ 0 & 0 & 0 & -1 & 0 & 1 & 0 & 1 & 0 & 1 & 0 & 0 \\ 0 & 0 & 1 & 0 & -1 & 0 & 1 & 0 & 0 & 0 & 1 & 0 \\ 1 & 0 & 0 & 0 & 0 & -1 & 0 & 0 & 0 & 1 & 0 & 1 \\ 0 & -1 & 0 & 0 & 1 & 0 & 1 & 0 & 1 & 0 & 0 & 0 \\ -1 & 0 & 0 & 1 & 0 & 0 & 0 & 1 & 0 & 0 & 0 & 1 \\ 0 & 1 & -1 & 0 & 0 & 0 & 0 & 0 & 1 & 0 & 1 & 0 \end{bmatrix} \tag{3.35}$$

Describing the scattering / connection process using the numbered nodes can become unwieldy, especially when stubs are added to the node to account for conductance, relative permittivity, relative permeability etc. Instead, the notation used to describe the node on the left hand side of Figure 3-5 uses three indices. The first describes the direction of the pulse (*x*, *y* or *z*). The second refers to whether it approaches the node from a negative, *n* or positive direction, *p* relative to the node centre and the third index refers to the polarisation of the pulse (*x*, *y* or *z*). Using this notation and letting the superscripts *r, i* to refer to reflected and incident pulses respectively, the scattering for a GSCN can be described using just two equations [41]:

$$V_{inj}^{r} = V_j \pm I_k Z_{ij} - V_{ipj}^{i} \tag{3.36}$$

$$V_{ipj}^{r} = V_j \mp I_k Z_{ij} - V_{inj}^{i} \tag{3.37}$$

where for the upper equation: $(i,j,k) \in (x,y,z),(y,z,x),(z,x,y)$ and for the lower $(i,j,k) \in (x,z,y),(y,x,z),(z,y,x)$.

The equivalent node voltage across the node in the *i*th direction can be expressed as [41]

$$V_i = \frac{2Y_{ki}\left(V_{kni}^i + V_{kpi}^i\right) + 2Y_{ji}\left(V_{jni}^i + V_{jpi}^i\right) + 2Y_{oi}V_{oi}^i}{2\left(Y_{ki} + Y_{ji}\right) + Y_{oi} + G_{ei}} \tag{3.38}$$

where the inclusion of stubs to facilitate the addition of electric losses (conductance), G_{ei}, magnetic losses , R_{mi} as well as those used to add capacitance and inductance are included (o, s refer to open and short circuit stubs) and Y refers to the admittance of the transmission lines.

The loop current, I_i is given by [41]

$$I_i = \frac{2(V_{jpk}^i - V_{jnk}^i + V_{knj}^i - V_{kpj}^i - V_{si}^i)}{2\left(Z_{jk} + Z_{kj}\right) + Z_{si} + R_{mi}} \tag{3.39}$$

where $\{i,j,k\} \in \{x,y,z\}$ and $i \neq j,k$.

The scattered voltages reflected to stubs are simply [41]

$$V_{oi}^r = V_i - V_{oi}^i \tag{3.40}$$

$$V_{si}^r = I_i Z_{si} + V_{si}^i \tag{3.41}$$

where $i \in \{x,y,z\}$

These equations can be used to describe all electromagnetic activity at points within the mesh by finding the node voltages and loop currents and using

$$E_i = -V_i/\Delta i \tag{3.42}$$

$$H_i = I_i/\Delta i \tag{3.43}$$

3.2.1 Introducing relative permittivity, permeability to the 3-D SCN mesh.

In its basic state the 3-D SCN describes an x-directed, y-directed and z-directed capacitance for a small volume dl^3 (3.44). Typically, the primary dielectric being modelled is air. A 1-D node augmented to represent other media was demonstrated in section 3.1.1. When dealing with 3-D TLM the situation is the same albeit a little more involved.

The capacitance of an SCN cell representing free space, is given by

$$C_0 = \varepsilon_0 \frac{A}{d} = \varepsilon_0 \frac{\Delta l \Delta l}{\Delta l} = \varepsilon_0 \Delta l \tag{3.44}$$

Let the desired capacitance be C_χ where

$$C_\chi = C_0 \chi_e \tag{3.45}$$

Here, χ_e is the electric susceptibility. In terms of relative permittivity, is can be defined as

$$\chi_e = \varepsilon_r - 1 \tag{3.46}$$

Therefore, the desired capacitance can be written

$$C_\chi = \varepsilon_0(\varepsilon_r - 1)\Delta l \tag{3.47}$$

Then referring to (3.25) for the impedance of a stub we have [42]

$$Z_\chi = \frac{\Delta t}{2C_\chi} = \frac{\Delta l\sqrt{\mu_0\varepsilon_0}}{4\varepsilon_0(\varepsilon_r - 1)\Delta l} = \frac{\sqrt{\mu_0}}{4\varepsilon_0(\varepsilon_r - 1)} = \frac{Z_0}{4(\varepsilon_r - 1)} \tag{3.48}$$

Conductance can be added as a lumped resistance, Z_σ

$$Z_\sigma = \frac{1}{\sigma \Delta l} \tag{3.49}$$

The various impedances are easily added to the node voltage equations (3.38) and node current equations (3.39) allowing the respective fields to be found in such environments.

3.2.2 Propagation through a 3-D mesh.

Previously when dealing with an array of 1-D TLM nodes the speed of EM wave propagation was the same as the speed of pulse propagation along the TL segment. When working within a 3-D TLM mesh the two speeds no longer coincide. To understand this, consider a plane wave propagating through a mesh [38]. In particular, for an x-directed, *y*-polarised plane wave, port 3 must be excited on all nodes in the y-z plane (Figure 3-5). Referring to the scatter matrix (3.35) reveals that the only non-zero scattered pulses will be given by

$$V_1^r = V_4^r = V_8^r = -V_{12}^r = 0.5 \tag{3.50}$$

Figure 3-7 depicts the situation. Scattered pulses emerge perpendicularly to the original pulse with their polarisation as shown in the diagram. These pulses will become the incident pulses at the neighbouring nodes in the same y-z plane. Likewise, pulses will arrive at the node of interest (*x*, *y*, *z*), i.e.

$$\begin{aligned} V_1^i(k+1,x,y,z) &= V_{12}^r(k,x,y-1,z) = -0.5 \\ V_4^i(k+1,x,y,z) &= V_8^r(k,x,y,z-1) = 0.5 \\ V_8^i(k+1,x,y,z) &= V_4^r(k,x,y,z+1) = 0.5 \\ V_{12}^i(k+1,x,y,z) &= V_1^r(k,x,y+1,z) = 0.5 \end{aligned} \tag{3.51}$$

Again all other incident pulses are zero.

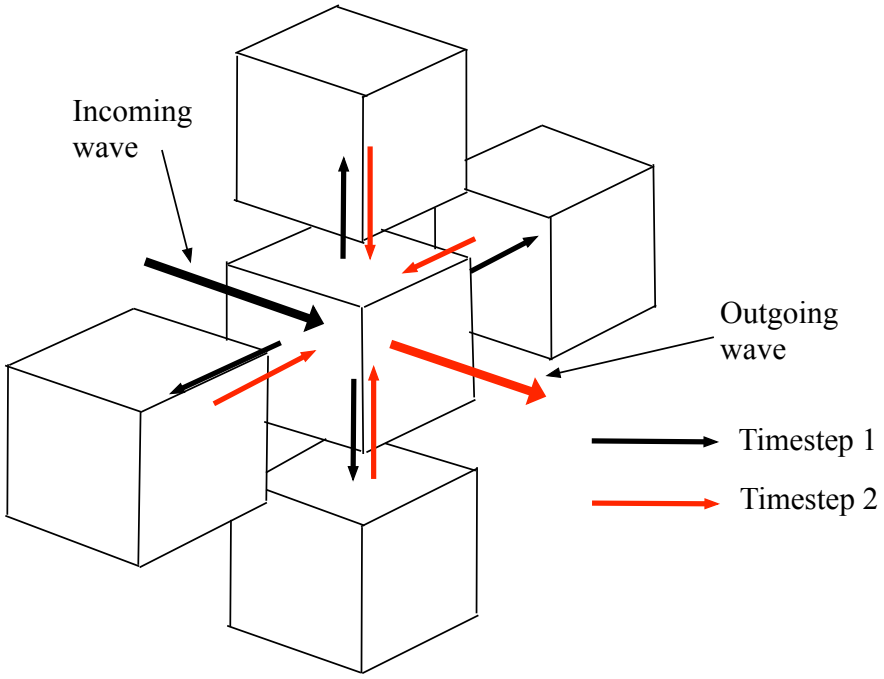

Figure 3-7 Propagation of a wave in a 3-D SCN mesh. The propagation takes place in two stages hence the speed of propagation on each TL segment must be twice the speed of light.

All these scatter in the node (x, y, z) in such a way that all amount to a pulse leaving the node at port 11, with magnitude of one. Therefore, the original pulse incident on the node (x, y, z) has left the node without dispersion in *two* time-steps:

$$\frac{\Delta x}{\Delta t} = 2v_p \tag{3.52}$$

or

$$v_{TLM} = 2v_p \tag{3.53}$$

where v_p is the speed of the wave in the given medium. In other words, the chosen speed on the TL segments that go to constitute the node must be twice the speed of electromagnetic wave propagation in the given background medium.

3.3 Introducing wires to the mesh.

Many simulations require the introduction of metallic objects to the mesh. For example, this thesis is mostly concerned with the simulation of coupling between electromagnetic fields and wires. To introduce, say a wire, to the mesh using the GSCN there are a couple of options available. One is to make a cell become perfectly conducting. This can be achieved by converting the cell into short-circuit node (Figure 3-8). Once a cell is chosen to be a short-circuit node, all pulses incident on that node are reflected back from where they originally came from with a reflection coefficient of -1; thus assuming the behaviour of a perfect conductor. Alternatively, we could add a stub to the cell of near infinite conductance. This will create the same effect.

However, there is a limitation when using differential numerical methods such as TLM. The wire diameter is constrained by the resolution of the mesh or vice versa. For example, if the resolution of the mesh is chosen to accommodate a fine wire then the overall problem space may have to be resolved to a much finer mesh than would be necessary if the wire was not included. This will place great demands on the computational hardware as well as lengthening the time required to reach a solution. To overcome this limitation, the Embedded-Wire Symmetrical Condensed Node (EW-SCN) is used [43]. For brevity, the node will be referred to as the the Embedded Wire Node (EWN), herein.

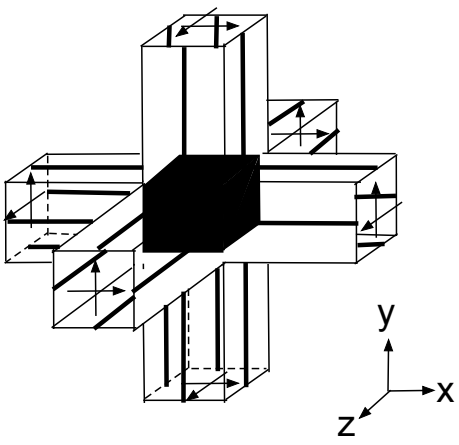

Figure 3-8 The short-circuit SCN: all pulses incident on the node are reflected away from the cell [27].

3.3.1 The Embedded Wire Node (EWN)

The node can be considered as a typical SCN but, as the name suggests with a wire embedded through its centre parallel to one of its faces Figure 3-9

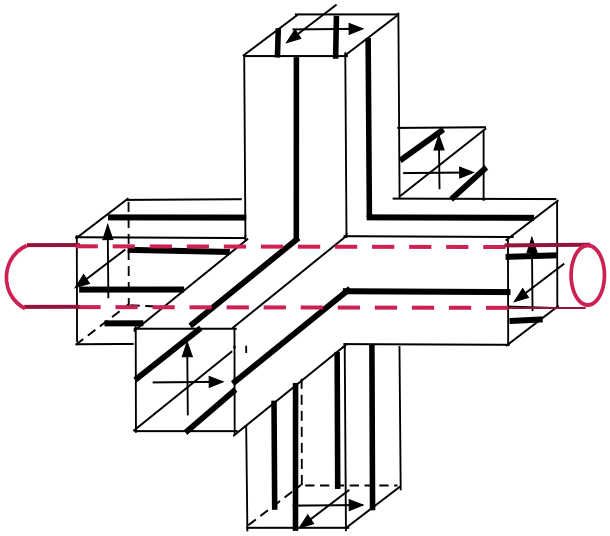

Figure 3-9 The position of the embedded-wire within the SCN.

Any extra capacitance and inductance the wire brings to the node is accounted for via a separate network of TL link-lines and TL stubs integrated into the SCN architecture. This additional wire network communicates with the basic SCN network and vice versa by means of an ideal transformer to correctly represent the coupling between field and wire. Once this is achieved a fully self-consistent simulation is available. To enable this, the two networks are linked via an ideal transformer.

Consider an *x*-directed wire embedded within an SCN node. The only relevant sub-circuit of the SCN that will couple with the wire are those that include the transmission lines with ports 1, 2, 9 and 12 (Figure 3-5) i.e. the lines that correspond to *x*-polarized waves. Figure 3-10 gives the Thévenin equivalent for such a sub-circuit.

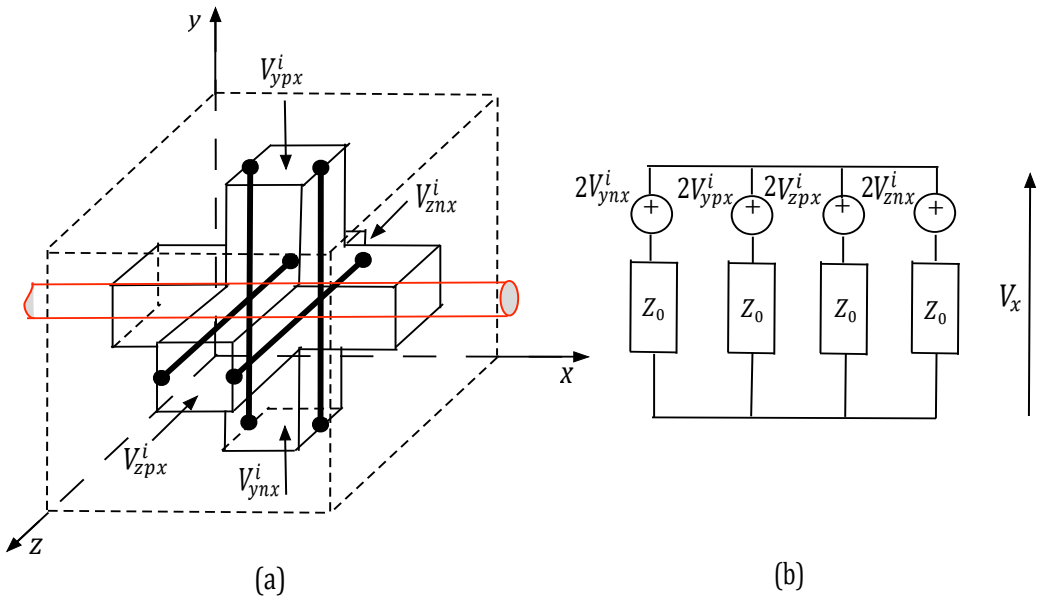

Figure 3-10 (a) The sub-circuit of the SCN coupled to the embedded wire (b) The Thévenin equivalent of the sub-circuit.

The equivalent impedance of such a network is given by

$$Z_x = (Y_1 + Y_2 + Y_9 + Y_{12})^{-1} \tag{3.54}$$

with the voltage across the sub-circuit network given by equation (3.38).

The wire introduced to the node will add distributed capacitance, C_{d_wi} and distributed inductance, L_{d_wi} to the node. These values should be representative of a wire in free space, with a reference at infinity (or a nearby ground). There are a number of ways to calculate these values. Trenkic et al [41] introduce a fictitious radius, r_{cf}, or r_{lf} , based on the cell size in which the wire is positioned to represent the cell boundary for capacitance and inductance calculations, respectively, reducing the problem to that of a coaxial transmission line.

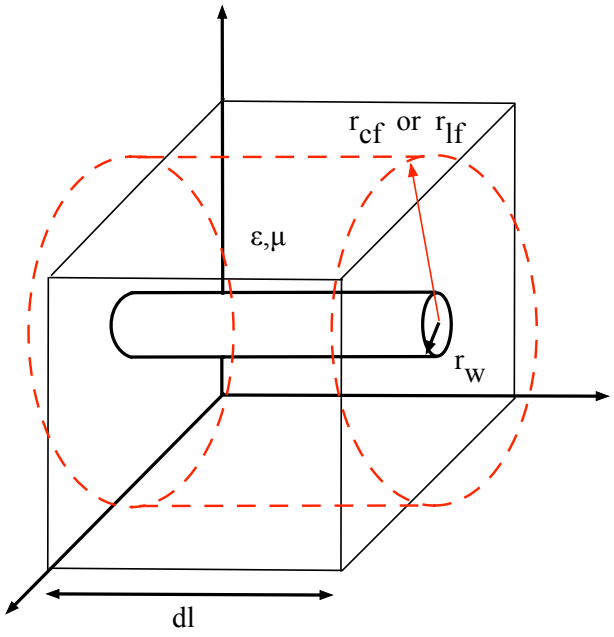

Figure 3-11 The cell can be approximated as a cylinder to which a fictitious radius can be assigned. This allows a capacitance or inductance value to be determined.

The radii are adjusted in such a way as to calculate the capacitance as if the reference is at infinity using dimensionless constants based on empirical results and are adjusted depending on whether or not the wire runs parallel to other metallic objects. Once equipped with these values the capacitance and inductance of the wire can be easily found

$$C_{d\_wi} + \frac{2\pi\varepsilon}{\ln(r_{cf}/r_w)} \tag{3.55}$$

$$L_{d\_wi} = \frac{\mu}{2\pi}\ln(r_{lf}/r_w) \tag{3.56}$$

where r_w is the radius of the wire.

This method has the clear disadvantage of the need for different radii to calculate the capacitance and inductance. Paul et al [44][45] provide an alternative approach:

The distributed wire capacitance and inductance can simply be written as

$$C_{d\_wi} = \frac{\varepsilon_0}{k_{wi}} \tag{3.57}$$

$$L_{d\_wi} = \mu_0 k_{wi} \tag{3.58}$$

where k_{wi} is a dimensionless geometrical factor.

The characteristic impedance , Z_{wi}, of the wire is then given by

$$Z_{wi} = \sqrt{\frac{L_{wi}}{C_{wi}}} = \eta_0 k_{wi} = \left(\frac{\eta_0}{2\pi}\right) \ln\left[\frac{1.08\Delta l}{2r_w}\right] \tag{3.59}$$

where the RHS of (3.57) is the equation for the impedance of a wire of radius, r_w, situated in the centre of a square metal exterior with side length, Δl (the cell boundary).

Hence the constant is given by,

$$k_{wi} = \left(\frac{1}{2\pi}\right) \ln\left[\frac{1.08\Delta l}{2r_w}\right] \tag{3.60}$$

This approach needs no consideration of nearby conductors and removes the need for differing return radii. One should note, however, this approximation is limited to wires that are thin compared to the cell size i.e. $20\, r_w \leq \Delta l$. (Note, the opposite problem to the original fine-wire issues).

Once the necessary capacitance and inductance to be added to the node is found, an equivalent transmission-line wire network can be constructed. The usual considerations such as the need for synchronization with the rest of the mesh apply.

The arrangement of transmission lines that constitute the separate network are somewhat similar to that used when describing the 1-D TLM approach; after all this is a 1-D wire embedded in a 3-D meshwork. It should be noted that any arrangement of link lines and stubs is acceptable provided the synchronization and correct capacitance and inductance is met.

Here, the capacitance will be introduced as two link lines just as [42]; their impedance representing $C_{d\_wi}/2$. The main reason for sharing the capacitance in this way is it allows wire bends to be situated within the node e.g. half the wire may couple with the sub-circuit of the SCN representing an x-polarized field whilst the other half couples with the y-directed sub-circuit. However, currently a straight wire will be incorporated.

Rarely will the link-lines model both the capacitance and the inductance precisely. As all the capacitance is added via the link-lines, there will be a need to introduce a TL to remedy a shortfall in the inductance, in the form of a stub. Incorporating a short-circuit stub to each of the wire segments within the node should account for any discrepancy. To find this deficit first the link line impedance must be found: A half segment of length, $\Delta i/2$ has a transit time, $\tau = \Delta t/2$ and therefore (cf. (3.25)) [43] .

$$Z_{wi} = \frac{\Delta t/2}{C_{d\_wi}\Delta i/2} = \frac{\Delta t}{C_{d\_wi}\Delta i} \tag{3.61}$$

Half the necessary wire inductance must be shared between the inductance provided by the link-line described above and the addition of a stub of impedance Z_{si} i.e.

$$L_{d\_wi}\frac{\Delta i}{2} = Z_{wi}\frac{\Delta t}{2} + Z_{si}\frac{\Delta t}{4} \tag{3.62}$$

However, one is also required to take into account the inductance of the four link lines parallel to the wire, something that was originally overlooked and later discovered [45].

The inductance provided by the link lines is simply

$$L_{link} = \frac{\Delta t\, Z_0}{4 \cdot 2} \tag{3.63}$$

Therefore, the impedance of the stub is required to be

$$Z_{si} = \frac{2}{\Delta t}\left(L_{d\_wi}\Delta i - Z_{wi}\Delta t - \frac{\Delta t Z_0}{4}\right) \tag{3.64}$$

Figure 3-12 demonstrates the resulting circuit representing the subsequent EWN.

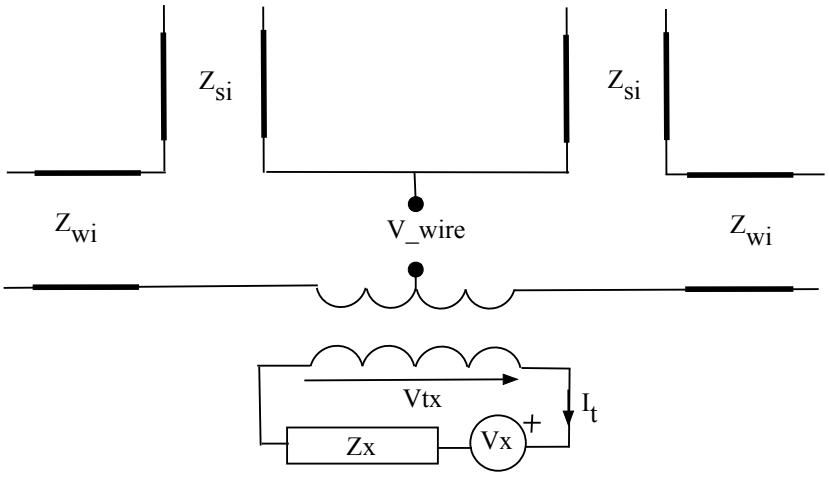

Figure 3-12 TL representation of the EWN. The upper circuit represents the wire while the lower circuit represents the relevant SCN sub-circuit.

As alluded to previously, the ideal transformer acts as a means of coupling the corresponding field (the sub-circuit SCN) and the wire. In particular, the field coupling to the wire is provided as a voltage source, V_{tx}. The wire to field coupling is represented as a current source, I_{tx} on the SCN sub-circuit [41]. Therefore, the self-consistent nature of TLM is maintained within the EWN.

All the above can be summarized with a Thévènin Equivalent Circuit (figure 3.11). When considering straight wires the transformer can be ignored. Then the node voltage is found simply by applying Millman's theorem as for the 1-D case [41].

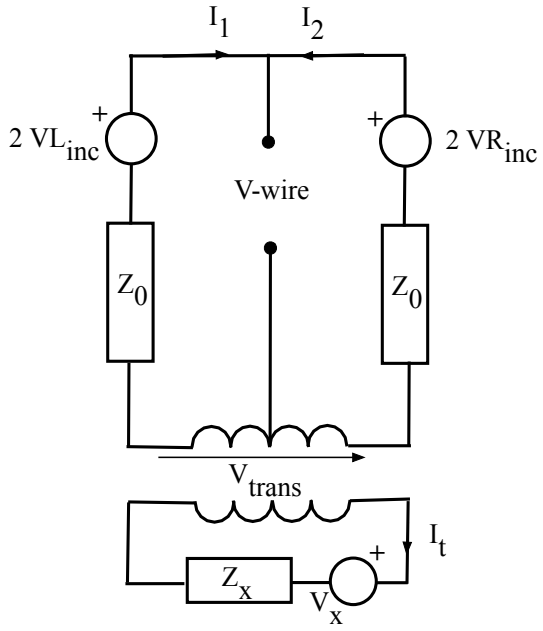

Figure 3-13 The Thévenin equivalent of the EWN.

3.4 Using the node output values to find other useful information.

The node voltages (electric fields) and node currents (magnetic fields) can be used to find other relevant information.

3.4.1 Electric Current

The currents flowing on conducting bodies is often required. This is easily obtained when using the EWN approach, but if a wire is represented by a string of short-circuited SCN nodes, no explicit current value is available.

In such circumstances, one option is to utilise the voltages incident on the conductive surface. For a short-circuit node with resistance R, the current is best visualised using the applicable Thévenin equivalent circuit (Figure 3-14).

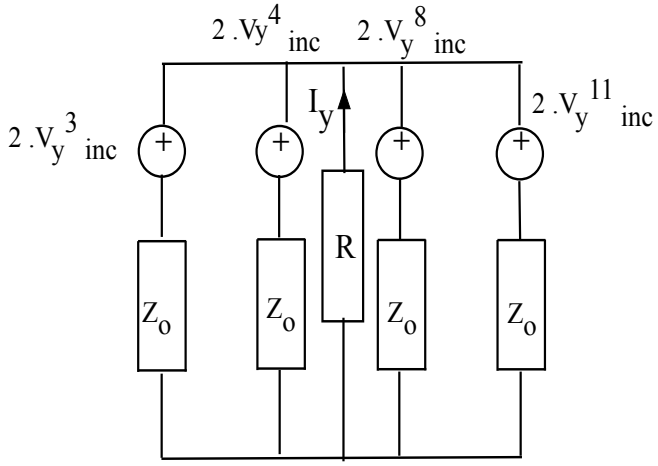

Figure 3-14 Thévenin equivalent circuit representing the *y*-directed current flowing through a short-circuited 3-D SCN node.

Referring to Figure 3-14 the current can easily be deduced using Millman's (parallel generator) theorem:

$$I_y = -2\frac{\left(V^3_{y-\mathrm{inc}} + V^4_{y-\mathrm{inc}} + V^8_{y-\mathrm{inc}} + V^{11}_{y-\mathrm{inc}}\right)}{4Z + R} \tag{3.65}$$

Alternatively, the current flowing along a *y*-directed wire can be calculated using Ampère's Law; using the curl of the magnetic field about the wire (Figure 3-15):

$$I = \oint \boldsymbol{H} \cdot \mathrm{d}\boldsymbol{l} \tag{3.66}$$

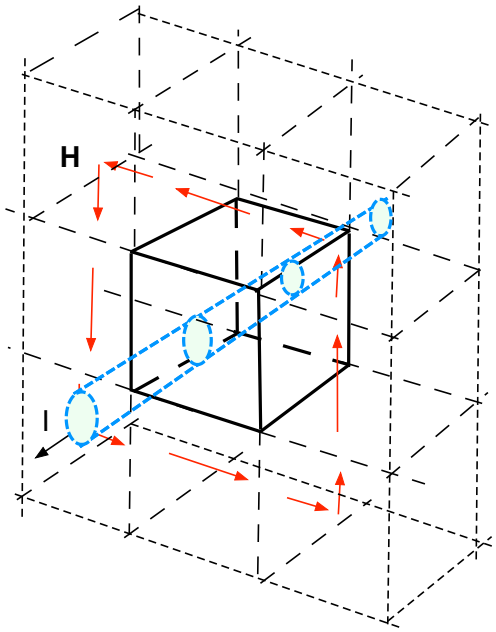

Figure 3-15. Using the closed path of magnetic field about a wire to calculate current (EWN)[40].

Both these example also demonstrate means of exciting wires within the mesh.

3.4.2 Electric charge

When dealing with corona, electric charge generation is also an important consideration. The aforementioned q-V characteristics represent the corona development. Also, the charge on the wire provides a simple means of obtaining the electric field on the surface of the wire. There are various means of finding the charge on a conductive body:

3.4.2.1 Gauss' law.

The applicable voltages at cells adjacent to the conductive body can give the charge on the conductor using Gauss' law (Figure 3-16).

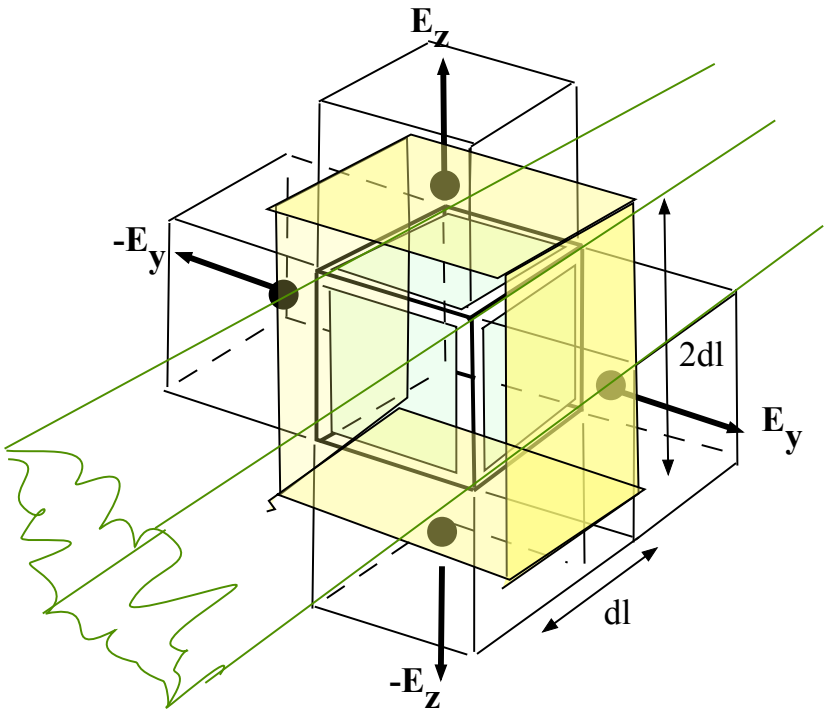

Figure 3-16 Using the relevant field values (node voltages) about a conductor to obtain charge (Gauss' Law)

Assuming a radial field, a closed surface can be drawn around the node as shown. The sum of the field flowing through the 'closed' surface allows the charge on the conductor, or in general the total charge enclosed within the surface, Q_{encl}, to be calculated:

$$Q_{wire} = \varepsilon_0 \oint \boldsymbol{E} \cdot \mathbf{d}\boldsymbol{A}$$

$$Q_{wire} = -\varepsilon_0 \frac{(V_{yl} + V_{yr} + V_{za} + V_{zb})}{dl} \cdot 2dl^2 \qquad (3.67)$$

where the additional subscripts 'l', 'r', 'a', 'b', refer to left of, right of, above and below the node whose contained charge is required, respectively.

3.4.2.2 Displacement Field.

Alternatively, the displacement field can be utilised. Essentially, the time derivative of the electric field at a point within the mesh gives the displacement current density there. For the node in Figure 3-17, the radial displacement current density passing through the surface is required. (for the purposes of a cuboidal node, the field normal to the surface is used).

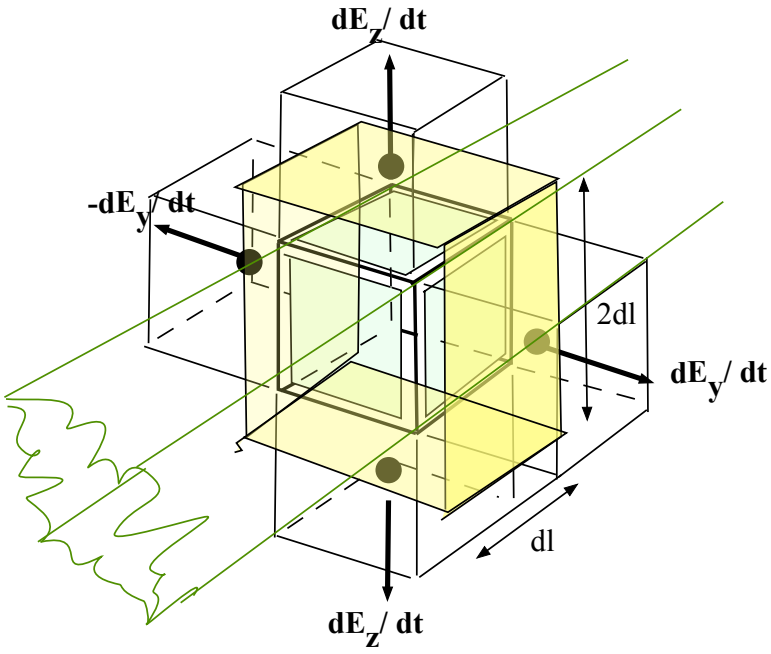

Figure 3-17. Using the radial displacement field from the conductor to obtain its charge.

$$\boldsymbol{J}_{r-disp} = \varepsilon_0 \frac{\partial E_r}{\partial t} \tag{3.68}$$

Hence, the current through the given surface can be obtained.

$$I_r = 4 \cdot \boldsymbol{J}_{r-disp} \cdot 2dl^2$$

Once the displacement current passing through the surface is found, the corresponding charge is given by (*k* refers to the particular time-step)

$$Q_{wire}(k) = Q_{wire}(k-1) + \frac{(I_r(k-1) + I_r(k))}{\Delta t} \tag{3.69}$$

3.4.2.3 Node Capacitance (EWN).

If an embedded wire node is being used to incorporate a wire within the mesh, the local capacitance(per-unit length) the wire introduces to a node, C_{EWN} can be used to find the charge. This is the capacitance calculated using one of the techniques encountered earlier (3.53), (3.55). Then, the wire charge per unit length, Q is found simply using

$$Q_{wire} = C_{\mathrm{EWN}} \cdot V_{\mathrm{EWN}} \tag{3.70}$$

Where V_{EWN} is the potential difference between the wire and the reference (fictitious radius of the cell).

Of course, if a coax is being modelled, the total capacitance could be used in a similar manner.

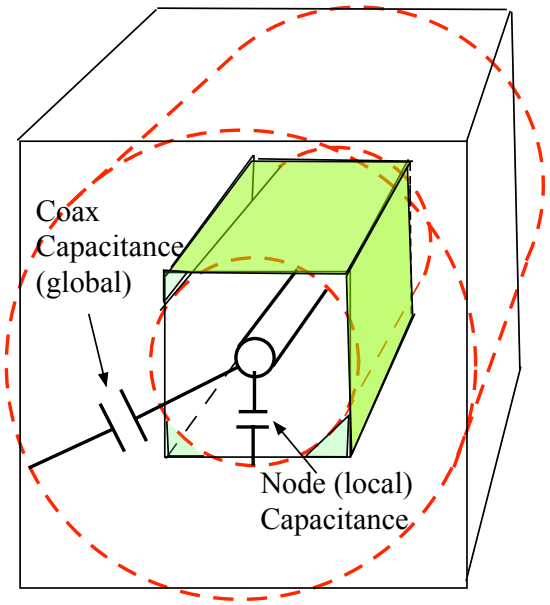

Figure 3-18. Using capacitance to find the charge (per unit length) of a wire.

Once the charge on the conductor is found using any of the above techniques, the radial electric field on the wire surface, $E_{\text{r-surf}}$, is found using

$$E_{\text{r-surf}} = \frac{Q_{wire}}{2\pi\varepsilon_0 R_{\text{wire}}} \tag{3.71}$$

In a conductive environment, e.g. buried wire, the shunt current leaving the wire can also be used to find the field on the surface of the electrode:

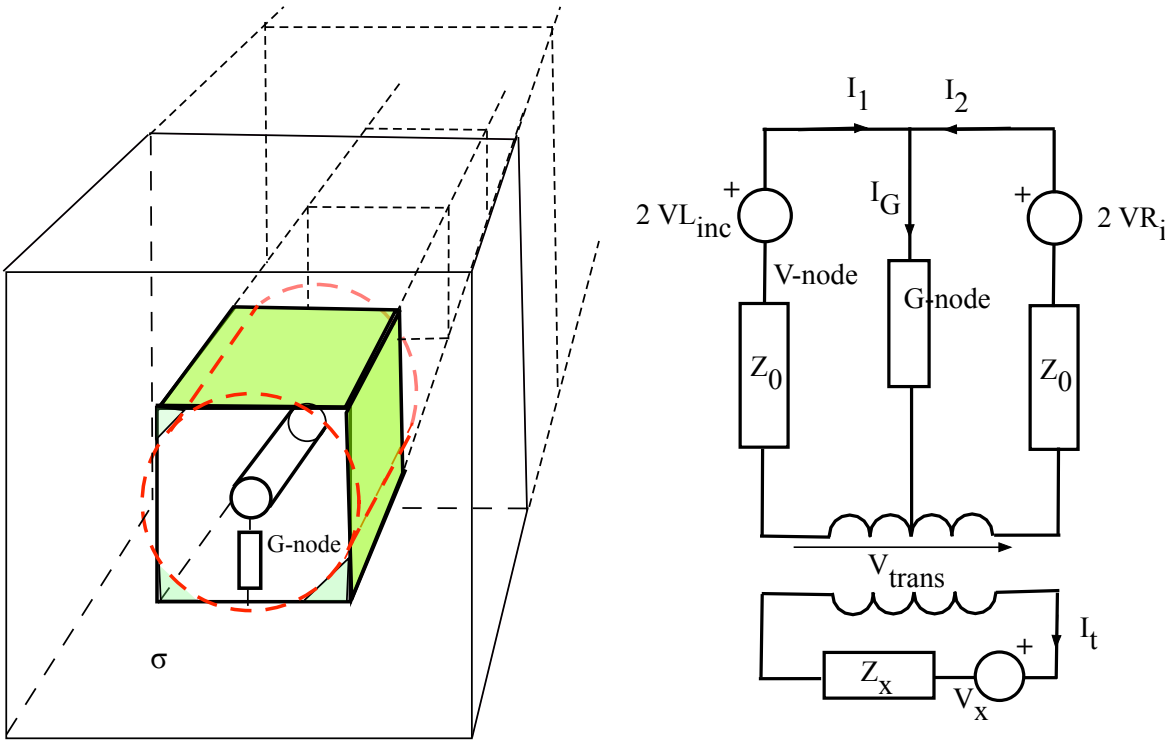

Figure 3-19. (a) EWN wire node adapted for conductive environment, (b) Thévenin equivalent of the EWN.

The shunt current, I_G, is easily deducted from the current on the limbs, I_1, I_2:

$$I_G = I_2 - I_1 \tag{3.72}$$

Then using $⊟ \sigma E$,

$$E_{\text{r-surf}} = \frac{I_G}{\sigma \cdot 2\pi R_{wire} dl} \tag{3.73}$$

3.5 Summary

The Transmission Line Modelling (Matrix) Method (TLM) uses circuit theory to solve complex electromagnetic environments. The region is discretized into mesh of transmission lines, joined by nodes, and the equivalences between field values and voltages, currents discovered by comparing the telegraphers (transmission line) equations and Maxwell's equations allow the region to be solved from an electromagnetic field perspective. Current and voltage pulses travel from one node to the next via a scattering procedure; the scattering being dependent on the impedance of the transmission lines.

The General Symmetrical Condensed Node (GSCN) is able to represent all orthogonal field components i.e. represent field propagation in a 3-D environment. Typically, the basic mesh/node the majority medium, usually air. Other media are then represented by introducing stubs to such nodes to account for extra capacitance (relative permittivity), inductance (relative permeability), conductance and resistance as required.

Although the GSCN can perform such duties, the introduction of fine wires to the mesh can mean a higher resolution throughout the mesh and therefore can exhaust valuable computing power. To overcome this issue, The Embedded Wire Node (EWN) is used to incorporate wires within a mesh. The EWN contains a separate network of transmission lines representing the additional capacitance, conductance, inductance and resistance that the wire introduces to the GSCN. The network communicates with the GSCN via an ideal transformer allowing a self consistent interaction between the wire and outside field.

In essence, TLM is a very versatile modelling technique. The technique is very suitable for non-linear or inhomogeneous environments as conditions are allowed to change at each solver update.

Chapter 4 Modelling the Effects of Corona on Coupled Transients.

The previous chapters have established:

- A nuclear explosion can generate a high-energy Electromagnetic Pulse capable of coupling to wires leading to hazardous consequences. Not only is the energy within the source region capable of such ill-effects but an EMP can be radiated much greater distances provided conditions are adequate (source region asymmetry). Hence, the radius of potential disruption extends many kilometres outside the source region. Such a waveform can incapacitate communication networks or power lines rendering an establishment or even a city impotent.

- Wire voltages, exceeding the breakdown threshold, can result in the breakdown of the dielectric surrounding the wire (e.g. air, soil) such that the signal propagating on the wire will be distorted. The surrounding medium becomes more conductive over time and energy losses ensue. The subsequent distortions are an important consideration when trying to mitigate against the EMP.

- Transmission-Line Modelling (TLM) can provide a suitable way of solving the electromagnetic fields resulting from such phenomena, providing a real-time, self-consistent depiction of events about the wire such that the distortions that are imposed on the waveform are depicted correctly. As its foundations lie in the solving of Maxwell's Equations from a differential perspective (as opposed to an integral approach), events local to the wire are suitably monitored.

The following now attempts to describe the various ways in which the advent and continuation of corona discharge around a causative wire can be introduced to the TLM framework as described in chapter 3.

First a knowledge of the corona related parameters that are subject to change is necessary as introduced in chapter 2.

4.1 Distortions on propagating waveforms due to electrical breakdown.

During electrical breakdown, in particular corona discharge development of a space charge around the wire is produced. Streamers emanate from the wire, maintained by currents either from the surrounding air (positive corona) or from the wire itself (via the conductive channels of the streamer). Both result in charge increasing on the wire for a given voltage. Hence, an increase in capacitance can be described. The relevance of free space charge accumulating around the wire undergoing corona become apparent around the 1920-30's [46]. Gardner, [47] and Boehne [48] discussed corona as a cylindrical sheath around the conductor whose radius increased with voltage and hypothesized that this could be modelled as an increase in capacitance. This was supported by the suggestion the distortions were proportional to the distance the surges had travelled [49].

As laboratory equipment improved the use of capacitance to describe experimental data made available from an experiment conducted in the US in 1954 was investigated [50] [51]. The results of such experiments can be neatly summarised using q-V graphs linking the increase in charge to applied voltage. Figure 4-1 provides a simple example of such a curve. The capacitance of the system is given by the gradient of the curve. It is evident from the graph that prior to the breakdown voltage, V_b being reached, the capacitance of the arrangement is

simply the characteristic capacitance of the wire. As the breakdown voltage is exceeded, a non-linear deviation from this capacitance value emerges. Once the peak voltage is reached the graph demonstrates a return to the original line capacitance although phenomena such as back corona can result in variations from the line capacitance post peak. This is described in greater detail later.

Such curves are useful as not only do they provide a quantitative insight into the development of corona but also allow comparisons between experiment and simulation. Other interesting features of the changes attributable to the corona can be gleaned from the graph. For example, the area beneath the curve represents the energy lost to the corona and indeed initial attempts to describe the distortions in propagation were based around such energy losses [49].

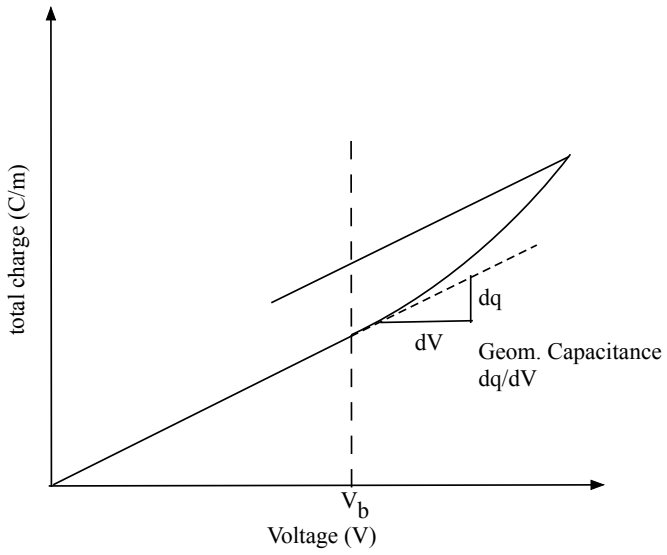

Figure 4-1 A typical q-V characteristic describing the relation between total charge (q) and applied voltage (V) on a wire. A deviation from the characteristic capacitance of the line is evident once the breakdown voltage (Vb) is exceeded.

Thus a dynamic capacitance approach to corona development became the traditional method of recreating such effects [51][52][53][54]. However, dynamic changes to other transmission line parameters can also be used to recreate such effects. The ionisation of the medium

represents a non-linear increase in conductivity in the wire vicinity. This change is exploited by Thang et al [55] and in soil (Gazzana, [56]).

A time varying corona charge also defines a corona current. This provides another alternative method of representing corona [57]. Before discussing these approaches in greater detail it is worth considering how changes in these parameters can create these distortions on a corona inducing waveform.

Wagner and Lloyd [51] provided a detailed paper on the relationship between the imposed distortions and corona inception relating the increase in capacitance and the distortions using the experimental data taken from the Tidd power plant as inspiration[50]. A voltage surge was applied to a matched line approximately 2222 m in length ignoring for sag. The wire had a radius of 0.927 inches (0.024 m). Figure 4-2 shows some of the actual results of the experiment. The graphs A, B, C and D represent the voltage profile against time, taken at successive points along the power line; 0 ft. (0m), 2040 ft. (622 m), 4200 ft. (1280 m) and 7290 ft. (2222 m) respectively.

Two notable features are evident. First, a wedge is formed at the anterior side of the waveform. The inferior edge of the wedge is found to correspond with the breakdown threshold of the wire. Second, an overall attenuation of the waveform occurs. Both these features increase with distance.

To understand how capacitance can explain such effects consider the equation for propagation speed, v, along a transmission line in terms of inductance, $L_{d,}$ and capacitance, C_d.

$$v = \frac{1}{\sqrt{L_d C_d}} \tag{4.1}$$

The individual voltage components, v_c, can be considered. Assuming these values above the threshold are affected by an increase in capacitance, ΔC_d, then (4.1) can be represented by [51]

$$v_c = \sqrt{\frac{1}{L_d(C_d + \Delta C_d)}} = v_L \sqrt{\frac{1}{1 + (\Delta C_d / C_d)}} \tag{4.2}$$

Where v_L, is the speed of the components under normal (no corona) conditions.

Equation (4.2) suggests the speed of voltage components above the threshold are slowed down or retarded compared to those unaffected.

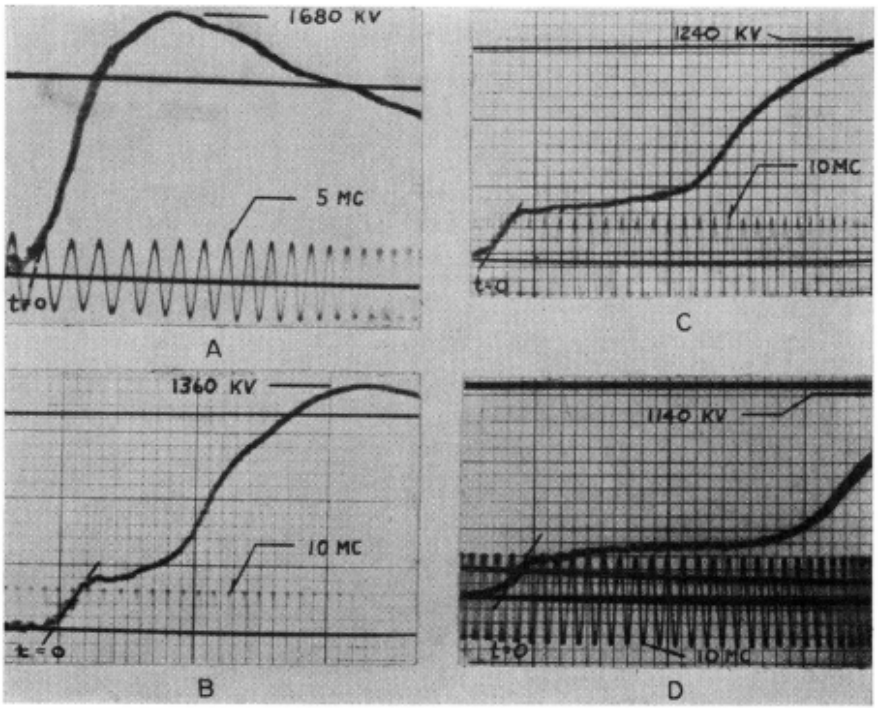

Figure 4-2 Distortions found experimentally on a propagating waveform. Readings taken at various points along the power line (sequentially from A to D) [50].

The wedge that develops on the graphs can be attributed to a delay in those voltage components above the threshold i.e. they appear at later times. For a particular component, a delay-per-distance travelled, $\Delta T/d$, can be assigned. This can be related to the increase in capacitance, ΔC_d, on the line using (4.3) as depicted in Figure 4-3 [51].

$$\frac{\Delta T}{d} = \frac{1}{v_L}\left[\sqrt{1 + \frac{\Delta C_d}{C_d}} - 1\right] \tag{4.3}$$

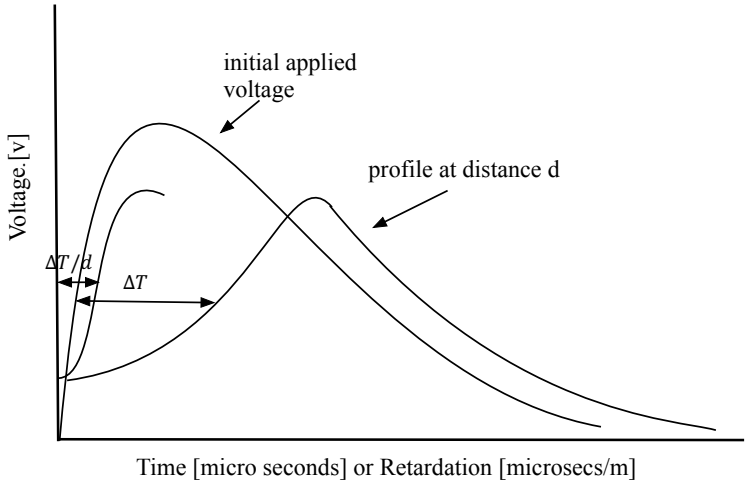

Figure 4-3 Simple diagram showing the typical distortions expected during corona. A retardation (delay per distance travelled) can be assigned to voltage components above the breakdown voltage threshold [51].

4.2 The Choice and Magnitude of Corona Parameter to Recreate Corona Effects.

Many approaches to quantify the time-varying parameters related to corona development have been attempted over the years. One very basic approach involves is to let the radial extension of the space charge amount to a new conductor radius value [48]. Valazquez and Mukhedkar [58] applied this method to a grounding rod in soil. In their model the radius is used to change all the transmission line parameters.

The radial extension can be determined by monitoring field values about the wire. Figure 4-4 demonstrates the concept. If the wire surface field exceeds the breakdown threshold, then the space charge extends until the breakdown field is met. (Note, in reality, once the breakdown threshold has been breached the space charge is assumed to extend to where the critical field for streamer propagation, E_c, is reached. However, this would lead to sudden and greater increase in the conductor radius than necessary). The method appears to lack rigour from a physical standpoint. If a new conductor radius is allowed to represent the radius of the corona sheath then theoretically, capacitance would increase whilst a corresponding decrease in the inductance simultaneously. Hence, based on the discussion regarding retardation of the voltage components above threshold, the changes would result in no change in voltage component speed. Hence, if this approach is applied to a wire in air, only the capacitance and/or conductance should be changed. However, the conductance this method would introduce to the model is much greater than that of the corona sheath.

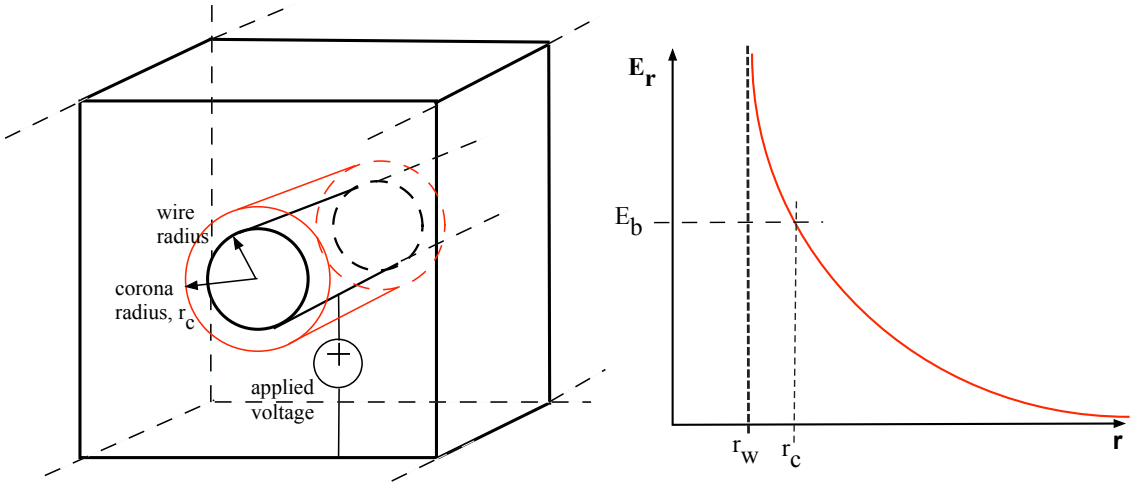

Figure 4-4 (a) corona development around a wire modelled as a radial extension of the conductor (b) relation to critical breakdown field, E_b.

Instead, the supplementary capacitance needed to represent the corona is usually found phenomenologically. If a q-V curve is established experimentally, then the increase in capacitance is easily deduced. Of course, the capacitance is non-linear, so a single value of

capacitance would be an approximation. Figure 4-5 presents a circuit analogue for a section of transmission line with the addition of a fixed capacitance, ΔC, above the threshold (V_B).

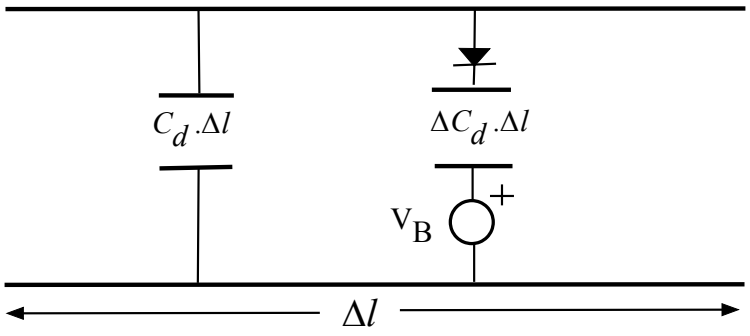

Figure 4-5 Transmission line graphic with the additional capacitance added when line voltage exceeds a given threshold

The associated q-V would appear as shown in Figure 4-6.

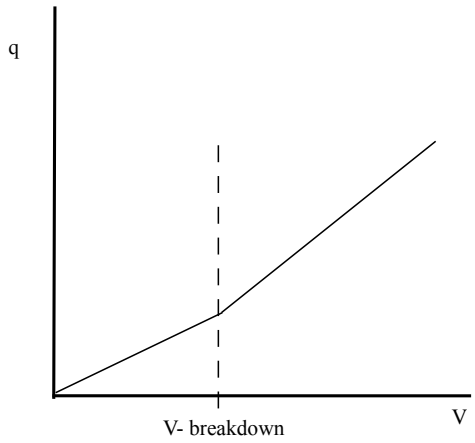

Figure 4-6 A linear capacitance is added when the line is represented as in figure 4.5.

A slightly more realistic depiction of events could be achieved by adding another fixed capacitance at a higher threshold (V_{B2}) as in Figure 4-7.

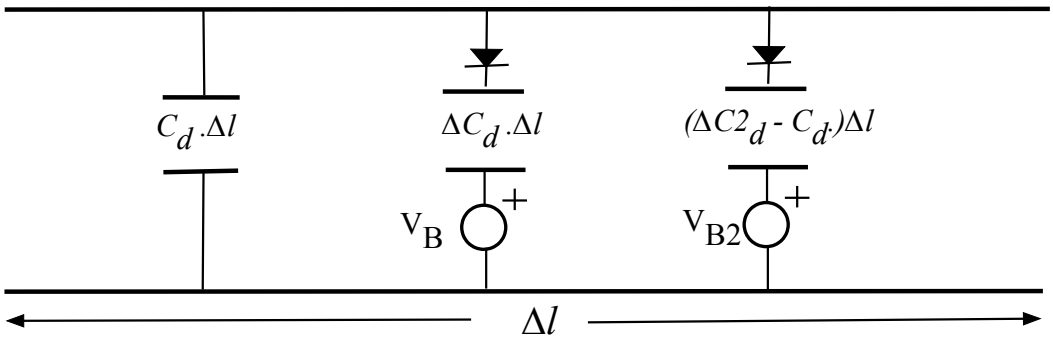

Figure 4-7 introduction of a second addition conductance at a higher threshold

Alternatively, a closer representation can be achieved using more capacitances at higher threshold voltages or introducing a non-linear equation relating additional capacitance to a particular voltage value above the threshold.

One such example is provided by Christopoulos [53]. He uses a 1-D TLM simulation with the inclusion of additional corona-related capacitance to recreate the distortions obtained in the Tidd experiments already alluded to [50]. Hence, the line is excited with a bi-exponential waveform similar to the source used in the experiments (and of the form typically encountered during a lightning strike). The paper uses parameters from a similar investigation by Kudran and Shih [54] who decided a fixed capacitance of 5.13 pF/m was suitable. The segment size, Δl, was set at 8.25m meaning a corona capacitance, $\Delta C = 42.3$ pF as soon as the voltage threshold, V_b (set at 386 kV), is exceeded. This remains provided the line voltage is above threshold and rising. Alternatively, an expression as shown in equation (4.4) can be used to describe the additional capacitance.

$$\Delta C = 42.3[1 - \exp(386\text{-V(n)})/50] \qquad [pF] \qquad (4.4)$$

This will act to smooth the transition to the value of 42.3 pF as the line voltage approaches the threshold value up and until a few hundred kilovolts above.

This additional capacitance is added as a stub as described in chapter 3.

Figure 4-8 demonstrates the Thévenin equivalent circuit of the 1-D TLM node used to simulate the effect.

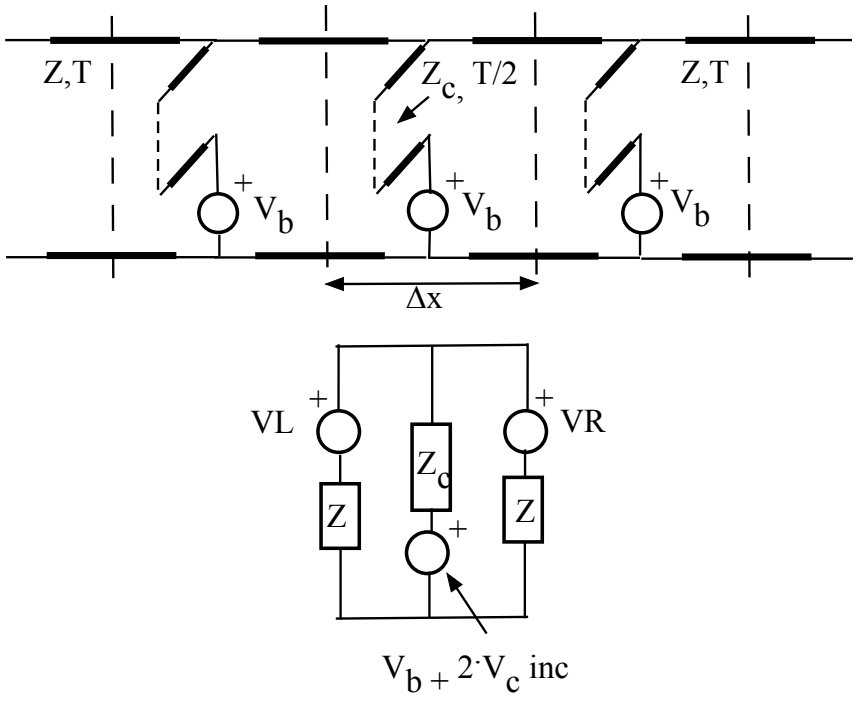

Figure 4-8 Top: 1D transmission line used to recreate corona effects. Below: Thévenin equivalent circuit used in a 1-D TLM node in the Christopoulos simulation (Z=695Ω, V_b = 386 kV) [53]

Figure 4-9 replicates the results obtained from the simulation using 1-D TLM. The segment length used was 4.12m, with a time step duration, Δt, of 0.02 μs. This equates to a propagation speed of 2.06×10^{8}m/s. Although not made explicit in his paper, the line capacitance can easily be calculated from the given parameters:

$$C_{seg} = \frac{\Delta t}{Z} \tag{4.5}$$

and is found to be 2.87×10^{-11}F. Substituting these values into (4.2) first predicts the speed of those voltage components above the threshold value for breakdown of 1.57×10^{8}m/s. Further, a retardation can be calculated using the given values in (4.3). This is found to be 1.54×10^{-9} s/m.

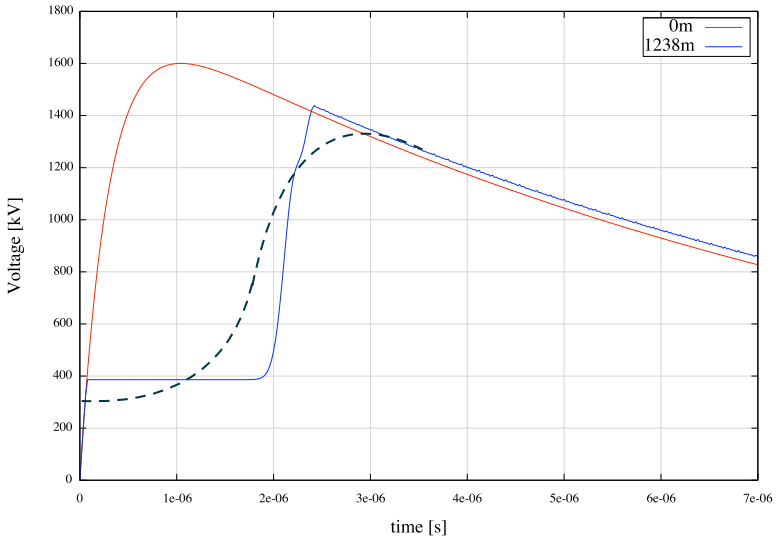

Figure 4-9 Corona related distortions imparted on a bi-exponential waveform propagating on a wire undergoing corona using the 1-D TLM node suggested by Christopoulos [53].Dotted line represents experimental results obtained by Wagner et al [50]

The characteristic wedge is immediately evident. Note there is decent agreement with the experimental results [50]. Figure shows the retardation found using the 1-D TLM model and the expected value found analytically. The two correlate very closely (1.54×10^{-9}m/s vs 1.52×10^{-9}m/s).

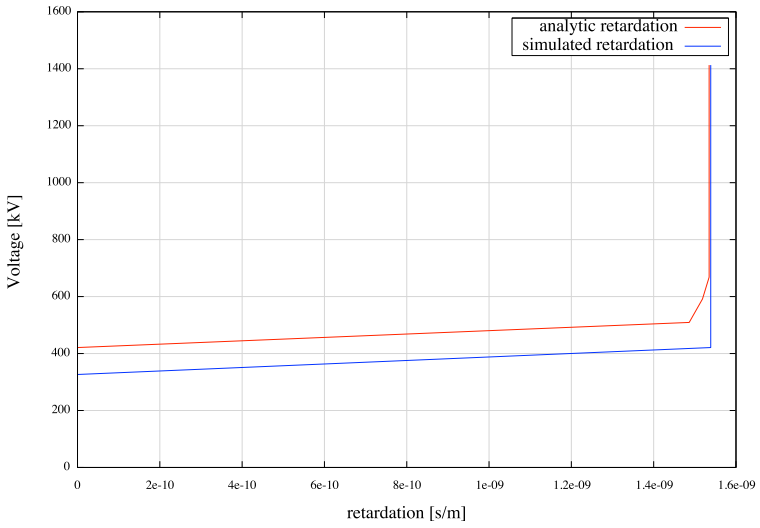

Figure 4-10 The retardation of voltage components above the breakdown voltage threshold using a single capacitance value to depict corona development.

An alternative approach to representing corona effects is to introduce increased conductivity to the node. First note, conductance (related to corona development) can be equated to a time varying capacitance:

$$G = \frac{\partial C}{\partial t} \tag{4.6}$$

Thang et al [55] used the introduction of conductivity to produce a simplified model of corona around overhead wires struck by lightning, using the finite-difference time-domain (FD-TD) method in 3-D. FD-TD allows radial electric field magnitudes to be sampled near the wire surface.

When the field breaches the critical electric field value (a version used by Hartmann [31]) at which the region is assumed to ionise and a finite conductance (20 or 40 μS/m) is added to the node. The values are chosen to emulate the ionisation process developing in the microsecond timescale. This is an important consideration in the corona modelling process as it accounts for the time necessary for the changes to air chemistry to occur. For example, finite times are required for the space charge to be removed from the wire vicinity once the line voltage falls below the critical breakdown voltage. This is particularly important if corona formation following an AC source is being considered [54]. The statistical nature of corona inception means a *statistical time lag* can be attributed. This relates to the need for a free electron once the breakdown voltage has been met as it is this electron that will initiate the electron avalanche under the influence of the electric field [23]. Finally, once initiated, there will be a streamer time lag otherwise known as the *formulative time lag* [23]. This pertains to the time for streamers and leaders to develop [23]. Many factors will influence these times; air density, peak applied voltage will, for example, made the availability of a free electron able to initiate corona development more likely. However, when simulating such phenomena a microsecond duration is typically suggested [59], [60]. If the node is considered as a simple RC circuit, where the initial capacitance, C, is analogous to the permittivity of free space and R is the resistance of the cylindrical corona discharge region developing around the wire a time constant can be attributed to the corona development; CR = ε_0/σ_c. This is found to be in the microsecond timescale for the chosen conductance values.

Figure 4-11 shows the cross-section of the wire and surrounding medium within the FD-TD node model.

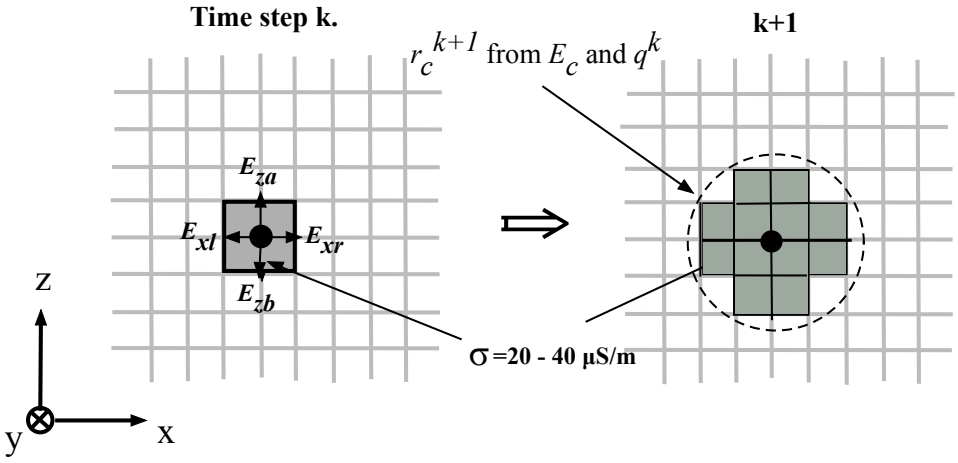

Figure 4-11 Diagram to describe the basic premise behind the FD-TD model presented by Thang et al [55]

The introduction of conductance to the nodes adjacent to the wire will induce a conduction current within the node as well as a subsequent fall in electric field, hence a fall in displacement current. At a particular time-step, k, the total radial current, $I^r(n,k)$ (conduction current plus displacement current) leaving a y-directed wire at the n^{th} node can be written

$$I^r(n,k) = \sigma\left[\left(E_{xl}^k + E_{xr}^k\right)\Delta z + \left(E_{za}^k + E_{zb}^k\right)\Delta x\right]\Delta y \tag{4.7}$$

$$+ \quad \varepsilon_0\left(\begin{array}{l}\left[\dfrac{E_{xl}^k - E_{xl}^{k-1}}{\Delta t} + \dfrac{E_{xr}^k - E_{xr}^{k-1}}{\Delta t}\right]\Delta z \\ + \left[\dfrac{E_{za}^k - E_{za}^{k-1}}{\Delta t} + \dfrac{E_{zb}^k - E_{zb}^{k-1}}{\Delta t}\right]\Delta x\end{array}\right)\Delta y$$

Where the electric field quantities are labelled by their position relative to the wire (l = left, r = right, a = above, b = below).

Using the current found above, the total charge, $Q\ (n,k)$, can be found using

$$Q(n,k) = Q(n,k-1) + \frac{I^r(n,k-1) + I^r(n,k)}{2}\Delta t \tag{4.8}$$

In chapter 2, it was noted that once breakdown has initiated, a critical background electric field, *Ec*, (less than that for breakdown) is necessary for streamer propagation. This value is quoted as being 0.5 MV/m for positive corona and 1.5 MV/m for negative corona by Thang et al [55] and can be used to determine the radial extent of the space charge, R_c , due to corona by rearranging

$$E_c = \frac{Q(n,k)}{2\pi\varepsilon_0 R_c} + \frac{Q(n,k)}{2\pi\varepsilon_0(2h - R_c)} \tag{4.9}$$

where *h* refers to the height of the wire above ground.

This radius is used to determine what nodes need to contain the increased conductivity. Equations (4.5),(4.6) and (4.7) are then iterated for each time step until the end of the simulation.

Cooray [61], provides a useful mathematical description of corona that relies on a cylindrical geometry about a wire. This seems the best approach for many reasons, assuming wires are the objects under consideration as the corona is often assumed to develop in an approximate cylindrical fashion, symmetrically about the wire. Second, many experiments investigating corona are also performed using a coaxial wire arrangement. For the purposes of this thesis, the cylindrical geometry has similarities to the Embedded Wire Node suggesting the theory can be applied there.

The mathematics / physics in developing the model is essentially based around capacitance. The voltage between inner and outer conductor is shared in proportion to the various capacitances of the wire and corona as they develop over time.

The critical field for corona inception, E_B, is determined using Peek's formula (2.18) [33]. Hence an equivalent breakdown voltage for inception can be found:

$$V_B = E_B \ln\left(\frac{R_b}{R_a}\right) R_a \tag{4.10}$$

where R_a is the radius of the inner wire and $R_b$is the radius of the outer (reference) conductor.

In the model, corona development is described in various stages:

Stage 1 is the pre-corona stage, where capacitance of the coaxial arrangement is simply that of the wire alone. Hence, he applied voltage is below the breakdown threshold.

Stage 2 describes the time interval where the field on the surface of the wire dictates the onset and development of corona. Once this stage initiates, the surface field on the wire, E_{r-surf} ($> E_B$), is allowed to fall exponentially, to the field necessary for streamer propagation, E_c, by introducing a decay constant, τ. This is employed to suit the statistical time lag referred to previously [23][54][59]. A value of 0.5 microseconds is suggested [61].

$$E_{r-surf} = E_c + (E_B - E_c)\exp\left[\frac{-t}{\tau}\right] \tag{4.11}$$

The reduction of the surface field can be linked to a fall in line charge (per unit length), q_a, on the inner conductor (wire) using

$$q_a = 2\pi\varepsilon_0 R_a E_{r-surf} \tag{4.12}$$

where R_a is the radius of the central wire.

As the (instantaneous) voltage between inner and outer conductor is to be maintained, the space charge outside the wire and the charge on the wire can be used to describe the voltage in terms of capacitance:

$$V(t) = \frac{q_a}{2\pi\varepsilon_0}\ln\left(\frac{R_b}{R_a}\right) + \frac{\rho_c}{\varepsilon_0}\left[(R_c - R_a) - R_a\ln\left(\frac{R_c}{R_a}\right)\right] + \frac{\rho_c}{\varepsilon_0}(R_c - R_a)\ln\left(\frac{R_b}{R_c}\right) \tag{4.13}$$

where a corona charge density , ρ_c, has been introduced (volume charge density per unit radial distance from the wire [C/m^2]). Figure 4-12 presents the stages pictorially. The charge density is contained within a corona radius, R_c

The total charge within the corona is given by

$$q_c = \int_{R_a}^{R_c} 2\pi r \frac{\rho_c}{r} dr = 2\pi\rho_c(R_c - R_a) \tag{4.14}$$

R_c can be found using

$$R_c = \frac{Q_{coax}}{2\pi\varepsilon_0 E_c} \tag{4.15}$$

where Q_{coax} is the total charge within the coaxial arrangement $(= q_a + q_c)$.

Hence, solving the equations requires iteration of equations (4.13), (4.14) and (4.15) to find the corona charge density, ρ_c. Note, the potential gradient within the corona sheath is assumed constant.

Stage 3 is entered after the applied voltage has reached its peak at the wire segment in question. At this stage, the reduction in voltage is maintained purely via a fall in wire charge only i.e. the corona charge (and therefore radial extension of the corona sheath) stays at its maximum value. Therefore, the instantaneous applied voltage can be described as in equation (4.14) but with the correspond values substituted with the maximum values found at the peak voltage (subscript 'm' refers to maximum values):

$$V(t) = \frac{q_a}{2\pi\varepsilon_0} \ln\left(\frac{R_b}{R_a}\right) + \frac{\rho_{cm}}{\varepsilon_0}\left[(R_{cm} - R_a) - R_a \ln\left(\frac{R_{cm}}{R_a}\right)\right] + \frac{\rho_{cm}}{\varepsilon_0}(R_{cm} - R_a)\ln\left(\frac{R_b}{R_{cm}}\right) \tag{4.16}$$

with the charge per unit length contained within the sheath given by

$$q_c = \int_{R_a}^{R_c} 2\pi r \frac{\rho_{cm}}{r} dr = 2\pi\rho_{cm}(R_{cm} - R_a) \tag{4.17}$$

Stage 4 refers to an interesting phenomenon. A time may arise when the voltage has fallen to such an extent that not only does the polarity of the wire change but the field on the surface of the wire reaches a value such that conditions for the development of negative corona are met. This discharge is termed back corona and acts to neutralize the charge of the original positive corona. The equations describing the back corona are almost identical to those describing the original. Taking into account the formation of this new space charge, the voltage can be described using (subscript 'b' refers to quantities associated with back corona)

$$\begin{aligned} V(t) = \frac{q_a}{2\pi\varepsilon_0}\ln\left(\frac{R_b}{R_a}\right) &+ \frac{\rho_{cb}}{\varepsilon_0}\left[(R_{cb} - R_a) - R_a \ln\left(\frac{R_{cb}}{R_a}\right)\right] \\ &+ \frac{\rho_{cb}}{\varepsilon_0}(R_{cb} - R_a)\ln\left(\frac{R_b}{R_{cb}}\right) \\ &+ \frac{\rho_{cm}}{\varepsilon_0}\left[(R_{cm} - R_{cb}) - R_{cb}\ln\left(\frac{R_{cm}}{R_{cb}}\right)\right] \\ &+ \frac{\rho_{cm}}{\varepsilon_0}(R_{cm} - R_{cb})\ln\left(\frac{R_b}{R_{cm}}\right) \end{aligned} \tag{4.18}$$

with the radius of the back corona given by

$$R_{cb} = \frac{q_{cb} + q_a}{2\pi\varepsilon_0 E_{cb}} \tag{4.19}$$

and the charge contained within the back corona sheath given by

$$q_{cb} = 2\pi\rho_{cb}(R_{cb} - R_a) \tag{4.20}$$

The charge density of the back corona, ρ_{cb} is found iterating the above equations as before.

The total charge is now a sum of three charge quantities:

$$Q = q_a + q_{cb} + 2\pi\rho_{cm}(R_{cm} - R_{cb}) \tag{4.21}$$

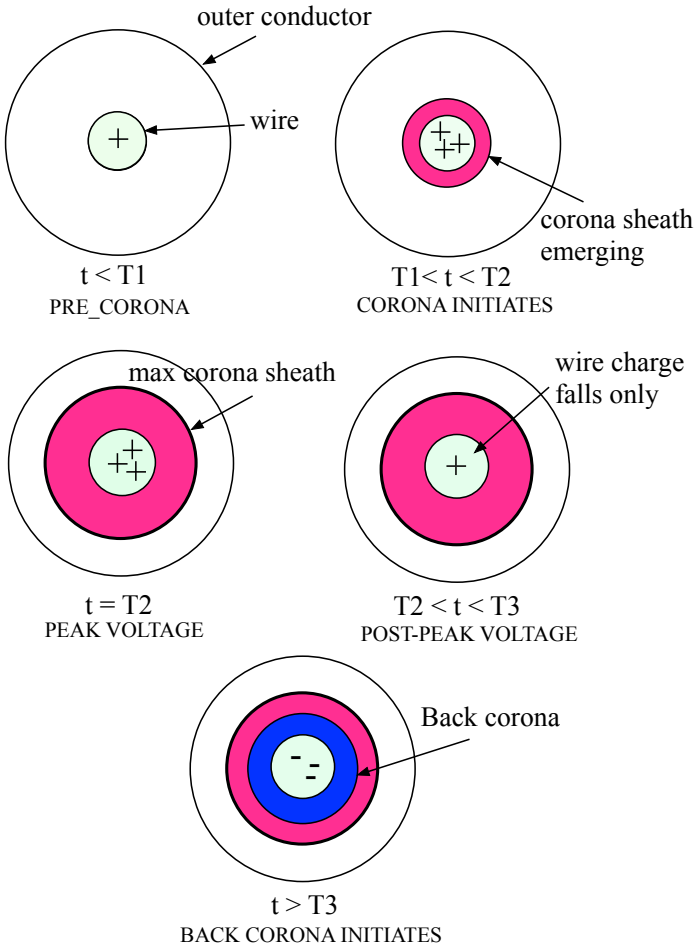

Figure 4-12 The stages chosen by Cooray to describe corona development about a wire assuming a cylindrical breakdown region [61]

This algorithm provides a real-time variation of the pertinent parameters related to corona development. Using these, many aspects of the corona development can be described in

further detail. These quantities should be able to recreate the observed distortions when integrated in a framework describing pulse propagation on a wire.

4.3 Transmission Line Equations adapted for Corona

Cooray and Theethayi [57] decided to re-derive the transmission line equations but in the presence of corona. Once achieved, the reliance on the various parameters to create the propagation characteristics becomes clearer. Appendix B describes the derivation in detail, based heavily on a derivation by Agrawal [62]. The transmission line equations for an *x*-directed wire at a height, h, above the ground in the undergoing corona become

$$\frac{\partial V^s(x,t)}{\partial x} + R_d I(t,x) + L_d \frac{\partial I(t,x)}{\partial t} = E_x^i(t,x,h) \tag{4.22}$$

$$\frac{\partial I(t,x)}{\partial x} + C_d \frac{\partial V^s(t,x)}{\partial t} = -I_c(t,x) \tag{4.23}$$

where

$$I_c(t,x) = \frac{\partial q_c(t,x)}{\partial t} \tag{4.24}$$

and $E_x^i(t,x,h)$ represents incident electric field components capable of coupling with the wire. R_d, L_d, C_d are the per-length line resistance, inductance and capacitance respectively. V_s refers to the scattered voltage.

The total voltage between line and ground , $V(x,t)$ is

$$V(x,t) = V^s(t,x) - \int_0^h E_x^i(t,x,z) \cdot dz \tag{4.25}$$

with boundary conditions

$$V^s(t,\xi_1) = -Z_1 \cdot I(t,\xi_1) + \int_0^h E_x^i\,(t,\xi_1,z)\cdot dz \tag{4.26}$$

$$V^s(t,\xi_2) = -Z_2 \cdot I(t,\xi_2) + \int_0^h E_x^i\,(t,\xi_2,z)\cdot dz \tag{4.27}$$

where Z_1, Z_2 are the termination impedances, and ξ_1, ξ_2 are the respective *x*-coordinates at each end of the line.

The first TL equation (4.22), suggests the scattered voltage, V^s, is based on the wire charge and the charge contained within the corona sheath. The inclusion of the corona current in the second equation (4.23), however, demonstrates an explicit effect on propagation. Further, the equation can be manipulated in such a way that dependency on the other parameters known to be able to describe the desired effects of corona are included.

First, the capacitance based term of (4.21) is simply the time derivative of the wire charge

$$C_d \frac{\partial V^s(t,x)}{\partial t} = \frac{\partial q_a(t,x)}{\partial t} \tag{4.28}$$

Hence, the transmission-line equation can be written

$$\frac{\partial I(t,x)}{\partial x} = -\frac{\partial Q(t,x)}{\partial t} \tag{4.29}$$

Q(t, x) being the total charge per-unit-length at a particular element at a particular time (4.8).

The total charge can be used to describe a total capacitance per-unit length of the wire and corona, $C_d^{tot}(t,x)$:

$$Q(t,x) = C_d^{tot}(t,x)\cdot V^s(t,x) \tag{4.30}$$

Substituting this expression into the transmission line equation (4.23) allows it to be written

$$\frac{\partial I(t,x)}{\partial x} + C_d^{tot}(t,x)\frac{\partial V^s(t,x)}{\partial t} = 0 \tag{4.31}$$

This equation pertains to the initial method of representing corona; a time-varying capacitance of the line under corona conditions.

Isolating the corona charge per-unit-length, $q_c(t,x)$, and relating this quantity to the scattered voltage allows a capacitance purely related to the corona to be defined, $C_d^c(t,x)$

$$q_c(t,x) = C_d^c(t,x) \cdot V^s(t,x) \tag{4.32}$$

Now (4.23) can be written as

$$\frac{\partial I(t,x)}{\partial x} + C_d\frac{\partial V^s(t,x)}{\partial t} + \frac{\partial [C_d^c(t,x) \cdot V^s(t,x)]}{\partial t} = 0 \tag{4.33}$$

The third term is the capacitance that is required to be added to the line to recreate the corona effects.

Finally, expanding the third term and rearranging allows the above equation to be written

$$\frac{\partial I(t,x)}{\partial x} + (C_d + C_d^c)\frac{\partial V^s(t,x)}{\partial t} + V(t,x)\frac{\partial C_d^c(t,x)}{\partial t} = 0 \tag{4.34}$$

and as the corona related capacitance can be related to a corona related conductance as

$$G_d^c(t,x) = \frac{\partial C_d^c(t,x)}{\partial t} \tag{4.35}$$

the transmission-line equation can be written to include a conductance term

$$\frac{\partial I(t,x)}{\partial x} + (C_d + C_d^c)\frac{\partial V^s(t,x)}{\partial t} + V^s(t,x) \cdot G_d^c(t,x) = 0 \tag{4.36}$$

Up until now, the distortion and attenuation of a propagating waveform has been attributed to the retardation of those voltage components above the breakdown threshold of the medium in which the wire is situated. However, equations (4.22) and (4.23) do not describe a retarded signal, that is, no explicit reference to an increase in capacitance is present such that the speed = $1/\sqrt{(LC)}$ is affected. Cooray and Theethayi [57] describe how the presence of a corona current creates the same effect despite this.

First, consider a wire in normal conditions. When an incident electric field component, $E_x^i(t,x)$, couples with an element of the wire, *dx,* two infinitesimal current waveforms are induced in the wire. Likewise, when a wire segment is subject to the effects of corona, a time-varying space charge is created in the vicinity of the wire. This can be described as a corona current, assumed to enter the wire radially (Figure 4-13).

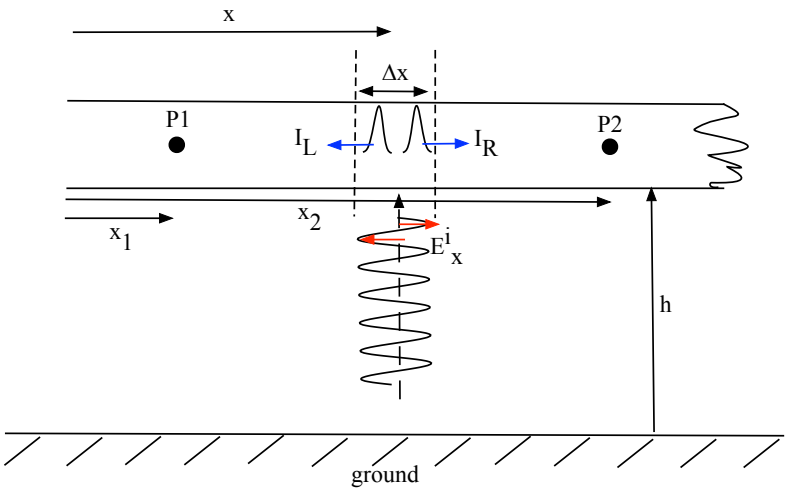

Figure 4-13 Interaction of an external electric field component with a line element inducing identical infinitesimal current pulses in the directions of P1 and P2[57].

Hence, at each time increment an infinitesimal current enters the wire when the conditions are deemed correct. This current 'wavelet' will split and propagate in both directions along the wire, towards points P1 and P2, and as the equation suggests at a speed =$1/\sqrt{(LC)}$, not a lesser speed. Hence at a time, *t*, the current at these points can be described using

$$dI_{P1}(t, x_1) = \frac{E_x^i\left(t - \frac{x - x_1}{c}, x\right) \cdot dx}{2Z} \tag{4.37}$$

$$dI_{P2}(t, x_2) = \frac{E_x^i\left(t - \frac{x_2 - x}{c}, x\right) \cdot dx}{2Z} \tag{4.38}$$

The total current at a point on the wire is the sum of these induced currents that have originated at various wire elements along the wire. (Note: the sign of the current is positive if positive charge is conveyed in the direction of positive *x*).

Under corona conditions, assuming an infinitesimal radial corona current enters the wire at a particular line segment, a similar situation to that above is suggested. The corona current will split and travel in both directions at speed c = $1/\sqrt{(LC)}$. The respective corona current at points P1 and P2 from an original corona current injected at a line element, Δx, at x, are given by

$$dI_{c\_P1}(t, x_1) = dI_c\left(t - \frac{x - x_1}{c}, x\right) \cdot dx/2 \tag{4.39}$$

$$dI_{c\_P2}(t, x_2) = dI_c\left(t - \frac{x_2 - x}{c}, x\right) \cdot dx/2 \tag{4.40}$$

Hence, under corona conditions there are four 'categories' of current element travelling on the wire, all at speed '*c*' At any given point on the wire, there will be three of these components potentially available. The total current at a line element is a sum of these different elements. Figure 4-14 demonstrates these components.

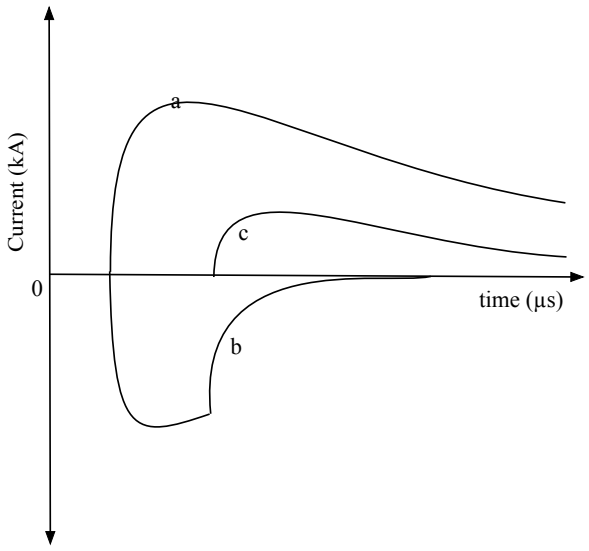

Figure 4-14 The three current components that constitute the total current at a particular point on a corona-affected wire [57]

Algebraically summing the components will give the distorted waveform expected in such circumstances creating an apparent retardation of those elements above the threshold. All the variations of the transmission line equations are essentially equivalent in their descriptions of propagation despite some of them not explicitly revealing a reduction in propagation speed.

4.4 Soil Ionisation

4.4.1 Introduction.

Ionisation effects are also an important consideration when trying to understand the reaction of grounded systems to surge phenomena. The surge phenomena are typically lightning strikes but threats from man made events such an NEMP also exist and so the incentive to model the behaviour of underground wires in such conditions is necessary. The environment and protection strategy is somewhat different to that when considering effects on wires overhead. Unlike the overhead arrangement where the aim maybe to propagate power /

signals over long distances such that power losses are undesirable, the alternative is true in the arrangements considered here. The overriding purpose of such underground installations is to intentionally intercept a surge transient and dissipate the energy to ground in an efficient way as possible before it is able to interact with sensitive equipment or worse, life itself.

The current wave shapes typically used to represent lightning have a slow rise time than that of EMP (1.2/50 μs, 8/20 s, 10/350μs) [63]. Peak currents are usually chosen to be around 30 kA travelling at near the speed of light along the channel, often referred to as the *return stroke* [34]. A ground flash has the potential to cause fires, structural damage and electrical destruction so Lightning Protection Systems (LPS) of various forms are designed to negate such effects, diverting the problematic surge to ground and dissipating it in a safe manner.

4.4.2 Grounding Systems - basic calculations and high frequency considerations.

From a modelling perspective, the grounding system is comprised of three components (Figure 4-15) [64]:

i) A metallic conductor that drives the current to the buried electrode.
ii) Metallic electrode buried in the soil.
iii) The material surrounding the electrode-soil.

The efficiency of the grounding system can be characterised by the impedance it provides to the surge transient; the less impedance the better. Hence, resistivity of the soil in which the electrode is situated plays a major role. The underground electrode is essentially any metallic material able to disperse current into the soil. However, the design of the electrode can vary tremendously allowing the current to dissipate in a desired way; from the simple vertical or horizontal electrode to more complex grid arrangements. This chapter will concentrate on the single electrode variety.

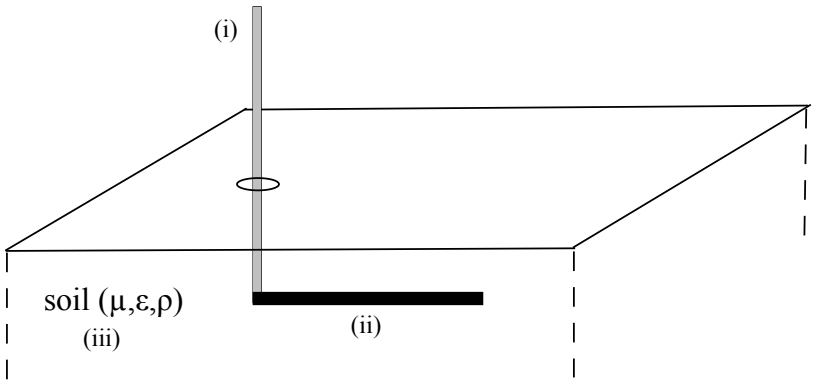

Figure 4-15 Major elements of a grounding system (adapted from [64]

The response of grounding electrodes to lightning currents can be expressed using the Ground Potential Rise (GPR). This is defined as the 'product of ground electrode impedance, referenced to remote earth and the current that flows through that electrode impedance' [65]. In essence, it refers to the potential at a given point in soil relative to a distant point in the earth where the potential is zero (by the very nature of the soil this should not be too far away). The initial termination or injection point is of paramount importance. With this in mind, the circuit description of a simple horizontal grounded rod is analogous to any basic transmission-line description; the primary parameters being the inductance per-unit length, L_d, capacitance per-unit length, C_d shunt conductance, G_d and line resistance, R_d. (Figure 4-16 (a)). All these parameters influence the impedance met by the injected current.

The inductance of the rod and the capacitance of the soil (related to soil permittivity, ε_s) will introduce frequency dependence to the grounding system's behaviour, while resistive effects are provided by the resistance of the rod and shunt conductance of the soil. Figure 4-16 (b) demonstrates the current components attributed to these parameters [64]. A longitudinal current, travelling along the electrode and a 'leakage' current or shunt current emerging radially from the rod can be described, both containing resistive and reactive components.

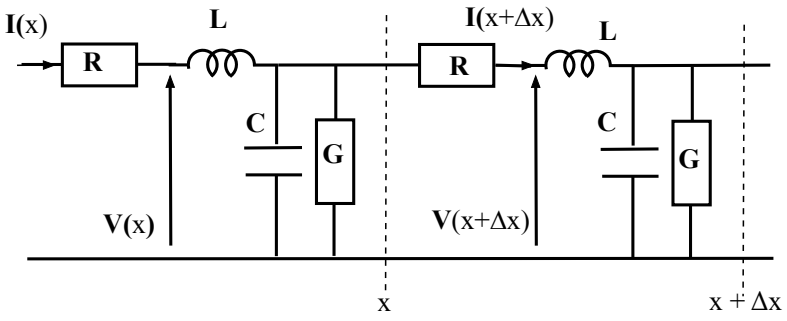

(a)

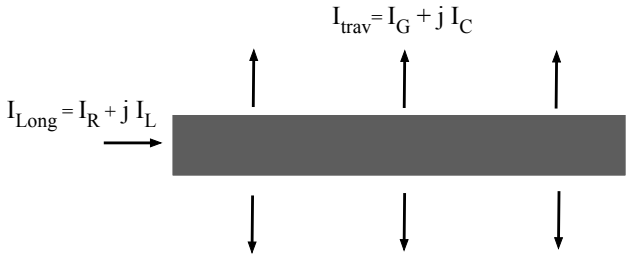

(b)

Figure 4-16 (a) Circuit description of an underground transmission line segment. (b) The complex nature of the currents entering and leaving a rod segment[64].

Longitudinal current can be related to a magnetic field about the wire through inductance (i.e. soil permeability) (I_L) and the that related to the resistance of the rod (I_R). The shunt (transverse or radial) current components relate to conductance of the soil (conduction current, I_G) and the displacement current, I_{disp}, relating to the soil permittivity, ε_s . These can be written

$$I_G = \frac{E_r}{\rho_s} . A \tag{4.41}$$

and

$$I_{disp} = \varepsilon_s \frac{\partial E_r}{\partial t} \tag{4.42}$$

The ratio of these currents is based on $\sigma_s/\omega\varepsilon_s$ where ω is the angular frequency of the current components. The impedance to the current components is therefore dependent on this ratio.

At low frequency, the frequency based parameters (L, C) have reduced impact and hence the impedance can be considered as a grounding resistance. Further, the rod resistance is typically much greater than that offered by the ground hence the conductance of the soil is the major consideration. Therefore, many researchers refer to a grounding resistance despite the theory clearly demonstrating reactive aspects as the frequency effects are ignored. Nevertheless, this is only acceptable if protection against a simple 60Hz power source is being considered (low-frequency phenomena). In this situation the grounding 'resistance' can be described using

$$R_T = \frac{V_T}{I_T} \tag{4.43}$$

where, the potential of the electrode is considered constant along its length (no voltage drop along its length)[64].

The grounding resistance is generally linked to the soil resistivity by a geometrical factor, K such that $R_T = K\rho_s$. Hence, this can be exploited to achieve greater efficiency at dissipating the problematic current surge. When considering simple arrangements, the factor can be established analytically. The technique would involve finding the potential on the wire surface relative to a distant (zero) potential. This can be found analytically or numerically as an integral of electric field values between the points but in principle relates to the radial current density values perpendicular to the rod surface. The transverse current density can therefore be described as a function of the injected current and the area about the electrode at various distances, r, from its surface [66]. Hence, the potential is a function of the soil resistivity, the impressed current and a geometrical factor, *K(r)*. This potential will be divided by the impressed current (4.43) to obtain the resistance and therefore the grounding resistance becomes simply a function of the soil resistivity and an expression related to the rod

geometry. A simple horizontal buried rod , length L, radius r, buried at a depth d , has its grounding resistance given by [67]

$$R_T = \frac{\rho_s}{2\pi L}\left(\left[\ln\frac{2L}{r}\right] + \left[\ln\frac{4L}{d}\right] - 2 + 2\frac{d}{L} + \cdots\right) \tag{4.44}$$

Usually, (4.44) is not the form used in modelling attempts. Instead, the equation offered by Sunde [68] is considered

$$R_T = \frac{\rho_s\left(\ln\left[\frac{2L}{\sqrt{2rd}}\right] - 1\right)}{2\pi} \tag{4.45}$$

Note, the longitudinal current is ignored as it is linked to minimal voltage drop. Similarly, displacement current is also omitted (low frequency transient)[67].

When subjected to lightning, the low-frequency approximation no longer applies due to the impulsive nature of lightning, and the possibility of ionisation effects. The high frequency content means that a constant potential can no longer be assumed. A significant difference in potential along the electrode can result (inductive and skin effects). On the other hand, complex impedance, $Z(\omega)$ is not suitable due to its transience. Instead, the peak potential,V_p and current I_p, are often used to give an impulsive impedance, Z_p. When this is obtained the grounding 'resistance' is easily obtained by multiplying by the peak current.

$$Z_p = \frac{V_p}{I_p} \tag{4.46}$$

However, this still is difficult to find from practical standpoint and so grounding resistance is measured instead.

The ionisation effect can reduce the grounding impedance. The effect is clearly more likely, when the current density on the surface of the electrode is more intense, as would be expected when short electrodes are subjected to high lightning currents [67]. This aspect is often omitted in models examining GPR. The next section investigates this phenomenon further.

4.4.3 Soil Ionisation Models

The steep front of a lightning surge implies the high frequency content contained therein, and a need for this aspect to be considered [69]. The highest voltage will appear between the injection point and a distant zero potential (ground). As has already been alluded to, the peak values of the impressed current and resulting voltage are often used to give a peak impedance. However, this does not provide a comprehensive view of the performance of grounding electrodes when protecting against lightning. The frequency related phenomena; inductance, skin depth may have an adverse effect on the efficiency of current dissipation. This makes the high-frequency related phenomena an area of important research.

However, the magnitude of the lightning strike means that soil ionisation should also be considered. Just as for air, a critical electric field for ionisation can be assigned to soil where the ionisation processes start to dominate the de-ionisation process. However, as the mean-free-path in soil is much less than that in air, the critical field for breakdown is much higher [70] (see also Chapter 2 - Electrical Breakdown).

Unfortunately, there is no fixed value as the composition of soil varies tremendously. Also, the spherical nature of the particles that comprise the soil means that many air pockets are present. These air pockets are subject to the same criteria as held for wire in air above ground scenario. Hence, the inclusion of air pockets actually reduces the critical field considerably. Experimentalists have provided their own range of values [71][72]. Mousa [73] suggested 3×10^5 V/m as a suitable value for theoretical investigations while CIGRE suggest a value of 4×10^5 V/m [74].

Once breakdown has initiated an increase in conductivity around the electrode will occur. This will improve the performance of the grounding system as the main objective of dissipating the current to earth is enhanced. Hence, a fall the the ground potential rise (GPR) is expected.

The following models have been devised by researchers to simulate the effects of soil ionisation. There are some similarities to those used to simulate corona discharge around

overhead wires. For instance, all rely on the assumption that ionisation occurs symmetrically around the electrode.

The concept of allowing the electrode radius to increase in radius was introduced at the beginning of this chapter. In its most basic form, the material within the extended radius has the conductivity of a perfect conductor e.g. [75]. Hence, for a horizontal electrode its grounding resistance is now time dependent:

$$R_T(t) = \frac{\rho_s \left(\ln \left[\frac{2L}{\sqrt{2d\, r_{ion}(t)}} \right] - 1 \right)}{2\pi} \tag{4.47}$$

where $r_{ion}(t)$ is the time-varying radius under breakdown conditions otherwise equal to the physical radius, r.

The approach is inaccurate as the ionised soil will have a finite conductivity less than that of the electrode. To overcome this problem, a model, whereby finite conductivity is used to represent the ionised region was introduced [76]. However, note the model also does not account for hysteresis and assumes all breakdown is an immediate event.

Valazquez and Mukhedkar [58], proposed a model, with the aim of modelling both the frequency dependency and soil ionisation by adjusting all the transmission line parameters with a new conductor radius related to the ionisation zone.

The distributed TL parameters are again based on the formulae proposed by Sunde [68] is used. The resistance of the rod, R_d (with rod resistivity , ρ_{cond}) is given by

$$R_d = \frac{\rho_{cond}}{\pi r^2} \qquad [\Omega/\mathrm{m}] \tag{4.48}$$

With the grounding conductance (per-unit length), G_d given by

$$G_d = \frac{2\pi}{\rho_s \left(\ln \frac{2L}{\sqrt{2dr}} - 1 \right)} \tag{4.49}$$

and inductance, L_d

$$L_d = \frac{\mu_0}{2\pi}\left(\ln\frac{2L}{\sqrt{2dr}} - 1\right) \tag{4.50}$$

and capacitance, C_d

$$C_d = \frac{2\pi\varepsilon_0\varepsilon_r}{\left(\ln\frac{2L}{\sqrt{2dr}} - 1\right)} \tag{4.51}$$

The simulation then involves discretizing the line into segments (cells) in a similar way to the 1-D TLM approach, using lumped parameters found by equations (4.48), (4.49), (4.50) and (4.51) for a given electrode radius. An increasing radius approach is then used to adjust the parameters accordingly. First, the current density, $J_T(n)$, leaving a conductor segment is found using the leakage current, I_T (Figure 4-17):

$$J_T(n) = \frac{I_T}{A_s} \tag{4.52}$$

where A_s is the area of the cylindrical surface of the wire segment.

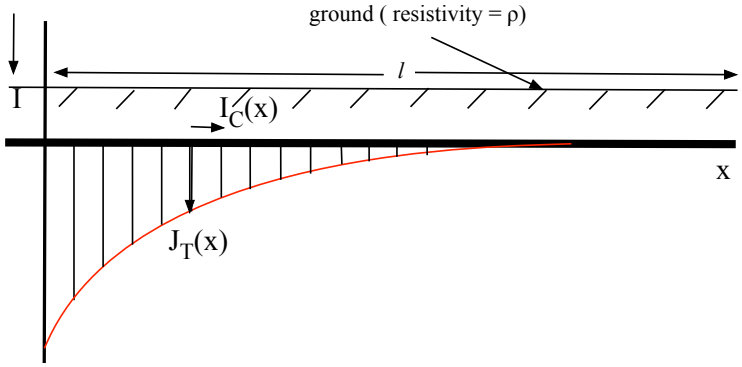

Figure 4-17 Injected current and leakage current density at various points on a grounded rod [58]

Once this is found the electric field intensity on the wire surface is easily found using

$$E_{r\_surf} = \rho_s J_T \tag{4.53}$$

This value can be monitored and once it is found the exceed the critical value, E_B, a corresponding radius at which that field value is met can be found (assuming a regular potential gradient throughout the ionised region:

$$r_{ion}(n,k) = \frac{I_T \rho_s}{2\pi l E_B} \tag{4.54}$$

The radius r_{ion} represents the radial extent of the ionisation. Using the extending conductor radius technique, this is allowed to become a new (fictitious) conductor radius, and all the parameters (4.48), (4.49), (4.50), (4.51) are adjusted accordingly. Note, this method involves changing line inductance and capacitance not just capacitance as suggested in the approach used for the wire above ground. Valazquez makes a point of mentioning both these parameters change under the influence of breakdown fields [58].

Gazzana [56] uses the 1-D TLM method to achieve the same objectives. The non-linear conductivity associated with the soil ionisation is introduced by modifying the grounding resistance with a factor, K_{ion}, related to the injected current, $I(t)$, and an associated threshold current, I_B, related to the critical field threshold, E_B (4.55) proposed by Imece [77], although his paper refers to overhead lines.

$$I_B = \frac{E_B \cdot \rho_s}{2\pi R_0^2} \tag{4.55}$$

$$K_{ion} = \sqrt{1 + \frac{I(t)}{I_B}} \tag{4.56}$$

Hence, a non-linear grounding resistance, $R(t)$, can now be inferred using (4.57)

$$R(t) = \frac{R_0}{\sqrt{1 + \frac{I(t)}{I_B}}} \tag{4.57}$$

An horizontal electrode, once discretized appropriately, into segments of length, Δx, will have an associated non-linear conductance for each segment , $G(t)$ given by

$$G(t) = \frac{2\pi \cdot \Delta l}{\rho_s \cdot \left[\ln\left(\frac{2L}{\sqrt{2ha}}\right) - 1\right]} \cdot \sqrt{1 + \frac{I(t)}{I_B}} \tag{4.58}$$

The ionization about each segment is considered concentric as in all the other methods discussed.

Variations in capacitance and inductance are discounted based on a work by Mousa [73] that suggests only small variations in permittivity and permeability during ionisation occur. Hence, ionisation effects are centred around changes in soil conductance and equations (4.50), (4.51) remain constant for a given electrode radius.

When finding the resistance of the electrode, the skin depth, δ, is considered. This is also dependent on frequency content of the injected waveform:

$$\delta = \sqrt{\frac{2\rho_{cond}}{\omega\mu_0}} \tag{4.59}$$

resulting in

$$R_e = \frac{\rho_{cond}\ \Delta l}{2\pi a\ \delta} \tag{4.60}$$

an electrode resistance, R_e.

A particular frequency, f = 500 kHz, is chosen to represent the surge signal as suggested by Inece [77].

For a given electrode radius, these parameters are easily introduced to the 1-D TLM routine.

To establish the field on the surface of the wire, a method similar to Valazquez [58] is used. First, the current density at the surface of each electrode segment (of node, *n*) is found

$$J_c(n,t) = \frac{I(n,t)}{2 \cdot \pi \cdot \Delta x \cdot a} \tag{4.61}$$

and the electric field intensity on the wire surface is found as in the Valazquez model (4.53).

If the surface field is found to be greater than E_c then the associated line current, $I(n,t)$ is used to calculate a new conductance , $G(n,t)$ using (4.58). It is questionable, why the leakage current is not used in a similar way to the Valazquez method as the ionisation is essentially due to this current. However, (4.56) and (4.58) do rely on the injected current. Perhaps the short length of the electrode allows this current to be used.

It is also worth mentioning that conductivity (soil or that elated to ionisation) is not included explicitly at the first node. Any effects of conductance at the first node are only experienced via the incident voltage pulses arriving from the adjacent node.

The model was used in a later paper to establish the Ground Potential Rise, GPR on a ground surface near an electrode struck by lightning [78]. IEEE Std. 80 [79] that governs electrode efficiency and human tolerances is based on industrial frequencies and steady state analysis. This is likely to be because human life is known to have increased susceptibility to frequencies around 50-60Hz. However, there is scope to improve on this as far as protection against the effects of lightning are concerned, provided the dynamic nature of lightning pulses and the ionisation can both be modelled. Potentials near a grounding rod can be high enough to injure fatally if the current passes through the heart by various means. The means by which the potentials are able to cause such adverse effects can be described by how the potential difference is achieved across the organism.

Figure 4-18 (a) depicts a *touch* potential. The potential difference results from a part of the body touching the conductor and another part being in contact with the soil surface near the injection point. Figure 4-18(b) refers to a *step* potential. Both feet are in contact with the

ground near the strike. The potential on the ground surface will be at its highest the closer to the strike point. Hence, one foot will be at a higher potential than another. The larger the distance between the feet, the higher the potential difference. Figure 4-18 (c) depicts a *transferred* potential. Here, the conductor is touched, remotely whilst standing on ground of zero potential. If using the 1-D TLM method, once the electrode potentials are found, the potentials on the soil surface can be found analytically using

$$V(x',y',z') = \frac{Ie^{-i\omega t}}{2\pi l(\sigma_s + i\omega \cdot \varepsilon_0 \cdot \varepsilon_r)} e^{i\gamma r} \cdot \ln\left(\frac{\sqrt{x^2+y^2+z^2}+x}{\sqrt{(x-l)^2+y^2+z^2}+x-l}\right) \tag{4.62}$$

where the (x',y',z') is a surface coordinate. γ is the propagation constant and r, refers to the distance between the midpoint of the electrode and the coordinate (x',y',z').

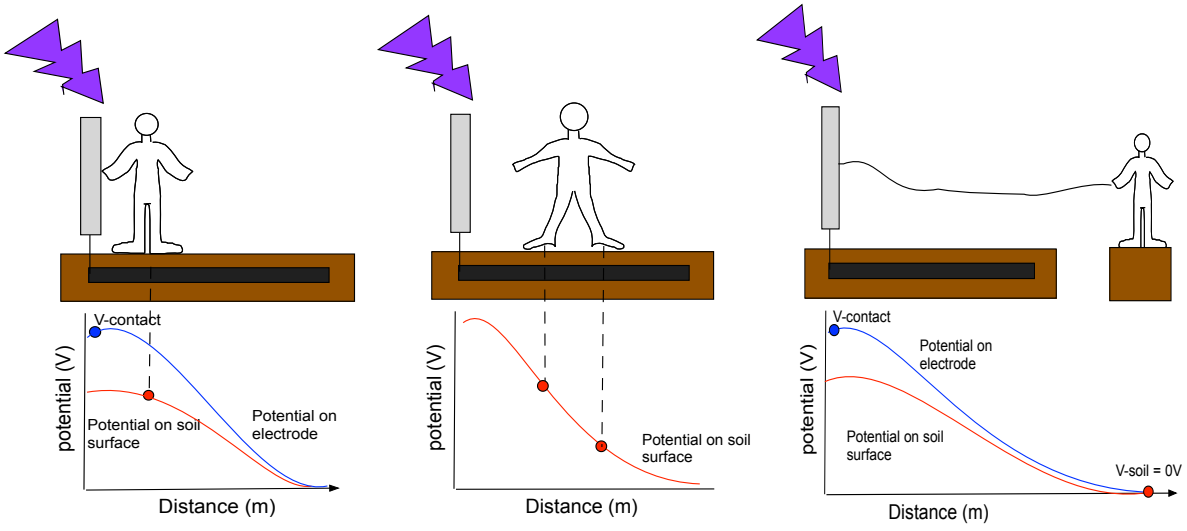

(a) (b) (c)

Figure 4-18 Various means of electrocution near a grounding rod subjected to a lightning strike: (a) touch potential , (b) step potential , (c) transferred potential [78]

It should be noted that papers by Grecv (2005) [80], (2009) [81] state that models based around circuit theory are inadequate when modelling high frequency phenomena. This is related to the quasi-static nature of the approach and the need of segment size to be at least one tenth of the (shortest) wavelength required to depict a waveform correctly. The high frequency content of NEMP means, such imitations cannot be ignored.

4.5 Summary

Ionisation of the medium surrounding wires carrying surge phenomena can cause the pulse to change its signature as it propagates. In air, the distortions are characterised by a clamping down of the anterior section of the pulse to the dielectric breakdown voltage and an overall attenuation. Further, these distortions are proportional to the distance the pulse travels along a corona inducing line. In soil, ionisation in the vicinity of the electrode will result in a greater dissipation of current to ground and hence a reduction of the ground potential rise (GPR). The modelling of corona discharge is, therefore. a necessary inclusion when determining the efficiency of grounding systems.

There are many approaches to modelling corona and its effects. This chapter has described a few based around the incorporation of changes in conductivity, capacitance or shunt current associated with the corona development. Many of the techniques rely on a prior knowledge of previous empirical data for a particular environment as there are many factors that can influence the final result from irregularities on the wire surface, to inconsistencies in the surrounding medium.

Chapter 5 Results and Discussion

The aim of this chapter is to contrast and compare the various approaches described in the previous chapters with a view to applying them to the 3-D TLM. TLM allows a differential approach to modelling and is primarily performed in the time-domain. Hence, it is ideally suited to modelling transients and their effects locally as encountered during dielectric breakdown. Further, the technique allows a self-consistent representation. This is very important when dealing with non-linear behaviour such as corona discharge. The author is unaware of any such simulations using 3-D TLM, especially using the 3-D EWN. The 3-D EWN is advantageous as it allows the consideration of fine-wires with relatively low resolution of the surrounding mesh. Here, the node will be used to represent ionisation based changes in air and is also adapted to accept soil parameters such as increases in permittivity and/or conductivity so that ionisation can be modelled there too.

The various models discussed in the previous chapter have respective strengths and weaknesses. In some respects, the methods overlap and elements of each approach can be used within the EWN to generate the desired effect. Firstly, corona discharge in air is considered. The rudimentary approach of allowing the corona sheath to be represented as an increase in conductor radius is demonstrated initially. This will then be followed by the introduction of nominal conductivity to the node similar to the method described by Thang et al[55] although adapted to suit the TLM architecture, in particular the EWN. The method described by Cooray will then be applied to the Embedded Wire Node. The various methods will be compared to results obtained by Wagner et al [50].

Before the various methods are attempted a few simple tests are demonstrated to confirm the basic requirements of the mesh are being met.

5.1 Tests

Before the modelling of corona is attempted the TLM software was tested to confirm basic tests meet analytical results.

5.1.1 Simple square coax (EWN):

Using the analytic equation for impedance of a square coaxial wire transmission line,

$$Z_{sc} = \frac{1}{2\pi}\sqrt{\frac{\mu}{\varepsilon}}\ln\left(\frac{R_b}{R_a}\right) \tag{5.1}$$

consider a coaxial wire, with the central conductor radius, R_{wire} = 0.0065m, and the outer conductor radius, R_{outer} = 0.77m, and 12m in length, the dielectric is free space (μ_0, ε_0). The Impedance of the line found analytically is approximately 287Ω.

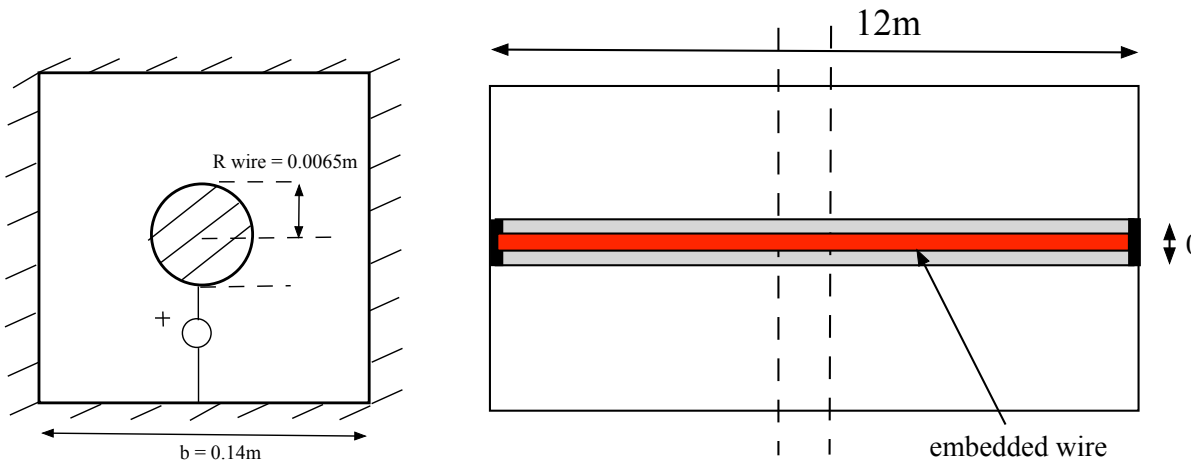

Figure 5-1: Square coaxial TL with central conductor of radius 0.0065m modelled using EWN. Outer conductor side length, b = 0.14m. Total length of coax = 12m.

Figure 5-2 plots the result once excited using a bi-exponential pulse waveform. The impedance is found to settle at the analytic value. Note the variation in impedance as the pulse is initially introduced to the wire. The pulse is actually injected into the EWN. Hence, the field has to settle throughout the dielectric before the characterisic impedance is met. This is somewhat analogous to the situation when a high intensity pulse is injected onto a grounding electrode.

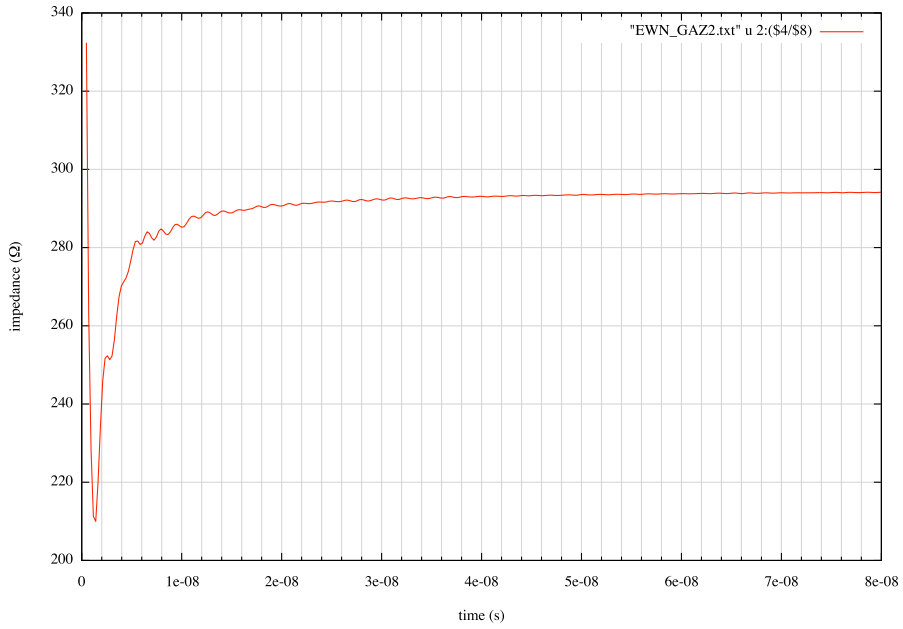

Figure 5-2 The impedance of a coaxial wire , measured at the midpoint modelled using the Embedded wire node within a GSCN mesh.

5.1.2 Square coaxial transmission line (using SCN only):

Similar tests can be performed using just a mesh of Symmetrical Condensed Nodes (SCN). The central conductor is now represented by an array of short-circuited SCN. Figure 5-2 depicts the impedance whilst Figure 5-4 plots the corresponding capacitance.

Dimensions: cell length, $dl = 0.1\text{m}$, inner wire 'radius' $R_a = 0.05\text{m}$, side length $= 4.1\text{m}$: Analytic Impedance, $Z = 222.8\ \Omega$.

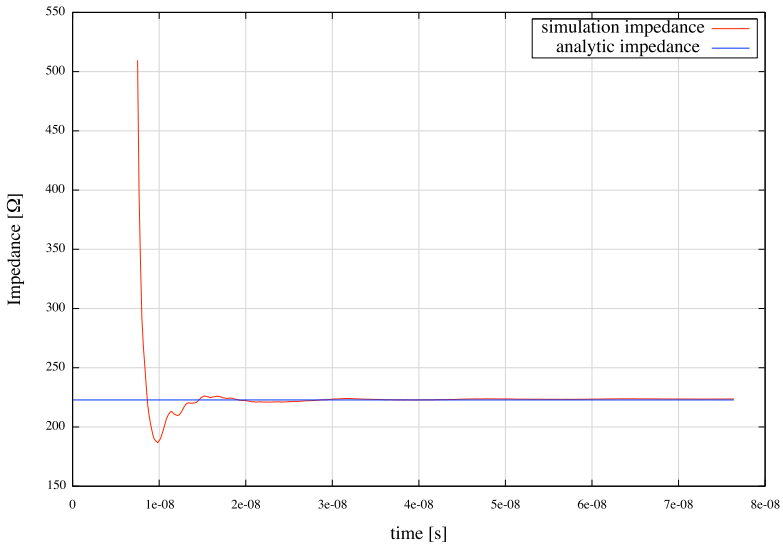

Figure 5-3 Impedance of square coax comprised of Symmetrical Condensed Nodes found analytically and via simulation.

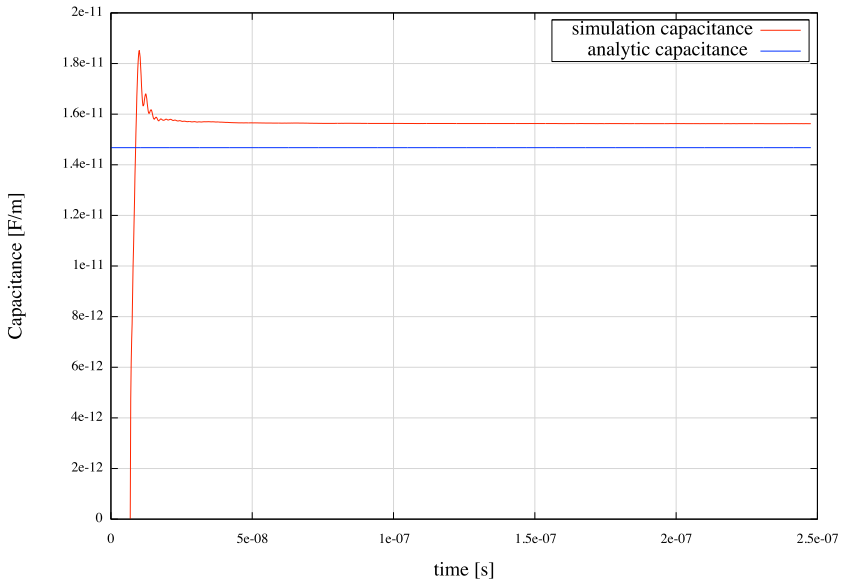

Figure 5-4 Capacitance per-unit length of square coaxial TL.

The simulations seem to agree with the analytical result in both cases.

5.1.3 Wire below ground – static resistance:

Wires below ground are to be considered. The static resistance of a horizontal wire a depth *h* below ground is quoted by Sunde as [68]

$$R(t) = \frac{\rho_s \cdot \left[\ln\left(\frac{2l}{\sqrt{2dr}}\right) - 1\right]}{\pi \cdot \Delta l} \tag{5.2}$$

Again the EWN is used to incorporate the electrode. The conductance contained within the node to adhere to the soil resistivity is found using

$$G = \frac{2\pi\sigma \cdot dl}{\ln\left[{R_b}/{R_a}\right]} \tag{5.3}$$

The soil is represented by SCN cells augmented with stubs to allow for the conductivity. The configuration is analogous to the arrangements used to demonstrate ionisation effects in soil later, namely a cylindrical electrode of radius r = 0.0065 m, 12 m in length, buried horizontally 0.48 m below ground (d = 0.48 m). The mesh dimensions were 27 cells x 27 cells x 36 cells. Each cell is cuboidal with cell length, dl = 0.333m. Figure 5-5 represents soil resistivity, ρ_s = 270 Ωm. Figure 5-6 plots the results for a soil with resistivity = 5000 Ωm while Figure 5-7 plots the same electrode but buried in soil of resistivity = 1000 Ωm. Measurements were taken at the injection point. All three examples exhibit an initial time-varying impedance that eventually converge to a static resistance. A good agreement with analytical values was obtained in all cases.

Now that the basic requirements are met, the next step is to introduce corona models to the framework.

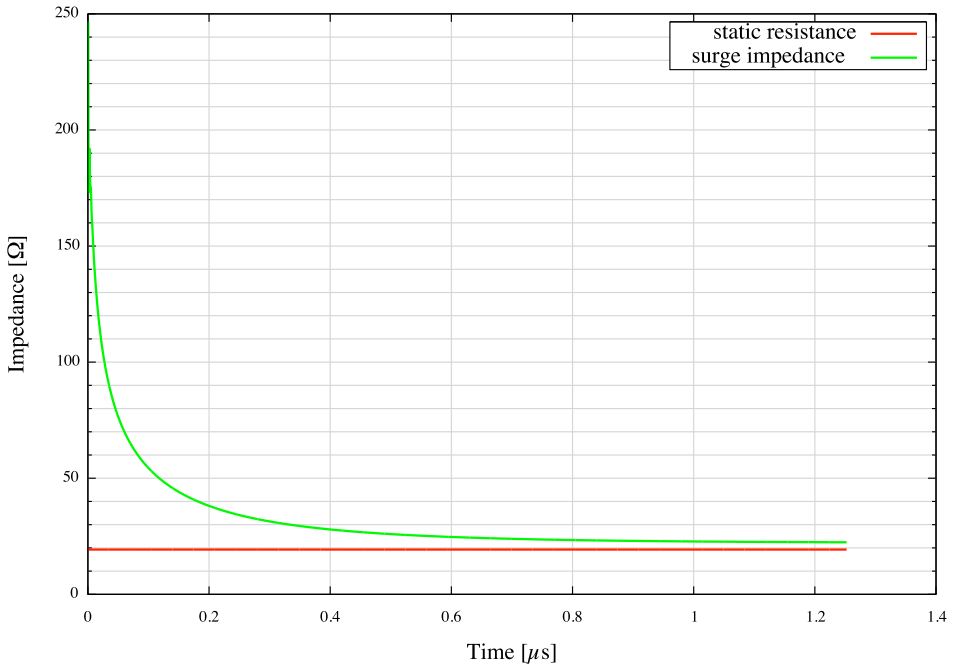

Figure 5-5. Horizontal electrode, 0.0065m radius, 12m length, depth = 0.48m in soil of resistivity = 270 Ω.

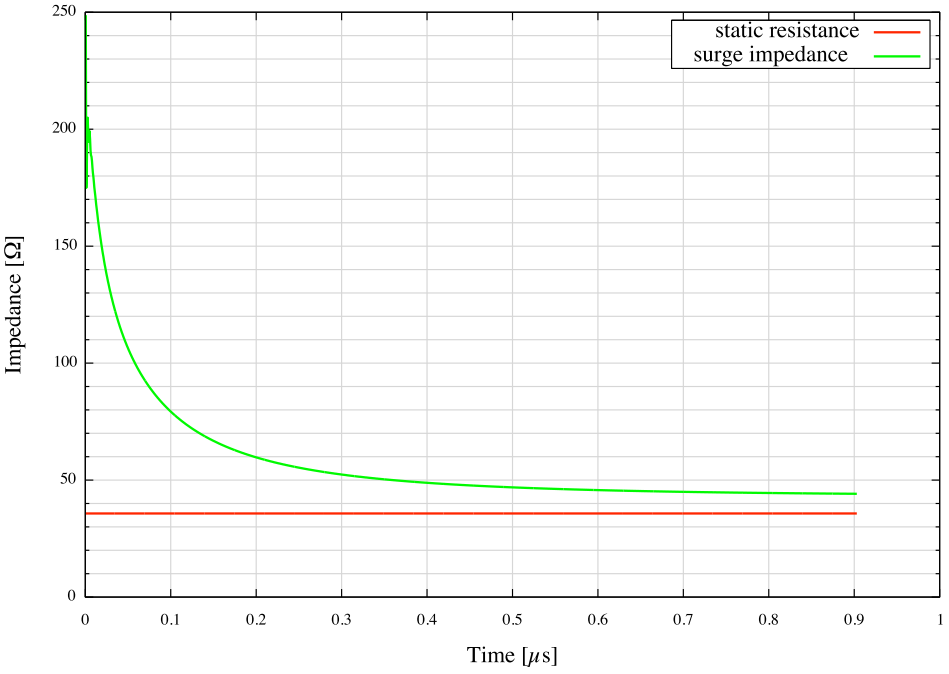

Figure 5-6: Horizontal electrode, 0.0065m radius , 12m length , depth = 0.48m in soil of resistivity = 500 Ω.

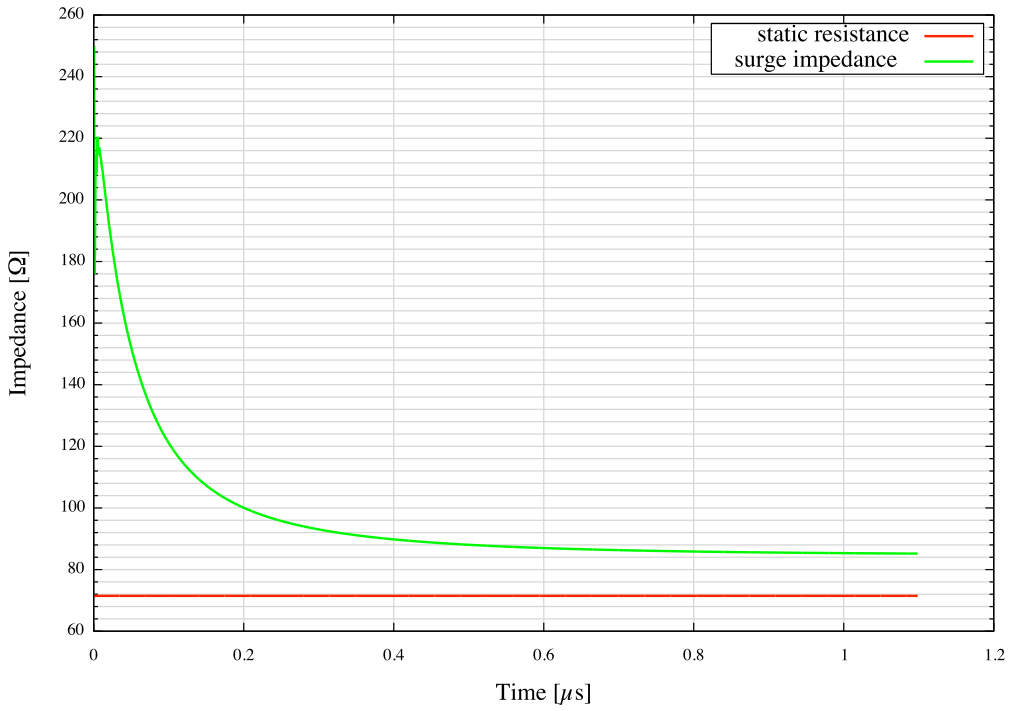

Figure 5-7: Horizontal electrode, 0.0065m radius , 12m length , depth 0.48m in soil of resistivity = 1000 Ωm.

5.2 Corona Models

The various methods of recreating ionisation of a medium under the stress of a high intensity electric field using TLM are demonstrated. First, a wire above ground (in air) is considered. The ultimate aim is to recreate the Tidd tests described by Wagner et al. [50]. These are a familiar set of results used regularly for comparison by various researchers [53][54][55][82][83]. Hence, unless otherwise stated, a wire 2200m in length is modelled, with a radius of 0.024m. The height above ground is accepted to be 14m (not accounting for wire sag). The wire is matched with a load impedance of 420 Ω.

The corona inception electric field (threshold) on the surface of the wire can be calculated using the formulae such as those proposed by Peek [33] or later versions (Hartmann [31]). These formulae contain factors that account for the surface quality of the wire and the surrounding air chemistry to compensate for variations in air humidity or density. However,

based on the empirical data the breakdown field can be extrapolated from the voltage at which distortions are found to occur. Any chosen electric field threshold will have an associated breakdown voltage and vice versa. In the simple arrangement of a cylindrical coax transmission line the equivalent breakdown voltage, V_b, is given by

$$V_b = E_b \ln\left(\frac{R_b}{R_a}\right) R_a \tag{5.4}$$

where R_b represents the radius of the outer reference conductor. The one-dimensional simulations of Christopoulos [53], Kudran [54] use a breakdown voltage of 386 kV/m. Hence, rearranging (5.4) gives an equivalent inception electric field, E_b , given by

$$E_b = \frac{386000}{\ln\left(\frac{R_b}{R_a}\right) R_a} \tag{5.5}$$

giving an approximate critical breakdown electric field, $E_b \approx 2$MV/m. These values seem consistent with the simulation provided by Thang et al [82][83]. To relate this to the predicted breakdown thresholds found using Hartmann, a wire surface factor of 0.45 is necessary.

Equation (5.4) also allows a local breakdown voltage threshold that relates to the Embedded Wire Node (not the overall arrangement) to also be calculated by letting R_b represent the equivalent radius of the EWN. This is useful when considering models that relate to the voltage represented by the EWN e.g. the Cooray method described later.

To begin, the basic principle of allowing the conductor radius to assume the increasing corona radius as it develops is considered.

5.2.1 Allowing conductor radius to increase to represent corona.

Here, the field on the surface of the wire, introduced to the TLM mesh using the embedded wire node, is monitored using the node capacitance. The voltage within the node is made available by solving the basic Thévenin equivalent circuit and therefore the wire charge,

$q_w(n)$ at a node n is easily calculated using the node capacitance calculated as shown in chapter 3.

$$q_w(n) = \frac{2\pi\varepsilon_0 \cdot V_{node}}{\ln[r_b/r_a]} \tag{5.6}$$

where r_b is the 'radius' of the EWN cell boundary. Hence, the radial electric field on the wire surface is given by

$$E_s(n) = \frac{q_w}{2\pi\varepsilon_0 r_a} \tag{5.7}$$

Once this is found to be greater than the breakdown threshold corona discharge is assumed to result. The radial extent of the breakdown is assumed to extend until the critical breakdown field is met. This technique is often used when considering breakdown in soil. It makes more sense in this environment if the radius is used to add conductivity as medium conductivity is closer to the conductivity of the rod in such circumstances than the ionised region in air. Also, a critical streamer field is not necessary in such environments. A critical breakdown field of 350 kV/m for soil is often suggested but the background field for the streamer propagation, E_c, is not necessary unlike corona discharge in air. However, for comparison with the Wagner experiments the method will be applied. Once the surface radial electric field exceeds the threshold for the wire in air, the fictitious conductor radius can be found using

$$r_c = \frac{q_w}{2\pi\varepsilon_0 \cdot E_b} \tag{5.8}$$

Figure 5-8 aims to represent the principle pictorially. The red area represents the original wire radius, $r(t_1)$. This will have a radial field depicted by the red curve. However, when considering corona, once the field reaches $E_{b,}$ the radius expands to the green area at he subsequent time-step - its associated radial field represented by the green curve. If the field is monitored at this new radius, then the radius extends to the blue area and so forth.

The new radius can be used to amend any transmission line parameter but here it will be used to add capacitance to the node to represent the corona. It should be noted that in the strictest

sense, as the wire radius increases within the node, if all related parameters are amended accordingly and hence the wire is treated as a new wire with an increased radius at each update then breakdown field threshold i.e. the Peek (or equivalent) equation should change accordingly. If this is allowed to occur, then as the wire expands the critical breakdown threshold will fall.

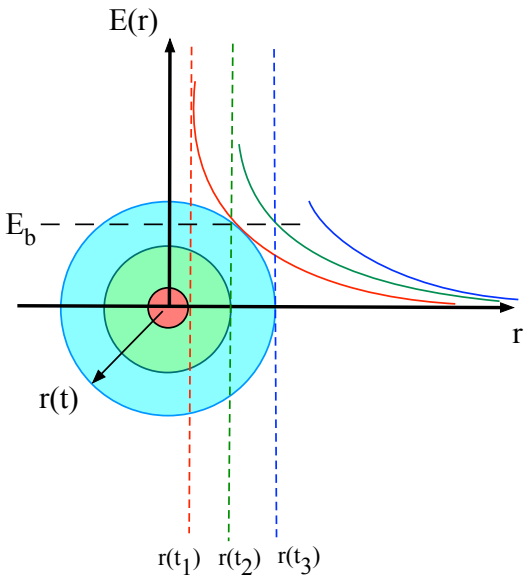

Figure 5-8 Schematic to demonstrate the principle behind the increasing radius approach to corona modelling.

Hence, here, the capacitance is increased whilst the inductance is kept at the original geometrical value. However, this does not mean that the stub representing inductance remains constant. The EWN used to model this representation is shown in Figure 5-9. As the capacitance increases, the link lines can be used to account for the new capacitance value, hence the associated impedance of the link lines will decrease. This means that the stubs being used to address the original deficit in inductance are no longer adequate. Now, more inductance needs to accounted for and therefore the stub impedance has to increase. Figure 5-10 reveals the results obtained using the technique. The EWN has a side length of 3m. The corona is represented by an increase in capacitance associated with an increase in conductor radius. The method seems to underestimate the amount of distortion and attenuation compared to that found experimentally.

Figure 5-11 plots the radius development at a point 10 nodes from the excitation node. The corresponding change in capacitance is shown in Figure 5-12.

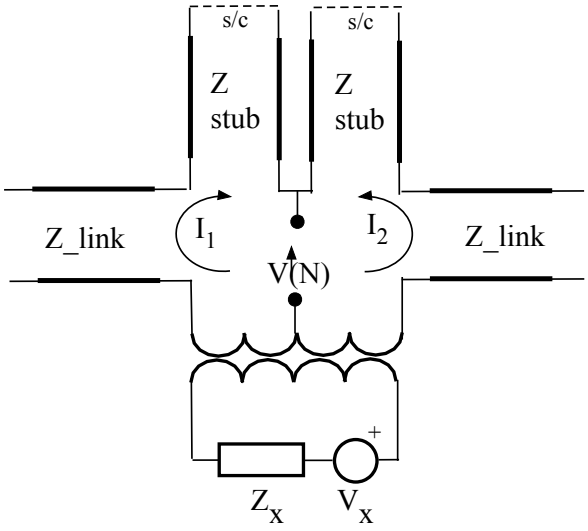

Figure 5-9 The basic EWN with link-line and stub TL to account for capacitance and inductance.

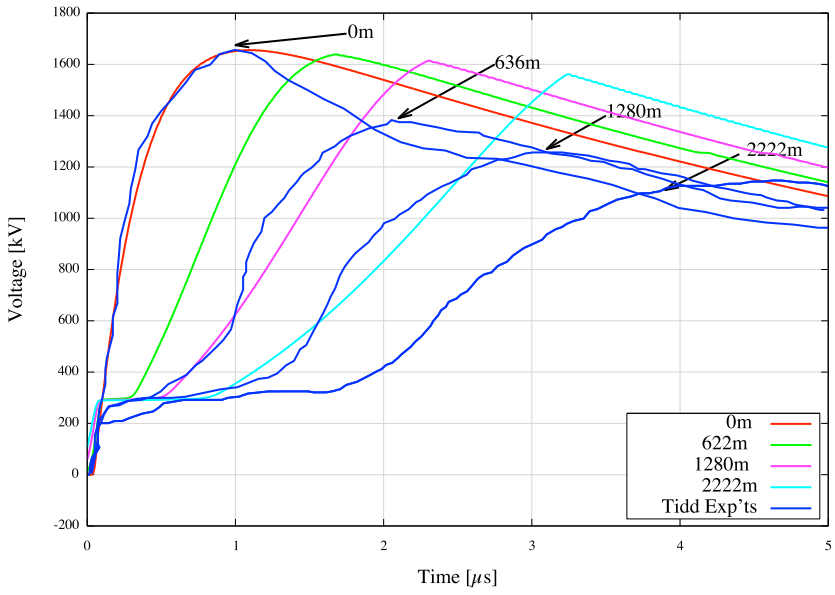

Figure 5-10 Distortions on a propagating waveform at various points along the line when corona is modelled as an increase in wire radius. The blue lines represent the experimental results [50]. Other colours are based on simulation.

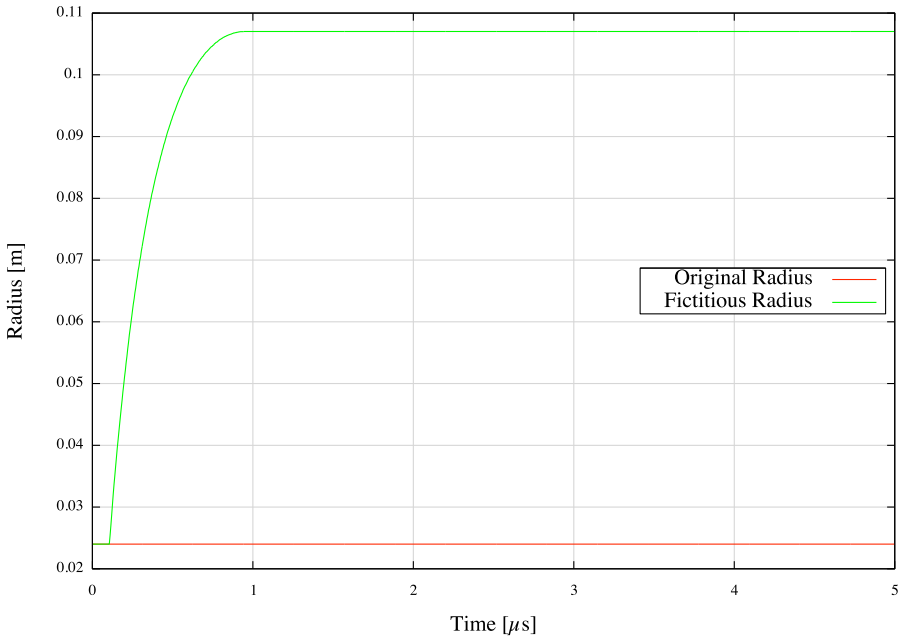

Figure 5-11 'Fictitious radius' development at a node close to the wire excitation node.

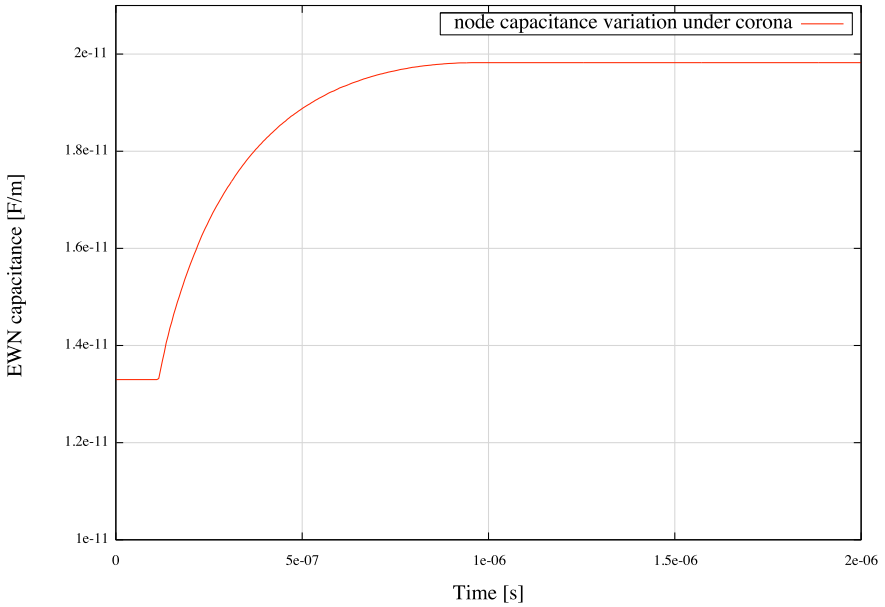

Figure 5-12: Change in node capacitance with radius increase.

An alternative approach to using the breakdown criteria to determine the radial extent of the corona is to allow the conductor radius to extend to the critical field for streamer propagation, ($E_{c.}$ = 0.5 MV/m). This is considerably less than the breakdown electric field for the wire and subsequently, the predicted radial growth of the corona is much greater. This is a truer depiction of events if using a more representative conductance or capacitance to describe the corona (see later). However, this is not the case when using the radius of the conductor. Using the streamer threshold in this situation places too great a demand for corona related change within too short a time. However, a decay constant can be employed to represent a gradual fall from the breakdown electric field to the streamer threshold. Chapter 4 refers to the general acceptance that the corona development is described as microsecond phenomena. Therefore, applying a decay constant, $\tau = 0.5\mu s$, gives a result as shown in Figure 5-13.

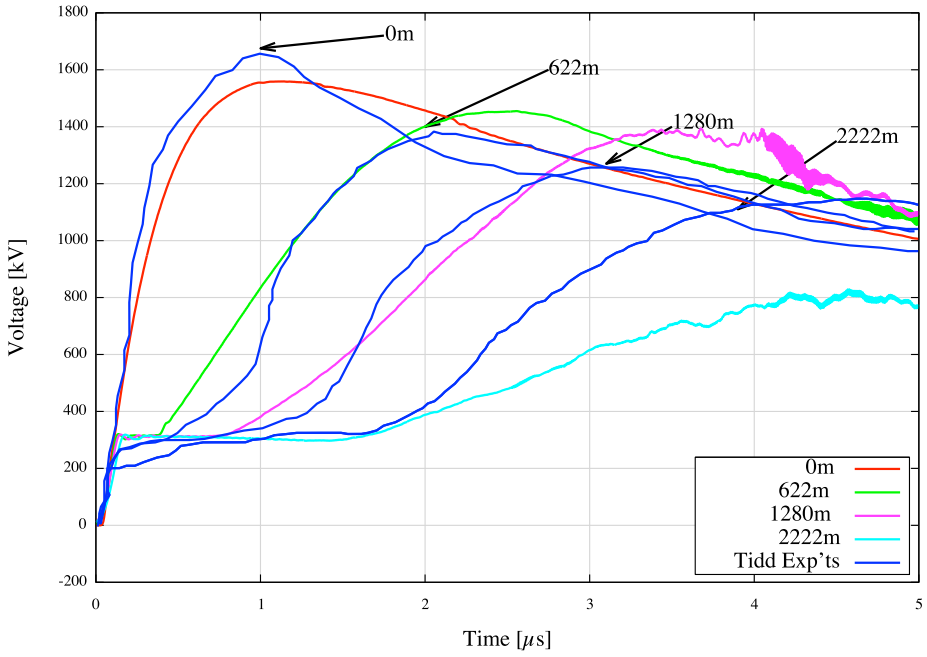

Figure 5-13: Using an increasing conductor radius to represent corona. The radial extent of the corona is governed by the streamer criterion (Ec = 0.5 MV/m) and a decay constant (= 0.5 μs).

The retardation of components near the breakdown field threshold are now closer to the experimental results although noise is evident on the waveform taken at points further down the line. This appears to be due to reflections from the end of the line.

If both capacitance and inductance are allowed to be represented by the increasing conductor radius the corona effects are (almost) negated (Figure 5-14). This is expected as the increase in capacitance is accompanied with a corresponding decrease in inductance such that the propagation speed is kept constant.

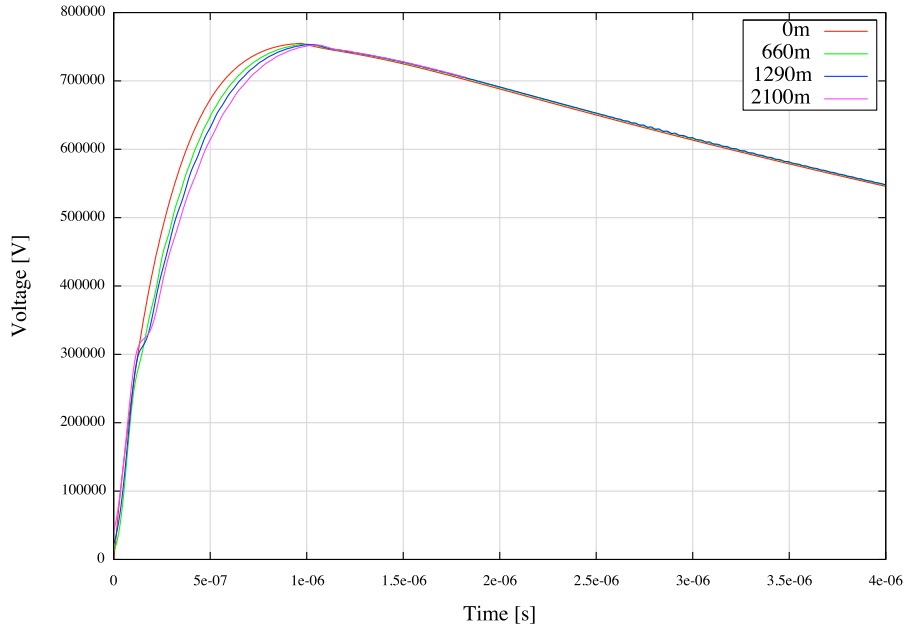

Figure 5-14: Both changes to inductance and capacitance are introduced to the EWN in accordance with the new conductor radius. The effects are dramatically reduced although some residual capacitance still appears to be unaccounted for.

The method demonstrates some success in recreating corona changes although the method lacks rigour for reasons already given.

5.2.2 Corona development as a region of nominal conductivity.

Next, an approach based on a method suggested Thang et al. is employed [55]. Their method relies on the introduction of a nominal conductivity to areas deemed to have undergone discharge around the wire. This is simplified by making the common assumption that discharge develops concentrically about the wire. Radial currents are instigated on the introduction of the conductivity and it is these that can be used to find the associated increase in charge generated. This allows a new radial progression of the discharge to be found at each subsequent time-step; the boundary dictated by the critical streamer threshold, E_c (= 0.5 MV/m), responsible for streamer propagation. The method is described in detail in chapter 4.

The team employ a graded mesh to allow the resolution about the wire to be increased, while at the same time employing a fine-wire technique to represent the wire boundary [84]. Here, the EWN is used to incorporate the wire. Using the EWN removes the need of increased resolution about the wire. Whereas many FD-TD cells were necessary to represent the corona sheath as it develops around the wire, now the EWN replaces many of them. Hence, the benefit of less computing is afforded. To adapt the methodology to suit the EWN, first, it is assumed the corona is limited to the EWN.

If the method described in chapter 4 is to be developed for the EWN, then the situation to consider, at least on an initial appraisal, is demonstrated in Figure 5-15. On initial reflection, it seems a simple calculation of the conductance based on the corona radius found using the equations (4.7)(4.8)(4.9) (Chapter 4) will suffice. However, this is not the case. This is clear from comparing radial corona currents; one from the calculations performed in the Thang et al. paper [55] and the other taken from the simulation (solving the Thévenin equivalent circuit) when the equivalent conductance is added to the node. The two currents are compared in Figure 5-16. The blue curve is the current as found leaving the wire within the simulation (Thévenin). The red curve is the radial conduction current calculated analytically (based on the local radial electric field on the surface of the wire within the simulation).

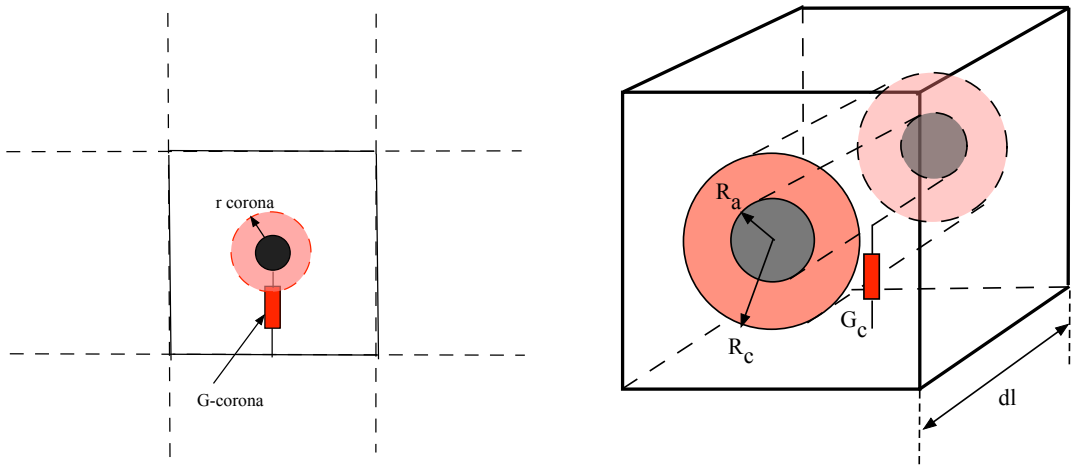

Figure 5-15: Development of conductance within the EWN as corona is deemed to develop.

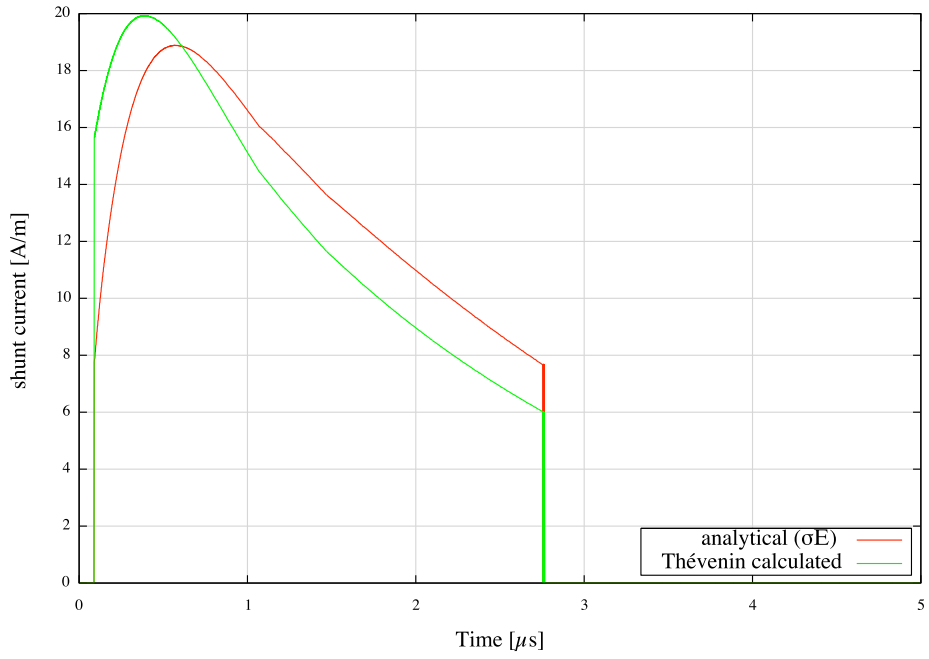

Figure 5-16 Comparison of the shunt corona current found analytically (red) and found solving the Thévenin equivalent circuit (blue).

Initially, the currents are quite similar but as the corona develops they become closer together. Mathematically, the comparison between the currents can be written as follows. For the simulation to behave correctly,

Shunt current (Thévenin circuit) = shunt current (Thang et al.)

That is,

$$G_c V_n = \sigma_c E_s \cdot 2\pi r_w \tag{5.9}$$

where G_c is the conductance representing corona within the node with a voltage V_n, and σ_c is the nominal conductivity representing the corona. E_s represents the radial electric field on the wire's surface. r_w is the wire radius. The corona conductance can be calculated using

$$G_c = \frac{2\pi\sigma_c}{\ln\left[r_c/r_w\right]}$$

The LHS of (5.9) can be written

$$G_c V_n = \frac{2\pi\sigma_c \cdot V_n}{\ln[r_c/r_w]} \tag{5.10}$$

The RHS of (5.9) can be written

$$\sigma_c E_s \cdot 2\pi r_w = \frac{\sigma_c q_w}{\varepsilon_0} \tag{5.11}$$

Where q_w is the per-metre wire charge. If the node capacitance is C_n, then $q_w = C_n V_n$, hence equating (5.10) and (5.11) :

$$\frac{2\pi\sigma \cdot V_n}{\ln[r_c/r_w]} = \frac{\sigma_c C_n V_n}{\varepsilon_0} \tag{5.12}$$

But

$$C_n = \frac{2\pi\varepsilon_0}{\ln\left[{}^{r_b}/_{r_w}\right]}$$

Hence,

$$\frac{2\pi\sigma \cdot V_n}{\ln[r_c/r_w]} = \frac{\sigma_c \cdot \ 2\pi \ \cdot V_n}{\ln[r_b/r_w]} \tag{5.13}$$

i.e. the equation is only satisfied when $r_c = r_b$. This makes sense when referring back to Figure 5-16 as during the corona development, r_c , will tend to r_b. If $r_c = r_b$ then the plots coincide (Figure 5-17).

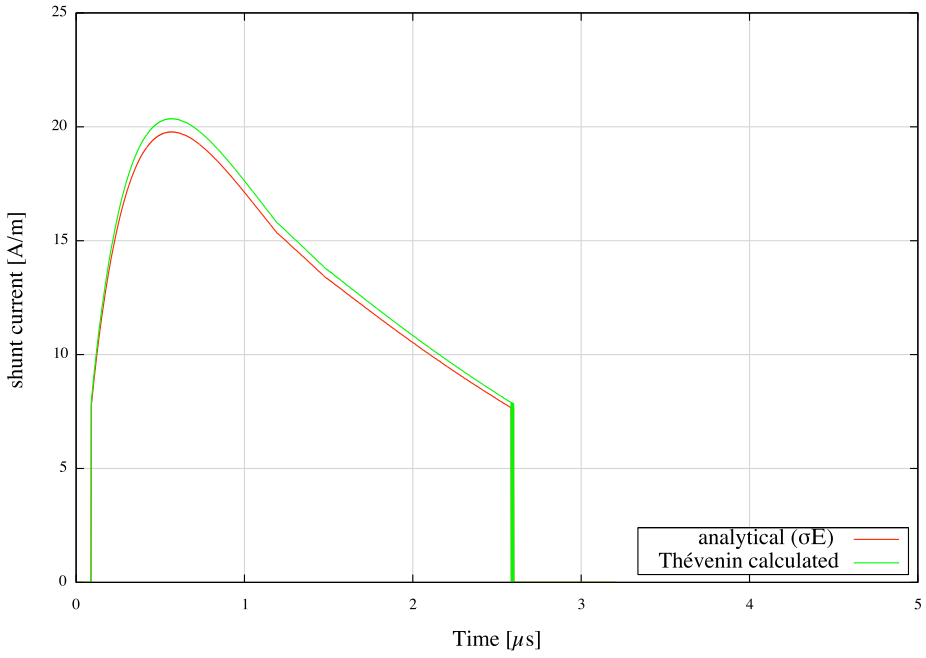

Figure 5-17 Radial corona current measured analytically and by solving the Thévenin circuit when the corona radius is fixed at cell boundary.

Instead, the situation that needs to be modelled is as shown in Figure 5-18.

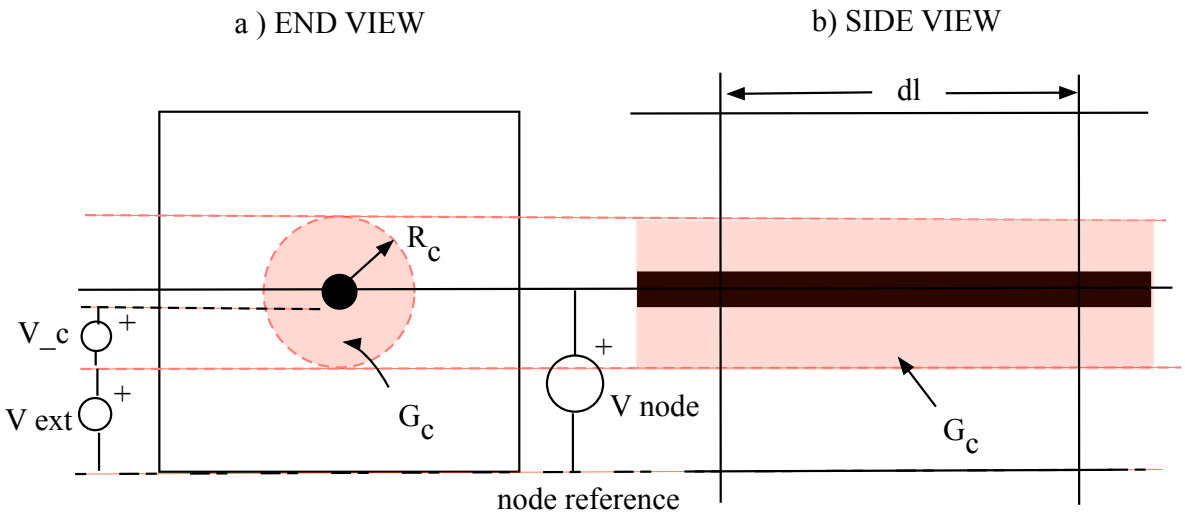

Figure 5-18 :The voltage distribution within the EWN during corona development.

The conductance associated with the corona sheath should only have a proportion of the total node voltage across it – depending on the corona radius. Figure (a) shows the corresponding Thévenin circuit, *V ext* is the voltage that remains within the EWN but outside the corona sheath. This appears to be the breakdown voltage for the node based on (5.4) with R_b equal to the equivalent node radius. This is intuitive as the effects are only exhibited when the node voltage exceeds the threshold. Alternatively, a current source can be placed in the circuit as shown. This current will be identical to the current in the Thévenin in figure (a) if the voltage outside the node is known. Despite this obvious solution it seems interesting to view the situation from a physical standpoint in both cases, especially, as there are some 1-D representations that use a corona conductance without seeming to take this into account [56].

The nominal conductivity chosen to represent the corona can be adjusted to suit the empirical results.

The routine that describes the simulation is as follows. For a particular wire segment (EWN):

1) Incident voltages from adjacent nodes allow the node voltage to be calculated. This can be used to obtain the charge on the wire (via the node capacitance-see chapter 3) and hence the radial electric field on the surface of the wire.

2) If the radial electric field is found to exceed the breakdown threshold of air, then corona is deemed to originate. Addition of nominal conductivity describes a radial corona current while a change in displacement current also occurs. These currents can be used to calculate the total charge on and about the wire.
3) This charge will exist in space about the wire within a radius dictated by the critical threshold for streamer propagation. Once this is obtained, a conductance that correlates with the charge formed and the conductivity chosen is added to the EWN to provide the corona related change.
4) The addition of this conductance for the given incident voltages means the wire charge has changed and hence the conditions on the wire surface also change. This can result in problems in terms of charge conservation. Hence, for a particular timestep an interaction is beneficial such that the wire charge, corona charge, corona radius and resulting conductance all converge.
5) The conductance is added and the scattered voltages allow voltages to be calculated at the subsequent time-step.

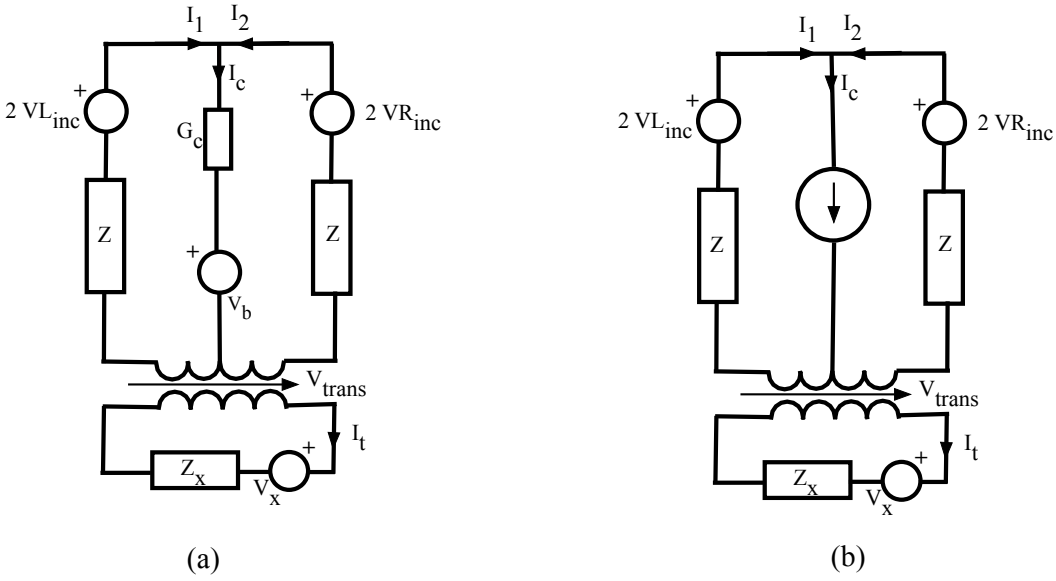

Figure 5-19: Thévenin equivalent node circuits representing the corona development: a) using conductance with a voltage source associated with node breakdown voltage, V_b. (b) Applying a current source, I_c, to the node to represent radial corona current predicted by the equations suggested.

5.2.2.1 Results

The following applies the theory to represent the Tidd experiments.

Mesh set up: conductor length 2222m, radius R_a, = 0.024m. Height = 13.5m above lossless ground. Critical background electric field, E_c= 0.5MV/m (positive corona). EWN side length, dl = 3m.

The conductivity chosen to represent the corona space charge about the wire can be chosen to meet the empirical data. Thang et al [83] settled on a value of 100 μS/m. It was found that a conductivity value of 110μS/m best suited the data in the simulations adopted here.

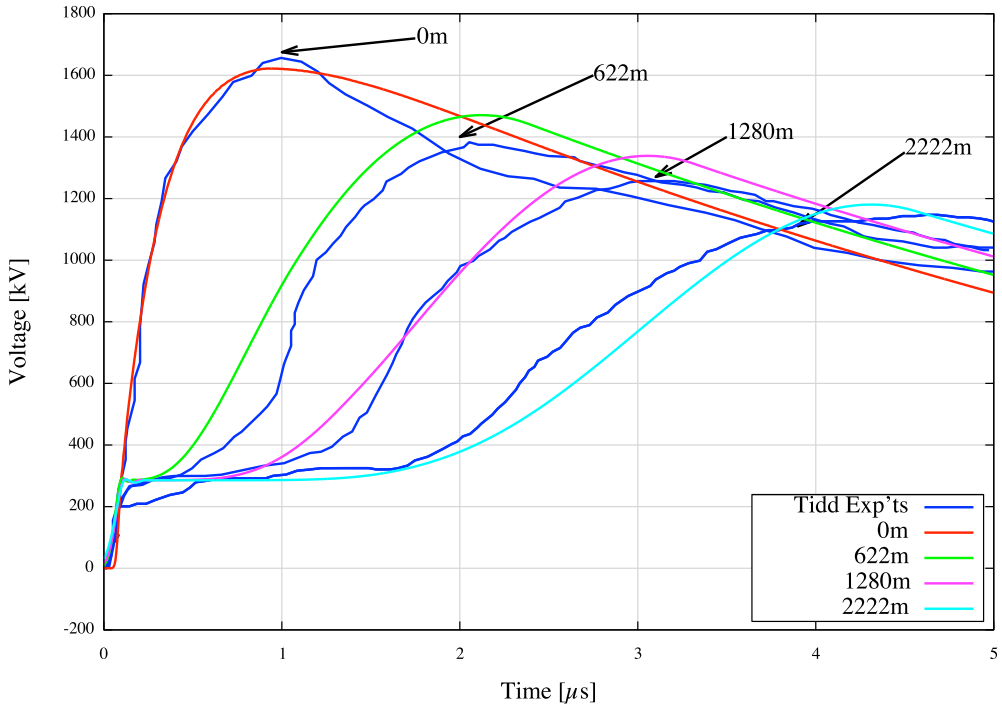

Figure 5-20 Distortions on a propagating waveform applying conductance obtained using a corona conductivity of 110μs using the method proposed by Thang et al [55] adapted to be used in the TLM-EWN.

The waveforms differ from those obtained by Thang et al [83] in two aspects. First, the distorted waveforms here demonstrate an 's' shape along the anterior edge of the corona associated wedge. This seems to be present on the experimental data also. The Thang et al

simulations do not seem to exhibit this. Secondly, an edge on the peak of each waveform is created in the simulations provided here. This is produced by forcing the charge formation to stop as the line voltage falls below the breakdown threshold. Figure 5-21 shows the waveforms when this aspect of corona development is removed.

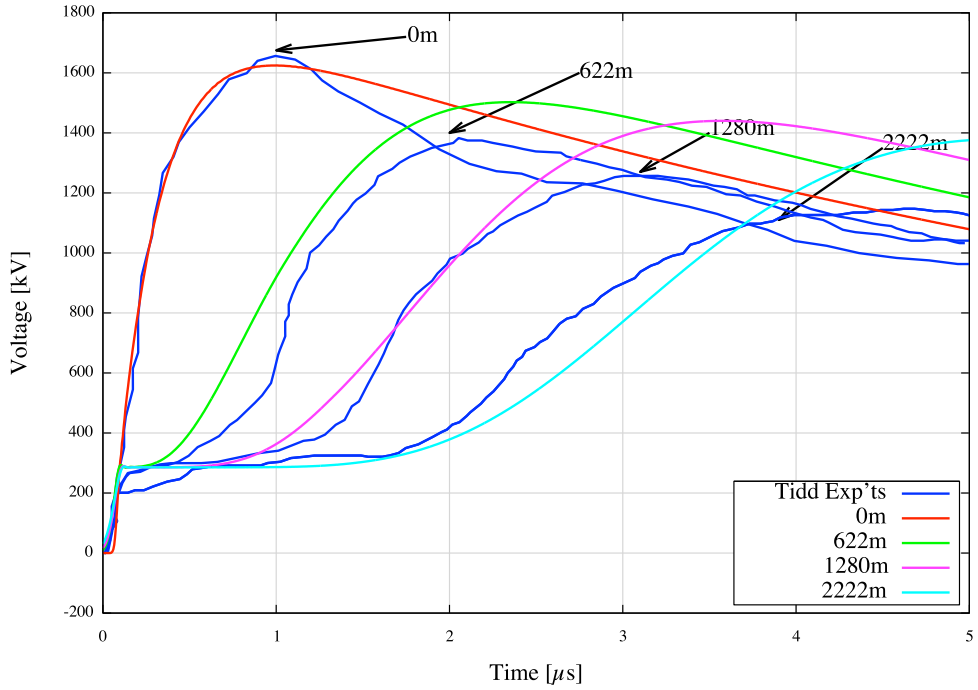

Figure 5-21 Corona distortions but allowing the corona space charge to remain post peak voltage despite surface electric field falling below E_b. Note the attenuation of the waveform is reduced.

It should be possible to incorporate the corona current predicted by equations (4.7)(4.8)(4.9). Augmenting the EWN with this corona current results in the Thévenin circuit as shown in Figure 5-19(b). However, the nearest recreation of the experimental data required a reduction in the nominal conductivity (40 μS/m). Results obtained using this node are revealed in Figure 5-22. An absence of the 's' shape at the anterior wavefront referred to previously is immediately evident similar to the plots obtained by Thang et al. [83]. This may imply there is

a better way of incorporating the current within the EWN. The need for reduced conductivity may suggest that the current is having a bigger effect within the node than is required and therefore a different circuit would best represent the current leaving the wire.

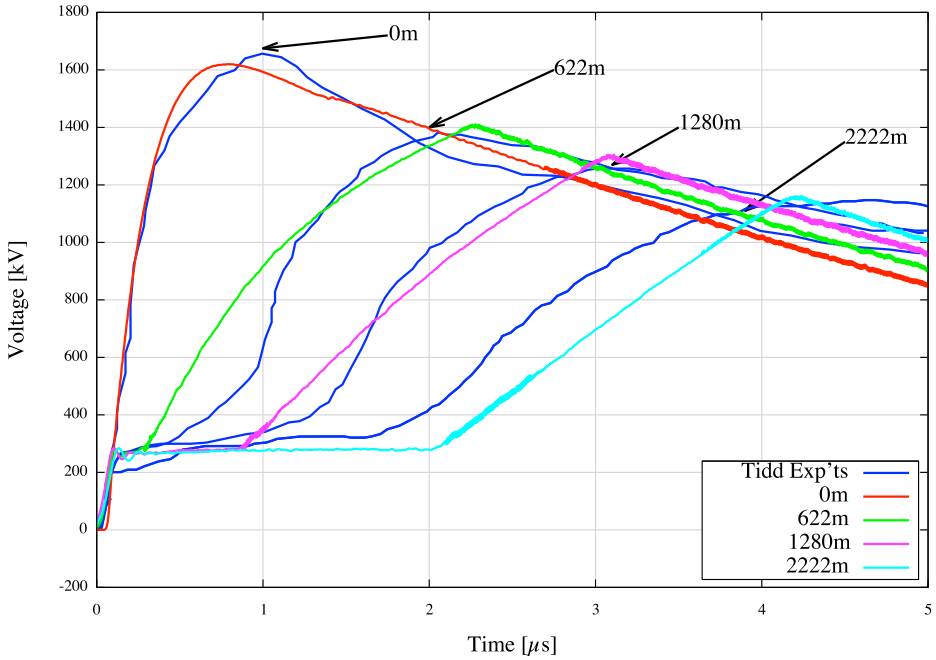

Figure 5-22 Using a corona conductivity of 40 μS/m to represent the corona sheath. The associated conduction current is added as a current source to the EWN.

The q-V characteristic for this particular simulation (taken at the initial output) is shown in Figure 5-23 . Also plotted are the independent charge quantities namely, the charge contained within the corona sheath and the line charge found by integrating the conduction current and the displacement current respectively. Both currents rely on the radial electric field on the wire surface found using the node capacitance as described in chapter 3.

If the displacement field outside the EWN is obtained by monitoring the radial electric field at nodes transversely adjacent to the EWN such that the field monitored is beyond the corona space charge (and wire charge) the same q-V is also obtained; the associated displacement current allowing the total charge to be found within the EWN (wire and space charge) Figure 5-24 compares both methods of finding the q-V relationship.

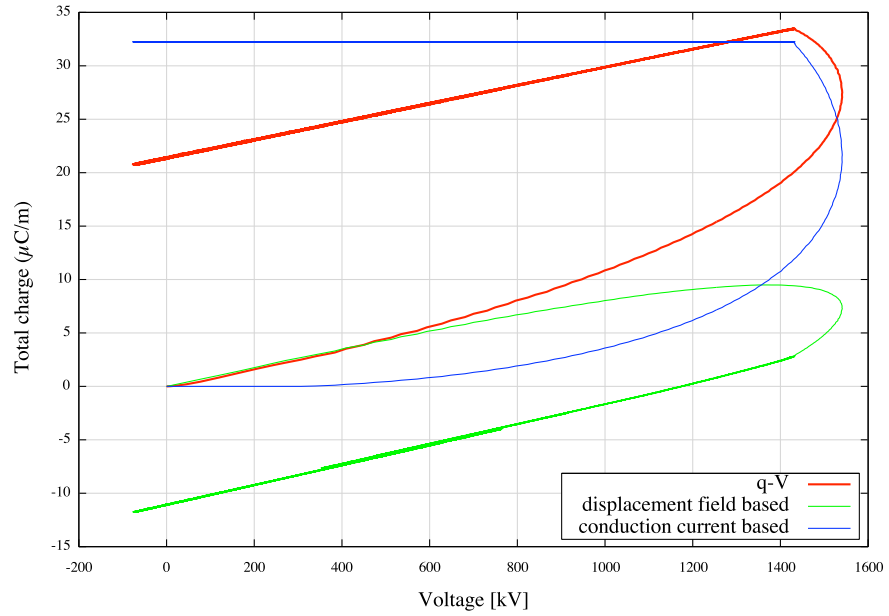

Figure 5-23 The q-V characteristic (red) for the method described by Thang et al. Also plotted are the individual charge quantities; blue - charge contained within corona sheath, green- line charge.

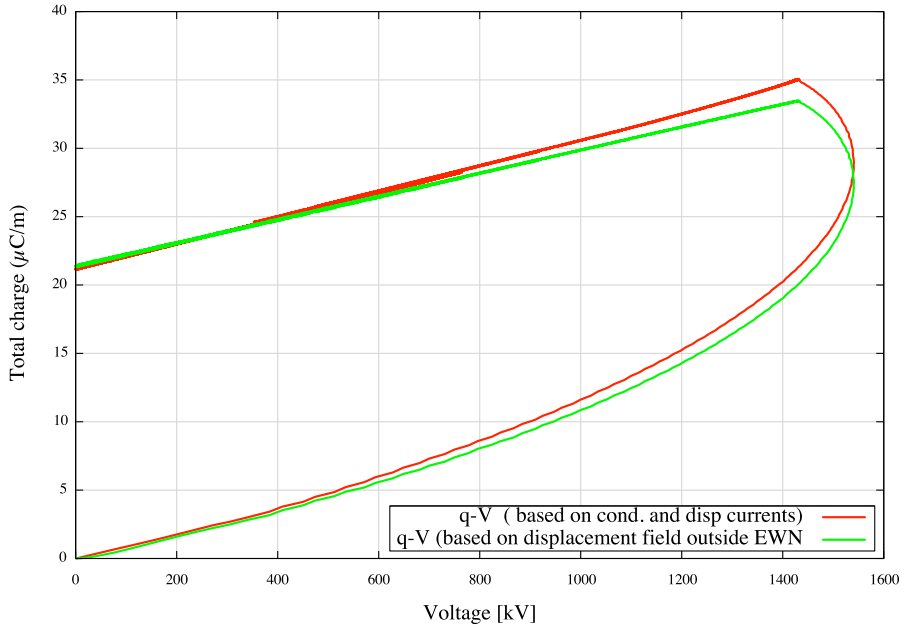

Figure 5-24 The q-V characteristic found by integrating the conduction and displacement currents within the EWN (red) and integrating the displacement current outside the EWN (green).

5.2.3 Simulating corona development based on parameters found using the Cooray Equations.

Chapter 4 presented the equations, (4.11) to (4.21), developed by Cooray [61] (henceforth termed the 'Cooray Equations') that described the corona development around a conductor in a coaxial arrangement when subjected to suitably high applied voltages. The corona is described in terms its charge content, corona charge density and radial development in relation to the applied voltage. The corona is assumed concentric about the central conductor. Hence, the theory is based on the respective capacitances that develop within the coaxial arrangement. The method forces the radial electric field on the wire surface to fall in accordance to a decay constant, $\tau = 0.5\ \mu$s, thus maintaining the corona development adheres to a microsecond timeframe.

It is hoped therefore that the equations can provide a real-time account of the expected charge development within the EWN. The EWN is essentially a coaxial system so the equations appear suited.

Before applying the theory to the voltage encountered in the Tidd experiments, the equations are applied to the coaxial system as defined by Cooray in his paper. The arrangement is comprised of a central conductor with radius $R_a = 0.0035$ m, and outer conductor radius, $R_b = 0.4$m.

The background field necessary for streamer propagation, E_c, deemed best to achieve correct results was set at 530 kV/m for positive corona. The conductor length was set at 1m to allow for 'per metre' parameters. The line is excited using a bi-exponential voltage with peak = 200 kV. The breakdown field is that predicted by Peek's equation [33]. Although Cooray does not explicitly provide this value, the value predicted for a perfect wire is approximately 19 MV/m. This would translate to a breakdown voltage above the peak voltage applied to the wire. From the q-V graphs Cooray provides, breakdown occurs around the 100 kV mark [61]. Hence, the wire-surface factor, k, included in Peek's formula, that pertains to the surface conditions of the wire can be adjusted accordingly to give the desired breakdown

field/voltage. This amounts to $k = 0.3$. For the given dimensions, this predicts a value for corona inception, E_b to be $\approx 6\ \mathrm{MV/m}$.

The Cooray corona equations [61] provide the modeller with the corona charge expected for a given voltage over threshold. The charge can then be used to calculate other related parameters, such as corona current, corona-related capacitance that can be introduced to the simulation. The charge development with applied voltage can be used to plot a q-V characteristic unique for a particular conductor arrangement. Applying the equations to an EWN with length dl = 0.8m creates an identical q-V graph to that developed by Cooray in his paper (Figure 5-25).

The q-V graph (red) demonstrates the deviation from the geometrical capacitance of the line once breakdown voltage is exceeded. The graph also shows the development of corona charge with voltage (blue) and the fall in wire charge once corona initiates (green). Once the peak voltage has passed, initially the corona charge stays at a maximum while the fall in voltage is maintained by the fall in line charge. However, eventually the charge on the wire falls to such an extent that a back corona initiates of opposite polarity to the original. At this point, the line charge is kept constant and a non-linear fall in total charge occurs from around 120 kV downwards.

The equations allow the radial development of the corona to be traced with time as shown in Figure 5-26. The corona radius is kept at a maximum once the peak voltage is met. As the equations allow the modeller to obtain the variation of corona charge within the corona sheath with time, a radial corona current ($I_c = dq_c/dt$) can be described. This is revealed in Figure 5-27. On corona inception, the current jumps to near its peak value. The rate of space charge formation decreases steadily until the peak voltage is met at which time the corona charge reaches its maximum value and the current falls to zero. The corona charge also allows additional capacitance attributable to the corona development to be plotted with time as can be seen in Figure 5-28. Finally, the additional capacitance can be used to calculate the associated conductance ($G_c = dC_c/dt$). The development of this conductance with time is plotted in Figure 5-29

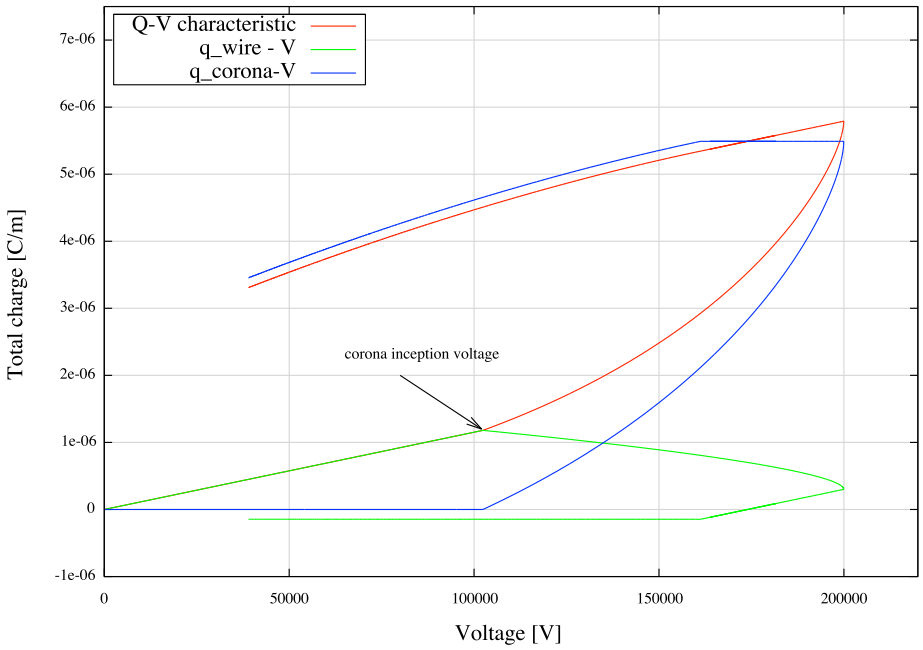

Figure 5-25: Q-V graph (red) created when applying the Cooray equations to an EWN with side length = 0.8m. R_a = 0.0035m, and outer conductor radius, R_b = 0.4m. Breakdown voltage V_b = 102kV. The other curves show the predicted increase in corona charge post breakdown (blue) and the simultaneous fall in line charge (green).

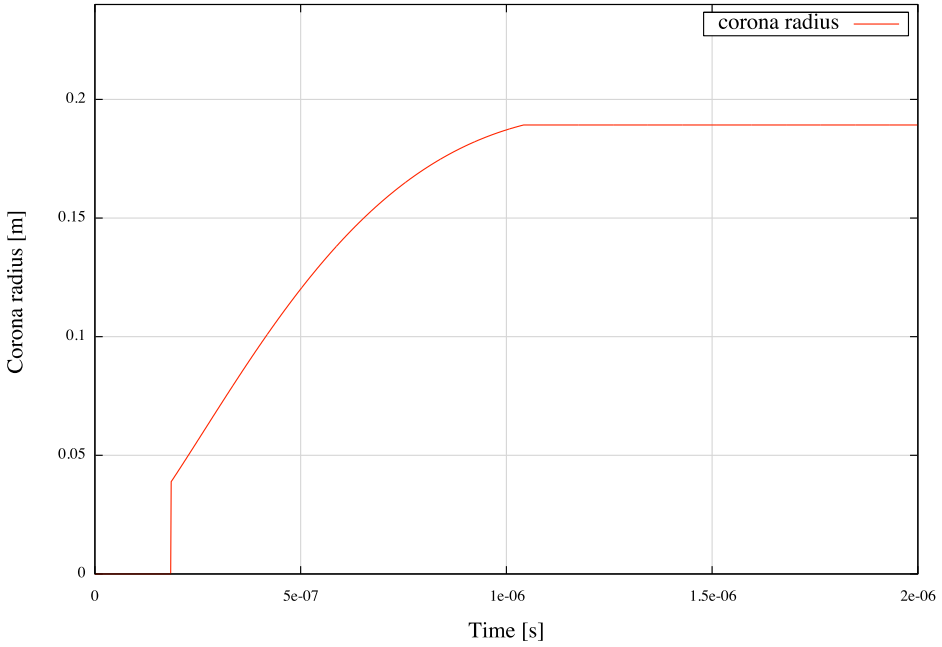

Figure 5-26 Radial development of corona

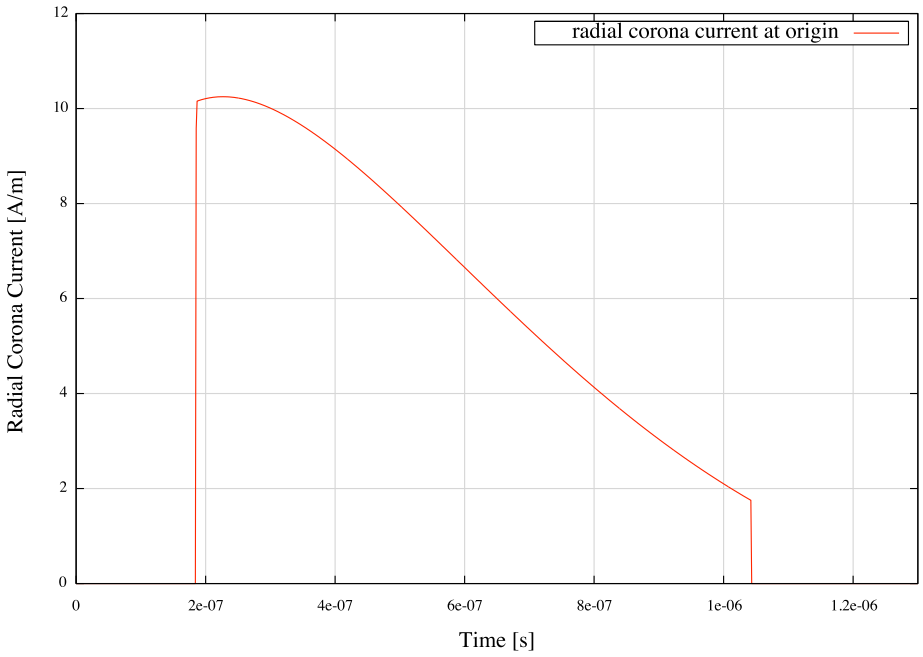

Figure 5-27 Radial corona current [A/m] variation with time.

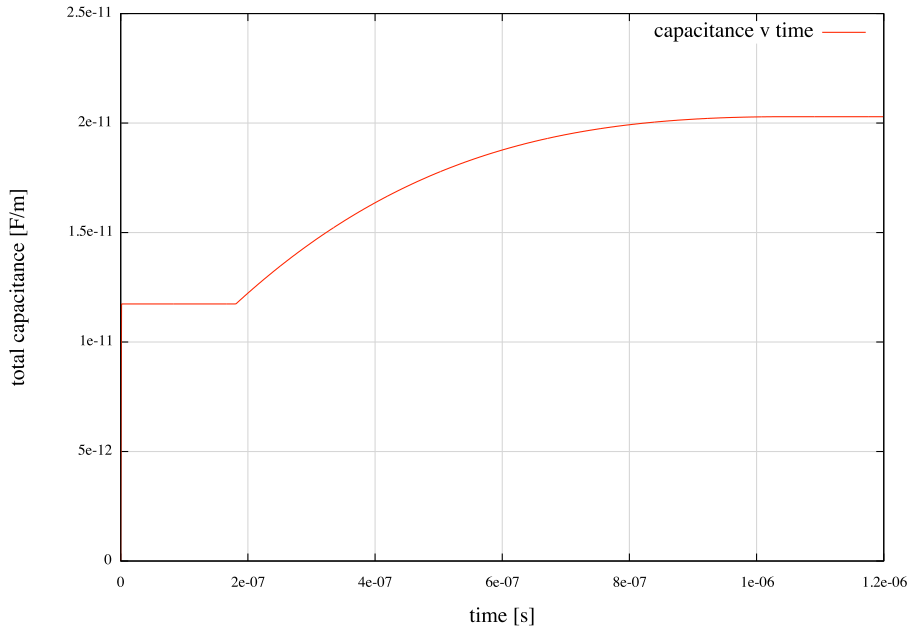

Figure 5-28 Capacitance increase during the corona development found using the corona charge given by the Cooray equations.

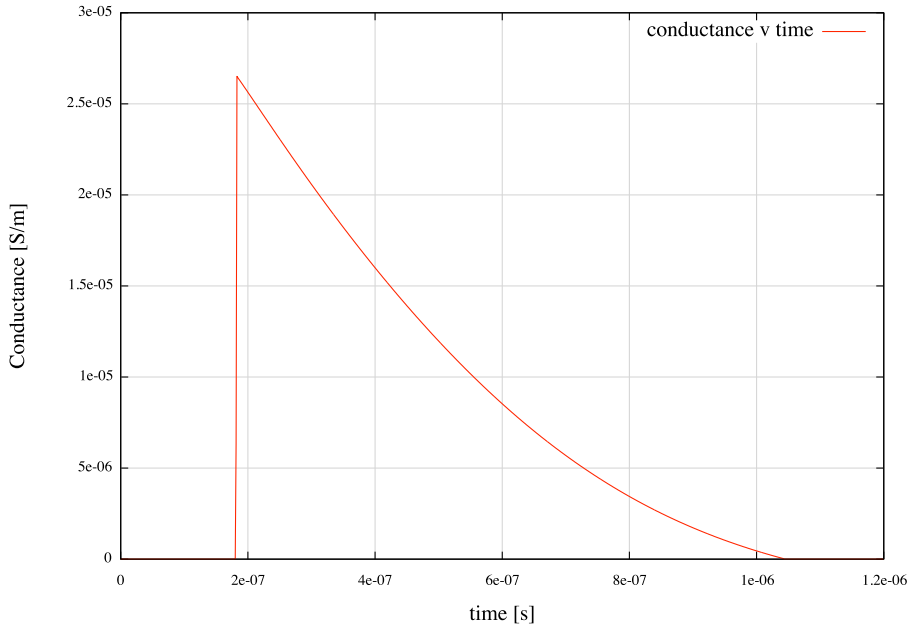

Figure 5-29 Conductance variation associated with corona development found using the time derivative of capacitance.

Hence, the equations have been shown to behave for a cell of length 0.8m when a peak voltage surge of 200 kV is applied. However, there will be a voltage magnitude that will cause the corona radius to exceed the radius of the EWN. Figure 5-30 compares the corona radii for a range of peak voltages. As can be seen from the graph, a peak voltage of 250 kV causes the corona radius to exceed the cell boundary of 0.8m. This cannot be allowed to occur as the equations become infinite as essentially they are based on capacitance; i.e. the terms 'ln $[R_b/R_a]$' tend to zero. This is a consideration in all of the simulations. When implementing the method to applied voltages of higher magnitude, such as those encountered at Tidd, an EWN of greater length is necessary to accommodate the corona development there.

When attempting to emulate the experimental data from the Tidd experiments, an EWN of side length 3m is used. First, the simulated space charge development within the corona is used to calculate the additional dynamic capacitance necessary to be added to the EWN.

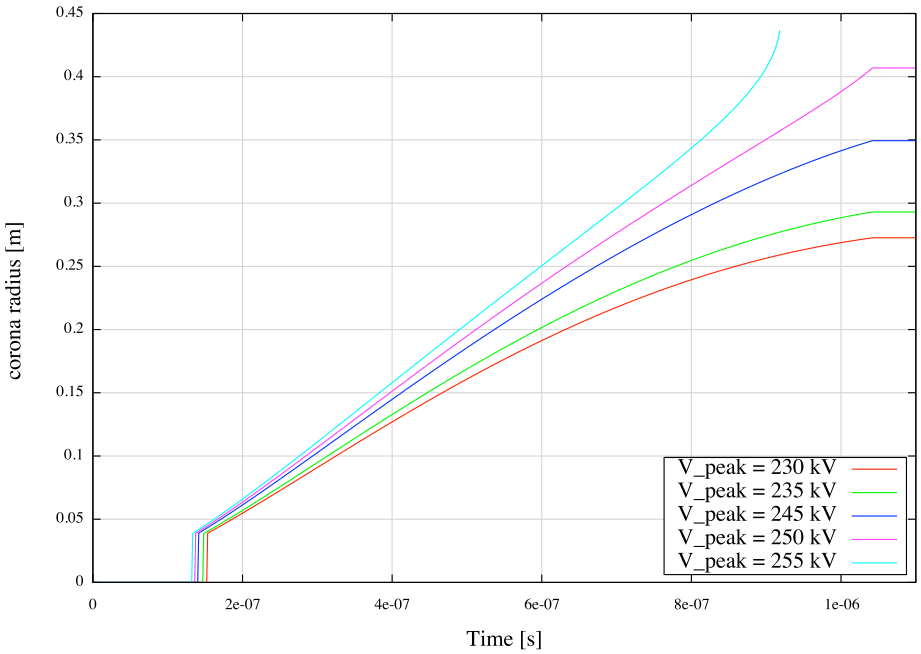

Figure 5-30 Comparison of corona radii that develop for a range of surge waveforms with differing peak voltages.

Figure 5-31 shows the Thévenin equivalent circuit of the EWN used to introduce the corona capacitance to the model, where Z_c is the impedance of the stub used to represent the additional capacitance. Again, the breakdown voltage must be accounted for such that the increase in capacitance only exist for voltages above this threshold. Note the similarity between this circuit and the circuit adapted to accept conductance in the previous section (Figure 5-19(a)). Pulses scattered via the impedance, Z_c are reflected back to the node at the next timestep. Pulses scattered by the conductance in Figure 5-19 (a) can be imagined to be sent along an infinitely long stub such that they are never returned to the node. The results generated are revealed in Figure 5-32.

The simulation appears to slightly underestimate the actual distortions found experimentally. The ‘S’ profile on the wave-front, above the voltage threshold is still apparent.

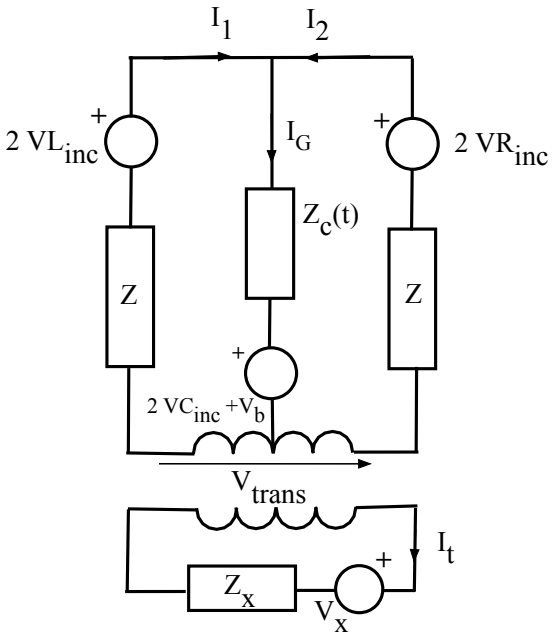

Figure 5-31Thévenin equivalent circuit used to deliver the extra capacitance suggested by the Cooray Equations to recreate corona effects.

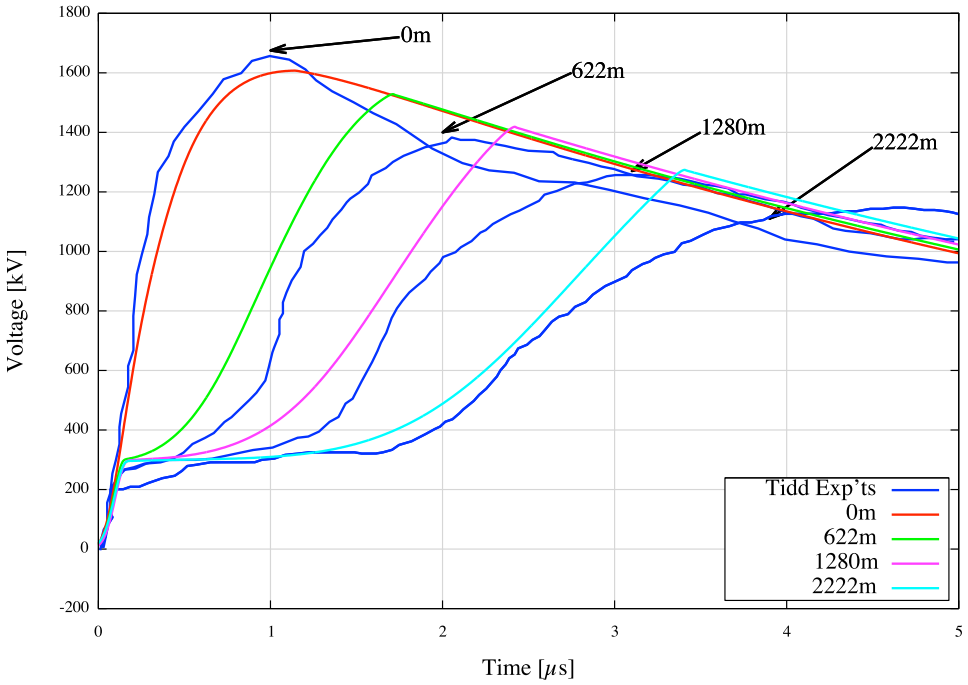

Figure 5-32 Using additional capacitance associated with the corona charge as predicted by the Cooray equations.

Increasing the additional capacitance predicted by the Cooray equations by a factor of 1.3 seems to achieve a greater correlation with the experiment as shown in Figure 5-33.

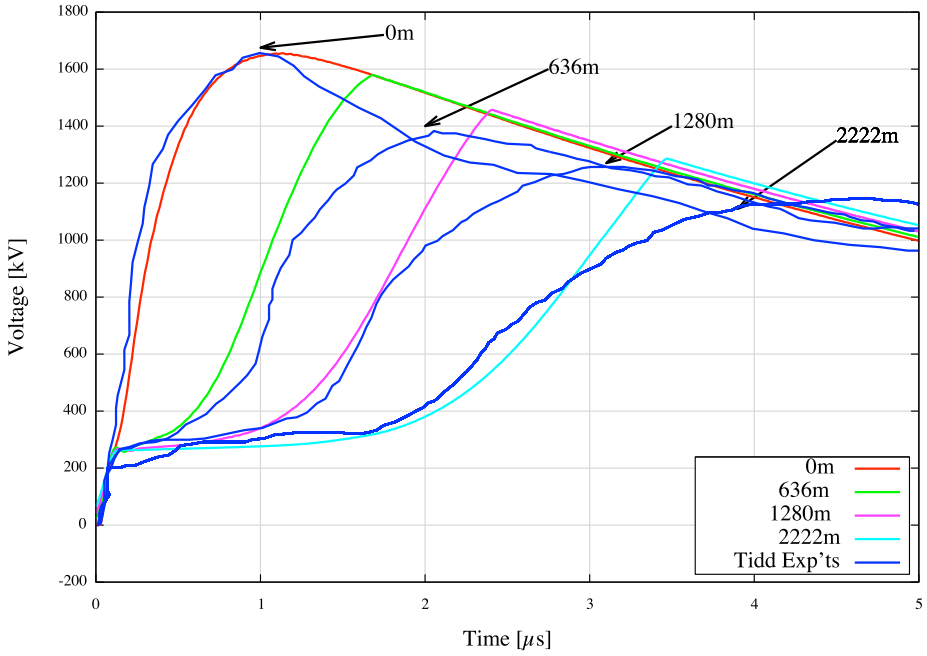

Figure 5-33: The distortions on a propagating waveform when the addition capacitance suggested by the Cooray equations in increased by a factor of 1.3. A closer match to the experimental data is achieved.

The retardation of voltage components towards the peak of the waveform seems reduced relative to those found experimentally.

The time-derivative of the additional capacitance gives the associated conductance increase. However, introducing time-derivatives to the simulation introduces numerical errors in so far as erratic conductance profile is created. This is exaggerated the further along the wire the signal has travelled. Figure 5-34 presents an indication of such a conductance profile. Hence, if the additional conductance related to the space charge within the corona sheath as predicted by the Cooray Equations is to be implemented, then another way of calculating this while still using the parameters offered by the Cooray Equations is necessary. One option is to allow the predicted radial development of the corona predicted by the equations and a nominal

conductivity to describe the space charge in a similar way to the model proposed by Thang et al [55]. Choosing a conductivity of 110 μS/m to represent the space charge as was used in the Thang approach gives a result as shown in Figure 5-35.

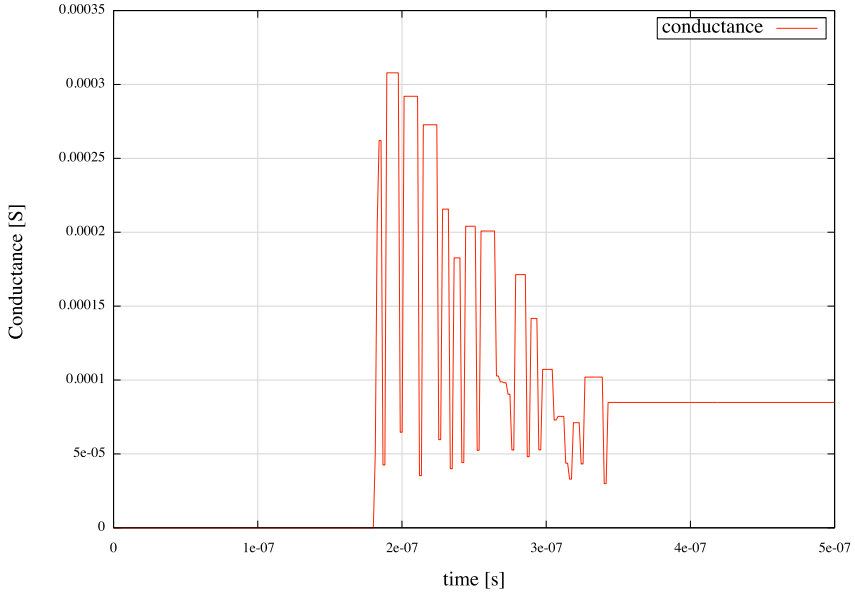

Figure 5-34: Typical corona conductance profile found by taking the time derivative of corona associated capacitance.

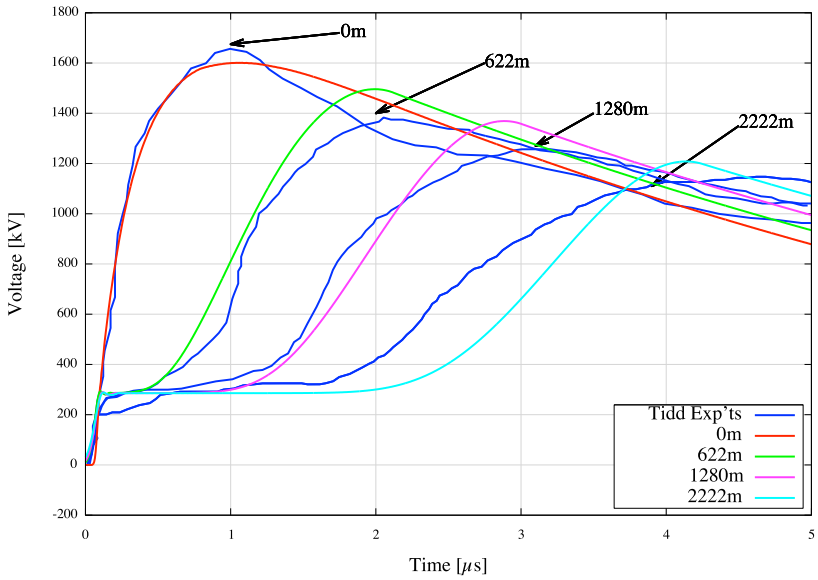

Figure 5-35 Using the corona radius as predicted by the Cooray equations and a nominal conductivity of 110 μS/m to obtain an associated corona conductance to create corona realated distortions on propagating waveform.

This choice of conductivity seems to overshoot the distortions slightly.

The shunt corona current can also be calculated from the corona charge development as predicted by the Cooray Equations. However, again this involves a time-derivative (of corona charge development) and so the same numerical noise occurs as in the case for the conductivity calculations. Cooray uses the corona current found by the equations he devised in a paper to recreate the characteristic distortions in an overhead line [57]. However, in his paper he acknowledges that the corona current profile will change as the signal propagates along the line. Instead, he injects a corona current profile as found at the injection point. Hence, using a similar principle, the corona current offered by the Cooray equations is used to recreate the results from the Tidd experiments.

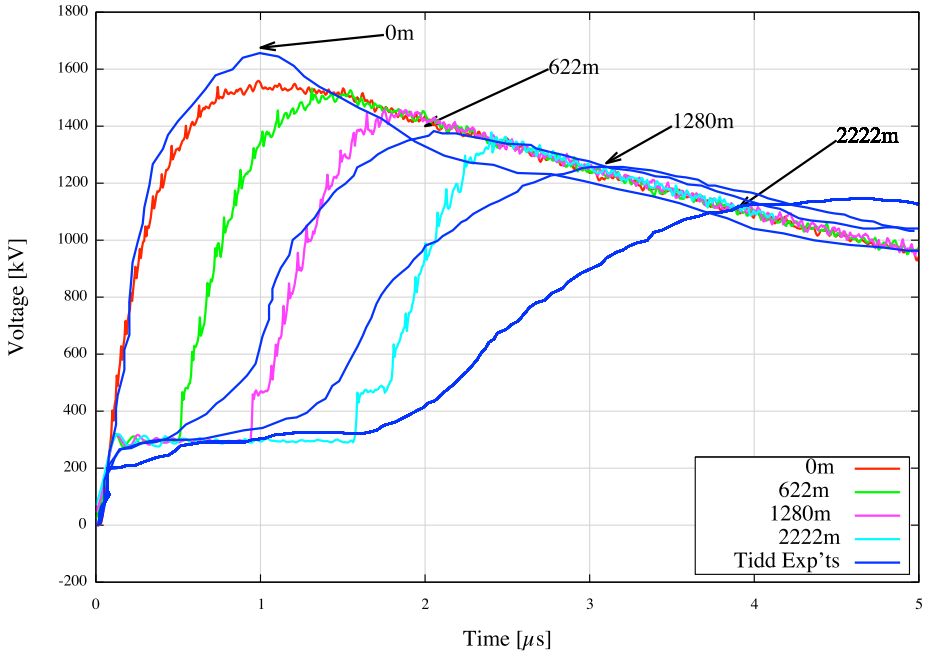

Figure 5-36 Using a corona current source as predicted by the Cooray equations to recreate distortions on a propagating waveform.

The results still exhibit some noise. Also, the results seem to misrepresent the experimental results as the applied voltage components becomes increasingly greater than the breakdown threshold.

5.2.4 Soil breakdown.

Dielectric breakdown of soil can occur under electromagnetic stresses such as those encountered in lightning strikes. Such phenomena were once a neglected aspect of modelling efficiency when investigating grounding protection systems but lately, the inclusion of this behaviour when simulating grounding efficiency in soil are more common place.

Gazzana [56][78] provides a 1-D simulation to investigate the phenomenon. The principle rests on assigning a critical line-current value, I_B, that relates to the critical surface electric field for ionisation in soil, chosen to be E_{cs} = 350kV/m. The actual ionisation in soil is again of a filamentary nature due to its inhomogeneity but for modelling purposes, the breakdown is usually confined to a uniform, concentric region about the electrode. This is then compared with the line current and when the field on the surface of the electrode exceeded the threshold (or equivalently when the line current exceeds I_B) a factor, K_{ion}, which relates the two currents, is used to increase the conductivity of the soil the electrode is situated and hence decrease the grounding resistance of the grounding system. The theory is described in more detail in chapter 4.

Being a 1-D TLM simulation begs the question how accurately the radial (transverse) voltage and current properties are represented. Sure, an electrode can be represented as a simple transmission line (see Figure 4-16(a)), such that the conductance in the absence of ionisation correlates to the spatial extreme at which the potential is zero. However, when considering ionisation about the electrode such variations in conductivity local to the wire are lumped in as if all the soil (to the radial extent at which potential is zero) has changed. Hence, the multiplication factor that relates to the electrical breakdown is essentially changing the conductivity of the whole environment that is soil based.

If the method is translated to a 3-D domain, then if the same principle is used to represent the ionisation effect, the option remains as to whether to change the conductivity of all the soil or instead limit the increase in conductivity to a region about the wire. This region could relate to the critical field in the usual way i.e.

$$r_c = \frac{I_c \cdot \rho_s}{2\pi \cdot dl \cdot E_c} \tag{5.14}$$

Hence, a 3-D representation of the method based on the method proposed by Gazzana is applied to a horizontal buried rod. Three potentials are calculated; the potential when no ionisation take place, the potential when a region dictated by the critical field is ionised (and hence increased locally by the factor K_{ion}) and finally a potential when all the conductivity is increased.

In his paper, Gazzana [56], applies the method to a number of soil resistivity / relative permittivity combinations. To compare the methods described above just a soil with resistivity of 270 Ωm and relative permittivity = 12 is investigated. Gazzana uses a pulse with a particularly slow rise-time (bi-exponential: $50(8\times20)$ kA). Here, for the purposes of the above investigation both the slow pulse and the original faster pulse used in all the previous simulations is applied to the electrode. The electrode has a radius of 0.0065m and is buried horizontally, at a depth of 0.5m.

First, bi-exponential current source, as used by Gazzana is injected into the origin of the electrode. Figure 5-37 compares the potential under the three options described above.

The results for electrode potential when no ionisation is considered and for potential when the whole soil conductivity is affected are very similar to those obtained using the1-D TLM approach. However, considering a smaller region about the electrode in accordance with radial region that is affected by ionisation subsequently reduces the effect.

If a faster rise-time pulse is used, the relative potentials are as shown in Figure 5-38. Hence, it appears 1-D approaches maybe slightly over-estimating the effect unless the field outside the ionised region is somehow accounted for.

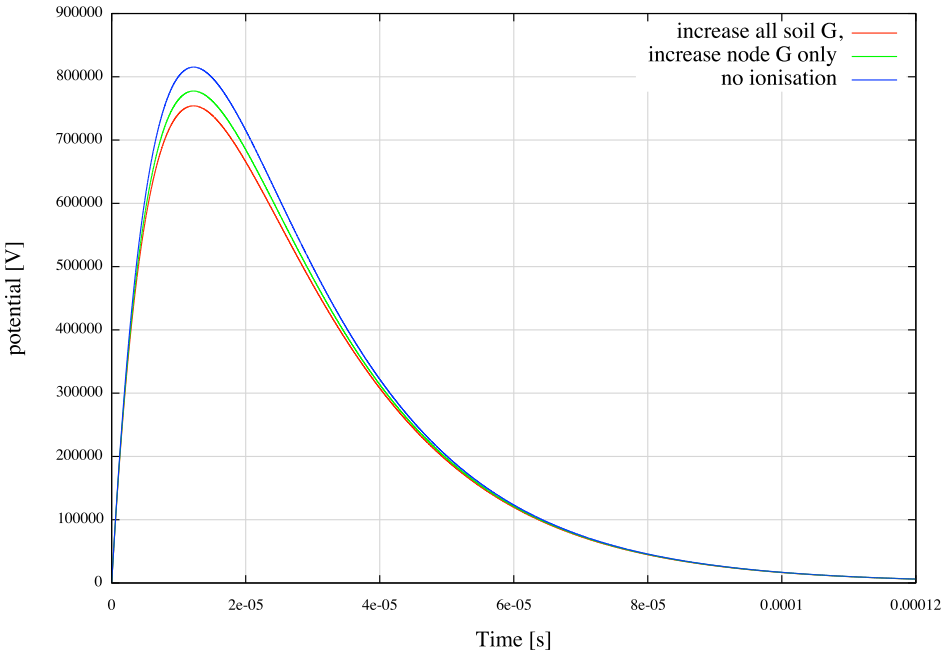

Figure 5-37 comparing the effect of the ionisation factor when applied to varying regions of soil.

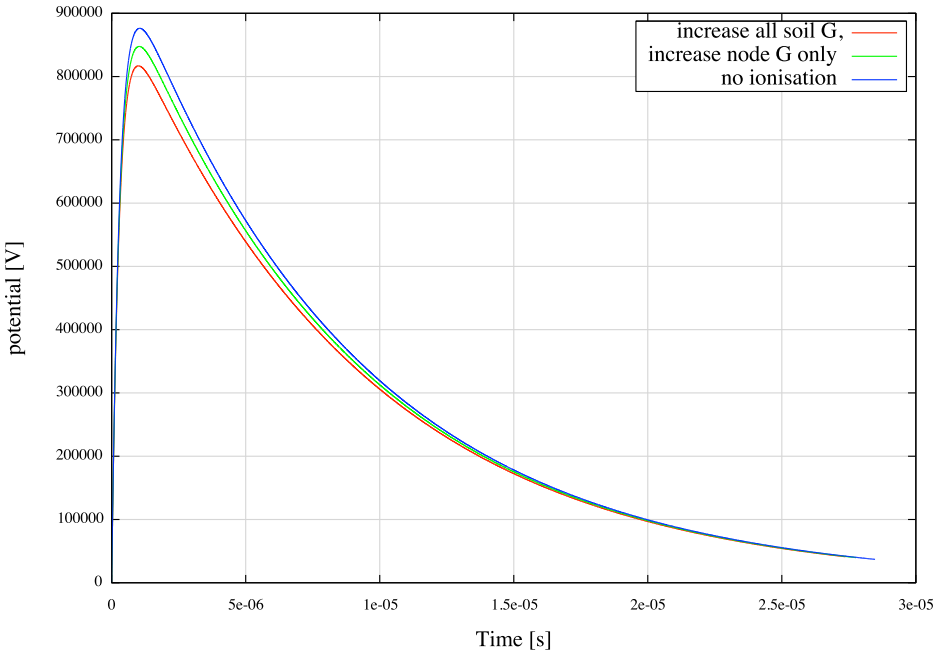

Figure 5-38 Varying regions of soil affected by the ionisation factor related to line current and critical electric field

The following uses the full conductive region to compare ionisation effects for a fast pulse injected into the origin of an horizontal electrode in soils of varying permittivity and resistivity as in the Gazzana papers [56][78].

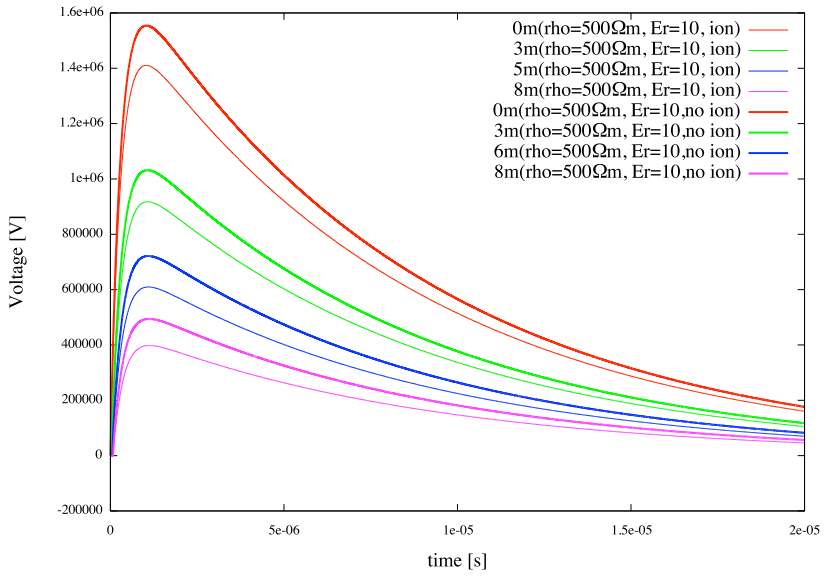

Figure 5-39 Comparing pulse waveform at equidistant points along a 12m grounded horizontal rod with and without the effects of soil ionisation ($\rho_s = 500\Omega\text{m}, \varepsilon_r = 10$).

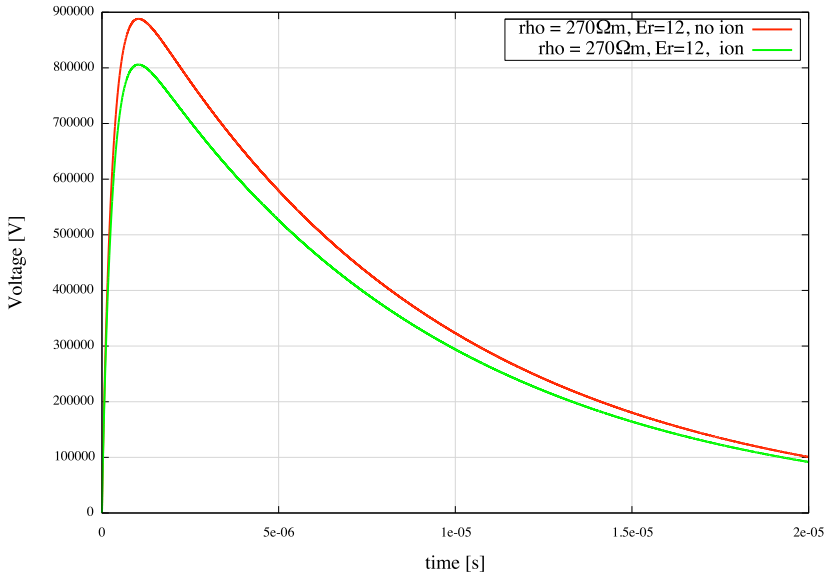

Figure 5-40 Comparing the inclusion of soil ionisation effects on the potential of a horizontal electrode buried in soil ($\rho_s = 270\Omega\text{m}, \varepsilon_r = 12$).

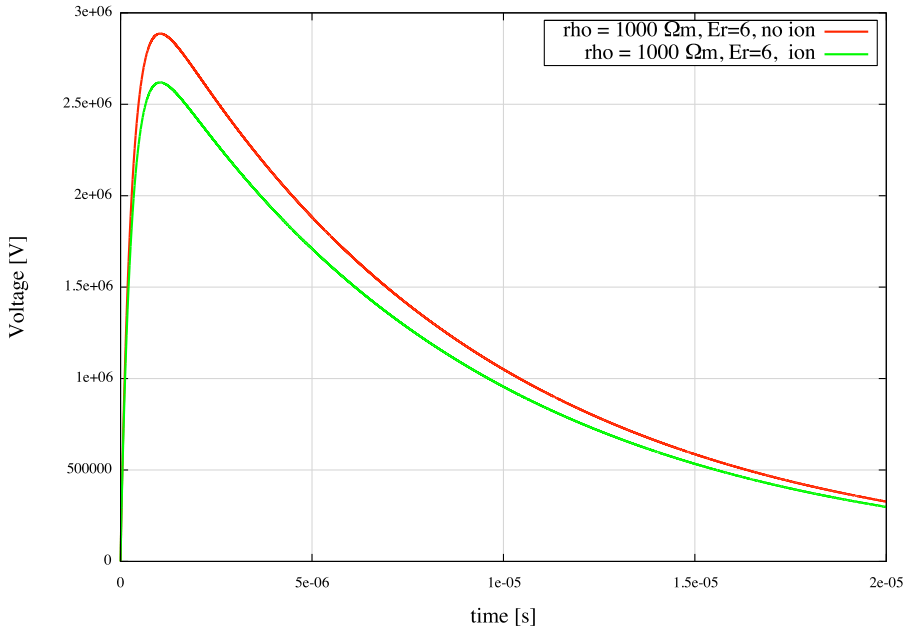

Figure 5-41 Comparing the inclusion of soil ionisation effects on the potential of an horizontal electrode buried in soil ($\rho_s = 270\Omega\text{m}, \varepsilon_r = 12$).

As expected, the grounding potential is reduced when ionisation effects are taken into account.

The ionisation plays an important role when considering threats to human and animal life when situated in areas close to lightning strikes as the potentials on the ground surface can lead to electrocution. The potential differences that pose the problem can be classed as 'touch', 'step' and 'transferred'.

The 'touch' potential difference would, as the name suggests be encountered if the subject it is contact with the stricken entity, with a hand, say, and another part of the body in contact with the ground near the electrode. Hence the potential difference between ground surface and electrode generates the current. Figure 5-42 plots the potential on a contact point connected to the electrode origin (red curve), and the potential on the ground surface when ionisation effects are ignored (blue curve) and ionisation effects are included (green curve) for a horizontal electrode buried in soil with resistivity = 1000 Ωm and relative permittivity = 6.

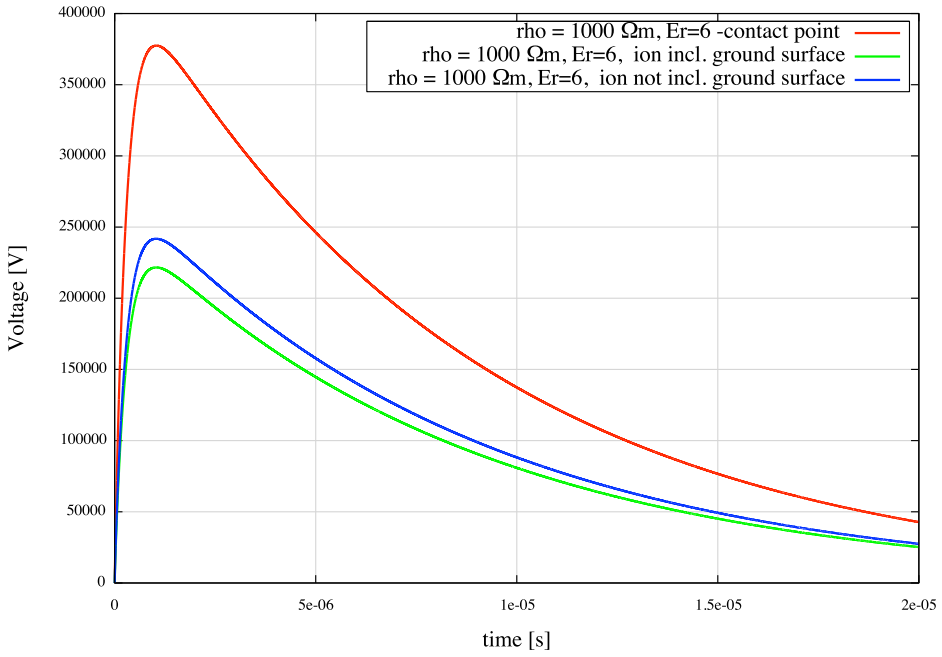

Figure 5-42 Touch potential: The difference between the contact potential and the ground potential is the touch potential ($\rho_s = 1000\Omega\text{m}, \varepsilon_r = 6$).

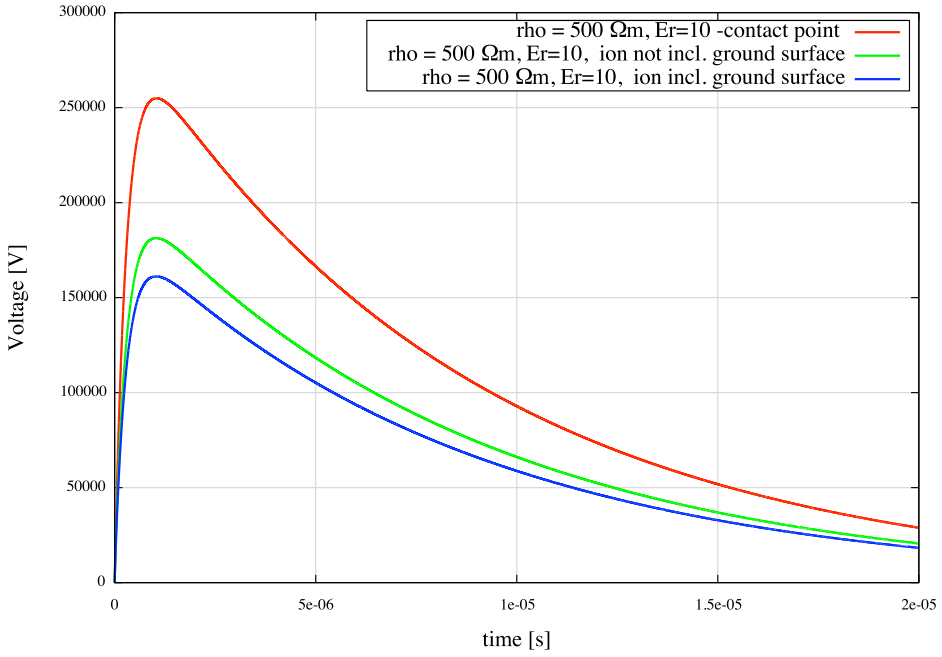

Figure 5-43. Touch potential ($\rho_s = 500\Omega\text{m}, \varepsilon_r = 10$).

The step potential is formed by the potential difference between the feet on the energised ground surface. In the example below, a person is assumed to be standing on the ground, above the electrode at about half its length. The person's feet are assumed to be 1m apart. Figure 5-44 plots three potentials. The red curve represents the electrode potential at the midpoint, while the green and blue curves represent the potentials on the ground at the left and right foot positions respectively.

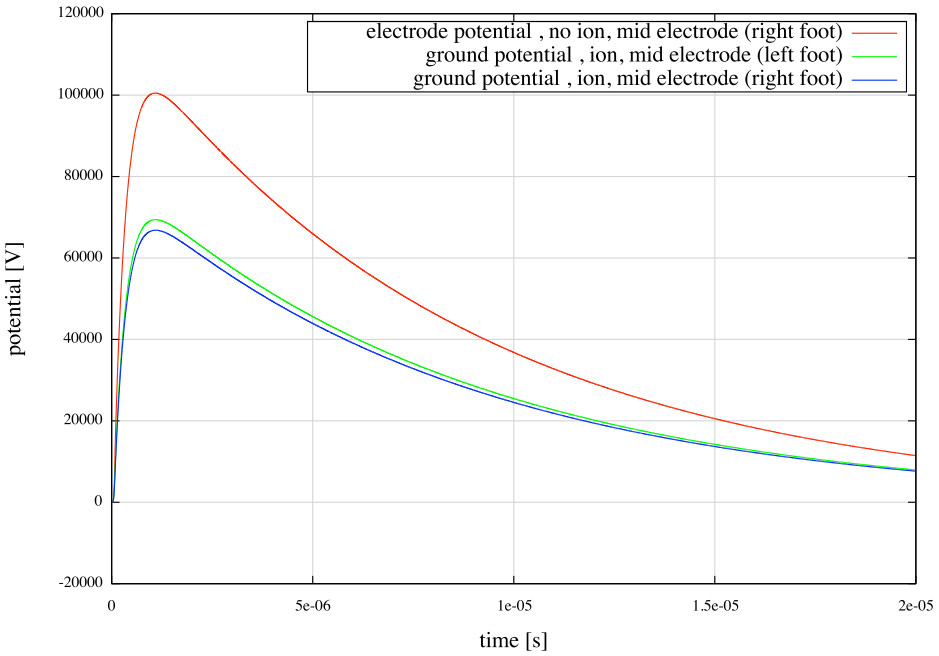

Figure 5-44 The potential on the electrode at its midpoint and ground potential 0.5m either side of the midpoint. ($\rho_s = 270\Omega\text{m}$, $\varepsilon_r = 12$).

Figure 5-45 plots the step potential between the two feet. Hence, a person would be subjected to a peak voltage of 2000 V.

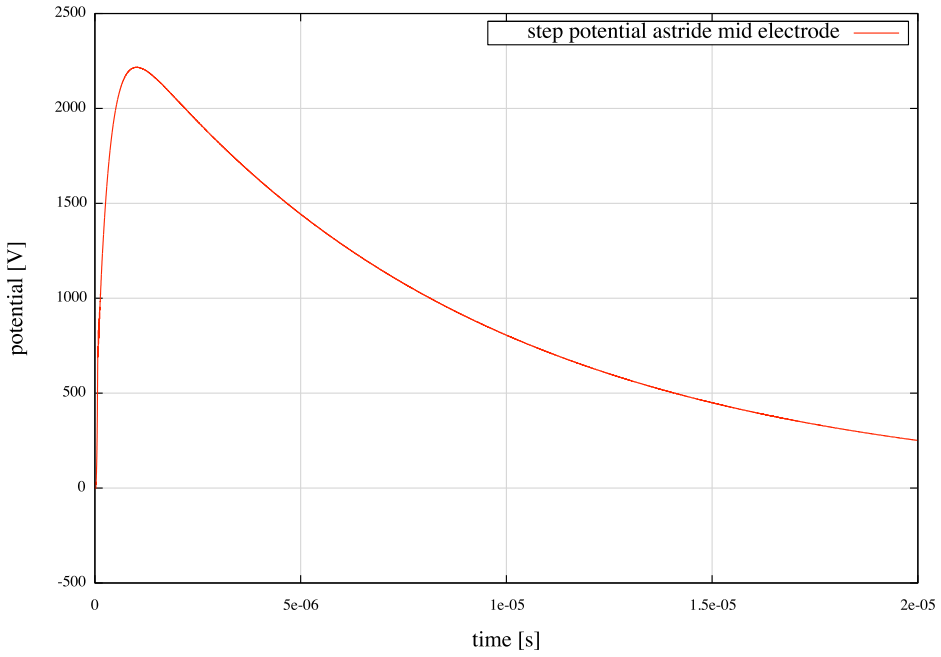

Figure 5-45: The step potential experienced above the midpoint of grounding electrode. ($\rho_s = 270\Omega\text{m}$, $\varepsilon_r = 12$).

It is interesting to see the radial electric field behaviour about the grounding electrode, and its development within the TLM mesh. The plot can be seen as if the electrode is entering the paper. The ground surface is at y=30. Figure 5-46 plots the cross section activity early within the simulation (100 time steps). An equipotential surface can be seen to develop within the soil. Later, the electric field becomes established in both soil and air. The field values at the mesh periphery are approximately zero. Figure 5-47 reveals the cross section activity after 4000 time-steps

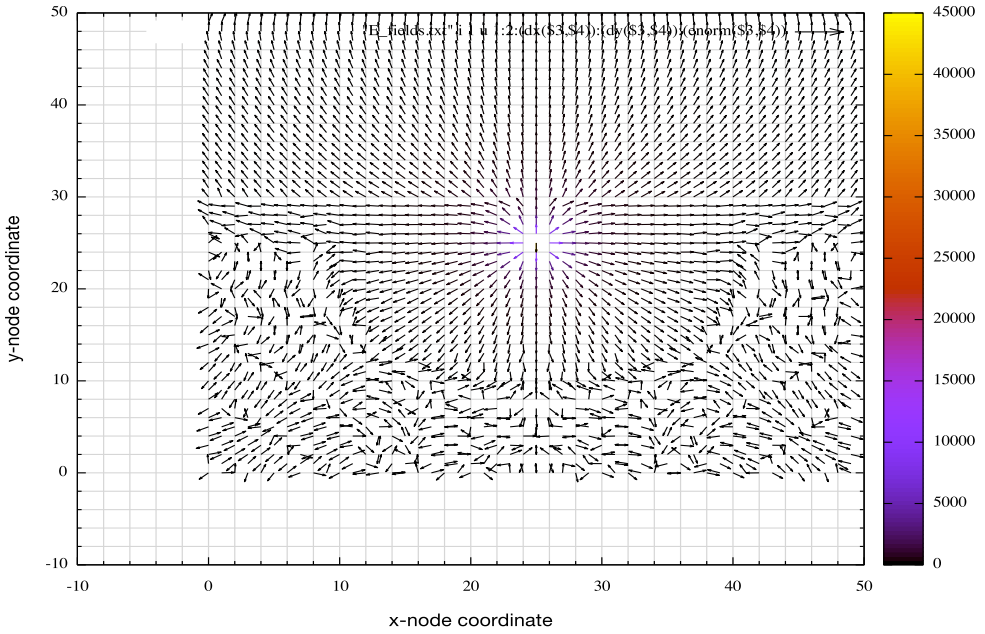

Figure 5-46: The cross-section of the wire under ground, showing the electric field finding its correct configuration early within the process (100 time steps).

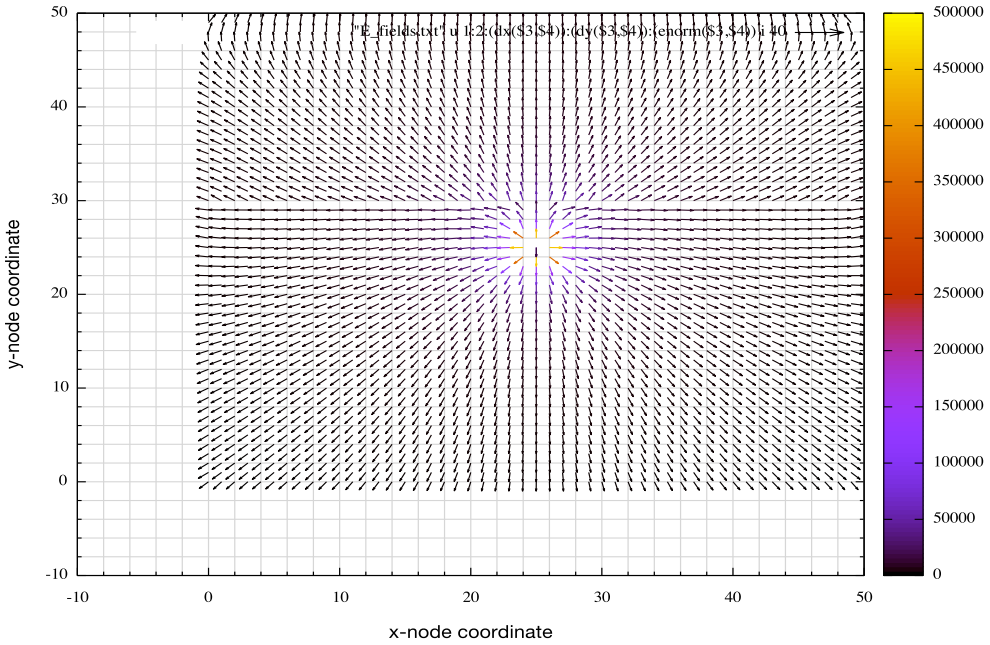

Figure 5-47 Further into the simulation the electric field behaviour is established (4000 time steps).

Chapter 6 Conclusions.

Transmission-Line Modelling lends itself ideally to the modelling of non-linear phenomena such as those encountered during corona discharge. It represents a differential approach to modelling, such that specific local changes in a particular environment within a larger domain can be represented. Calculations are easily performed in the time-domain; a necessary requirement when modelling transient behaviour. The modelling showcased in this thesis utilises the fine-wire approach based around the Embedded Wire Node (EWN). This node saves on computer processing reserves by reducing the need for high-resolution meshes that would otherwise be necessary when fine wires are represented in large spacial domain. Further, this node is easily adapted to accommodate time-varying parameters related to corona development. The node couples with the general TLM mesh in such a way that self-consistency is maintained; a requirement when the cause and effect of corona local to wires is to be represented in real-time.

Chapter One summarised the generation and threat posed by the Electromagnetic Pulse (EMP) emitted via nuclear explosions. The essential points to take from this chapter are the fast rise-time (high frequency content) from such pulses and the high peak electric field. The source region is a region of complex electromagnetic activity resulting from the interaction of gamma radiation, immediately emitted from the detonation (prompt gamma), with the surrounding medium. A Primary Compton current is generated and a subsequent conduction current; the latter competing with the former. These currents are responsible for the signature of the EMP. The effects of these currents are influenced by the Height of Burst (HOB). This will dictate the asymmetry of the source region which in turn is responsible for net currents to occur and hence the radiated EMP. Surface bursts can generate EMP can affects infrastructure tens of kilometres from the burst epicentre. Further, susceptible infrastructure can be affected

when positioned within the source region. However, arguably, High-Altitude EMP (HEMP) poses the biggest threat. The interaction of the Compton current with the Earth's magnetic field leads to a transverse component as well as the original radial component, and it is the transverse component that creates a radiated EMP in the direction of the ground below. The height at which the detonation takes place means it is able to illuminate large geographical areas with the potential of disrupting electric and electronic equipment of various sensitivities and, ultimately, rendering communities impotent. Therefore, strategies are necessary to protect against these harmful effects. Due to the nature of the pulse being considered, simulations are of paramount importance. This thesis concentrates on the corona effect about wires that can be induced when pulses couple to wires.

Chapter Two describes the physics behind the electrical breakdown of dielectric media of which corona discharge is a particular example; Although it is a complex subject area, especially at the molecular level, the pertinent points to take from this chapter are the ionisation and recombination processes competing within a dielectric when presented with a high electric field. The processes for ionisation and attachment ultimately decide the critical field breakdown magnitude. When such a threshold is met, electron avalanches initiate, producing streams of electrons all accelerating towards the anode unless hindered by collisions. Secondary processes facilitate the production of streamers, leader channels. These will continue to increase in length provided the critical field for streamers (E_c) is met (lower than the breakdown field, E_B. The effects of ionisation are relevant in soil too. An EMP has the potential to be able to penetrate ground so there is need for simulations in these environments too.

Chapter three describes the Transmission Line Modelling (Matrix) method (TLM) with an emphasis on application to three-dimensional modelling. This relies on the Symmetrical Condensed Node (SCN) to describe a particular domain and the propagation of electromagnetic fields in all orthogonal directions. The node can be used to represent all media, to solve complex field environments in the time-domain and is self-consistent. The Embedded Wire Node (EWN) allows the introduction of 'fine-wires' and is easily augmented to accept corona related changes.

Chapter Four describes various modelling approaches towards corona. First, it reveals the characteristic distortions expected on transient waveforms on wires inducing corona discharge. These distortions are characterised by a wedge that forms on the anterior surface of the waveform, above the breakdown threshold. Further, the distortion is proportional to the distance travelled and can be attributed to a delay in voltage components above the breakdown threshold.

Considering the wire as a transmission-line from a mathematical perspective, corona development can be described by an increase in capacitance, of conductance or a radial current; all related to the increase in charge that develops about the wire during breakdown of the proximal medium. Hence, any of these parameters can be used to describe the corona development within a simulation. A few examples are discussed. The major emphasis is on the equations devised by Cooray [61] that seemed to be ideally suited towards the modelling of corona in the EWN as they both rely on a coaxial description. The equations provide a running commentary of the changes occurring at a node, in real-time allowing necessary changes to the node to be incorporated. The very nature of the EWN, with the relatively large dielectric-to-wire ratio allows a large proportion; if not the entire corona sheath to develop within the node without the need to involve other surrounding nodes. All that is necessary is for the critical field for streamer propagation to not exist beyond the cell boundary. Soil ionisation models were also presented. These are generally a little crude compared to their above-ground counterparts as they mostly involve increasing the conductivity only.

Chapter Five presented the results when the various models described in the previous chapter are adopted within the EWN. Very large applied voltages will require large embedded wire nodes to accommodate the corona sheath.

The increasing conductor radius technique is considered to be a basic method of recreating corona effects. The radius of the conductor is increased to represent the conductive region about the wire as breakdown occurs. It is interesting in so far as it does (cannot) rely on the critical field for streamer propagation to define the radial growth of the corona once inception has initiated. Instead, the wire is treated as a different wire at each update, each with its own

particular critical breakdown field (found using Peek or Hartmann's formula). Although the technique is considered crude, it was not greatly inferior to the other techniques.

Methods based upon the use of capacitance and conductance seem to emulate the experimental results from the Tidd power station most accurately. When using conductance to represent corona effects, techniques used here required a nominal conductivity of the corona space charge to be chosen. Results suggested that 110 μS/m was a decent estimate. If using the Cooray Equations to calculate the capacitance (and hence the conductance) the need for calculations based on differentiation (with respect to time) appears to introduce numerical error especially as the Cooray equations rely on iterative processes. However, the equations do offer a corona radius and hence a nominal conductivity can be used in conjunction with this radius with decent results (and a similar conductivity value). It should be noted that in both models the distortions imparted on the propagating waveform share similarities to the experimental data notably the characteristic 's' shape at the anterior side of the waveform. This seems absent in the method exhibited by Thang et. al.

The Cooray equations allow an increase in capacitance associated with corona to be obtained. Augmenting the basic EWN with a stub representing the addition capacitance provides a decent depiction of the corona effects when compared to the experimental data. The shape, distortion and attenuation of the simulated waveforms seemed closest to the original using this technique, although the method seemed to underestimate the required capacitance by around 30%.

As has already been alluded to, the Cooray equations rely on an iteration of three equations to converge to obtain the values of corona radius, corona charge and corona charge density. They can easily be caused to diverge when confronted with large changes at a node or numerical error. Hence, corona current being a parameter calculated on the differentiation of corona charge with respect to time results in poor results.

The Cooray Equations are essentially a capacitance-based algorithm and hence voltage-based and not based on electric field intensity. This could be construed as negative as a distant reference is required to find voltages as opposed to a model based on electric fields that will

respond to local changes. However, the EWN is essentially a voltage description of the region about a wire so the equations are suitably applicable within that region. That said, precise field values are not available within the node except for the wire surface, and to some extent, the cell boundary. Using the EWN means there is a limit to how much voltage (field) can be contained within the node. An issue arises when the corona radius exceeds or even encroaches onto the SCN cell wall. Once this has happened a parameter such as node capacitance will tend to infinity. Increasing the cell: wire ratio of the EWN would go someway to solving this problem, but mesh resolution suffers and hence the representation of particular frequencies can be hindered.

When representing breakdown in soil, the technique by Gazzana was investigated. His model was performed using 1-D TLM. Hence, here the method was translated to the 3-D domain. The application to soil requires the EWN to be adapted to represent increased permittivity (relative to air) via the use of stubs before any ionisation consideration takes place. The method itself presents a few interesting considerations. The major consideration is based on how the degree of ionisation about an electrode is accounted for in a 1-D model. Hence, the increase in conductance associated with ionisation was applied to a single node and then to the whole region as would be the case in the 1-D model. A difference in potential in both cases was found albeit to a small extent. Hence, it appears the 1-D does suffice for the examples shown. The inhomogeneity of soil does make modelling such media difficult. However, clearly, soil ionisation does have an impact on the grounding qualities of protection schemes.

Other pertinent issues are as follows:

1) The surface field responsible for corona inception on a wire is usually given by equations proposed by Peek or Hartmann (or similar). There is a possibility that fast rise-times may influence these predictions [52].

2) Extraneous factors such as air density, humidity of the quality of the wire's surface will affect the predicted breakdown field of streamer field. Peek or Hartmann's equations contain factors to allow for such changes but it is difficult to use such values to predict a result as opposed to emulating a result.

3) The development of corona has a statistical dependence. Hence, a time lag is necessary to describe the development of corona. This is accepted to be within the microsecond time-scale. The decay constant used in the Cooray equations is typically chosen to be 0.5 μs. However, this may depend on wire radius [61].

4) The Cooray equations rely on the wire voltage assuming an instantaneous value during discharge, whereby all the charges immediately adjust to maintain the voltage. However, there is a delay, probably in the realms of nanoseconds [85]. Cooray, points out that this is important when considering fast transients as the streamers that develop may lag the fast moving field front expanding from the wire surface.

Hence, the description of corona development and the resulting distortions on transients relies on many factors. These can be manipulated to replicate a given empirical outcome, but this does imply a heuristic approach.

To summarise, corona-related distortions have been demonstrated using various parameters to a decent accuracy within the TLM framework whilst ionisation effects have also been demonstrated in soil. The TLM method presents an accurate and viable 3-D modelling approach to corona development.

Chapter 7 Future Work

The major obstacle during this work was the limitations introduced by the size of the Embedded Wire Node. Once the corona exceeds the node boundary, the simulations fail. Increasing the cell size will sometimes overcome the issue, but this can introduce a lack of accuracy, not to mention an inability to represent high frequencies (based on cell size being at least one tenth of the shortest wavelength being modelled).

If conductance is being used to represent the corona sheath, then conductivity can be added to the SCN adjacent to the EWN. However, these will be large in relation to the necessary radial increase and so such an approach is not ideal. Perhaps an EWN with a moving outer boundary can be devised. This would mean a time-varying node capacitance; something that was happening when the conductor radius was being used to reproduce the corona, only now the outer reference is changing with time not the inner conductor radius. Further, cells adjacent to the EWN (transversely to the wire direction) would be impacted. Alternatively, a form of EWN for cells outside the true EWN without the wire - essentially a node able to change its parameters according to variations in conductance and capacitance in the same way as the EWN has done here to account for changes about the wire (as well as accounting for the wire itself).

Chapters one and two delve fairly deeply into the chemistry of the ionised regions that develop. Considering electrical breakdown, the simulations rely on relatively crude representations of the medium. Perhaps, as computers become progressively powerful, the corona development can be described from a microscopic perspective.

References

[1] Baum, C.E. "*From the Electromagnetic Pulse to High Power Electromagnetics*". Proc. IEEE, Vol. 80, Issue 6. pp. 789-817,1992.

[2] Bainbridge, K.T., "*Trinity*", Report LA-6300-H), Los Alamos Scientific Laboratory. May 1976. p. 53

[3] Lee, K.S.H., Ed. "*EMP Interaction: Principles, Techniques and Reference Data*". New York: Hemisphere, 1986 (from AFWL-TR80-402,1980)

[4] Baum, C.E. "*Reminiscences of High-Power Electromagnetics.*" IEEE. Trans. on Elect. Comp., Vol.9. No.2, May 2007.

[5] Defense Atomic Support Agency. 23 September 1959. "*Operation Hardtack Preliminary Report. Technical Summary of Military Effects. Report ADA369152*". pp. 346–350.

[6] Defense Nuclear Agency. *"Operation Dominic I. 1962."* Report DNA 6040F Archived 2012-08-23 at the Wayback Machine (web.archive.org). Page 228–229.

[7] Vittitoe, C. N., "*Did High-Altitude EMP Cause the Hawaiian Streetlight Incident?*" http://ece-research.unm.edu/summa/notes/SDAN/0031.pdf. Sandia National Laboratories, June 1989, p.5.

[8] Karsas, W.J., Latter, R., "*Electromagnetic radiation from a nuclear explosion in space*," Phys. Rev., pp.1919-1926, 1962.

[9] U.S. Department of State , "*Treaty Banning Nuclear Weapon Tests in the Atmosphere, in Outer Space and Under Water*" https://www.state.gov/t/isn/4797.htm

[10] Baum, C. E., Breen, E.L., Giles, J.C., O'Neill, J., Sower, G.D., "*Sensors for electromagnetic pulse measurements both inside and away from nuclear source regions*", AP-26, January 1978, pp 22-35.

[11] Blanchard, J.P., Tesche, F.M., McConnell, B.W., "*The effects of corona on current surges induced on conducting lines by EMP: a comparison of experiment data with results of analytic corona models"*. ONRL/Sub/85-27461/i, Sep. 1987

[12] Volland, H., *Atmospheric Electromagnetics*, Springer. ISBN 978-3-642-69813-2

[13] Longmire, C. L. "*On the Electromagnetic Pulse Produced by Nuclear Explosions*." IEEE Trans. on Antennas and Propagation. Vol. AP-26. No.1, Jan. 1978.

[14] Longmire, C. L., "*Justification and Verification of High-Altitude EMP Theory, Part 1"* . LLNL-9323905, Lawrence Livermore National Laboratory. June 1986

[15] Legro, J. R., Abi-Samra, N. C., Hileman, A. R., Tesche, F. M. "Study to assess the effects of nuclear surface burst electromagnetic pulse on electric power systems (phase I), Final report" ORNL/Sub/83-44374/1/V4, Oak Ridge National Laboratory, Sept 1985.

[16] Longmire, C. L., Gilbert, J.L., "*Theory of the EMP coupling in the source region*", DNA 5678F, Feb. 1980.

[17] Hoad, R., Radasky, W., "*Progress in High-Altitude Electromagnetic Pulse (HEMP) Standardization*", IEEE Trans. Elect. Compatibility, Vol.55, No.3, June 2013.

[18] Savage, E., Gilbert, J., Radasky, W. "*The early time (E1) High-altitude Electromagnetic Pulse (HEMP) and its impact in the U.S. power grid"* Metatech Publication." Meta-R-320, Jan. 2010.

[19] Electromagnetic compatibility (EMC) - Part 2: Environment - Section 9: Description of HEMP environment - Radiated disturbance. Basic EMC publication IEC 61000-2-9

[20] Wang, J., Liew, A. C., *"Extension of dynamic model of impulse behaviour of concentrated grounds at high currents",* IEEE Trans. On Power del, Vol. 20, No. 3, Jul 2005.

[21] Serway, R., "Physics for Scientists and Engineers with Modern Physics", 3rd Ed, Saunders College Publishing, (1990)

[22] Rizk, F. A. M, Trinh, G. H, "High Voltage Engineering" CRC. Press. ISBN 13:978-1-4665-1377 (2014).

[23] Cooray, V., "The Lightning Flash", IET Power and Energy Series. No.34. ISBN:0 85296 780 2 (2008)

[24] Thomson, J. J, "*Philos. Mag",* Vol. 23, p449 (1912)

[25] Weissler, G. L., "Encyclopaedia of Physics", Springer Berlin (1956).

[26] Schottky, W., "Uber kalte und warme Elektronenentladungen" , Z. Phys, Vol. 14, p. 63 (1923).

[27] Bortnik, L.M., Kushko, A.N., and Lobanov, A.N., "*Proceedings of second all-union conference on Physics of electrical breakdown of gases",* Tartu, 1984.

[28] Raether, H., Z. Agnew. Phys., Vol. 7, p. 50 (1955).

[29] Raether, H., Z. Agnew. Phys., Vol. 112, p. 464 (1939).

[30] Meek, J.M., *Phys. Rev* Vol. 57, p. 722, (1940).

[31] Hartmann, G., *Doctorat d'Thesis,* University of Paris-Sud, France, 1977.

[32] Gao, L., Akyuz, M., Larsson, A., Cooray, V., Scuka,V., "*Measurement of positive steamer discharge"* Journal of Physics D:Applied Physics , 33(15), pp. 1861-1865 (2000)

[33] Peek, F.W., 'Dielectric Phenomena in High Voltage Engineering' 2nd edition, McGraw-Hill. New York (1920).

[34] Cooray, V (editor)., 'Lightning Protection' IET Power and Energy Series 58, Chapter 5, ISBN. 978-1-84919-106-7(pdf) pp 274

[35] Kron G., "Equivalent Circuit of the Field Equations of Maxwell", Proc. IRE, 32, 1944, pp289-299.

[36] Johns P.B, Beurle R.L. "*Numerical Solution of 2-Dimensional Scattering Problems using a Transmission-Line Matrix*", Proc.IEE, 118, 1971, pp 1203-1208.

[37] Paul, C. R., "Introduction to Electromagnetic Compatibility" (2nd edition), John Wiley and Sons, Inc. ISBN-13: 978-0-471-75500-5 (2006)

[38] Christopoulos C., "The Transmission-Line Modelling Method in Electromagnetics", Morgan and Claypool Publishers. ISBN 159290509 (2006).

[39] Boctor, S.A. "Electric Circuit Analysis" Englewood Cliffs, NJ: Prentice-Hall (1987).

[40] Christopoulos, C., 'The Transmission line modelling method: TLM', IEEE Press, New York, 1995.

[41] Trenkic, V, Christopoulos, C, and Benson, T, "*Development of a general symmetrical condensed node for the TLM method*", IEEE Trans. Microwave Theory Tech., Vol. 44, 12, pp 2129-2135 (1996).

[42] Smart, C. "GGI-TLM solver documentation", University of Nottingham.

[43] Trenkic, V., Wlodarzyck, A. J., Scarramuzza, R. A., "*Modelling of coupling between transient electromagnetic field and complex wire structures*" Int.J.of Num.Model. Vol12, pp 257-273 (1999).

[44] Paul, J., Christopoulos, C. Thomas, D.W.P., Liu, X. "*Time-domain modelling of electromagnetic wave interaction with thin wires using TLM*", IEEE. Trans. On Elect. Comp. Vol 47, No.3, Aug. 2005.

[45] Paul, J., Christopoulos, C. Thomas, D.W.P., "*Correction to Time-domain modelling of electromagnetic wave interaction with thin wires using TLM*", IEEE. Trans. On Elect.Comp.Vol.50, No.2, May 2008.

[46] Ryan, H. J., Henline, H. H., "*The Hysteresis Character of Corona formation*", AISS Trans. Vol 43, pp. 1118-24, 1924.

[47] Gardner, M.F., "*Corona investigation on an artificial line*", AIEE Trans. Vol 44, pp 897-904, 1925.

[48] Boehne, E.W., "*Discussion of paper by Bewley and Dowell* " , AIEE.Trans.,Vol 50, p.558, 1931.

[49] Skilling, H. H., Dykes, de K, P., "*Distortion of travelling waves by corona*", AIEE, Jul 1937.

[50] Wagner, C. F., Gross, I.W., Lloyd, B. L., "*High-Voltage Impulse Tests on Transmission Lines*", AIEE. Trans, Vol 73, pt.-III-A, pp196-210, 1954.

[51] Wagner, C. F., Lloyd, B. L., "*Effects of Corona on Travelling Waves*", AIEE Power Apparatus and Systems, pp 858-72, 1955.

[52] Maruvada, P.S, Menemenlis, H., Malewski, R., "*Corona characteristics of conductor bundles under impulse voltages*", IEEE Trans. PAS-96, pp 102-115, 1977.

[53] Christopoulos, C. "*The propagation of surges above the corona threshold on a line with a lossy earth return*", Int. J. Comp. Elect. Eng. Vol 4, No.2, pp 91-102 (1985).

[54] Kudyan, K.H., Shih, C.H., A non-linear circuit model for transmission lines in corona", IEEE Trans. PAS-100 pp1420-1430 (1981)

[55] Thang, T.H., Baba, Y., Nagaoka, N., Ametami, A., Takami, J., Okabe, S., Rakov, V., "*A simplified model of corona discharge on overhead wires for FD-TD calculations*", IEEE Trans Electromagnetic Compatibility Vol 54, No3, June 2012.

[56] Gazzana, D. S., et al, "*The transmission line modelling method to represent the soil ionization phenomenon in grounding systems*", *IEEE Trans. Magn*. Vol. 50. No. 2, Feb. 2014.

[57] Cooray, V., Theethayi, N., "*Pulse propagation along Transmission Lines in the presence of Corona and their implication to Lightning Return Strokes*," IEEE Trans. Antennas and Propagation. Vol. 56. No.7. July 2008.

[58] Valazquez, R., Mukhedkar, D., "*Analytical Modelling of grounding electrodes transient behavior*", IEEE Trans. Apparatus Systems, Vol. PAS-103, No. 6, Jun. 1984.

[59] Noda, T. "*Development of a transmission line model considering the skin and corona effects for power transient analysis*", Ph.D. Dissertation. Dep't. Elect. Eng., Doshima Univ., Kyoto, Japan, 1996.

[60] Hermosillo, V., Cooray, V., "*Space charge generation and neutralisation in a coaxial cylindrical configuration in air under a negative voltage impulse*", J. Electrostatics, Vol 37, pp139-149. (1996).

[61] Cooray, V., "*Charge and Voltage Characteristics of Corona Discharges in a Coaxial Geometry*, "IEEE. Trans. Dielect. Elect. Insul., vol. 7, no.6, pp 734 – 743, Dec 2000.

[62] Agrawal, A.K., Price, H.J., Gurbaxani, S.H., "Transient Response of Multiconductor Transmission Lines excited by a nonuniform electromagnetic field," IEEE Trans. Electromag. Compat., Vol. 22. No.2, pp. 119-129, May 1980.

[63] Thottappillil, R. "*Electromagnetic pulse environment of cloud to ground lightning for EMC studies*", IEEE Trans. EMC, Vol 44, pp 203-213, 2002.

[64] Visacro, S. '*A comprehensive approach to the grounding response to lightning currents*'., IEEE Trans. Power Del. B Vol. 22, pp 381-386 Jan. 2007.

[65] IEEE "*Recommended Practice for Determining the Electric Power Station Ground Potential Rise and Induced Voltage from a Power Fault*," IEEE Std. 367-2012 (Revision of IEEE Std. 367-1996), vol., no., pp.1-168, May 21 2012.

[66] Whitehead, J. T., Chisholm, W. A., "IEEE Working Group Report Estimating Lightning Performance of Transmission Lines II- updates to analytical models", IEEE trans. on Power Del, Vol. 8, No.3, July 1993.

[67] Cooray, V (editor). 'Lightning Protection' IET Power and Energy Series 58 Chapter 9 (Visacro), ISBN 978-1-84919-106-7(pdf) p 480.

[68] Sunde, E. D., "Earth Conduction Effects in Transmission Systems", Dover publications, Inc., New York (1949).

[69] Riley, K.F., Hobson, M.P., "Mathematical Methods for Physics and Engineering", third edition, Cambridge University Press ISBN-10 0-521-67971-0 (2006).

[70] Cooray, V (editor). 'Lightning Protection' IET Power and Energy Series 58 Chapter 11(Cooray), ISBN 978-1-84919-106-7(pdf) p480

[71] Towne, H.M., 'Impulse characteristics of driven grounds', *Gen.Elect.Rev*.vol.31no.11, pp605-609 (1928)

[72] Bellaschi, P. L., Armington, R. E., and Snowden, A.E., '*Impulse and 60-cycle characteristics of driven grounds'*, Part 2II, AIEE Trans. Vol.61, No. 61, pp349-363(1942).

[73] Mousa, A.M., '*The soil ionization gradient associated with discharge of high currents into concentrated electrodes*', IEEE Trans. Power Deliv. Vol 9, pp. 1669-77 (1994).

[74] CIGRE, "*Guide to procedures for estimating the Lightning Performance of Transmission Lines*" IEEE Trans. Power Del., Vol 9, pp1669-77 (1994).

[75] Geri, A. "*Behaviour of grounding Systems Excited by High Impulse currents: the model and its validation",* IEEE Trans. Power Del. Vol. 14, No 3, Jul. 1999.

[76] Liu,Y., Theethayi, N., Gonzalez, R.M., Thottappillil, R., "*The residual resistivity in soil ionization region around grounding system for different experimental results*", Proc. IEEE Int. Symposium on EMC, Boston, pp 794-99. USA, 2003.

[77] Imece, A.F., et al. '*Modeling guidelines for fast front transients*', IEEE Trans. Power Del. Vol.11, No. 1, Jan. 1996.

[78] Gazzana, D. S et al., "*A study of human safety against lightning considering the grounding system and the evaluation of the associated parameters"* Electr. Power Syst. Res. (2014) http://dx.doi/10.1016/j.espr.2014.03.015

[79] IEEE Std.80, 'Guide for safety in AC Substation Grounding', IEEE, New York (2000).

[80] Grecv, L., Popov, M., "*On high-frequency circuit equivalents of a vertical ground rod.",* IEEE Trans. Power Del., Vol.20, No.2, pp1598-1603, Apr 2005.

[81] Grecv, L. "*Modelling of grounding electrodes under lightning currents",* IEEE Trans. On Elect. Comp. Vol 51, No.3, Aug. 2009.

[82] Thang H. T. et al., "*FDTD simulation of lightning surges on overhead wires in the presence of corona discharge*", IEEE Trans. On Comp. Elect. Vol.54, No.6, Dec 2012.

[83] Thang H. T. et al., "Lightning surges on an Overhead Wire in the presence of Corona: FDTD simulation of Wagner et al.'s Experiment", 2012 Asia Pacific Symposium on Electromagnetic Compatibility, Published by IEEE. pp 845-848 DOI:10:1109 /APEMC.2012.6237802

[84] Noda, T., Yokoyama, S., "*Thin wire representation in finite difference time domain surge simulation*", IEEE Trans. Power Delivery, Vol. 17, no. 3, pp 840-847, Jul.2002.

[85] Galimberti, I., “The mechanism of the long spark formation”, Journal de physique. Vol. 40, pp C7-C193, 1979.

Appendix A

A.1 The Source Region.

To understand the local fields developed within the source region as well as though radiated from the region, an understanding of the air chemistry is necessary. The expulsion of energy from the burst point releases electrons from the surrounding material and hence initiates currents within the region. These become the sources for the various fields allowing approximate solutions to Maxwell's equations.

As Chapter One suggests, the explosion results in the emission of gamma radiation. Gamma radiation is usually described in terms of a gamma flux, $\dot{\Phi}_\gamma$ i.e. the energy passing through unit area in unit time [MeV/(m^2s)]. Alternatively, a Dose rate, $\dot{D}$ is used. Dose rate, whose unit is the *rad*, is a measure of the rate of energy deposited per unit mass of the material through which the radiation is passing [10^{-2} J/kg = 1 Rad]. These two descriptions of energy flow are related by

$$\dot{\Phi}_\gamma \approx 2\times10^{13}\dot{D} \tag{A.1}$$

The prompt gamma, that emerge from the burst has a rise-time of nanoseconds. The rise of *prompt* gamma flux is assumed exponential in time

$$\dot{D} = Ae^{\alpha t} \tag{A.2}$$

where A is a constant and α is a rate constant taken as $2\times10^{8}\ s^{-1}$ although will vary according to conditions [16].

To obtain an approximation of the Compton current density, J_r^c, the flux of electrons, $\dot{\Phi}_e$ can be related to the gamma flux using

$$\dot{\Phi}_e = \dot{\Phi}_\gamma \frac{R_{mf}}{\gamma_s} \cong 0.007\dot{\Phi}_\gamma \tag{A.3}$$

Where R_{mf} is the mean forward range of the recoil electrons (the average distance the recoil electron travels before expending its energy via scattering collisions) and γ_s is the scattering mean path of the gamma (the average distance between collisions). This holds for media of low atomic number including air. The radial Compton current density is then given by [16].

$$J_r^c = q_e\dot{\Phi}_e = 2\times10^{-8}\dot{D} \tag{A.4}$$

where q_e is the electronic charge.

At altitudes above 30 km, a *transverse* current density, J_t^c , arises due to deflection by the Earth's magnetic field. This can be expressed in terms of the radial Compton current density. As the magnetic field affects the mean forward range the transverse current has to be adjusted accordingly:

$$J_t^c = J_r^c\left(\frac{R_{mf}}{2R_L}\right) \tag{A.5}$$

Where R_L is the Larmor radius alluded to in Chapter one. As well as descriptions of the Compton current densities, conduction current densities (related to the free electrons once their energy has been expended) also arise that also need to be accounted for. To achieve this, the free electron number density within the source region must be monitored. Certain

processes within the source region will hinder the available number of electrons (and ions) that contribute to the conductivity:

1. Electron attachment

Let the rate constant of the electron attachment process be k_1; dependent on air density and electric field. Then considering , for example, an oxygen molecule, O_2 :

$$O_2 + e^- \rightarrow O_2^- \tag{A.6}$$

Electrons will acquire energy in the electric field. If too high, the probability of re-attachment decreases. The probability will increase as the air density increases (low altitudes), firstly, as the greater number of electron collisions will cause them to lose energy and secondly, due to the simple observation that there are more molecules for electrons to attach to. The attachment process accounts for most of the electron removal.

2. Dissociative recombination:

Under high electron and ion densities, both can be removed from the region via dissociative recombination. A free electron neutralises a positive ion and then splits into two atoms (dissociates). Considering the two major constituents, oxygen (O), and nitrogen, (N):

$$O_2 + e^- \rightarrow O^- + O \tag{A.7}$$

$$N_2^+ + e^- \rightarrow N + N \tag{A.8}$$

Let the rate constant k_2 represent this process.

3. Mutual Neutralisation.

The positive and negative ions can mutually neutralise each other.

$$O_2^- + O_2^+ \rightarrow O_2 + O_2 \tag{A.9}$$

$$O_2^- + N_2^+ \rightarrow O_2 + N_2 \tag{A.10}$$

Let the ionic recombination of the air molecule ions be represented by a rate constant, k_3.

Using the rate constants , air chemistry equations relating the number density (number of the particular particle per unit volume) of the various charged particles can be defined (N_e, N_+, N_- refer to the number densities of the electrons, positive and negative ions respectively):

$$\frac{dN_e}{dt} = S_e + k_a N_e - k_1 N_e - k_a N_e N_+ \tag{A.11}$$

$$\frac{dN_+}{dt} = S_e + k_a N_e - k_2 N_e N_+ - k_3 N_+ N_- \tag{A.12}$$

$$\frac{dN_-}{dt} = k_1 N_e - k_3 N_+ N_- \tag{A.13}$$

Here, S_e is the production rate of free electrons (related to the dose rate, $\dot{D}$) and k_a is the electron avalanche rate constant representing the number of ionisations per freed electron per unit time. Its value is proportional to the local electric field and air density; both affecting particle acceleration.

The rate constants at sea level are typically

$$k_1 \approx 10^8 \quad [s^{-1}]$$

$$k_2 \approx 2\times10^{-7} \quad [cm^3 s^{-1}]$$

$$k_3 \approx 2\times10^{-6} \quad [cm^3 s^{-1}]$$

The conduction current, $\boldsymbol{J_\sigma}$, will be a function of the time varying conductivity related to the processes above and the electric field

$$\boldsymbol{J_\sigma} = \sigma \boldsymbol{E} \tag{A.14}$$

or alternatively, can be described as a net flow of electrons

$$\boldsymbol{J}_\sigma = -q_e N_e \boldsymbol{v}_e \tag{A.15}$$

where $\boldsymbol{v}_e$ is the average velocity of the electrons.

Electron mobility , μ_e, is defined as the ratio of average velocity to driving electric field:

$$\mu_e = \frac{-v_e}{E} \tag{A.16}$$

Combining and rearranging the above equations the conductivity can be written in terms of the number density and mobility

$$\sigma = q_e N_e \mu_e \tag{A.17}$$

or if the ions are to be included (subscript, I, refers to negative and positive ions collectively)

$$\sigma = e^{-}(N_e \mu_e + N_I \mu_I) \tag{A.18}$$

At sea level, the mobility of electrons is typically [16]

$$\mu_e \approx 0.3 \qquad \left[\frac{\mathrm{ms^{-1}}}{\mathrm{Vm^{-1}}}\right]$$

The mobility of the ions, μ_i is approximately [7] check

$$\mu_i \approx 2.5\times10^{-4} \qquad \left[\frac{\mathrm{ms^{-1}}}{\mathrm{Vm^{-1}}}\right]$$

Hence, approximations of the current densities (sources) can now be made. To understand how these contribute to the fields within the source region, the usual approach is to first consider the hypothetical symmetrical source region.

A.1.1 The Symmetrical Source Region.

The time-dependent Maxwell Equations applied to the symmetrical source region are

$$\mu_0 \frac{\partial \boldsymbol{H}}{\partial t} + \nabla \times \boldsymbol{E} = 0 \tag{A.19}$$

$$-\varepsilon_o \frac{\partial \boldsymbol{E}}{\partial t} + \boldsymbol{\nabla} \times \boldsymbol{H} = \boldsymbol{J^c} + \sigma \boldsymbol{E} \tag{A.20}$$

The ejection of gamma photons, considered radial from the burst point is assumed to generate a likewise radial Compton current. The charge-separation model describes the charge separation that emerges as electrons are accelerated to the outer extremities of the source region whilst the lesser mobile positive ions congregate nearer the burst point. A radial electric field, E_r results. Such a field, by nature of the symmetry, is irrotational or curl-free. Note too, that the field outside the source region is zero (Figure A1).

Then, by equation (A.19) a constant magnetic field in time results and provided this is zero to begin with, remains at zero. Subsequently, (A.20) simplifies to

$$\varepsilon_0 \frac{\partial E_r}{\partial t} + \sigma E_r = -J_r^c \tag{A.21}$$

At early times, the conductivity within the source region can be considered small such that the conductivity current is much smaller than the Compton current. Ignoring the conductivity current completely, the above equation can be solved for E_r

$$E_r = -\frac{1}{\varepsilon_0} \int_{-\infty}^{t} J_r^c \, dt \tag{A.22}$$

Assuming the Compton current rises exponentially as a result of the electron avalanche, the equation above suggests the radial electric field will also too (the equation is linear). This describes the charge separation model; the current is charging up the capacitance of space as the positive ions with their lesser mobility reside closer to the burst region while the electrons are expelled to the extremities of the source region.

Eventually, the radial conduction current density, = σE_r, will become comparable with the radial Compton current density as secondary electrons increase within the source region, provided the dose rate is large enough. The displacement current term can now be neglected in equation (A.21). A point will be reached when both the Compton current and the conductance are proportional to the dose rate, $\dot{D}$. Then the field will saturate at a particular value, E_s

$$E_r \cong -\frac{J_r^c}{\sigma} \equiv E_s \tag{A.23}$$

In other words, the conduction current cancels the Compton current (Figure A1). In such circumstances, the time derivative of E_r will be near zero, hence confirming the absence of the displacement current.

If saturation occurs as the gamma flux is rising exponentially, with $\alpha = 2\times10^{8}\ \mathrm{s}^{-1}$ the peak $E = E_s$ can be approximated:

$$E_s \approx 1.8\times10^{5} \qquad [\mathrm{V/m}]$$

and after the peak ($\alpha = 0\ \mathrm{s}^{-1}$)

$$E_s \approx 2\times10^{4} \qquad [\mathrm{V/m}]$$

At later times, the ion conductivity becomes dominant and the radial field falls.

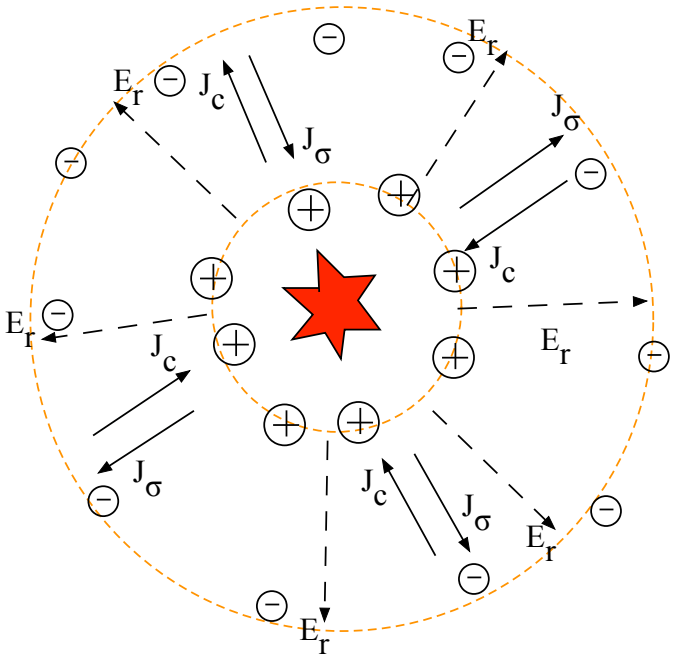

Figure A1. The charge separation model: Electrons are accelerated radially from the burst epicentre forming the border of the source region. Later, secondary processes start to dominate. a radial conduction current density J_σ results.

The symmetrical source region presents a simplified view of the mechanisms that contribute to the fields within the source region used in conjunction with the charge separation model and the radial field it describes. More importantly, there in no radiated field emitted from a symmetrical source region. For this to occur a net current density must develop, facilitated by the introduction of asymmetry. This asymmetry will vary considerably depending on the height of burst.

A.1.2 Source Region related to a Surface Burst

When a burst occurs on or near the ground, the ground imposes asymmetry to the source region. It can be approximated to be a hemispherical region above ground. The development of the currents and fields can be described using three phases:

I. **The Wave Phase**. $\left(\sigma E_r \ll \varepsilon_0 \frac{\partial E_r}{\partial t}\right)$

Just as for the symmetrical source region, very early into the EMP generation, the conductivity current in the air is relatively small and the displacement current dominates. Due to the geometry of the source region Longmire [13][16], consider the spherical coordinate form of Maxwell's Equations. The actual field components of interest are $H_\varphi, E_r,$ and E_θ (Figure A2).

The two time-dependent equations simplify to

$$\mu_0 \frac{\partial H_\varphi}{\partial t} = -\frac{1}{r}\frac{d}{\partial r}(rE_\theta) + \frac{1}{r}\frac{\partial}{\partial \theta}(E_r) \tag{A.24}$$

$$\varepsilon_0 \frac{\partial E_\theta}{\partial t} + \sigma E_\theta + J_\theta^c = -\frac{1}{r}\frac{\partial}{\partial r}(rH_\varphi) \tag{A.25}$$

$$\varepsilon_0 \frac{\partial E_r}{\partial t} + \sigma E_r + J_r^c = -\frac{1}{r \sin\theta} \frac{\partial}{\partial \theta} \left(\sin\theta \, H_\varphi \right) \tag{A.26}$$

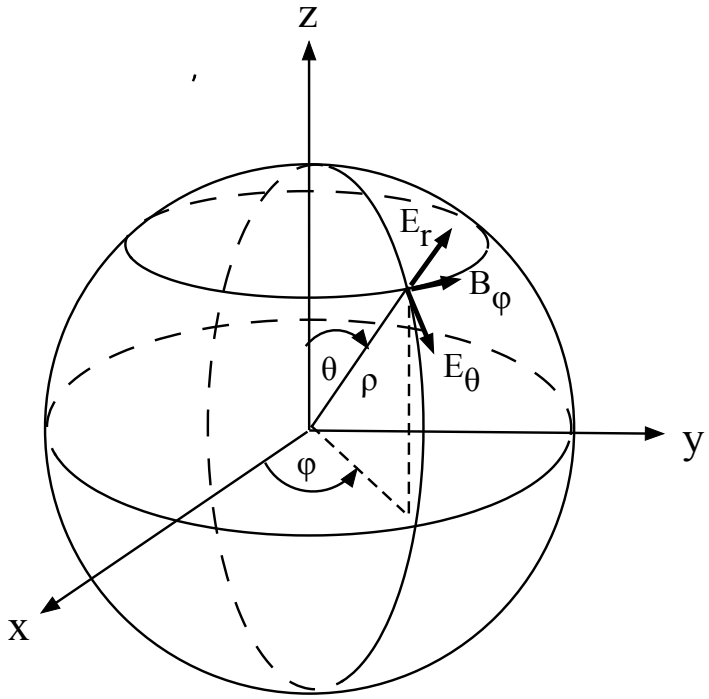

Figure A2. The spherical coordinate basis vectors used to describe the source region.

To simplify further, the fields are simplified by describing outgoing and incoming fields, F and G respectively

$$F_r = r(E_\theta + Z_0 H_\varphi) \tag{A.27}$$

$$G_r = r(E_\theta - Z_0 H_\varphi) \tag{A.28}$$

Introducing a retarded time transformation:

$$\tau = ct - r \tag{A.29}$$

where τ is in length units ($\tau = ct'$).

The partial derivatives transform as

$$\frac{1}{c}\frac{\partial}{\partial t} \rightarrow \frac{\partial}{\partial \tau} \tag{A.30}$$

$$\frac{\partial}{\partial r} \rightarrow \frac{\partial}{\partial r'} - \frac{\partial}{\partial r} \tag{A.31}$$

Under these transformations, and as the incoming field is small compared to the outgoing field (see later description on HEMP for an explanation) in conjunction with the initial premise that the conductivity current is small, the wave-phase equations can be deduced:

$$\frac{\partial F_r}{\partial r} + \frac{Z_0}{2} F_r = \frac{\partial E_r}{\partial \theta} \tag{A.32}$$

$$\frac{\partial E_r}{\partial \tau} = -Z_0 J_r^c + \frac{1}{2r^2}\frac{\partial F_r}{\partial \theta} \tag{A.33}$$

where it is assumed, J_θ^c, is again small compared to , J_r^c, and sin θ has been replaced by unity since the outgoing field is confined to angles near the ground surface.

Examining the equations , we see that the outgoing wave *F* is confined to a region near the ground surface (as $\partial F/\partial \theta$ is largest there) . The *z* dependence implies the wave moves upwards as it it propagates outwards.

II. The Diffusion Phase

As the diffusion phase begins, the conductivity becomes relevant and begins to dominate the displacement current. Referring to the original Maxwell equations (A.24), (A.25) and (A.26) all time-derivative terms can therefore be eliminated. Also, as the magnetic field is confined close to the ground surface the vertical coordinate $z \approx r(\pi/2 - \theta)$ can be introduced. Hence, equations (A.24)(A.26) reduce to

$$\mu_o \frac{\partial H_\phi}{\partial t} = \frac{\partial}{\partial z}\left(\frac{J_r^c}{\sigma}\right) + \frac{\partial}{\partial z}\left(\frac{1}{\sigma}\frac{\partial}{\partial z}H_\phi\right) \tag{A.34}$$

This is the standard diffusion equation for the skin effect and can be solved for various magnitudes of conductivity, σ. Hence the term 'diffusion phase'.

The diffusion phase is generally described in a qualitative way. Figure A3 reveals the situation.

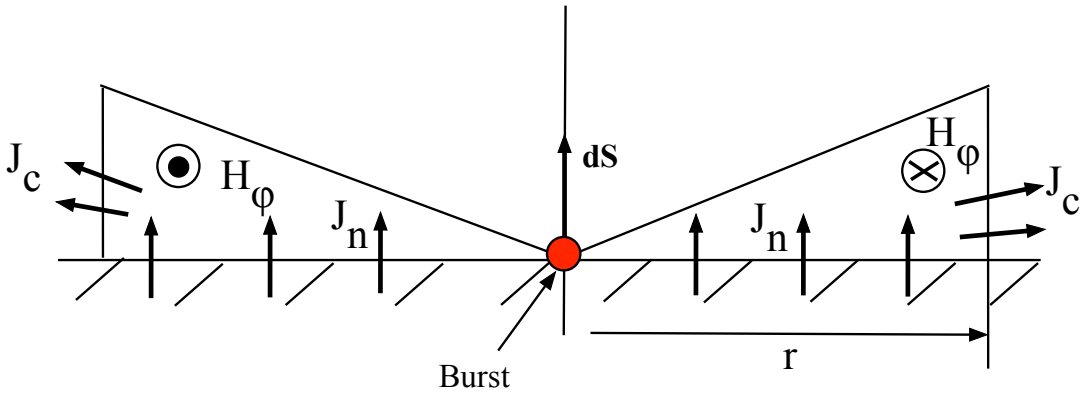

Figure A3 Geometry used for describing the magnetic field behaviour within a surface burst[2]

If displacement current is ignored, the integral form of Maxwell's equation can be written

$$\oint \boldsymbol{H} \cdot \boldsymbol{dl} = \iint \boldsymbol{J}.\boldsymbol{dS} \tag{A.35}$$

Applying this to a circular region on the ground surface, centred about the z-axis, radius, r, gives

$$2\pi r H_\phi = \pi r^2 J_n \tag{A.36}$$

where, J_n, is the normal current density perpendicular to the ground.

Hence,

$$H_\phi = \frac{I}{2\pi r} \tag{A.37}$$

where I is the normal component of current flowing through the ground.

Referring again to Figure A3 the total current equals the current through the right hand vertical end of the wedge, i.e.

$$I = 2\pi r \delta J^c \tag{A.38}$$

where δ is the skin depth, and therefore the magnetic field is

$$H_\phi = \delta J^c \tag{A.39}$$

III. The Quasi-Static phase:

Longmire showed that during this phase the electric field and the conduction current are nearly in the θ direction. Hence the conduction current flows to earth in the same direction. In this phase the Compton and conductivity currents are almost in a state of balance, i.e. a quasi-static state.

A.1.3 The High-Altitude EMP (HEMP).

The EMP generated by explosions above 100km [3] are classified as high-altitude EMP or HEMP. The asymmetry of the source region is imposed by the atmosphere; the increasing density of the air with proximity to ground results in a flattened 'pancake' shaped source region. This, in conjunction with the geomagnetic field enables an EMP to be directed towards the Earth capable of causing mass disruption over large geographical areas.

A solution of the HEMP fields created exists in the spherical coordinate system as used in the previous surface-burst description [8]. However, Longmire [13], provides a simplified solution by reducing the geometry to a planar system to demonstrate the salient aspects of the pulse development. The following gives a breakdown of the theory applied. However, Longmire presents the theory in cgs units. Here, the theory is presented in SI units [18].

In planar geometry, the gamma stream, and therefore the initial primary Compton current (before deflection) can be considered vertical and incident on a flat source region (Figure A4).

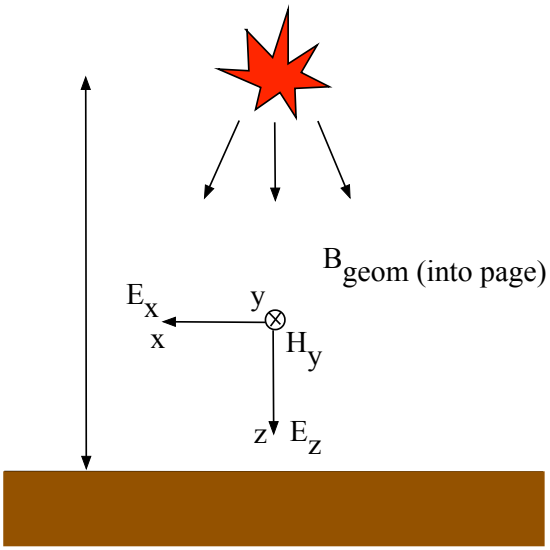

Figure A4. The field and current components of HEMP when considered in the simplified planar geometry [18]

Referring to the planar geometry, the Earth's geomagnetic field is directed in into the page. Hence, the Compton current density is deflected in the *x*-direction as is the electric field component of the radiated field. There will be an associated magnetic field component that points in the *y*-direction. Hence, the three Maxwell's equations that describe these field components, taking into account the radial and deflected Compton currents and the conductivity are:

$$\mu_0 \frac{\partial H_y}{\partial t} = -\frac{\partial E_x}{\partial z} \tag{A.40}$$

$$\varepsilon_0 \frac{\partial E_x}{\partial t} + \sigma E_x + J_x^c = \frac{\partial H_y}{\partial z} \tag{A.41}$$

$$\varepsilon_0 \frac{\partial E_z}{\partial t} + \sigma E_z + J_z^c = 0 \tag{A.42}$$

The third equation represents the charge-separation field, E_z, within the source region as in the symmetric case. This field is only important for self-consistency purposes due to the altitude of the region.

Applying the transformations as before

$$\tau = ct - z \tag{A.43}$$

$$F = E_x + Z_0 H_y \tag{A.44}$$

$$G = E_x - Z_0 H_y \tag{A.45}$$

where τ is the retarded-time and F, G are the outgoing (downwards) and ingoing (upwards) waves respectively. The derivative, under the transformation, become

$$\frac{1}{c}\frac{\partial}{\partial t} \rightarrow \frac{\partial}{\partial \tau}$$

$$\frac{\partial}{\partial z} \rightarrow \frac{\partial}{\partial t} - \frac{\partial}{\partial \tau}$$

and Maxwell's equations (A.40), (A.41), (A.42) become

$$\frac{\partial F}{\partial z} + \frac{\sigma Z_0 F}{2} = -Z_0 J_x^c - \frac{\sigma Z_0 G}{2} \tag{A.46}$$

$$\frac{\partial G}{\partial \tau} + \frac{\sigma Z_0 G}{4} = \frac{1}{2}\frac{\partial G}{\partial z} - \frac{Z_0 J_x^c}{2} - \frac{\sigma Z_0 F}{4} \tag{A.47}$$

$$\frac{\partial E_z}{\partial \tau} + \sigma Z_0 E_z = -Z_0 J_z^c \tag{A.48}$$

Hence, *F* represents the E1-HEMP wave.

Under this transformation, the field components are found using

$$E_x = \frac{F + G}{2} \tag{A.49}$$

$$H_y = \frac{F + G}{2Z_0} \tag{A.50}$$

Referring back to equations (A.46) and (A.47) the same three phase criteria can be applied that were used in the surface-burst description. Again, at early times, the conductivity has not reached significant values, hence terms related to σ, can be omitted from the Maxwell equations allowing them to simplify to

$$\frac{\partial F}{\partial z} = -Z_0 J_x^c \tag{A.51}$$

$$\frac{\partial G}{\partial \tau} = \frac{1}{2}\frac{\partial G}{\partial z} - \frac{Z_0 J_x^c}{2} \tag{A.52}$$

providing an equation for the outgoing wave (A.51), and incoming wave (A.52). Initially, the outgoing wave, F, dominates.

Equation (A.51) suggests the outgoing wave will increase as it propagates downwards, within the source region. As the conductivity becomes considerable, and the radial field increases, the conduction currents will begin to compete with the Compton currents. Again, assuming incoming field is negligible, equation (A.46) becomes

$$\frac{\partial F}{\partial z} + \frac{\sigma Z_0 F}{2} = 0 \tag{A.53}$$

and so the saturation condition results

$$F(z,\tau) \cong \frac{2J(z,\tau)}{\sigma(z,\tau)} \tag{A.54}$$

This condition places a limit on the size of the E1 HEMP. It also explains why variations in weapon yield result in minimal differences in E1 magnitude.

Comparing the outgoing and incoming waveforms it is noticed that the outgoing wave only has a spatial derivative in altitude, z, that relates to an increasing air density. Usually, air density can be defined by its *scale height*. Scale height is defined the distance over which atmospheric density changes by e^{-1}. This is around 7 kilometres in the lower atmosphere. The equation describing the incoming wave, upward pointing in the planar geometry, has a retarded-time derivative. This is relevant for the retarded-time width of the pulse is equivalent to a few metres (e.g. a 50ns pulse has a spatial width of $c\Delta t = 3{\times}10^8 * 50{\times}10^{-9} = 15\text{m}$). Hence, turning attention to the incoming-wave equation above (A.47) and disregarding derivatives gives

$$\frac{\partial G}{\partial \tau} + \frac{\sigma Z_0 G}{4} = -\frac{Z_0 J_x^c}{2} - \frac{\sigma Z_0 F}{4} \tag{A.55}$$

where the only sources present are the transverse current and the outgoing wave's conduction current (the right hand side of the equation). However, the left hand side of equation (A.55)

suggests the size of the incoming wave is mediated by the air conductivity. Also, when *F* saturates the right hand side is approximately zero (the currents cancel), resulting in

$$\frac{\partial G}{\partial \tau} + \frac{\sigma Z_0 G}{4} \cong 0 \tag{A.56}$$

that is, the incoming wave has no significant source. This supports the idea of neglecting the incoming wave altogether.

The original transformations simplify to

$$F \cong 2E_x \tag{A.57}$$

$$E_x \cong Z_0 H_y \tag{A.58}$$

Hence, referring to the first of the original transformed equations(A.46) and transforming back to the original form but with G = 0, gives

$$2\frac{\partial E_x}{\partial z} + \sigma Z_0 E_x = -Z_0 J_x^c \tag{A.59}$$

This the called the *outgoing-wave equation* or the *high-frequency approximation [8]* Solving for the early time (low conductivity) phase, provides

$$E_x \cong -\frac{Z_0}{2}\int_0^z J_x \, dz' \tag{A.60}$$

(Karzas and Latter's [8] result for the more appropriate spherical geometry is

$$E \cong \frac{Z_0}{2r}\int_0^r r' J \, dr' \tag{A.61}$$

The saturated field approximation result is

$$E_x \cong -\frac{J_x}{\sigma} \tag{A.62}$$

These equations are used to explain the E1–HEMP. However, the other relevant Maxwell equations provide other field values that will influence the conductivity and ionisation processes within the source region and are a necessary in solvers to provide a self-consistent result.

Appendix B

B.1 The Transmission Line Equations (Telegraphers equations)

The transmission-line equations, sometimes called the telegraphers equations describe the propagation of signals along the line. They can be derived in the frequency domain or the time domain. The frequency domain description is usually adopted when considering steady-state analysis. When considering arbitrary waveforms, the time-domain description is usually most valuable. Both rely on the distributed element model in their description.

The equations are the essence of the Transmission Line Modelling technique. The link-lines and stubs that constitute the cells all rely on this description allowing fields to be mapped throughout the domain under investigation.

This appendix will demonstrate how the equations are derived and their relevance for different situations including propagation in the presence of corona development.

Here, a field based derivation will be presented [37].

B.1.1 Related to Two Conductor Transmission Line

The following theory is applied to the x-directed line in Figure B1

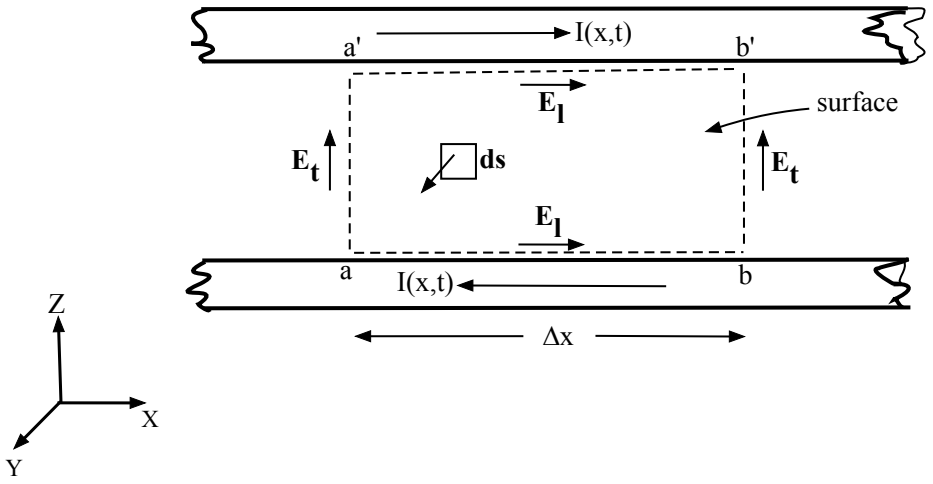

Figure B1 The surface described between a two wire transmission line segment[37].

Assuming the fields obey the quasi-static approximation, that is no TE or TM modes are conveyed, the line integral form of the Maxwell-Faraday equation can be applied to the surface traced in the diagram:

$$\oint \boldsymbol{E} \cdot \mathbf{d}\boldsymbol{l} = \mu \oiint \boldsymbol{H} \cdot \mathbf{d}\boldsymbol{s}$$

giving

$$\int_{a}^{a'} \boldsymbol{E_t} \cdot \mathbf{d}\boldsymbol{l} + \int_{a'}^{b'} \boldsymbol{E_l} \cdot \mathbf{d}\boldsymbol{l} + \int_{a'}^{b} \boldsymbol{E_t} \cdot \mathbf{d}\boldsymbol{l} + \int_{b}^{a} \boldsymbol{E_t} \cdot \mathbf{d}\boldsymbol{l} = \mu \frac{d}{dt} \oiint \boldsymbol{H_t} \cdot \mathbf{d}\boldsymbol{s} \tag{B.1}$$

where $\boldsymbol{E_t}$ and $\boldsymbol{E_l}$ denote the transverse and longitudinal electric fields respectively. The longitudinal integrals on the LHS of (B.1) will be zero if the line and ground are considered perfectly conducting. Otherwise, imperfect conductors will demand a per-unit resistance.

Hence, assuming this situation, the integrals on the left hand side become:

$$V(x,t) = -\int_{a}^{a'} \boldsymbol{E}_t(x,y,z,t) \cdot \mathbf{d}\boldsymbol{l} \tag{B.2}$$

$$V(x+\Delta x,t) = -\int_{b}^{b'} \boldsymbol{E}_t(x+\Delta x,y,z,t) \cdot \mathbf{d}\boldsymbol{l} \tag{B.3}$$

$$-\int_{a'}^{b'} \boldsymbol{E_l} \cdot \mathbf{d}\boldsymbol{l} = -R_1' \Delta x \, I(x,t) \tag{B.4}$$

$$-\int_{b}^{a} \boldsymbol{E_l} \cdot \boldsymbol{dl} = -R_0' \Delta x \, I(x,t) \tag{B.5}$$

The introduction of the imperfect conductor elements is possible only if their presence is assumed not to significantly perturb the fields from the quasi-TEM structure thus maintaining the unique definitions of *V, I* to the relevant transverse field components. (Equations (B.1), (B.2))

Substituting equations (B.2) - (B.5) into equation (B.1), and dividing by Δx we obtain

$$\frac{V(x+\Delta x,t) - V(x,t)}{\Delta x} = -R_1' \, I(x,t) - R_0' \, I(x,t) + \mu \frac{1}{\Delta x} \frac{d}{dt} \oiint \boldsymbol{H_t} \cdot \mathbf{d}\boldsymbol{s} \tag{B.6}$$

The transverse magnetic flux density $\boldsymbol{B_t} = \mu \boldsymbol{H_t}$ produces a magnetic flux $\psi = \oiint \boldsymbol{H_t} \cdot \mathbf{d}\boldsymbol{s}$ Thus a section of line will have an associated inductance *L*. The per-unit length inductance, L', is given by

$$L' = \lim_{\Delta x \to 0} \frac{L}{\Delta x} \tag{B.7}$$

Letting $\Delta x \longrightarrow 0$, equation (B.7) becomes the first transmission line equation:

$$\frac{\partial V(x,t)}{\partial x} = -R' I(x,t) - L' \frac{\partial I(x,t)}{\partial t} \tag{B.8}$$

where $R' = R'_0 + R'_1$.

To derive the second transmission line equation, the continuity equation is used. This ensures conservation of charge through the cylindrical surface depicted in Figure B2

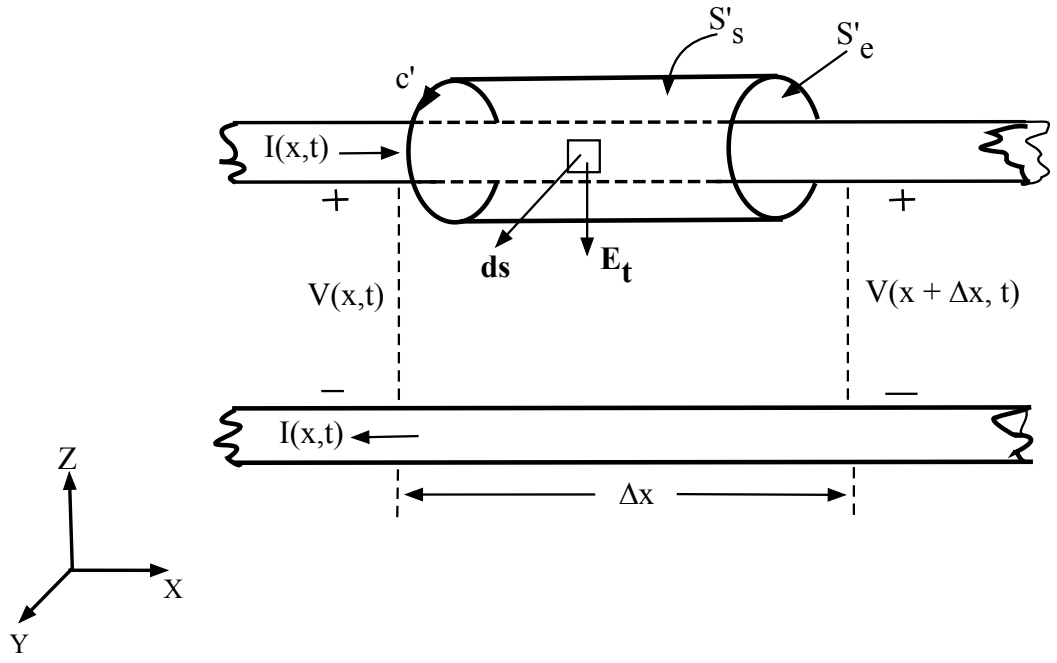

Figure B2. The cylindrical contour introduced to enable derivation of the second transmission-line equation.

$$\oiint \boldsymbol{J} \cdot \mathbf{d}\boldsymbol{s}' \;=\; -\frac{d\, Q_{enc}}{dt} \tag{B.9}$$

Splitting the surface into the ends and sides of the cylinder, the net current density can be described as

$$\oiint \boldsymbol{J} \cdot \mathbf{d}\boldsymbol{s}' \;= I(x + \Delta x, t) - I(x, t) \tag{B.10}$$

For a surrounding medium characterized by a conductivity, σ and permittivity, ε , both conduction current, $\boldsymbol{J_c} = \sigma \boldsymbol{E_t}$ and displacement current, $\boldsymbol{J_d} = \varepsilon\, \partial \boldsymbol{E_t}/\partial t$ penetrate the sides of the cylindrical surface. We have

$$\oiint \boldsymbol{J} \cdot \mathbf{d}\boldsymbol{s}' \;=\; \sigma \oiint \boldsymbol{E_t} \cdot \mathbf{d}\boldsymbol{s}' \tag{B.11}$$

The conductivity, σ, and be described in terms of a per-unit conductance, G', transversely, between the two conductors:

$$G'V(x,t) = \; \sigma \lim_{\Delta x \to 0} \frac{1}{\Delta x} \oiint \boldsymbol{E_t} \cdot \mathbf{d}\boldsymbol{s}' \tag{B.12}$$

The enclosed charge is related to the transverse electric field via Gauss' law

$$Q_{enc} = \; \varepsilon \oiint \boldsymbol{E_t} \cdot \mathbf{d}\boldsymbol{s}'_{\boldsymbol{s}} \tag{B.13}$$

In a similar manner to how the conductivity was related to a per-unit conductance, the charge per unit length can be defined in terms of a per unit capacitance, C' such that

$$C'V(x,t) = \; \varepsilon \lim_{\Delta x \to 0} \frac{1}{\Delta x} \oiint \boldsymbol{E_t} \cdot \mathbf{d}\boldsymbol{s}'_{\boldsymbol{s}} \tag{B.14}$$

Substituting (B.12), (B.13), (B.14), into (B.9) dividing by Δx and letting $\Delta x \longrightarrow 0$ gives the second transmission line equation:

$$\frac{\partial I(z,t)}{\partial z} = -G'V(z,t) - C'\frac{\partial V(z,t)}{\partial t} \tag{B.15}$$

B.2 Relating the TL equations to the Embedded Wire Node (EWN).

The equations can be applied to the behaviour within the EWN. Figure B3 demonstrates the field components associated with an *x*-directed embedded wire.

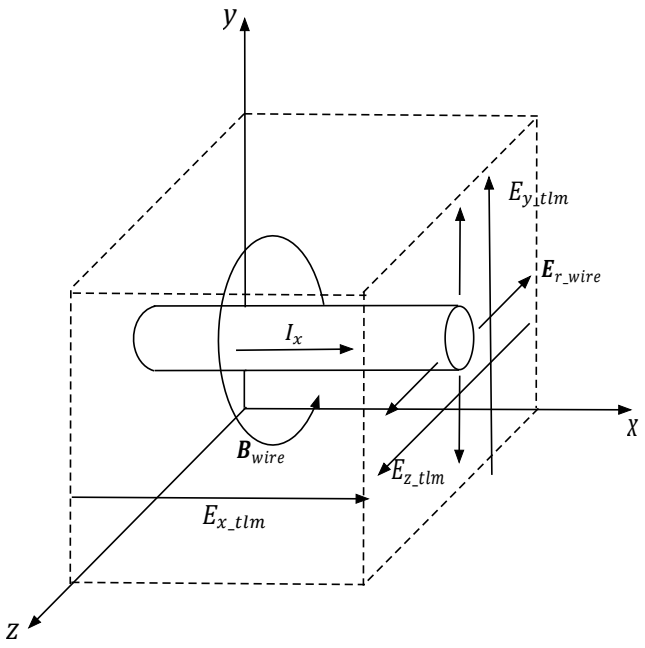

Figure B3. Cuboidal EWN depicting the relevant field components for an *x*-directed embedded wire.

The derivations in the previous section can easily be applied to the node resulting in the following Transmission-line equations for propagation within the EWN:

$$\frac{\partial V(x,t)}{\partial x} + R_0 I_x + L_0 \frac{\partial I}{\partial t} = E_{x\_tlm} \tag{B.15}$$

$$\frac{\partial I(x,t)}{\partial x} + G_0 V(x,t) + C_0 \frac{\partial V(x,t)}{\partial t} = 0 \tag{B.16}$$

The major difference being the field component (E_{x_tlm}) capable of coupling with the embedded wire offered by the outer conductor (SCN) in (B.15).

B.3 TL Equations in the presence of Corona.

The previous sections have demonstrated how propagation of voltage and current pulses along a transmission line with inherent L, C, R, G can be described by two equations. However, a valuable derivation is provided by Cooray and Theethayi (2008) [57] for propagation along lines under the influence of corona. Now, other than the characteristic line parameters, there will be time varying, non-linear parameters related to the corona to consider.

The derivation closely follows that by Agrawal[62] although that derivation refers to multi-conductor arrangements. The derivation is similar to those met previously, but is proposed for a wire above ground, at a height h, and the field about the wire is separated into the scattered and incident components. The ground is considered perfectly conducting.

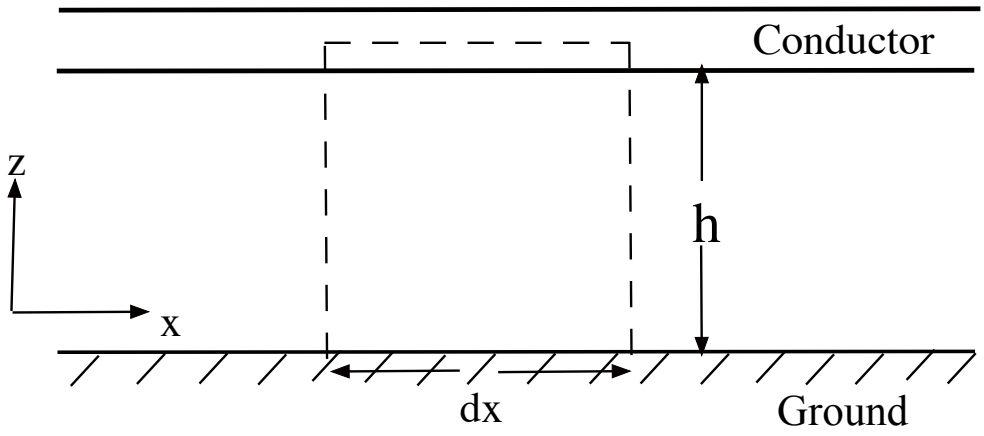

Figure B4. Section of wire above ground. Dotted line traces a surface used to derive the transmission line equation.

Again, the quasi-TLM format is assumed. Starting with Faraday's law

$$\oint \boldsymbol{E} \cdot \mathbf{d}\boldsymbol{l} = \frac{\partial}{\partial t} \iint \boldsymbol{B} \cdot \mathbf{d}\boldsymbol{S} \tag{B.17}$$

$$\int_{\mathbf{0}}^{\boldsymbol{h}} [E_z(x+dx,z,t) - E_z(x,z,t)] \cdot dz = \int_x^{x+dx} E_x(x,h,t)\, dx + \frac{\partial}{\partial t} \int_x^{x+dx} dx \int_0^h B_y(x,z,t) dz \tag{B.18}$$

Dividing by dx, letting $dx \to 0$ and noting $E_x(x,0,t)] = 0$,

$$\frac{\partial}{\partial x} \int_{\mathbf{0}}^{\boldsymbol{h}} E_z(x,z,t)\, dz - E_x(x,h,t) = \frac{\partial}{\partial t} \int_0^h B_y(x,z,t) dz \tag{B.19}$$

The fields around the wire are the sum of incident fields (superscript 'i') and scattered fields (superscript 's') that result from the charges and currents on the wire. In particular:

$$E_x = E_x^i + E_x^s \tag{B.20}$$

$$E_z = E_z^i + E_z^s \tag{B.21}$$

$$B_y = B_y^i + B_y^s \tag{B.22}$$

Substituting (B.20), (B.21) and (B.22) into (B.19) gives

$$\frac{\partial}{\partial x}\int_{\mathbf{0}}^{\boldsymbol{h}} E_z^s(x,z,t)\,dz - \frac{\partial}{\partial t}\int_0^h B_y^s(x,z,t)dz - E_x(x,h,t) = -\frac{\partial}{\partial x}\int_{\mathbf{0}}^{\boldsymbol{h}} E_z^i(x,z,t)\,dz - \frac{\partial}{\partial t}\int_0^h B_y^i(x,z,t)dz \tag{B.23}$$

Based on the assumption all fields are TEM, a unique scattered voltage, $V^s(x,t)$, can be ascribed to the line integral of the transverse electric field component between wire and ground:

$$V^s(x,t) = -\int_0^h E_z^s(x,z,t)\cdot dz \tag{B.24}$$

and the flux linkage, related to the inductance per-unit length, L':

$$\int_0^h B_y^s(x,z,t)\cdot dz = L'\cdot I(x) \tag{B.25}$$

Substituting (B.24) and (B.25) into (B.23)

$$\frac{\partial V_s(x,t)}{\partial x} + L' \frac{\partial I(x,t)}{\partial t} + E_z(x,h,t) = \frac{\partial}{\partial x}\int_{\mathbf{0}}^{\boldsymbol{h}} E_z^i(x,z,t)\, dz - \frac{\partial}{\partial t}\int_0^h B_y^i(x,z,t) dz \quad \text{(B.26)}$$

The RHS of (B.26) can be simplified again applying Faraday's law (B.17), i.e.

$$\frac{\partial}{\partial x}\int_{\mathbf{0}}^{\boldsymbol{h}} E_z^i(x,z,t)\, dz - \frac{\partial}{\partial t}\int_0^h B_y^i(x,z,t) dz = E_x^i(x,z,t) \quad \text{(B.27)}$$

while on the LHS,

$$E_z(x,h,t) = R' \cdot I(x,t) \quad \text{(B.28)}$$

where R is the resistance per-unit-length of the wire.

Hence, substituting (B.27) (B.28) into (B.26) results in the first transmission line equation (B.29):

$$\frac{\partial V^s(x,t)}{\partial x} + R' I(t,x) + L' \frac{\partial I(t,x)}{\partial t} = E_x^i(t,x,h) \quad \text{(B.29)}$$

The scattered voltage is now a result of charges on the line and charge within the coronal sheath.

The second transmission line is derived in a similar way to the previous sections, starting with the continuity equation. However, the equation is now applied to the closed cylindrical surface around the wire with length Δx and radius R_c corresponding to the radius of the

coronal sheath around the wire as in Figure B5. The continuity equation directly results from the Maxwell-Ampere equation:

$$\nabla \times \boldsymbol{H} = \boldsymbol{J} + \frac{\partial \boldsymbol{D}}{\partial t} \tag{B.30}$$

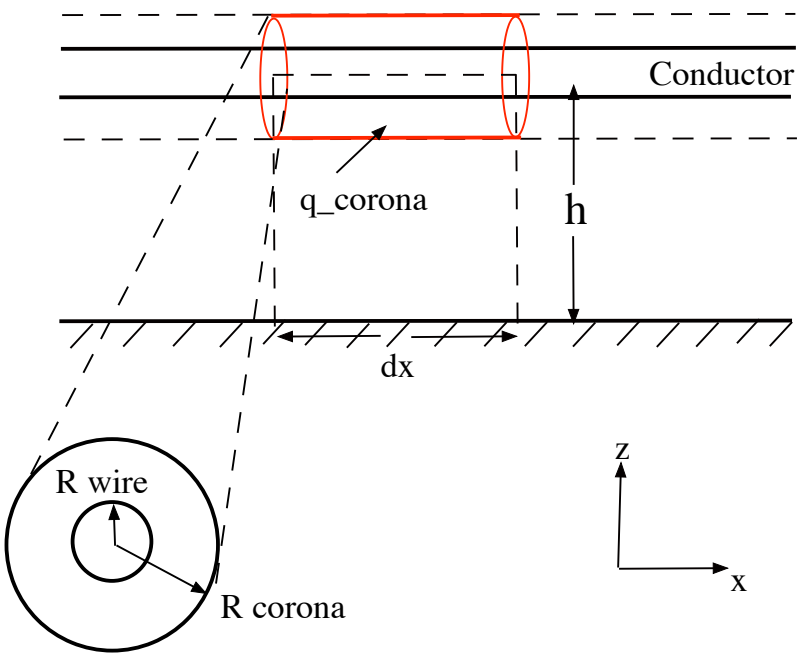

Figure B5 The cylindrical Gaussian surface around the conductor used to derive the second transmission line equation.

Taking the divergence of both sides of (B.30), gives

$$\nabla \cdot \left(\boldsymbol{J} + \frac{\partial \boldsymbol{D}}{\partial t} \right) = 0 \tag{B.31}$$

and in its integral form, can be written

$$\iint \boldsymbol{J} \cdot \mathrm{d}\boldsymbol{s} = -\frac{\partial}{\partial t} \iint \boldsymbol{D} \cdot \mathrm{d}\boldsymbol{s} \tag{B.32}$$

The current density passing through the cylindrical surface can be split into parts; the ends of the cylinder and the main cylindrical surface. The only non-trivial current density is that passing through the wire:

$$\iint J_{ends} \cdot \mathrm{d}s = I(x + dx, t) - I(x, t) \tag{B.33}$$

$$\iint J_{surf} \cdot \mathrm{d}s = 0 \tag{B.34}$$

The RHS of (B.32) refers to the rate of change of displacement field, with time, through the given surface. This equates to the rate of change of total charge , $Q(x,t)$ enclosed within the surface (wire and space charge)

$$\frac{\partial}{\partial t} \iint D \cdot \mathrm{d}s = \frac{\partial Q(x,t)}{\partial t} \tag{B.35}$$

Where

$$Q(x,t) = q_a(x,t) + q_c(x,t) \tag{B.36}$$

The total charge ; comprised of the wire charge , q_a, and the corona charge , q_c can be related to the line voltage (scattered) , $V^s(x,t)$ via a capacitance per unit length. Hence, the line capacitance, C' relates to the wire charge as

$$q_a(x,t) = C'V^s(x,t) \tag{B.37}$$

Substituting equations (B.33) to (B.37) into (B.32) gives

$$I(x+dx,t) - I(x,t) = -C' \frac{\partial V^s(x,t)}{\partial t} dx - \frac{\partial q_c(x,t)}{\partial t} dx \tag{B.36}$$

Dividing through by dx and taking the limit as $dx \to 0$ gives the second transmission line equation in the presence of corona:

$$\frac{\partial I(x,t)}{\partial x} + C' \frac{\partial V^s(x,t)}{\partial t} = -\frac{\partial q_c(x,t)}{\partial t} \tag{B.37}$$

The significance of the transmission line equations in the presence of corona development is detailed in chapter 4.